THE SCIENTIST DOES NOT STUDY NATURE BECAUSE IT IS USEFUL; HE STUDIES IT BECAUSE HE DELIGHTS IN IT, AND HE DELIGHTS IN IT BECAUSE IT IS BEAUTIFUL. IF NATURE WERE NOT BEAUTIFUL, IT WOULD NOT BE WORTH KNOWING, AND IF NATURE WERE NOT WORTH KNOWING, LIFE WOULD NOT BE WORTH LIVING.

HENRI POINCARÉ, SCIENCE AND METHOD, 1908

RAYMOND E. GOLDSTEIN AND ERIC LAUGA

BIOLOGICAL PHYSICS AND FLUID DYNAMICS

(A GRADUATE COURSE IN 24 LECTURES)

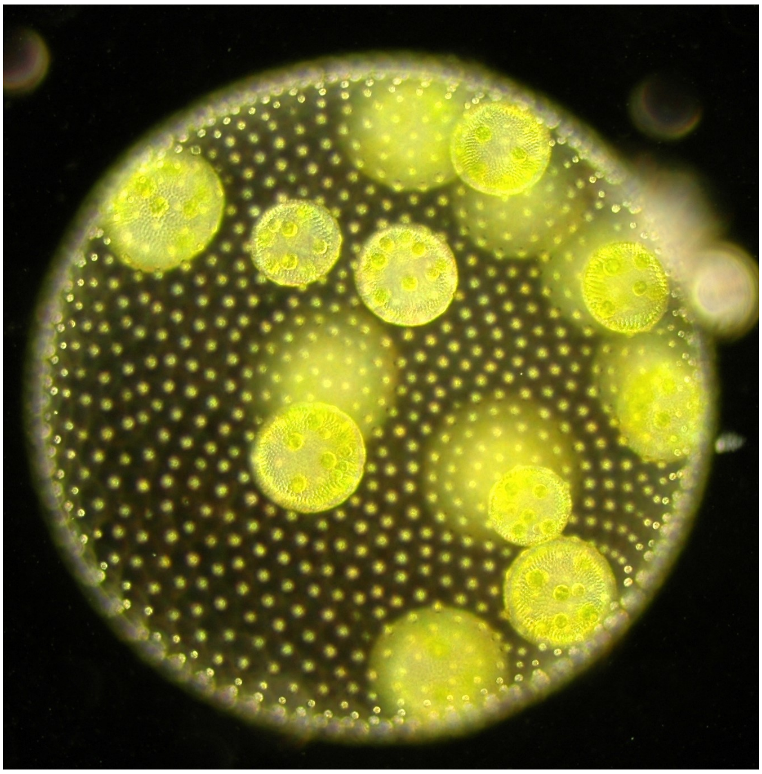

DEPARTMENT OF APPLIED MATHEMATICS AND
THEORETICAL PHYSICS, UNIVERSITY OF CAMBRIDGE

PUBLISHED BY DEPARTMENT OF APPLIED MATHEMATICS AND
THEORETICAL PHYSICS, UNIVERSITY OF CAMBRIDGE

First printing, June 2023

Contents

List of Figures

List of Tables

Dedicated to John O. Kessler (1928-2022) and Howard C. Berg (1934-2021), whose enthusiasm for biological physics and deep physical insight were a profound inspiration.

Preface

Physics and Biology have been intertwined since the dawn of modern science, from Antony van Leeuwenhoek's use in 1700 of advanced optics to reveal the hidden world of microscopic life,[1] to Bonaventura Corti's 1774 discovery of the persistent fluid motion inside large eukaryotic cells,[2] Robert Brown's 1828 study of random motion at the microscale[3] and Theodor Engelmann's determination in 1882 of the wavelength dependence of photosynthetic activity.[4] Although at the time it might have been difficult to define the precise disciplines of each of these scientists—perhaps they were all 'natural philosophers'—in hindsight we can see clearly the way in which their discoveries impacted both biology and physics. Despite this long history of discoveries at the boundary between the two fields, and the innumerable fundamental contributions to both disciplines over the long arc of time, the field of *biological physics* as a discipline within the research enterprise of physics has only risen to great prominence since the postwar era, particularly since the mid 1980s. We are now at the point that most academic physics departments have an identifiable group in biological physics alongside those in high energy, condensed matter, atomic and astrophysics.

As a subject, biological physics is in a much earlier stage of development than the traditional ones found in physics or applied mathematics curricula. This makes it an exciting field in which to work, but also poses challenges for students and faculty, as there is no universally accepted canon to follow. Instead, each lecturer has had to cobble together concepts and presentations from a number of disparate sources to arrive at a syllabus. These lecture notes have been developed very much in that spirit. They derive from several master's level (Part III) courses taught by each of us, sometimes in collaboration with Prof. Ulrich Keyser of the Cavendish Laboratory. We have attempted to strike a balance between *coverage*, *depth*, and *pedagogy* in order to address —in the 24 lectures of a Cambridge term—topics in biological physics that cover length scales from the molecular to the terrestrial. We presume no prior exposure to the subject, but assume familiarity with the basic ideas of statistical physics, electromagnetism, nonlinear dynamics, and fluid mechanics. As this is primarily a course for Part III students in the mathematical Tripos, the presentation often includes digressions into the applied mathematical aspects of the problems at hand.

We have organised the topics covered by these notes roughly in or-

[1] van Leeuwenhoek, A. IV. Part of a letter from Mr. Antony van Leeuwenhoek, concerning the worms in sheeps livers, gnats, and animalcula in the excrements of frogs. *Philos. Trans. R. Soc.*, 22:509–18, 1700

[2] B. Corti. *Osservazioni Microscopische sulla Tremella e sulla Circolazione del Fluido in Una Pianta Acquajuola*. Appresso Giuseppe Rocchi, Lucca, Italy, 1774

[3] Brown, R. XXVII. A brief account of microscopical observations made in the months of June, July, and August, 1827, on the particles contained in the pollen of plants; and on the general existence of active molecules in organic and inorganic bodies. *Philos. Mag.*, 4:161–73, 1828

[4] Engelmann, T.W. Ueber Sauerstoffausscheidung van Pfalnzenzellen im Mikrospektrum. *Pflüger, Arch.*, 27: 485–89, 1882

der of increasing length scales, from the basic molecular forces that govern the cohesion and interaction of molecules and supramolecular assembles, the elastic properties of filaments and membranes, the role of thermal fluctuations in their conformation and interactions, on to cellular motion, chemical kinetics and pattern formation. Our approach is to give a sampling of the phenomena and their analysis at each of the length scales of interest. Even with the goal of brevity in mind, it is likely that covering *all* of these notes in 24 lectures is a challenge. For further readings, we refer the student to a number of excellent textbooks that have appeared in recent years covering various aspects of biological physics[5] and physical biology,[6] as well as more specialized works on elasticity.[7] Much motivation for the physicist's approach to biology comes from D'Arcy Wentworth Thompson's classic book,[8] and we recommend highly the classic text on applied mathematics by Lin and Segel.[9] Where possible, we have included references to the original, often old literature, in the belief that reading such scientific works is highly worthwhile.[10]

Associated with these notes is a set of Example Sheets. In many places throughout the text we have deliberately left out certain calculational details to encourage the reader to fill them in. At the same time, we have taken pains to explain in a fair amount of detail the ins and outs of various key calculations. While we emphasize analytical calculations throughout the text, there are many contexts in which numerical work is an important adjunct to those calculations, whether for something as simple as understanding the detailed shape of a function, finding the roots of a transcendental equation, or to solve a nonlinear PDE to understand its global behaviour. To that end we have provided a series of simple Matlab programs for these various tasks, named according to the figure(s) produced by them. In addition, we have organized the references so that clicking on the author names links to a collection of pdfs of all of the references (apart from books), while clicking on the article title takes one to the original journal article.

These lecture notes are meant to be a living document, easily changed in response to comments and corrections suggested by students and colleagues who use them, and also able to expand over time to cover more topics in biological physics. We can already see the possibility of chapters on population biology, systems biology, taxes (chemotaxis, phototaxis), a more in-depth treatment of elasticity, and computation.

We are grateful to George T Fortune for a careful proofreading of this entire set of notes, and to Thomas Powers, xxx, and yyy for detailed comments on drafts. Any remaining errors or omissions are of course our own, and we look forward to hearing from users of these notes of any further corrections or suggested modifications.

R E Goldstein and E Lauga, July 2023

---

[5] P. Nelson. *Biological Physics: Energy, Information, Life*. Chiliagon Science, Philadelphia, PA, student edition, 2020

[6] R. Phillips, J. Kondev, J. Theriot, H.G. Garcia, and N. Orme. *Physical Biology of the Cell*. Garland Science, Boca Raton, FL, 2nd edition, 1998

[7] B. Audoly and Y. Pomeau. *Elasticity and Geometry: From hair curls to the non-linear response of shells*. Oxford University Press, Oxford, UK, 2010

[8] D.W. Thompson. *On Growth and Form*. Dover Publications, Mineola, N.Y., the complete revised edition, 1992

[9] C.C. Lin and L.A. Segel. *Mathematics Applied to Deterministic Problems in the Natural Sciences*. Macmillan Publishing Co., Inc., New York, 1974

[10] Goldstein, R.E. Coffee stains, cell receptors, and time crystals: Lessons from the old literature. *Phys. Today*, 71:32–38, 2018

1

Overview (Lecture 1)

1.1 Length scales and methodologies

The field of biological physics covers phenomena spanning an enormous range of length scales. Historically, there was great emphasis placed on the cellular scale of microns,[1] but as the field broadens to include problems ranging from neuroscience to development and even ecology, that range now extends to kilometers (Fig. 1.1).

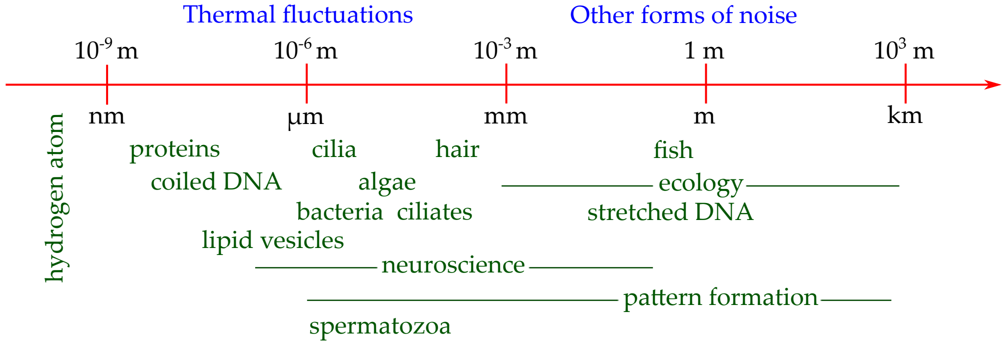

Figure 1.1: The range of length scales considered in these notes and a sampling of the living systems of interest.

In this course we will study methods to quantify the physics of living systems on many of these scales. While many of the underlying properties of the components of cells, tissues, and organisms can be described by molecular physics and its continuum generalisations, life is inherently out of equilibrium and characterized by "noise" from many sources. At the smallest scales—from nanometers up to hundreds of microns—equilibrium thermal fluctuations may be dominant, but even there, and certainly at larger scales, descriptions must incorporate such features as biochemical fluctuations within single organisms and organism-to-organism phenotypic variability. Thus, the mathematical methods utilized here include not only equilibrium statistical physics, but also deterministic and stochastic ordinary and partial differential equations of various types. In addition, many of the important questions in biological physics involve understanding the time-dependent geometry of living matter and its constituents. In order to make these notes self-contained we have included where appropriate some background material on differential geometry and geometric evolution, and provided references to more complete treatments in the literature.

[1] Berg, H.C. and Purcell, E.M. Physics of chemoreception. *Biophys. J.*, 20:193–219, 1977

One of the key lessons of applied mathematics is the importance of proper rescaling of the governing equations to reveal the relevant (dimensionless) control parameters that determine the behaviour. Not only is this good practice in solving problems, it also promotes a point of view that focuses on the size of the parameter space and the scaling laws that underlie a given phenomenon. It serves to make clear the conclusions of models in interdisciplinary collaborations.[2]

A corollary to the above is that, in biological physics, *numbers matter*. That is to say, gaining an intuitive feel for the typical sizes of things, energy scales, and time scales is very important in building a quantitative picture for a given problem. But what system of units should we use? Many physicists and applied mathematicians have been educated to use the MKS system, but its use can lead to very awkward numbers; take for example the bending modulus k_c of a cell membrane, whose typical value might be 4×10^{-20} N·m, thus having the units of energy. We shall see that the typical forces on the cellular scale are picoNewtons (pN), and with typical sizes of molecular constituents being nanometres (nm), the scale pN·nm is more appropriate, for then $k_c \sim 40$ pN· nm. And, most importantly, with the Boltzmann constant $k_B = 1.38 \times 10^{-23}$N·m/K and the absolute temperature $T = 300$K, thermal energy $\mathrm{k}_B\mathrm{T}$ is $\sim 4 \times 10^{-21}$ N·m or

$$k_B T \simeq 4\,\mathrm{pN} \cdot \mathrm{nm}. \tag{1.1}$$

Thus, concisely, the bending modulus is $k_c \sim 10\, k_B T$.

Table 1.1 collects the first set of physical quantities that will appear in these notes. Other tables will follow as we develop the subject.

quantity	symbol/definition	value	alternate units
viscosity of water	μ	0.01 g/cm·s (1 cP)	0.001 kg/m·s
density of water	ρ	1 g/cm^3	10^3 kg/m^3
kinematic viscosity of water	ν	0.01 cm^2/s	10^6 μm^2/s
dielectric constant of water	ϵ	80	
acceleration of gravity	g	10 m/s^2	10^7 μm/s^2
size of a bacterium	major axis	$(1-3) \times 10^{-4}$ cm	$1-3\,\mu$m
size of unicellular algae	radius	5×10^{-4} cm	$5\,\mu$m
size of multicellular algae	radius	$(100-400) \times 10^{-4}$ cm	$100-400\,\mu$m
charge of the proton	e	1.6×10^{-19} C	
membrane thickness	δ	$(3-5) \times 10^{-9}$ m	3-5 nm
membrane elastic modulus	k_c	4×10^{-20} N·m	10 k$_B$T

Table 1.1: Some physical quantities used in these notes.

1.2 *Scaling arguments*

We now turn to several examples that illustrate the power of scaling arguments (sometimes called dimensional analysis, as usually attributed to Rayleigh[3]) to reveal the essential physics in a problem, and to point out several particular features of the cellular scale that will become our primary focus.

Although quantum phenomena will make only a cursory appearance in these notes (when we discuss molecular interactions in Chapter 2), the hydrogen atom provides our first example of scaling arguments. Letting m be the reduced mass of the two-body system

[2] Goldstein, R.E. Are theoretical 'results' results? *eLife*, 7:e40018, 2018

[3] Maxwell, J.C. Remarks on the mathematical classification of physical quantities. *Proc. London Math. Soc.*, s1-3:224, 1869

(proton + electron), the kinetic energy is $p^2/2m$, where p is the momentum, while the potential energy (in the Gaussian system of units) is $-e^2/r$, where r is the separation between electron and proton. If we invoke the de Broglie relation $p = h/\lambda$ between the momentum p and the associated particle wavelength λ, and the quantization condition $\lambda = 2\pi r/n$ for some integer n, then $p = n\hbar/r$, there is a single length scale r that governs the physics, and the total energy is

$$E(r) \sim \frac{n^2\hbar^2}{2mr^2} - \frac{e^2}{r}. \tag{1.2}$$

The function $E(r)$ diverges to $+\infty$ as $r \to 0$ and approaches 0 from below as $r \to \infty$, having thus a single minimum. We find r by minimising $E(r)$, yielding the minimiser

$$r_n^* = \frac{n^2\hbar^2}{me^2} \quad \text{and} \quad E_n(r_n^*) = -\frac{me^4}{2n^2\hbar^2}. \tag{1.3}$$

Here, r_n^* is $n^2 r_B$, where r_B is the Bohr radius, and $E_n = Ry/n^2$, where Ry is the Rydberg constant. These are the exact values for the hydrogen atom. Note that this approach required none of the intricate analysis of Laguerre polynomials or any other aspects of the full solution to the Schrodinger equation,[4] and even obtains the correct factor of 2 in the Rydberg constant.

A second approach to Eq. 1.2, more in keeping with the ethos of Applied Mathematics,[5] is to balance the two terms on the r.h.s., so $n^2\hbar^2/mr^2 \sim e^2/r$ (ignoring the factor of 2), which implies the existence of a length $r_n \sim n^2\hbar^2/me^2$. If we define a dimensionless radius R and dimensionless energy $\mathcal{E}$ as

$$R = \frac{r}{r_n} \quad \text{and} \quad \mathcal{E} = \frac{E}{me^4/2n^2\hbar^2}, \tag{1.4}$$

then we obtain the marvellously simple result

$$\mathcal{E} = \frac{1}{R^2} - \frac{2}{R}, \tag{1.5}$$

which is minimised at $R = 1$, giving $\mathcal{E} = -1$, as above. The absence of any explicit physical parameters from (1.5) indicates that a "natural" system of units has been identified.

Let us now turn to an important biophysical question concerning the role of inertia in the motion of microscopic organisms such as bacteria.[6] Suppose we have a spherical body of radius a and density ρ equal to that of the surrounding fluid, whose viscosity is μ. Let $x(t)$ be its position during one-dimensional motion. Then the equation of motion is

$$\frac{4}{3}\pi a^3 \rho \frac{d^2x}{dt^2} = -6\pi\mu a \frac{dx}{dt}, \tag{1.6}$$

where we have invoked the Stokes drag force $6\pi\mu a v$ on a particle moving with speed $v = dx/dt$. We wish to answer the question: if the particle initially is moving with speed v_0, how long will it take to come to rest under the action of drag, and how far will it

[4] L.D. Landau and E.M. Lifshitz. *Quantum Mechanics. Non-relativistic theory*. Pergamon Press, Oxford, UK, 2nd edition, 1965

[5] C.C. Lin and L.A. Segel. *Mathematics Applied to Deterministic Problems in the Natural Sciences*. Macmillan Publishing Co., Inc., New York, 1974

[6] Purcell, E.M. Life at low Reynolds number. *Am. J. Phys.*, 45:1–11, 1977

travel during that time? Without solving this explicitly we can simply assume there is a characteristic time τ and displacement ℓ (the "coasting length") and balance terms, setting

$$\frac{4}{3}\pi a^3 \rho \frac{\ell}{\tau^2} \sim 6\pi\mu a \frac{\ell}{\tau} \tag{1.7}$$

to obtain

$$\tau = \frac{2}{9}\frac{a^2}{\nu} \quad \text{and} \quad \ell = v_0\tau, \tag{1.8}$$

where $\nu = \mu/\rho$ is the kinematic viscosity, with units of length^2/time. From the structure of Eq. 1.6, we expect exponential decay of the motion, with decay time τ.

To get a feel for these quantities, let us consider a bacterium with $a \sim 2\,\mu$m; from Table 1.1 we then have $\tau \sim 10^{-6}$ s: one *microsecond*! If the initial speed is, say, $v_0 = 10\,\mu$m/s, the distance traveled is $\ell \sim 10^{-5}\,\mu$m $= 10^{-2}$ nm, far less than the size of the bacterium, and indeed just a small fraction of the Bohr radius (0.05 nm)! We conclude that inertia is completely irrelevant to the motion of micron-sized objects in water. In this simple picture, inertia would only begin to matter when the coasting length is comparable to the particle radius. Setting these equal leads to the critical radius

$$a_c \sim \frac{9\nu}{2v_0}. \tag{1.9}$$

From this we see that even when the speed is $\sim 500\,\mu$m/s, which is among the highest speeds known for large multicellular algae such as *Volvox carteri* shown in Fig. 1.2,[7] the critical radius would still be ~ 1 cm, an order of magnitude larger than those organisms. Thus, there is a vast range of organisms that swim in the low Reynolds number world. This subject will be covered in detail in Chapter 6.

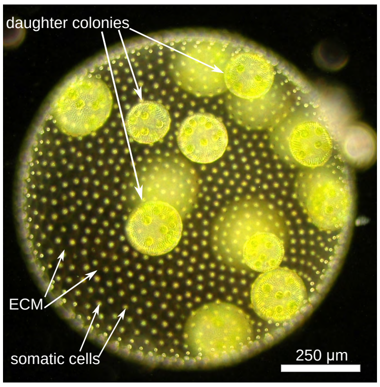

Figure 1.2: The green alga *Volvox*. It consists of $\sim 10^3$ biflagellated somatic cells embedded in a transparent extracellular matrix (ECM), with a small number of daughter colonies that grow up inside the spheroid.

We are now in a position to understand the relationship between thermal energy and diffusion, as first done by Einstein[8] and Sutherland.[9] The basic idea is to consider a suspension of microscopic particles at concentration $c(x)$, with diffusion constant D, acted on by a force $F(x) = -d\phi/dx$, where ϕ is the potential energy. The flux J of particles is the sum of a Fick's law contribution and an advective term with some speed u,

$$J = -D\frac{dc}{dx} + uc. \tag{1.10}$$

In the viscous regime, the speed u is determined by the force balance $\zeta u = -d\phi/dx$, where $\zeta = 6\pi\mu a$ for spherical particles. To determine D by the principles of equilibrium statistical physics we must indeed be in equilibrium, with $J = 0$. Integrating (1.10), we obtain

$$c \sim \exp(-\phi/D\zeta). \tag{1.11}$$

If this is to be consistent with the Boltzmann factor of statistical physics, then $D\zeta = k_BT$ or

$$D = \frac{k_BT}{6\pi\mu a} \simeq \frac{0.2}{\tilde{a}}\frac{\mu\text{m}^2}{s}. \tag{1.12}$$

[7] Goldstein, R.E. Green algae as model organisms for biological fluid dynamics. *Annu. Rev. Fluid Mech.*, 47:343–375, 2015

[8] Einstein, A. Investigations on the theory of the Brownian movement. *Ann. d. Phys.*, 17:549–560, 1905

[9] Sutherland, W. LXXV. A dynamical theory of diffusion for non-electrolytes and the molecular mass of albumin. *Phil. Mag.*, 9:781–785, 1905

The second relation holds for water at room temperature, where $\tilde{a}$ is the radius in microns. This immediately reveals that a small molecule on the order of 2Å ($\tilde{a} \sim 2 \times 10^{-4}$) has $D \sim 10^3\,\mu\text{m}^2/\text{s}$, whereas a $2\,\mu$m microsphere of the kind used to trace flows has $D \sim 0.1\,\mu\text{m}^2/\text{s}$.

From the diffusion equation

$$\frac{\partial c}{\partial t} = D\nabla^2 c, \tag{1.13}$$

we see by dimensional analysis that lengths ℓ and time t are related by $Dt \sim \ell^2$ or

$$t \sim \frac{\ell^2}{D}. \tag{1.14}$$

From the values of D derived above, we see that the time it takes a small molecule to diffuse across a bacterium ($\ell \sim 1\,\mu$m) is 10^{-3}s, while that to cross a colony of *Volvox* ($\ell \sim 300\,\mu$m) is about 10^3 s $\sim$ 16 minutes. On the other hand, consider the aquatic plant *Chara corallina* (Fig. 1.3). Its cells are some of the largest known to science; they can reach $\ell \sim 10\,\text{cm} = 10^5\,\mu$m, giving a diffusive timescale of $\sim 10^7$ s. Remembering that there are about 10π megaseconds in a year (3.15×10^7), this time is about 4 months!

Figure 1.3: The aquatic plant *Chara corallina*.

Clearly, diffusion is not effective for large eukaryotic cells, and some active transport mechanism is needed. This point was emphasized eloquently by J.B.S. Haldane many years ago in a famous essay.[10] One such mechanism involves cargo transport by "motor proteins" moving along filaments in the cell, or indeed by the fluid entrained by their motion, a phenomenon termed *cytoplasmic streaming* that was first discovered in plants such as *Chara* as long ago as 1774.[11] At larger scales there are ever more complex vascular systems driving by muscular pumps.

As a final exercise in the use of dimensional analysis we ask about the typical scale of voltages to be expected inside living systems. We have in mind a situation like that in neurons, in which there are differences in ionic concentrations across membranes. Since the chemical potential for a dilute solution of ions at concentration c is $k_BT\ln c$, the difference in chemical potential between the inside and outside of a membrane must be $k_BT\ln(c_{\text{in}}/c_{\text{out}})$. Setting this equal to the electrostatic energy eV for an elementary charge to move through the voltage difference across the membrane, we find

$$V \sim \frac{k_BT}{e}\ln\left(\frac{c_{\text{in}}}{c_{\text{out}}}\right). \tag{1.15}$$

From Table 1.1 we obtain $k_BT/e \sim 25\,\text{mV}$, which is indeed the basic scale of voltages across neuronal membranes,[12] as we shall discuss in Chapter 7.

[10] Haldane, J.B.S. On Being the Right Size, 1927

[11] B. Corti. *Osservazioni Microscopische sulla Tremella e sulla Circolazione del Fluido in Una Pianta Acquajuola*. Appresso Giuseppe Rocchi, Lucca, Italy, 1774

[12] Hodgkin, A.L. and Huxley, A.F. A quantitative description of membrane current and its application to conductance and excitation in nerve. *J. Physiol.*, 117:500–544, 1952

2

Microscopic Physics (Lectures 2-4)

2.1 Review of molecular physics

At the smallest scales of interest in these lectures we are concerned with the elementary interactions between molecules, and how they determine interactions between more extended objects such as membranes. To that end, we review the basics features of van der Walls interactions between atoms, and of screened electrostatics, along with some basic principles in non-ideal gas theory that serve as the basis of molecular solutions, including those that can separate into distinct phases. Although it might seem that a discussion of matters related to equilibrium phase transitions is somewhat off-topic in a course on biological physics, it is important to note that a rapidly growing body of recent work has shown that the phenomenon of liquid-liquid phase separation plays a crucial role inside many cells.[1]

The ideal gas law,

$$pV = Nk_BT \quad \text{or} \quad \frac{p}{k_BT} = \rho\ , \tag{2.1}$$

relates the pressure p, volume V, and number of molecules N, where k_B is the Boltzmann constant, T is the absolute temperature and $\rho = N/V$ is the density. It is, of course, only an approximation. At low densities real gases are described by a "virial expansion",

$$\frac{p}{k_BT} \simeq \rho + B_2(T)\rho^2 + B_3(T)\rho^3 + \cdots\ . \tag{2.2}$$

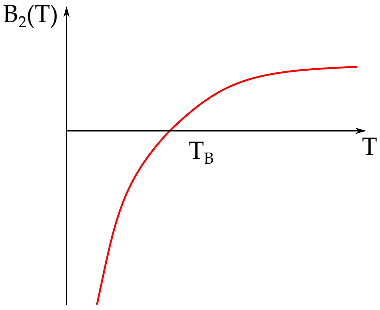

Figure 2.1: Temperature dependence of the second virial coefficient of a gas.

where the B_i are termed "virial coefficients". Intuitively, the quadratic term in ρ involves 2-body interactions, the cubic term captures 3-body effects, and so on. Experimental measurements (Fig. 2.1) of the second virial coefficient B_2 show that it is negative at low temperatures (indicating attraction between pairs) and becomes positive (repulsive) at high temperatures, crossing through zero at the so-called Boyle point T_B.

One of the great early triumphs of statistical physics was to show how $B_2(T)$ arises from the underlying intermolecular potential. Its derivation gives us an opportunity to review some basic features of classical statistical physics that will be needed later. For the purpose of this deviation, it is more convenient to work in the canonical ensemble, although the more systematic approach uses the grand

---

[1] Hyman, A.A., Weber, C.A. and Jülicher, F. Liquid-liquid phase separation in biology. *Annu. Rev. Cell Dev. Biol.*, 30:39–58, 2014

canonical ensemble.[2] We assume that classical statistical physics is valid, whereby if the energy of a system of N particles of mass m is

$$E = \sum_i \frac{\mathbf{p}_i^2}{2m} + \sum_{i<j} u(\mathbf{r}_i, \mathbf{r}_j), \tag{2.3}$$

where $\mathbf{p}_i$ is the momentum of particle i. Here, u is the intermolecular potential that we assume is only a function of the distance $r_{ij} = |\mathbf{r}_i - \mathbf{r}_j|$, and the restriction on the sum avoids double-counting. The classical partition function for the N-particle system is then

$$Z = \frac{1}{h^{3N}} \frac{1}{N!} \int d^{3N}p \int d^{3N}r \, \mathrm{e}^{-\beta E}, \tag{2.4}$$

where $\beta = 1/k_B T$ and the notation $d^{3N}p$ stands for $d\mathbf{p}_1 d\mathbf{p}_2 \ldots$, etc. Recall that the factor of h^{-3N} is a vestige of the fully quantum approach, where one must measure volumes in phase space, and serves to render Z dimensionless (recall that the product of a coordinate and a momentum has units of angular momentum (energy×time), as does h). The factor of $1/N!$ arises from the indistinguishability of the particles.

Recognising that the configurational integral $\int d^{3N}r \cdots$ is V^N for a non-interacting system ($u = 0$), where V is the volume of the system, and that the momentum integrals can be done explicitly, independent of the presence of u, we can factor out the ideal, non-interacting partition function Z_0, leaving the interacting part Q, as

$$Z = \underbrace{\frac{1}{N!} \left(\frac{V}{\Lambda^3} \right)^N}_{Z_0} \underbrace{\frac{1}{V^N} \int d^{3N}r \prod_{i<j} \mathrm{e}^{-\beta u_{ij}}}_{Q}, \tag{2.5}$$

where $u_{ij} = u(r_{ij})$ and $\Lambda = (2\pi\hbar^2/mk_B T)^{1/2}$ is the thermal de Broglie wavelength, and we have written the exponential of a sum as the product of exponentials.

The next step in developing a perturbation theory is to use the first important method of mathematical physics (adding zero), and thus to write

$$\mathrm{e}^{-\beta u_{ij}} = 1 + f_{ij} \quad \text{with} \quad f_{ij} = \mathrm{e}^{-\beta u_{ij}} - 1, \tag{2.6}$$

and observe that f_{ij} vanishes for a non-interacting system, and serves as a small parameter for an expansion in density. The quantity f_{ij} is known as the Mayer f-function.[3] From the exact expression $\prod_{i<j} (1 + f_{ij})$ we can expand for small f, noting that there are $N(N-1)/2 \sim N^2/2$ identical terms linear in f_{ij}, leading to

$$Q = \frac{1}{V^N} \int d^{3N}r \left(1 + \sum_{i<j} f_{ij} + \cdots \right) \tag{2.7}$$

$$\simeq 1 + \frac{N^2}{2V} \int d^3r f(r) + \cdots, \tag{2.8}$$

where, having done $N-1$ integrals, there is one remaining factor of V in the denominator. From the partition function Z we obtain

[2] D.A. McQuarrie. *Statistical Mechanics*. Harper & Row, New York, 1976

[3] Mayer, J.E. Statistical Mechanics of Condensing Systems. I. *J. Chem. Phys.*, 5:67, 1937

the free energy $F = -k_B T \ln Z$, and then from F the pressure $p = -(\partial F/\partial V)_{T,N}$ in the form of Eq. 2.2, and thus we identify

$$B_2 = -\frac{1}{2}\int d^3r \left(\mathrm{e}^{-\beta u(r)} - 1\right) . \tag{2.9}$$

This is an exact expression for B_2.

A typical intermolecular potential $u(r)$ has a strong repulsion at short distances and a long-range attractive tail falling off as r^{-6} as $r \to \infty$ due to van der Waals interactions (the details of which are discussed below), as in Fig. 2.2. It was van der Waals who, in his revolutionary 1873 PhD thesis,[4] had the crucial idea that the thermodynamics of liquids and gases potential could be understood by partitioning the intermolecular potential into two parts: a purely repulsive part that leads to "excluded volume" around each molecule, and a purely attractive part whose effects on the thermodynamics could be estimated within perturbation theory. We can compare this calculation to our results on the virial coefficient.

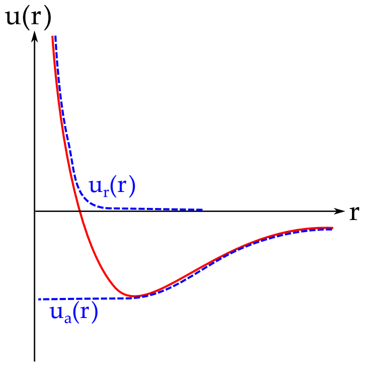

Figure 2.2: Decomposition of molecular interaction potential (red) into purely attractive and purely repulsive components (dashed).

In van der Waals' calculation of the contribution of u_a to the energy of a gas, it is assumed that the probability distribution of particles around a given one (the radial distribution function) is uniform, rather than having the characteristic oscillations due to particle impenetrability. Under this assumption the energy E_a is

$$E_a = \frac{1}{2}N\rho \int d^3r u_a(r) , \tag{2.10}$$

where again the factor of $1/2$ avoids double-counting. We then define the parameter a as

$$a = -\frac{1}{2}\int d^3r\, u_a(r) , \tag{2.11}$$

so $E_a = -aN\rho$ and the contribution to the pressure is $-(\partial E_a/\partial V)_{T,N} = -a\rho^2$. Thus, a first correction to the equation of state is

$$p \simeq \rho k_B T - a\rho^2 . \tag{2.12}$$

Further, van der Waals realized that effect of the hard-core interactions could be accounted for by subtracting from the total volume V an amount proportional to the number of particles N, with an effective excluded volume per particle b. Putting these two effects together one has the revised equation of state

$$(p + a\rho^2)(V - Nb) = Nk_B T \tag{2.13}$$

Expanding p for small ρ we find

$$B_2(T) = b - \frac{a}{k_B T}. \tag{2.14}$$

This has a form that is qualitatively like that seen in experiment (Fig. 2.1), with saturation at high temperatures to a constant, reflecting entropic effects, and a divergence to $-\infty$ at low temperatures as the attractive part of the potential dominates. We conclude that the essence

[4] van der Waals, J.D. *Over de Continuiteit van den Gas- en Vloeistoftoestand (On the continuity of the gas and liquid state)*. PhD thesis, Leiden University, 1873

of the temperature dependence of $B_2(T)$ is captured by the ideas of excluded volume and mean field attraction.

A final point to make is that this result emerges naturally from the exact form of B_2 in Eq. 2.9 if we assume the interaction potential is $+\infty$ between $r = 0$ and some radius σ and sufficiently weak beyond σ that the $\beta u_a(r) \ll 1$. Then,

$$B_2(T) = \frac{2\pi\sigma^3}{3} - \frac{a}{k_B T}, \tag{2.15}$$

where a is defined in (2.11), with the integration from σ to ∞. This gives a precise meaning to the excluded volume parameter b; σ is twice the hard-core radius, so b is four times the particle volume.

An important lesson from above is that interaction terms quadratic in a density or concentration must be interpreted as *free energies*, involving energy and entropy, rather than being purely energetic. Moreover, we see how the integrated strength of the pairwise interaction, as appears in (2.11), arises naturally by mean field arguments. They may also be understood as the zero-momentum values of the Fourier transform of the potential, but for that transform to be well-defined it is necessary to remove the singular repulsive contribution to the potential, as we did in the decomposition of Fig. 2.2.

2.2 *Van der Waals interactions*

2.2.1 *The pairwise intermolecular potential*

Van der Waals' name is of course also associated with the *fluctuating-dipole* interactions between neutral objects. To get insight into the physics responsible for the long-range attraction between neutral atoms or molecules, we follow essentially verbatim the very nice derivation by Holstein.[5] The model of interacting atoms employed is two charged harmonic oscillators with positive charges that are fixed in place at some separation R and whose negative charges can oscillate back and forth under the action of a spring of constant k, as in Figure 2.3. The artifice of a spring connecting each proton and electron introduces a natural oscillation frequency $\omega_0 = \sqrt{k/m}$ for each "atom", where m is the electron mass. The Hamiltonian $\mathcal{H}$ is a sum of the electron kinetic energy and spring energy $\mathcal{H}_0$,

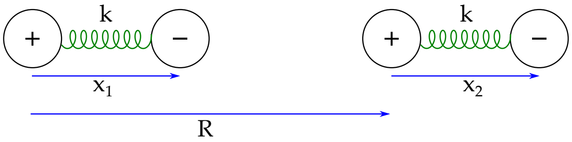

Figure 2.3: Geometry of two interacting "atoms" separated by a distance R, each with electron and proton connected by a spring of constant k, with internal displacements between each electron and its nucleus of $x_{1,2}$.

$$\mathcal{H}_0 = \frac{p_1^2}{2m} + \frac{1}{2}m\omega_0^2 x_1^2 + \frac{p_2^2}{2m} + \frac{1}{2}m\omega_0^2 x_2^2 \tag{2.16}$$

and the electrostatic interactions $\mathcal{H}_1$,

$$\mathcal{H}_1 = e^2\left[\frac{1}{R} + \frac{1}{R - x_1 + x_2} - \frac{1}{R - x_1} - \frac{1}{R + x_2}\right]. \tag{2.17}$$

[5] Holstein, B.R. The van der Waals interaction. *Am. J. Phys.*, 69:441, 2001

This is exact but cumbersome. The physically interesting limit is that of large separations, with $R \gg |x_1|, |x_2|$, where $\mathcal{H}_1$ becomes

$$\mathcal{H}_1 \approx -\frac{2e^2 x_1 x_2}{R^3}, \tag{2.18}$$

whose R^{-3} fall-off with distance we recognize as a dipole term. This cross term can be eliminated through the coordinate transformation

$$x_\pm = \frac{x_1 \pm x_2}{\sqrt{2}} \quad \Rightarrow \quad x_1 = \frac{x_+ + x_-}{\sqrt{2}}, \quad x_2 = \frac{x_+ - x_-}{\sqrt{2}} . \tag{2.19}$$

The total Hamiltonian then becomes

$$\mathcal{H} \simeq \frac{p_1^2}{2m} + \frac{1}{2}m\omega_+^2 x_+^2 + \frac{p_2^2}{2m} + \frac{1}{2}m\omega_-^2 x_-^2, \tag{2.20}$$

where the new frequencies are

$$\omega_\pm^2 = \omega_0^2 \pm \frac{2e^2}{mR^3}. \tag{2.21}$$

Having diagonalised the Hamiltonian, the interaction potential $u(r)$ is just the change to the ground state energy of the system due to the Coulomb interactions, namely the shift is zero-point energies,

$$\begin{aligned} u(r) &= \frac{1}{2}\hbar\omega_+ + \frac{1}{2}\hbar\omega_- - 2\cdot\frac{1}{2}\hbar\omega_0 \\ &\simeq -\frac{1}{2}\hbar\omega_0 \frac{(e^2/m\omega_0^2)^2}{R^6} + \cdots , \end{aligned} \tag{2.22}$$

where we have expanded the frequencies $\omega_\pm$ to leading order. Crucially, this is an *attractive* interaction. In grouping the factors in (2.22), we have isolated the characteristic energy $\hbar\omega_0$ that sets the overall scale for the interaction. It would be typical of an internal excitation energy from an s state to a p state, since the interaction is fundamentally due to virtual transitions to states with dipole moments. Hence, $\hbar\omega_0$ is typically several electron volts, where 1 eV is $40\,\mathrm{k}_B\mathrm{T}$.

Recognizing the R^{-6} dependence, we observe that $e^2/m\omega_0^2$ must be a characteristic volume (remember we are working in Gaussian units!). To check this note that the simplest relationship between an induced electric dipole moment **d** and an applied electric field **E** is

$$\mathbf{d} = \alpha\mathbf{E}, \tag{2.23}$$

where α is the "polarisability". **d** has units of charge×length ($Q \cdot L$), and the units of **E** are Q/L^2, and thus $\alpha \sim L^3$; it is a *volume*. For a hydrogen atom we thus deduce that $\alpha \sim a_0^3$, as the Bohr radius a_0 is the only characteristic length scale.

That it is proper to interpret $e^2/m\omega_0^2$ as the polarisability can be seen by placing the charged harmonic oscillators in Fig. 2.3 in an electric field $E_0\hat{\mathbf{x}}$ acting to displace the electrons only (recall that the positive charges are fixed in place), so

$$\mathcal{H} = \mathcal{H}_0 + eE_0x_1 + eE_0x_2. \tag{2.24}$$

A little manipulation shows that this can be rewritten as

$$\mathcal{H} = \frac{1}{2} m\omega_0^2 z_1^2 + \frac{1}{2} m\omega_0^2 z_2^2 + \cdots; \quad z_{1,2} = x_{1,2} + \frac{eE_0}{m\omega_0^2}\,, \tag{2.25}$$

where the ellipses represents unimportant constants. We thus have a new pair of oscillators whose equilibrium positions are linearly shifted by the field. The induced dipole moment is the electron charge times that shift, namely $e^2E_0/m\omega_0^2$, and thus $\alpha = e^2/m\omega_0^2$.

Putting together all of the pieces, we see that the interaction between two fluctuating dipoles can be written in the compact form

$$u(r) = -\frac{1}{2}\frac{\hbar\omega_0\alpha^2}{r^6}\,. \tag{2.26}$$

It follows that the typical scale of this energy within a condensed phase of number density n is obtained by setting $r^{-6} \sim n^2$, giving

$$u \sim \hbar\omega_0\left(\alpha n\right)^2. \tag{2.27}$$

For most dense strongly insulating liquids the product $\alpha n \sim 0.1 - 0.2$. This is relevant to the calculation of interacting extended bodies, as we discuss in the next section. The quantity αn also occupies a very important role in the theory of metal-insulator transitions, which are predicted to occur when it exceeds an $\mathcal{O}(1)$ threshold.[6]

2.2.2 *Interaction of extended objects*

We now use the basic results from the previous section to understand the van der Waals interaction between extended objects. A prime example is the stacks of thylakoid membranes found in chloroplasts of green algae, as shown in Fig. 2.4.[7] The balance of forces that determine the spacing observed in these structures has been analysed along the lines we discuss below.[8]

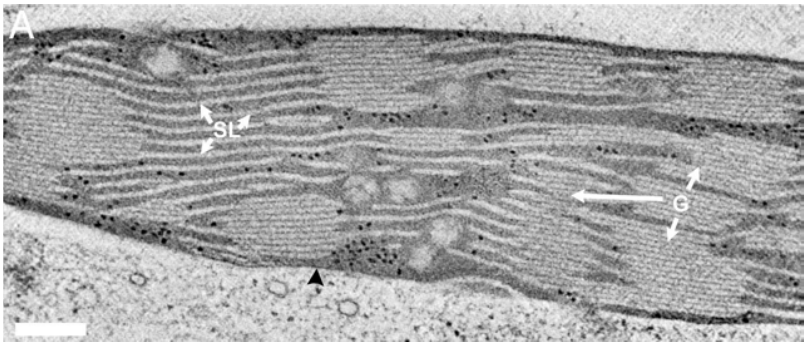

Figure 2.4: Thylakoid membranes. A 10 nm thick slice of lettuce chloroplast imaged with electron microscopy. The so-called "grana" (G), stacks of disc-shaped thylakoid membranes are interspersed with unstacked "stroma" thylakoids (SL), all immersed in water and enclosed in the chloroplast envelope (black arrow). Scale bar is 200 nm. From Ref. 7.

To calculate the interaction between slabs we start with the interaction of a single atom with a laterally infinite slab with atom number density n, as indicated in Fig. 2.5. Let us denote the interaction between two atoms as

$$u_{11}(r) = -\frac{C}{r^6}. \tag{2.28}$$

[6] Herzfeld, K.F. On atomic properties which make an element a metal. *Phys. Rev.*, 29:701–705, 1927

[7] Bussi, Y., Shimoni, E., Weiner, A., Kapon, R., Charuvi, D., Nevo, R., Efrati, E., Reich, Z. Fundamental helical geometry consolidates the plant photosynthetic membrane. *Proc. Natl. Acad. Sci. USA*, 116:22366–22375, 2019

[8] Sculley, M.J., Duniec, J.T., Thorne, S.W., Chow, W.S. and Boardman, N.K. The stacking of chloroplast thylakoids. Quantitative analysis of the balance of forces between thylakoid membranes of chloroplasts, and the role of divalent ions. *Arch. Bioch. Biophys.*, 201:339–346, 1980

Working in cylindrical coordinates the interaction u_{1S} between one atom and the slab is

$$\begin{aligned} u_{1S}(z) &= n\int_{-\delta}^{0} dz' \int_0^{2\pi} d\phi \int_0^\infty r dr u_{11}\left(\sqrt{(z-z')^2+r^2}\right) & (2.29)\\ &= -2\pi C n \int_z^{z+\delta} dz' \int_0^\infty r dr \frac{1}{(z'^2+r^2)^3} & (2.30)\\ &= -\frac{\pi C n}{6}\left(\frac{1}{z^3}-\frac{1}{(z+\delta)^3}\right), & (2.31) \end{aligned}$$

where we changed variables from z' to $z'' = z - z'$ in the second line (and dropped the prime). The power law r^{-6} of the interparticle potential has become z^{-3} by integration over three dimensions.

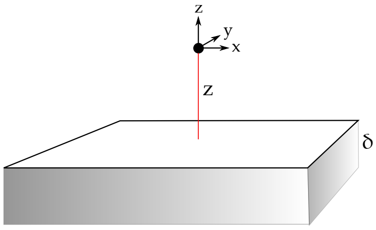

Figure 2.5: Geometry of an atom interacting with a laterally infinite slab of thickness δ.

Now we consider two slabs separated by a distance d (Fig. 2.6). With the result 2.31, the slab-slab interaction $u_{SS}(d)$ is obtained by integrating $u_{1S}(z)$ over the thickness of the second slab. If A is the area of that slab, then there are $Andz$ atoms in differential thickness dz, and the interaction energy per unit area $V_A(z) \equiv u_{SS}(z)/A$ is

$$\begin{aligned} V_A(d) &= \int_d^{d+\delta} dz n u_{1S}(z) dz & (2.32)\\ &= -\frac{A_H}{12\pi}\left(\frac{1}{d^2}-\frac{2}{(d+\delta)^2}+\frac{1}{(d+2\delta)^2}\right), & (2.33) \end{aligned}$$

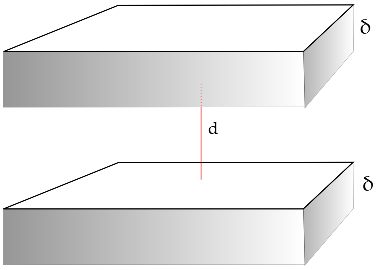

Figure 2.6: Geometry of two slabs of thickness δ separated by face-to-face distance d.

where have introduced the Hamaker constant[9]

$$A_H = \pi^2 n^2 C, \tag{2.34}$$

with units of energy. Based on our simple picture of the constant C in Eq. 2.26, we see that $A_H \sim (1/2)\pi^2\hbar\omega_0(\alpha n)^2$, so with $\hbar\omega_0 \sim 3\,\text{eV}$ and $\alpha n \sim 0.1 - 0.2$ as discussed above, we estimate $A_H \sim 5 - 25\,\text{k}_B\text{T}$.

2.3 *Screened electrostatic interactions*

2.3.1 *Poisson-Boltzmann and Debye-Hückel theory*

Many of the interesting objects in biology interact both through van der Waals forces and (screened) electrostatic interactions. The behaviour of systems with these two competing forces was first established in the classic work of Verwey and Overbeek.[10] As the van der Waals forces decay as an inverse power of distance, and the electrostatic contribution decays exponentially (as we shall see), the combined potential is attractive at long distances and repulsive at short distances, leading to a potential minimum. It is this balance of forces that sets the spacing of thylakoid membranes (Fig. 2.4), for example.

Two elementary charges in vacuum separated by a distance r have an electrostatic energy (in cgs units) of

$$E = e\phi(r) = \frac{e^2}{r}, \tag{2.35}$$

where $\phi = e/r$ is the electrostatic potential. Essentially all of living matter is infused with water, whose dielectric constant $\epsilon \sim 80$

[9] Hamaker, H.C. The London-van der Waals attraction between spherical particles. *Physica*, 4:1058–1072, 1937

[10] Verwey, E.J.W. and Overbeek, J.Th.G. *Theory of the Stability of Lyophobic Colloids*. Elsevier Publishing Company, Inc., New York, 1948

reduces the energy scale to

$$E = \frac{e^2}{\epsilon r}. \tag{2.36}$$

While reduced by nearly two orders of magnitude, this interaction still falls off as an inverse power of distance. A sense of the scale of E is obtained by finding the distance at which it is comparable to thermal energy. This *Bjerrum length* is

$$\lambda_B = \frac{e^2}{\epsilon k_B T} \sim 0.7\,\mathrm{nm}. \tag{2.37}$$

Even pure water has small amounts of ionic species, since water molecules are in equilibrium with protons (H^+) and hydroxyl ions (OH^-) according to the reaction scheme

$$\mathrm{H_2O} \rightleftharpoons \mathrm{H}^+ + \mathrm{OH}^-. \tag{2.38}$$

Recall that the pH of a solution is defined as $-\log_{10}[\mathrm{H}^+]$, where the notation $[\cdots]$ means concentration in moles/litre. Thus, a neutral pH of 7 corresponds to a proton concentration of $10^{-7}\,\mathrm{M/l} \sim 6 \times 10^{13}\,\mathrm{cm}^{-3}$. These and any additional ions present will screen the bare electrostatic interactions considered above; mobile charges opposite in sign to a given charge cluster around it in a diffuse cloud, screening it from other distant charges. The standard formalism to compute the ionic distribution and resulting interactions is Poisson-Boltzmann theory, or, in its linearised form, Debye-Hückel theory.[11] They are based on two principles. The first is the Poisson equation relating the electrostatic potential ϕ to the charge density ρ

$$\nabla^2\phi = -\frac{4\pi\rho}{\epsilon}. \tag{2.39}$$

The second is the Boltzmann distribution relating the ionic concentrations c_s of the species s of charge $z_s e$ (with z_s the "valence") to the electrostatic potential,

$$c_s = c_0^s e^{-\beta z_s e\phi}, \tag{2.40}$$

where c_0^s is a background concentration. Combining these, we obtain the *Poisson-Boltzmann equation*,

$$\nabla^2\phi = -\frac{4\pi}{\epsilon}\sum_s z_s e c_0^s e^{-\beta z_s e\phi}. \tag{2.41}$$

It is simplest to consider the case of a $z:z$ electrolyte, in which the dissolved neutral species dissociates into two ions of equal and opposite charges, such as sodium chloride (1:1; $\mathrm{NaCl} \to \mathrm{Na}^+ + \mathrm{Cl}^-$) or copper sulfate (2:2; $\mathrm{CuSO_4} \to \mathrm{Cu}^{2+} + \mathrm{SO_4^{2-}}$). Then we have

$$\nabla^2\phi = \frac{8\pi z e c_0}{\epsilon}\sinh(\beta z e\phi). \tag{2.42}$$

This is a very nonlinear equation for which analytical solutions can be found only in simplified geometries. Much of the important physics of screened electrostatics can be seen in the *weak field* limit,

[11] Debye, P. and Hückel, E. The theory of electrolytes. I. Lowering of freezing point and related phenomena (English translation). *Phys. Zeit.*, 24:185–206, 1923

when $\beta z e \phi \ll 1$, where we keep only the linearised r.h.s. of 2.42 and obtain the *Debye-Hückel equation*

$$\left(\nabla^2 - \kappa^2\right)\phi = 0, \tag{2.43}$$

where κ^{-1} is the Debye-Hückel length

$$\kappa^{-1} = \left[\frac{\epsilon k_B T}{8\pi z^2 e^2 c_0}\right]^{1/2} \sim \frac{10 \text{ nm}}{\sqrt{c_0[\text{mM}]}}. \tag{2.44}$$

Here, we have expressed the concentration in the units of millimolar (mM), as typical concentrations of ions such as sodium are in the range $1 - 200$ mM. We conclude that the screening length is nanometric in typical biophysical contexts.

The mathematical problem presented by the Debye-Hückel equation 2.43 is the *modified Helmholtz equation*. Let us first solve this in one spatial dimension, for the half-space above a surface lying in the $x - y$ plane ($z = 0$). The relevant general solution of 2.43 involves the functions $\exp(\pm\kappa z)$, and the requirement that the solution be bounded as $z \to \infty$ leaves only the decaying exponential. If the surface potential is fixed at ϕ_0, say, then

$$\phi(z) = \phi_0 \, \mathrm{e}^{-\kappa z}. \tag{2.45}$$

The induced charge density σ_0 on the surface can be computed in the usual way (by considering a Gaussian pillbox that straddles the surface). It obeys

$$-\hat{\mathbf{n}} \cdot \boldsymbol{\nabla}\phi\Big|_{z=0} = \frac{4\pi\sigma_0}{\epsilon} \Rightarrow \sigma_0 = \frac{\epsilon\kappa}{4\pi}\phi_0, \tag{2.46}$$

where $\hat{\mathbf{n}}$ is the *outward* normal to the surface. An analogous calculation yields the potential when the surface charge itself is specified,

$$\phi(z) = \frac{4\pi\sigma_0}{\epsilon\kappa}\mathrm{e}^{-\kappa z}. \tag{2.47}$$

Within Debye-Hückel theory the surface charge and surface potential are linearly related, but in the more general Poisson-Boltzmann setting this relationship is nonlinear.

Observe that the DH equation $\left(\nabla^2 - \kappa^2\right)\phi = 0$ is the Euler-Lagrange equation for the functional

$$\mathcal{G} = \frac{\epsilon}{4\pi}\int d^3r \left[\frac{1}{2}(\boldsymbol{\nabla}\phi)^2 + \frac{1}{2}\kappa^2\phi^2\right], \tag{2.48}$$

where we employ the general Euler-Lagrange formula

$$\frac{\delta\mathcal{G}}{\delta\phi} = -\frac{\partial}{\partial x}\frac{\partial(\cdots)}{\partial\phi_x} + \frac{\partial(\cdots)}{\partial\phi}, \tag{2.49}$$

where $(\cdots)$ is the integrand of the functional. The DH equation holds as the minimisation condition on (2.48) for any constant factor in front of the integral, but with the choice in (2.48), we recognize the first term as the standard form of the electrostatic energy density

$\epsilon\mathbf{E}^2/8\pi$ in a medium of dielectric constant ϵ. The second term is the weak-field approximation of an entropic contribution.

If we integrate by parts the term in 2.48 involving $(\boldsymbol{\nabla}\phi)^2$, we obtain from Green's first identity a bulk contribution that vanishes by the DH equation, leaving only the surface term

$$\mathcal{G} = \frac{1}{2}\int_S dS\sigma\phi, \tag{2.50}$$

where we have used 2.46 to express the normal derivative of the potential in terms of the charge density σ. This is the appropriate free energy for a system in which the surface charge is specified, and it is completely determined by those Neumann boundary conditions on the surface. There is no free lunch, for of course the potential on the surface must be found from the solution of the DH everywhere.

For situations with fixed surface potential rather than fixed charge, the surface free energy must be Legendre transformed, which is equivalent to accounting for the work done against the battery that held the potential fixed. This new free energy $\mathcal{F}$ is

$$\mathcal{F} = \mathcal{G} - \int_S dS\sigma\phi = -\frac{1}{2}\int_S dS\sigma\phi. \tag{2.51}$$

The factors of $1/2$ in Eqs. 2.50 and 2.51 arise from the linear relation between surface potential and surface charge. In the more general case, the free energy is expressed as a "charging integral" of the form

$$-\int_S dS\int^{\phi_0}\sigma(\phi')d\phi'. \tag{2.52}$$

For our simple planar examples above,

$$\frac{\mathcal{G}}{A} = \frac{2\pi\sigma_0^2}{\epsilon\kappa} \quad \text{and} \quad \frac{\mathcal{F}}{A} = -\frac{\epsilon\kappa\phi_0^2}{8\pi}, \tag{2.53}$$

where A is the total area of the surface.

2.3.2 *Electrostatic interactions between surfaces*

Now we move on to calculate the electrostatic interaction between two surfaces, considering both the case of fixed charged density and the case of fixed potential. Although the case of a specified charge density is more biophysically relevant than a specified potential, which one would imagine is appropriate to an electrochemical context, the comparison between the two serves to illustrate some general features of the way that quadratic field theories determine interactions between surfaces. This takes on added relevance for neutral, dipolar membranes, which are believed to polarize the intervening water molecules and produce a "hydration repulsion" between them,[12] measured by clever experiments some years ago.[13]

For two surfaces held at the same potential ϕ_0 and located at $\pm d/2$, the potential is the symmetric combination of the fundamental exponential solutions found previously,

$$\phi = \phi_0\frac{\cosh(\kappa z)}{\cosh(\kappa d/2)}. \tag{2.54}$$

[12] Marcelja, S. and Radić, N. Repulsion of interfaces due to boundary water. *Chem. Phys. Lett.*, 42:129–130, 1976

[13] Lis, L.J., McAlister, M., Fuller, N., Rand, R.P. and Parsegian, V.A. Interactions between neutral phospholipid bilayer membranes. *Biophys. J.*, 37:657, 1982

Using this we find the charge density at the plate at $z = d/2$. Here, $-\hat{\mathbf{n}} \cdot \boldsymbol{\nabla} = d/dz$, thus

$$\sigma(d/2) = \frac{\epsilon\kappa\phi_0}{4\pi}\tanh(\kappa d/2)\ . \tag{2.55}$$

At the bottom plate $-\hat{\mathbf{n}} \cdot \boldsymbol{\nabla} = -d/dz$, but with $\sinh(-d/2\lambda) = -\sinh(d/2\lambda)$ the charge density is the same. As the charge and potential do not vary with position over these flat surfaces the surface integration will just give a factor of the surface area A. The free energy per unit area $V(d) \equiv \mathcal{F}(d)/A$ is

$$V(d) = -\frac{\epsilon\kappa\phi_0^2}{4\pi}\tanh(\kappa d/2). \tag{2.56}$$

In the limit $d \to \infty$ we recover twice the single-surface result 2.53.

Subtracting the "self energy" of the surfaces, we obtain the repulsive interaction potential $V_R(d) = V(d) - V(\infty)$,

$$V_R(d) = \frac{\epsilon\kappa\phi_0^2}{4\pi}\left[1 - \tanh\left(\frac{\kappa d}{2}\right)\right]. \tag{2.57}$$

At large argument, tanh approaches unity from below, so this is clearly a repulsion, as expected. In detail, if $\kappa d \gg 1$ we note that $\tanh(z) \simeq 1 - 2e^{-2z} + \cdots$, and thus

$$V_R(d) \simeq \frac{\epsilon\kappa\phi_0^2}{2\pi}e^{-\kappa d}\ , \tag{2.58}$$

which therefore has the same exponential decay as the electrostatic potential itself. A second important point is that $V_R(d)$ is bounded as $d \to 0$; when the two charged surfaces are brought closer together, their induced charges decrease fast enough to avoid a singularity.

Now we consider the case of two surfaces with fixed charge density σ_0. A simple calculation shows that the required potential is

$$\phi(x) = \frac{4\pi\sigma_0}{\kappa\epsilon}\frac{\cosh(\kappa z)}{\sinh(\kappa d/2)}, \tag{2.59}$$

with corresponding potential energy per unit area

$$V_R(d) = \frac{4\pi\sigma_0^2}{\kappa\epsilon}\left(\coth\left(\frac{\kappa d}{2}\right) - 1\right). \tag{2.60}$$

The function coth approaches unity from above at large argument, and thus we again have a repulsive interaction. However, this time there is a divergence at short distances due to the fixed charge densities that are brought ever closer together.

Let us estimate the scale of energies involved in the case of charged lipid membranes. Lipid molecules are "amphiphilic", with a structure that is a fusion of parts that are hydrophilic (having an affinity for water) and hydrophobic (repelling water). Figure 2.7 shows the structure of the lung surfactant dipalmitoylphosphatidylcholine (DPPC), which has two 16-carbon hydrophilic "tails" and a phosphatidylcholine head group. In diagrams of this type, the zig-zag line represents the repeating group CH_2, terminated by the methyl

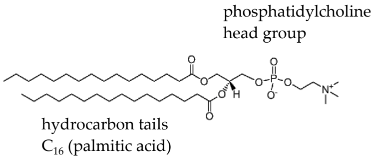

Figure 2.7: The chemical structure of the phospholipid DPPC (dipalmitoylphosphatidylcholine).

group CH_3, with the hydrogen atom labels omitted for clarity. These particular hydrocarbon chains are said to be "saturated" because every carbon atom is 4-fold coordinated, bonded to two carbon atoms and two hydrogen atoms (the maximum possible), unlike "unsaturated" lipids with one or more C=C double bonds, thereby having carbon atoms that have only a single bond to a hydrogen atom.

When placed in water, lipids self-organize into structures that isolate the oily hydrocarbon tails from contact with water molecules, leaving the hydrophilic headgroups in contact with water. This "hydrophobic effect" plays a central role in cellular biology, dictating the structure of lipid assemblies, the folding of proteins, and localization of channels in membranes.[14] The simplest structure is a "micelle", a spherical or cylindrical structure with the tails on the inside and the heads facing outwards.

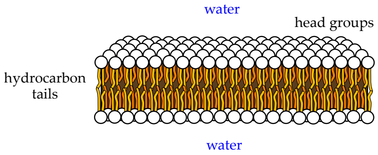

Figure 2.8: Structure of a lipid membrane in water.

Bilayer membranes have the structure shown in Fig. 2.8. They are essentially thin fluid sheets a few nm thick in which typically (but not always) the lipid molecules are free to diffuse laterally. A typical charged head group has a single elementary charge in an area of $\sim 1\,\mathrm{nm}^2$. If the Debye-Hückel screening length is $\sim 1\,\mathrm{nm}$, then $4\pi\sigma_0^2/\kappa\epsilon \sim 40\,\mathrm{mN/m}$, which can be compared to the surface tension of water ($80\,\mathrm{mN/m}$). Expressed another way, $40\,\mathrm{mN/m}$ is $40\,\mathrm{pN{\cdot}nm/nm^2}$, or about $10\,\mathrm{k_BT/nm^2}$.

Returning to the motivational problem of systems such as stacks of thylakoid membranes, we now add the van der Waals interaction 2.33 between two membranes to the screened electrostatic repulsion 2.60. A convenient set of nondimensionalisations involves scaling distances with the membrane thickness δ and the potential energy with the Hamaker constant. Thus defining

$$x = \frac{d}{\delta}, \quad K = \kappa\delta, \quad \mathcal{V} = \frac{12\pi\delta^2}{A_H}(V_A + V_R), \tag{2.61}$$

we obtain

$$\mathcal{V}(x) = \Gamma\left(\coth\left(\frac{Kx}{2}\right) - 1\right) - \frac{1}{x^2} + \frac{2}{(x+1)^2} - \frac{1}{(x+2)^2}, \tag{2.62}$$

where

$$\Gamma = \frac{24\pi^2\sigma_0^2\delta^2}{\epsilon\kappa A_H}. \tag{2.63}$$

Using our estimates from above, and taking a membrane thickness of $3-6\,\mathrm{nm}$, we find $\Gamma \sim 100$ and $K > 5$. While the large size of Γ seems to imply a very large mismatch between the electrostatic and van der Waals scales of energy, the exponential attenuation of the former allows a competition with the latter at distances beyond a few screening lengths. The graph shown in Fig. 2.9, reveals an essential feature of this competition, namely a minimum in $\mathcal{V}$ at values of x of order unity. This would correspond to the equilibrium spacing of the thylakoid membranes. Moreover, the global minimum of the energy is at contact ($x = 0$), where the van der Waals term diverges. As K increases (corresponding to an increase in salt concentration)

---

[14] C. Tanford. *The hydrophobic effect: formation of micelles and biological membranes*. Wiley, New York, 1973

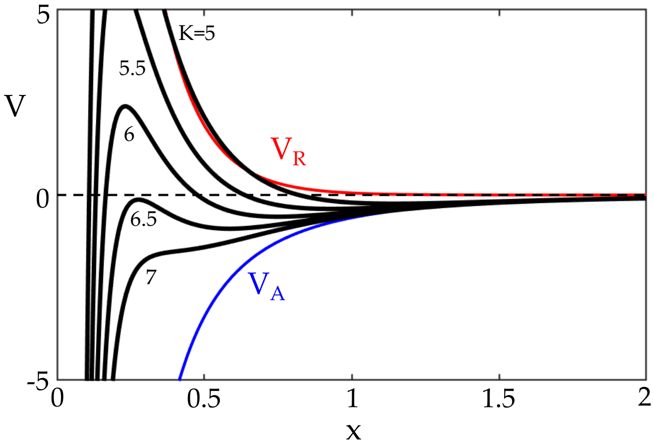

Figure 2.9: Interaction energy 2.62 between membranes for $\Gamma = 30$ and various values of K, as shown. Obtained using the program `Figure_209_DLVO.m`.

the minimum at larger x disappears, leaving only the minimum at contact. This implies the well-known "salting-out" effect in colloidal suspensions, whereby an increase of dissolved salt leads to precipitation of the suspended particles.

2.4 *Geometrical aspects of screened electrostatics*

In the previous section we considered only the simplest planar geometries, but many of the interesting structures in biology have nontrivial curvatures. As the Debye-Hückel screening length is nanometric, while the radius of curvature R of structures within the cell is often much larger, it is natural to exploit that separation of length scales to develop a systematic, perturbative approach using κR as a small parameter. Of particular interest historically has been the contribution of screened electrostatic interactions to the elasticity of membranes. Intuitively, bending a charged surface brings the surface charges closer together, producing a repulsion that effectively increases the stiffness of the surface.

In Chapter 5 we develop the necessary differential geometry of surfaces to deal with detailed problems in membrane physics. Here, we simply recall that at every point on a surface there are two principal radii of curvature, termed R_1 and R_2, and from these we can construct two important geometric quantities; the *mean curvature*

$$H = \frac{1}{2}\left(\frac{1}{R_1} + \frac{1}{R_2}\right) \tag{2.64}$$

and the *Gaussian curvature*

$$K = \frac{1}{R_1 R_2}. \tag{2.65}$$

In the early 1970s, Canham[15] and Helfrich[16] independently introduced a model for the elasticity of "fluid" membranes of fixed area, composed of lipids that are free to diffusive within the sheet, that have vanishing shear modulus. They proposed that the characteristic biconcave discoid shapes of red blood cells (erythrocytes), shown in Fig. 2.10, are minimisers of this energy under the constraint of a

[15] Canham, P.B. The minimum energy of bending as a possible explanation of the biconcave shape of the human red blood cell. *J. Theor. Biol.*, 26:61–76, 1970

[16] Helfrich, W. Elastic properties of lipid bilayers: theory and possible experiments. *Z. Naturforsch. Teil C*, 28:693–703, 1973

fixed enclosed volume of water less than the equivalent sphere (the sphere having the same surface area as the membrane).

This functional is a surface integral of a quadratic form in the curvatures,

$$E = \int dS \left[\frac{1}{2} k_c (H - H_0)^2 + \frac{1}{2} \bar{k}_c K \right]. \tag{2.66}$$

Here, k_c and $\bar{k}_c$ are the bending modulus and Gaussian curvature modulus of the membrane, and H_0 is the *spontaneous curvature* that incorporates the possibility of a preferred curvature in the ground state. It is often a constant, but can vary spatially if the membrane composition is inhomogeneous. From the Gauss-Bonnet theorem, the second integral in 2.66 is a constant that depends only on the topology of the closed surface of interest.

The problem of quantifying the electrostatic contribution to the elastic moduli and H_0 can be addressed several ways. The first[17] is a method by which comparison of the energies of planes, cylinders, and spheres yields those quantities directly. The second is a boundary perturbation method for nearly planar surfaces,[18] while the third utilizes a "multiple-scattering" method[19] introduced in the context of the wave equation.[20] We outline the essential features of the first two approaches, leaving full calculations to the Example Sheets.

2.4.1 *Comparative approach*

For simplicity we focus on the problem of fixed surface charge density σ_0. On dimensional grounds we expect the elastic constants (units of energy) to scale as

$$k_c, \bar{k}_c \sim \frac{4\pi\sigma_0^2}{\epsilon\kappa^3}, \tag{2.67}$$

and based on the estimate $4\pi\sigma_0^2/\epsilon\kappa \sim 10\,\mathrm{k_B T/nm^2}$ above Eq. 2.61 and an assumed screening length of 1 nm, these moduli are on the order of $10\,\mathrm{k_B T}$. Likewise, as the screening length is the only length scale in the problem, we expect $H_0 \sim \kappa^{-1}$. The purpose of these calculations is to make these estimates precise.

As we have already solved the problem for a single plane, we next consider the cylinder. We wish to solve the modified Helmholtz equation 2.43 inside and outside a cylinder of radius R, assuming axisymmetry. The Debye-Hückel equation becomes

$$\left(r^2 \frac{\partial^2}{\partial r^2} + r \frac{\partial}{\partial r} - (\kappa r)^2 \right) \phi = 0. \tag{2.68}$$

As this is homogeneous in powers of r, the solution is a function of κr. The two solutions are *modified Bessel functions* $K_0(\kappa r)$ for the outer problem (decaying at infinity) and $I_0(\kappa r)$ for the inner problem (well-behaved at the origin). We solve the problem in those two domains.

Using the identity $I_0'(z) = I_1(z)$, the inner solution is found to be

$$\phi(r) = \frac{4\pi\sigma}{\epsilon\kappa} \frac{I_0(\kappa r)}{I_1(\kappa R)}. \tag{2.69}$$

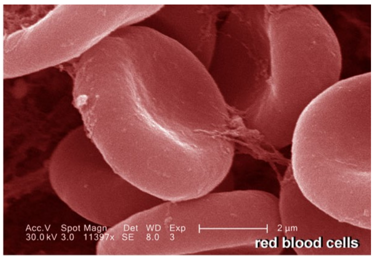

Figure 2.10: Electron micrograph of red blood cells.

---

[17] Winterhalter, M. and Helfrich, W. Effect of surface charge on the curvature elasticity of membranes. *J. Phys. Chem.*, 92:6865–6867, 1988

[18] Goldstein, R.E., Pesci, A.I. and Romero-Rochín, V. Electric double layers near modulated surfaces. *Phys. Rev. A*, 41:5504–5515, 1990

[19] Duplantier, B., Goldstein, R.E., Romero-Rochín, V. and Pesci, A.I. Geometrical and topological aspects of electric double layers near curved surfaces. *Phys. Rev. Lett.*, 65:508–511, 1990

[20] Balian, R. and Bloch, C. Distribution of eigenfrequencies for the wave equation in a finite domain: I. Three-dimensional problem with smooth boundary surface. *Ann. Phys. (N.Y.)*, 60:401–447, 1970

The (uniform) free energy per unit area of the inner surface is

$$\frac{1}{2}\sigma\phi\bigg|_S = \frac{1}{2}\frac{4\pi\sigma_0^2}{\epsilon\kappa}\frac{I_0(\kappa R)}{I_1(\kappa R)}. \tag{2.70}$$

As outlined above, the limit of interest is $\kappa R \gg 1$. We then appeal to the asymptotic results for modified Bessel functions [Abramowitz & Stegun[21] (henceforth, "A&S") # 9.7.1],

$$I_\nu(z) = \frac{e^z}{\sqrt{2\pi z}}\left\{1 - \frac{\mu-1}{8z} + \frac{(\mu-1)(\mu-9)}{2!(8z)^2} + \cdots\right\}, \tag{2.71}$$

where $\mu = 4\nu^2$. From these results, we see that the exponential prefactors of the asymptotic forms cancel in the ratio 2.70, leaving a simple expansion in inverse powers of κR,

$$\frac{I_0(\kappa R)}{I_1(\kappa R)} \sim 1 + \frac{1}{2\kappa R} + \frac{3}{8(\kappa R)^2} + \cdots. \tag{2.72}$$

Carrying through an expansion of the energy density for a spherical surface also yields an expansion in $1/\kappa R$, allowing a direct comparison to be made with the Helfrich formula. Precise calculations must account for the finite thickness of the membrane and the possibility of a charge density difference between the two sides. We leave it to the student (Example Sheet 1) to complete these calculations.

2.4.2 *Perturbative approach*

Next, we sketch the basic features of a perturbative approach to finding the energetics of electric double layers near a non-flat boundary. Let the surface position be $z = h(x)$, where h is a single-valued height function independent of y, and the surface is held at a fixed potential ϕ_0 (Fig. 2.11). Thus, we must solve the Debye-Hückel equation for the potential $\phi(x,z)$ subject to the boundary condition

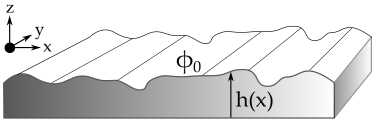

Figure 2.11: A ripply surface held at fixed potential.

$$\phi(x, h(x)) = \phi_0, \tag{2.73}$$

and $\phi = 0$ at $z = \infty$. The mathematical challenge arises from the fact that in general we do not know the Green's function of the modified Helmholtz operator for a domain bounded by an arbitrary function $h(x)$. But, we can perturbatively connect the solutions at finite $h(x)$ to those at $h = 0$, where we know the solution. This "boundary perturbation theory" is a method of broad applicability.

We introduce a dimensionless small parameter ε as a counting device, and expand the surface boundary condition in a Taylor series,

$$\phi(x, \epsilon h(x)) \simeq \phi(x,0) + \varepsilon h(x)\phi_z(x,0) + \frac{1}{2}\varepsilon^2 h(x)^2\phi_{zz}(x,0) + \cdots, \tag{2.74}$$

where subscripts denotes partial differentiation. We expect that the solution itself—in the bulk—also has an expansion in powers of ε,

$$\phi(x,z)) \simeq \phi^{(0)}(x,z) + \varepsilon\phi^{(1)}(x,z) + \varepsilon^2\phi^{(2)}(x,z) + \cdots. \tag{2.75}$$

---

[21] M. Abramowitz and I.A. Stegun. *Handbook of Mathematical Functions with Formulas, Graphs, and Mathematical Tables*. Dover Publications Inc, Mineola, N.Y., 1965

The governing equation does not depend on ε; if we substitute 2.75 into 2.43, at every order we will have

$$(\partial_{xx} + \partial_{zz} - \kappa^2)\phi^{(n)}(x,z) = 0. \tag{2.76}$$

Merging the expansion of the boundary condition with the expansion of the solution we arrive at a sequence of boundary conditions for each order of solution. At leading order, we recover the boundary condition at a flat surface,

$$\mathcal{O}(\varepsilon^0): \quad \phi^{(0)}(x,0) = \phi_0. \tag{2.77}$$

Clearly, the solution for all (x,z) is

$$\phi^{(0)}(x,z) = \phi_0 \mathrm{e}^{-\kappa z}. \tag{2.78}$$

At first order we find the boundary condition

$$O(\varepsilon^1): \quad \phi^{(1)}(x,0) = -h(x)\phi_z^{(0)}(x,0) = \kappa h(x)\phi_0\,. \tag{2.79}$$

Thus, the problem with a boundary condition on a ripply surface has become one with a flat boundary but an inhomogeneous potential. At quadratic order we have a similar kind of result,

$$O(\varepsilon^2): \quad \phi^{(2)}(x,0) = -\frac{1}{2}h^2(x)\phi_{zz}^{(0)}(x,0) - h(x)\phi_z^{(1)}(x,0). \tag{2.80}$$

A convenient way to solve these boundary-value problems is to work in Fourier space. Let us define the Fourier transforms of the potential and h with respect to x (keeping the z-dependence of ϕ),

$$\hat{\phi}^{(m)}(k,z) = \int dx \mathrm{e}^{ikx}\phi^{(m)}(x,z) \quad \text{and} \quad \hat{h}(q) = \int dx \mathrm{e}^{iqx}h(x). \tag{2.81}$$

The modified Helmholtz equation $(\partial_{xx} + \partial_{zz} - \kappa^2)\phi = 0$ becomes

$$\left(\partial_{zz} - \kappa_q^2\right)\hat{\phi}^{(n)}(q,z) = 0\,, \quad \text{where} \quad \kappa_q^2 = \kappa^2 + q^2, \tag{2.82}$$

and is solved by

$$\hat{\phi}^{(n)}(q,z) = \hat{\phi}^{(n)}(q,0)\mathrm{e}^{-\kappa_q z}. \tag{2.83}$$

To solve the sequence of boundary-value problems, we need the Fourier transform of ϕ at $z = 0$; this can be determined directly from the order-by-order boundary conditions. For example, at order ϵ^1 we have from (2.79)

$$\hat{\phi}^{(1)}(q,0) = \kappa\phi_0\hat{h}(q). \tag{2.84}$$

To complete the calculation, it is necessary to expand such quantities as the surface normal vector

$$\hat{\mathbf{n}} = -\frac{-h_x\hat{\mathbf{e}}_x + \hat{\mathbf{e}}_z}{\sqrt{1 + h_x^2}} \tag{2.85}$$

in order to compute the surface charge as

$$\sigma(x) = -\frac{\epsilon}{4\pi}\hat{\mathbf{n}} \cdot \boldsymbol{\nabla}\phi(x, \epsilon h(x))\,. \tag{2.86}$$

Details are left for the Example Sheet.

3

Fluctuations & Brownian Motion (Lectures 5-7)

3.1 Equipartition theorem

In Chapter 2 we used the standard formulation of classical statistical physics to derive the second virial coefficient. Now we wish to use that same starting point to discuss one of the most important results in equilibrium statistical physics; the theorem of equipartition.

We consider a system whose potential energy $U(q^N)$ depends on a set of generalized coordinates q^N. As in the derivation of (2.5), the partition function can be factorised into an ideal part Z_0 that only depends on temperature and the "configurational" partition function

$$Z = \int dq^N e^{-\beta U(q^N)}. \tag{3.1}$$

We have written this as an integral over continuous variables q; in the discrete case Z is a sum of Boltzmann factors.

Recall from elementary statistical physics that the probability $p(E)$ that a system has energy E is simply

$$p(E) = \frac{e^{-\beta U}}{Z}, \tag{3.2}$$

and the expectation value of a quantity A (denoted by $\langle A \rangle$) is

$$\langle A \rangle = \frac{1}{Z} \int dq^N A(q^N) e^{-\beta U}. \tag{3.3}$$

When U is quadratic in the q^N, as in the $N = 1$ case

$$U = \frac{1}{2} k q^2, \tag{3.4}$$

then

$$\left\langle \frac{1}{2} k q^2 \right\rangle = \frac{\int_{-\infty}^{\infty} dq \frac{1}{2} k q^2 e^{-\beta k q^2/2}}{\int_{-\infty}^{\infty} dq e^{-\beta k q^2/2}} = -\frac{\partial \ln Z}{\partial \beta}. \tag{3.5}$$

The final form on the r.h.s. of (3.5) tells us that $\ln Z$ is a *generating function*. Now we change coordinates in Z to obtain

$$Z = \int_{-\infty}^{\infty} dq e^{-\beta k q^2/2} = \sqrt{\frac{2}{\beta k}} \int_{-\infty}^{\infty} dx e^{-x^2}, \tag{3.6}$$

and thus

$$\ln Z = -\frac{1}{2} \ln \beta + (\text{terms independent of } \beta). \tag{3.7}$$

Hence, $-\partial \ln Z/\partial\beta = 1/2\beta = k_BT/2$ and the average energy per degree of freedom is

$$\left\langle \frac{1}{2}kq^2 \right\rangle = \frac{1}{2}k_BT. \tag{3.8}$$

This is the equipartition theorem; when the energy is a quadratic form in the coordinate, the average energy of that degree of freedom is $k_BT/2$. It is clear from this derivation that if the energy 3.4 were replace by a sum over a discrete set of modes, each with a quadratic contribution, since the partition function would factorise into a product of terms, each mode separately would satisfy the theorem.

3.2 *Fluctuating continuous objects*

3.2.1 *The tense string*

Now we apply the equipartition theorem to fluctuating continuous objects such as strings, biological filaments and membranes. The simplest example is a string hanging from two pulleys, with masses attached at its two ends so that gravity produces a tension γ in the string. If the string is at a finite temperature T, then it will exhibit thermal fluctuations which we characterise by a height function $h(x)$ as shown in Fig. 3.1. Relative to a straight string, the excess energy E of the string is the product of the tension γ and the excess arclength,

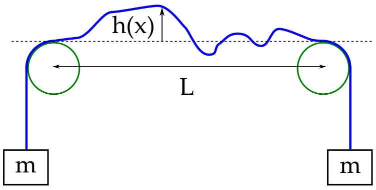

Figure 3.1: A string under tension.

$$E = \gamma \left[\int_0^L dx\sqrt{1+h_x^2} - L \right] , \tag{3.9}$$

where $h_x = \partial h/\partial x$. Expanding the square root under the assumption of a weakly-sloping curve ($|h_x| \ll 1$), we have

$$E \simeq \frac{\gamma}{2}\int_0^L dx h_x^2. \tag{3.10}$$

While 3.10 is quadratic in the displacement function $h(x)$, we can not apply the equipartition theorem directly because there are no identifiable *independent* degrees of freedom. This is where a Fourier (or other appropriate) representation is useful. Suppose we have Dirichlet boundary conditions $h(0) = h(L) = 0$. Then we can write

$$h(x) = \sum_{n=1}^{\infty} a_n \sin\left(\frac{n\pi x}{L}\right). \tag{3.11}$$

To be clear, with the dual views of ensemble averages and time averages in statistical mechanics, this representation holds for any particular member of the ensemble of systems or at any particular moment in time for a single string as it fluctuates; we view the amplitudes a_n as the new fluctuating quantities and, in the usual way in statistical physics, we draw conclusions about the statistical properties of h from those of the set $\{a_n\}$. By the orthogonality of the modes,

$$E = \frac{\gamma L}{4}\sum_{n=1}^{\infty}\left(\frac{n\pi}{L}\right)^2 a_n^2. \tag{3.12}$$

Note the explicit appearance of the system size L.

The form of 3.12 is the desired sum of independent quadratic contributions, so if the string is in thermal equilibrium at temperature T, then the probability distribution of each mode is proportional to $\exp(-\gamma(n\pi)^2 a_n^2/4Lk_BT)$, from which we deduce that $\langle a_n \rangle = 0$ and (by equipartition) the mean squared mode amplitudes are

$$\langle a_n^2 \rangle = \frac{2k_BTL}{\gamma\pi^2 n^2}. \tag{3.13}$$

We trace the n^2 in the denominator of 3.13 to the role of *tension* in the energy, which involves *two* powers of the *derivative* of h.

It is of interest to calculate the average envelope of the fluctuating string, the variance of the displacement $\langle h^2(x) \rangle$,

$$\begin{aligned}\langle h^2(x) \rangle &= \sum_m^\infty \sum_n^\infty \langle a_m a_n \rangle \sin\left(\frac{m\pi x}{L}\right) \sin\left(\frac{n\pi x}{L}\right) \\ &= \frac{k_BTL}{\gamma}\frac{2}{\pi^2}\sum_{n=1}^\infty \frac{\sin^2(n\pi x/L)}{n^2} \\ &= \frac{k_BT}{\gamma}LF(\xi),\end{aligned} \tag{3.14}$$

where the final form defines the scaling function F shown in Fig. 3.2, which depends on x and L only through the ratio $\xi = x/L$. The linear scaling of the variance with system size L is reminiscent of the scaling $\ell^2 \sim t$ for diffusion discussed in Chapter 1, and for the analogous quantity in random walks, as we show later.

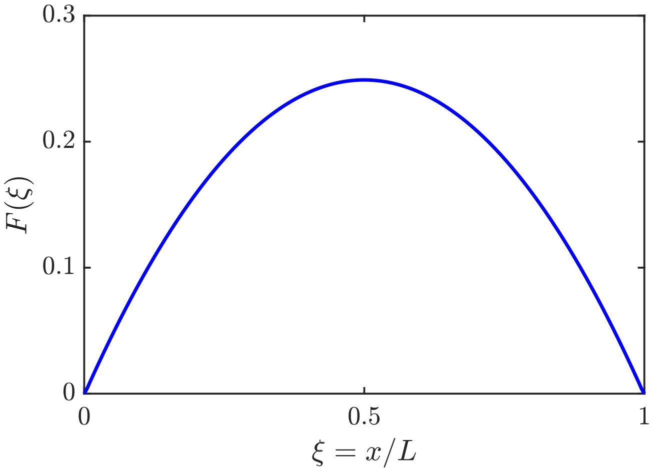

Figure 3.2: Scaling function for variance of fluctuating string. Obtained using the program `Figure_302_stringvar.m`.

3.2.2 *Continuum limit*

In many cases we will consider a system large enough that it is reasonable to consider a continuum of modes. as an example, we return to the tense string. Adopting a complex notation

$$h(x) = \sum_q e^{-iqx}\hat{h}(q), \tag{3.15}$$

and to be clear on the algebraic steps, we first write each factor of h_x in the energy in terms of its Fourier coefficients as

$$E = \frac{\gamma}{2}\int_0^L dx \sum_q \sum_{q'} (-iq)(-iq')e^{-i(q+q')x}\hat{h}(q)\hat{h}(q'). \tag{3.16}$$

The integration over x is performed using the identity

$$\int_0^L dxe^{-ipx} = L\delta_{p,0}, \tag{3.17}$$

where $\delta_{p,0}$ is the Kronecker delta. For a real function $h(x)$, we have $\hat{h}(-q) = \hat{h}^*(q)$, and thus the energy takes on the simple form

$$E = \frac{\gamma L}{2}\sum_q q^2|\hat{h}(q)|^2. \tag{3.18}$$

Equation 3.18 is the generalization of 3.12, so equipartition yields

$$\left\langle |\hat{h}(q)|^2 \right\rangle = \frac{k_B T}{\gamma L}\frac{1}{q^2}. \tag{3.19}$$

In addition to the thermal average of any quantity, we may also be interested in the *system average*, denoted by an overbar, where

$$\overline{(\cdots)} = \frac{1}{L}\int_0^L dx(\cdots). \tag{3.20}$$

The thermal average of the system average has a very compact form in the case of the height function,

$$\langle \overline{h^2} \rangle = \sum_q \langle |\hat{h}(q)|^2 \rangle. \tag{3.21}$$

These results are expressed as discrete Fourier sums. Moving to the continuum limit, we replace sums by integrals using the relation

$$\frac{1}{L}\sum_q \rightarrow \int \frac{dq}{2\pi}. \tag{3.22}$$

Combining (3.19) and (3.21), we find

$$\langle \overline{h^2} \rangle = \frac{k_B T}{2\pi\gamma}\int \frac{dq}{q^2}. \tag{3.23}$$

In passing to the continuum limit, we may find it necessary to introduce cutoffs to these kinds of integrals to obtain finite results. A small-scale cutoff on a length a represents the finite molecular size, below which the continuum theory may not make sense, while a large-scale cutoff represents, for example, the finite system size L. The corresponding cutoff wavevectors are $q_{\max} = \pi/a$ and $q_{\min} = \pi/L$. Accounting for such cutoffs, the variance 3.23 becomes

$$\begin{aligned} \langle \overline{h^2} \rangle &= \frac{k_B T}{2\pi\gamma}\left(\frac{1}{q_{\min}} - \frac{1}{q_{\max}}\right) \\ &= \frac{k_B T}{2\pi^2\gamma}(L-a). \end{aligned} \tag{3.24}$$

In this case, the molecular cutoff scale a may be set to zero without introducing any divergence in the average of interest, but, as mentioned earlier, the variance grows linearly with the large-scale cutoff L and there is no sensible $L \to \infty$ limit.

The average energy of the filament is proportional to the average mean variance of the filament slope. A simple calculation shows

$$\begin{aligned} \langle E \rangle = \frac{\gamma L}{2} \langle \overline{h_x^2} \rangle &= \frac{k_B T}{4\pi} L \int dq \\ &= \frac{k_B T}{4} \left(\frac{L}{a} - 1 \right). \end{aligned} \tag{3.25}$$

This result shows that the energy density $\langle E \rangle$ diverges as the small-scale cutoff is taken to zero. This "ultraviolet" divergence is exactly what the quantum theory of blackbody radiation[1] managed to tame by introducing a discreteness to the modes at small scales.

If we generalize this calculation to d spatial dimensions and thus a $d-1$ dimensional surface, we find

$$\langle \overline{h^2} \rangle \sim \int \frac{d^{d-1}q}{(2\pi)^{d-1}} \frac{k_B T}{\gamma q^2} \sim \frac{k_B T}{\gamma} \int dq \frac{q^{d-2}}{q^2} \tag{3.26a}$$

$$\sim \begin{cases} \frac{k_B T}{\gamma} \frac{1}{3-d} \left(q_{min}^{d-3} - q_{max}^{d-3} \right), & d \neq 3 \\ \sim \frac{k_B T}{\gamma} \ln\left(L/a \right), & d = 3. \end{cases} \tag{3.26b}$$

The behaviour at $d = 3$ is interesting and subtle. The interface "width" clearly diverges, both as the molecular cutoff $a \to 0$ and in the limit of an infinite system, but it is a very weak divergence. Taking L to be 1 cm and a to be 1 nm, we have $L/a = 10^7$, but $\ln(L/a)$ is only ~ 16. If we take the surface tension $\gamma = 72\,\mathrm{mN/m}$ of an air-water interface, and note that 1 mN/m is 1 pN·nm/nm^2, then the width of such a macroscopic air-water interface is $\langle \overline{h^2} \rangle^{1/2} \sim 1\,\mathrm{nm}$, i.e. it is *molecular* in size, despite the "formal" divergence.

For pedagogical purposes,[2] it is instructive to consider how the above is modified when there is a symmetry-breaking field in the energy that penalises large excursions in the height function h. If we view the surface bounded by the height function $h(x, y)$ as the liquid-vapor interface across which there is a density difference $\Delta\rho$, and recall that the energy density for a column of fluid of height h is $\Delta\rho g h^2/2$, then the energy functional is

$$E = \frac{\gamma}{2} \int\int dx dy \left[(\boldsymbol{\nabla} h)^2 + 2\ell_c^{-2} h^2 \right]. \tag{3.27}$$

where $\ell_c = \sqrt{2\Delta\rho g/\gamma}$ is the *capillary length* (for water, $\ell_c \sim 5\,\mathrm{mm}$). Now we expand the surface deformation as

$$h(\mathbf{x}) = \sum_{\mathbf{q}} e^{-i\mathbf{q}\cdot\mathbf{x}} \hat{h}(\mathbf{q}), \tag{3.28}$$

and obtain

$$E = \frac{\gamma A}{2} \sum_{\mathbf{q}} (q^2 + 2\ell_c^{-2}) |\hat{h}(\mathbf{q})|^2, \tag{3.29}$$

---

[1] Planck, M. Ueber das Gesetz der Energieverteilung im Normalspektrum. *Ann. Phys.*, 309:553–563, 1901

[2] J.S. Rowlinson and B. Widom. *Molecular Theory of Capillarity*. Oxford University Press, Oxford, 1982

where $A = L^2$ is the surface area. Again by equipartition we find

$$\langle|\hat{h}(\mathbf{q})|^2\rangle = \frac{k_B T}{\gamma A} \frac{1}{2\ell_c^{-2} + q^2}\ . \tag{3.30}$$

This shows that the capillary length provides a cutoff on what would otherwise be divergent fluctuation amplitudes as $q \to 0$.

Introducing both small-scale and large-scale cutoffs $2\pi/a$ and $2\pi/L$, and assuming a circular geometry in Fourier space, the average variance of the displacement field is

$$\langle\overline{h^2}\rangle = \frac{k_B T}{2\pi\gamma} \int \frac{q dq}{2\ell_c^{-2} + q^2} = \frac{k_B T}{4\pi\gamma} \ln\left[\frac{1 + 2\left(\pi\ell_c/a\right)^2}{1 + 2\left(\pi\ell_c/L\right)^2}\right]. \tag{3.31}$$

The thermodynamic limit $L \to \infty$ is now possible at finite g, with

$$\langle\overline{h^2}\rangle \sim \frac{k_B T}{4\pi\gamma} \ln\left[1 + 2\left(\frac{\pi\ell_c}{a}\right)^2\right]. \tag{3.32}$$

3.3 *Brownian Motion and Diffusion*

Now we start to consider the dynamical properties of objects subject to thermal fluctuations. The simplest example are microspheres that execute Brownian motion (named after the botanist Robert Brown, whose 1828 paper[3] and a follow-up in 1829[4] are two of the greatest of all papers in the old scientific literature). We introduce and study the simplest examples of stochastic ODEs to describe this process. These "Langevin equations" have random forces that represent the effects of collisions with water molecules, and have an amplitude that is determined by appealing to equilibrium statistical physics arguments in suitable limits.

A convenient starting point for the description of Brownian motion is the dynamics of a microsphere that is acted on by an optical trap and subject to thermal fluctuations. First invented in the 1970s at Bell Laboratories,[5] and extended later,[6] optical trapping (or "laser tweezers" [7]) localises a particle near the waist of a tightly-focused laser beam through gradients in the electric field. This is a consequence of the general result that dielectric objects experience a force moving them towards regions of higher electric field. In this case, the microspheres that are typically used have higher dielectric constants than water *at optical frequencies*, but lower values than water at zero frequency. In addition to gradient forces, radiation pressure acts to push the particle along the optical path, so only for sufficiently high gradients is the particle trapped. This requires microscope objectives with high Numerical Aperture (NA) (those with a very short focal length relative to their diameter).

Close enough to the trap centre, the effective potential experienced by the particle is quadratic in displacement from the centre. If we restrict consideration to motion in one lateral dimension the equation of motion of a trapped microsphere is the Langevin equation

$$\zeta\dot{x} = -kx + \xi(t), \tag{3.33}$$

---

[3] Brown, R. XXVII. A brief account of microscopical observations made in the months of June, July, and August, 1827, on the particles contained in the pollen of plants; and on the general existence of active molecules in organic and inorganic bodies. *Philos. Mag.*, 4:161–73, 1828

[4] Brown, R. XXIV. Additional remarks on active molecules. *Philos. Mag.*, 6:161–66, 1829

[5] Ashkin, A. Acceleration and trapping of particles by radiation pressure. *Phys. Rev. Lett.*, 24:156–159, 1970

[6] Ashkin, A. Optical trapping and manipulation of neutral particles using lasers. *Proc. Natl. Acad. Sci. USA*, 94:4853–4860, 1997

[7] Neuman, K.C. and Block, S.M. Optical trapping. *Rev. Sci. Instrum.*, 75:2787–2809, 2004

where $\zeta = 6\pi\mu a$ is the Stokes drag coefficient and $\xi(t)$ is the random force. For μm sized spheres and moderate laser power, $k \sim 10$ fN/nm, so that when the particle is displacement is a fraction of the particle size ($1\,\mu\text{m} = 10^3\,\text{nm}$), the trapping force will be in the pN range. From (3.33) we see that there is a relaxation time

$$\tau = \frac{\zeta}{k}. \tag{3.34}$$

If $a \sim 1\,\mu$m and k is as above, $\tau \sim 2\,$ms.

It is important to understand the meaning of the random force $\xi(t)$. First, note that the typical velocity of a water molecule is found by equipartition to be $\sqrt{3k_BT/m} \sim 600\,\text{m/s}$, and hence it takes only about $3 \times 10^{-13}\,$s for a water molecule to traverse its own size (0.2 nm), which in turn implies that the collision rate of molecules with a test particle is perhaps $10^{20}\,\text{s}^{-1}$. These time scales are vastly shorter than anything we measure when tracking the microsphere's motion, and it is thus natural to exploit this separation of time scales in the analysis. A second point regards what it means to "solve" a stochastic ODE such as (5.41). As we shall see below, for any particular *realisation* of the random noise $\xi(t)$ the Langevin equation is simply a linear ODE with a time-dependent force. Yet, in the typical experiment we perform averages over many stochastic trajectories of the particle to arrive at the average behaviour. This process corresponds to averaging over the realisations of $\xi(t)$. Denoting such averages with angular brackets, we assume $\langle \xi \rangle = 0$ by symmetry.

To see these issues in action, first simplify (3.33) to

$$\dot{x} + \tau^{-1}x = \eta(t), \tag{3.35}$$

where $\eta = \xi/\zeta$. Assuming the initial condition $x(0) = x_0$, use of an appropriate integrating factor yields the solution

$$x(t) = x_0 e^{-t/\tau} + \int_0^t dt' e^{-(t-t')/\tau}\eta(t'). \tag{3.36}$$

If we average this result over realisations of the noise, then the deterministic term is unchanged, while the integral term vanishes by the assumed zero value of the mean of the noise, leaving

$$\langle x(t) \rangle = x_0 e^{-t/\tau}. \tag{3.37}$$

Thus, on average the particle's trajectory is the deterministic one, relaxing exponentially to the trap centre.

After the mean position of the particle loses memory of its initial condition, it still fluctuates in the harmonic trapping potential, exhibiting a nonzero variance that follows from (3.36) as

$$\langle (x(t) - x_0 e^{-t/\tau})^2 \rangle = \int_0^t dt' \int_0^t dt'' e^{-(2t-t'-t'')/\tau} \langle \eta(t')\eta(t'') \rangle. \tag{3.38}$$

Now we make use of the separation of time scales in the Langevin approach, and assume that that the correlation $\langle \eta(t')\eta(t'') \rangle$ inside the integral is a sharply-peaked function of the difference $|t' - t''|$, decaying much faster than any relevant timescale of the particle. Calling this function $\phi(t'-t'')$, making the change of variables $s = t'+t''$ and $q = t'-t''$ (with Jacobian $1/2$), we obtain the r.h.s. of (3.38) as

$$\frac{1}{2}e^{-2t/\tau}\int_0^{2t} ds e^{s/\tau} \underbrace{\int_{-\infty}^{\infty} dq\phi(q)}_{\Gamma}, \tag{3.39}$$

where the final integral is just a number we label Γ. The variance of interest is then

$$\langle (x(t)-x_0e^{-t/\tau})^2\rangle = \frac{\Gamma\tau}{2}(1-e^{-2t/\tau}). \tag{3.40}$$

In the long time limit ($t/\tau \to \infty$), the result simplifies to

$$\langle x(t)^2\rangle = \frac{\Gamma\tau}{2}. \tag{3.41}$$

Here we appeal to equipartition, since the linear force law (3.33) arises from an energy $kx^2/2$, which in turn implies $\langle x^2\rangle = k_BT$, so

$$\Gamma = \frac{2k_BT}{\zeta}. \tag{3.42}$$

A further test of the result is found by examining the result (3.40) in the short-time limit $t/\tau \ll 1$. If we assume for convenience that $x_0 = 0$, then

$$\langle x^2(t)\rangle \simeq \frac{2k_BT}{\zeta}t + \cdots . \tag{3.43}$$

This is the expected result for a one-dimensional random walk, with diffusion constant D, where $\langle x^2\rangle = 2Dt$. We therefore deduce

$$D = \frac{k_BT}{\zeta} \tag{3.44}$$

and the Stokes-Einstein relation is recovered. An illuminating calculation in the Example Sheet involves the Langevin description of a free Brownian particle with inertia.

Looking back at the calculation above it is clear that the separation of scales between the noise and the dynamical variable was key to implementing the connection with equipartition. Since the integral Γ of the noise correlation is the only quantity that was needed, it is possible to assume that the noise is delta-function correlated in time. This leads to the standard assumptions on the Langevin noise in the original form (3.33) or the scaled dynamics (3.35),

$$\langle \xi\rangle = 0, \quad \langle \xi(t)\xi(t')\rangle = 2D\delta(t-t'), \tag{3.45a}$$
$$\langle \eta\rangle = 0, \quad \langle \eta(t)\eta(t')\rangle = 2k_BT\delta(t-t'). \tag{3.45b}$$

3.4 *Polymers and Entropic Forces*

In this section we will develop basic concepts of polymer physics, with emphasis on the concept of an *entropic spring*. Polymers are structures composed of repeating subunits held together with cohesive forces that may be of various types. In the case of DNA there are true covalent bonds between the nucleotides, while in the case of microtubules, non-covalent bonds hold together the individual protein subunits and the whole structure can grow and shrink over time through reversible polymerisation. Polymers can be linear sequences, as in the case of proteins, or branched or even crosslinked to form networks. We consider a few of the simplest models of linear polymers.

3.4.1 Freely-hinged chain

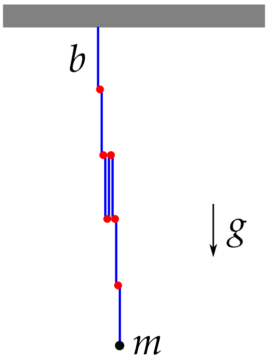

Figure 3.3: A freely-hinged chain, hanging under gravity from a support.

The simplest model of a polymer has N identical links of length b, each of which can be oriented in one of two directions. To include the effects of an external force, we imagine the polymer hangs from a support in a gravitational field and a mass m is attached to the last segment (Fig. 3.3). Note that there is no resistance to bending in this model, and indeed there are no internal forces at all.

With a reference energy at zero extension, the potential energy of the freely-hinged chain is $E = -mgz$, where the extension z is

$$z = \sum_{n=1}^{N} b s_n, \tag{3.46}$$

and $s_n = \pm 1$ denotes the orientation of the nth link. The configurational partition function is

$$Z = \sum_{s_1=\pm 1} \cdots \sum_{s_N=\pm 1} \exp\left(\beta F b \sum_{n=1}^{N} s_n\right), \tag{3.47}$$

where $F = mg$ is the gravitational force on each link. By the independence of the s_n, this can can be simplified to

$$Z = \prod_{n=1}^{N} \sum_{s_n=\pm 1} e^{f s_n} = [2\cosh(f)]^N, \tag{3.48}$$

where $f = \beta F b$. From this we calculate the mean extension as a function of the force, using Z as a generating function,

$$\langle z \rangle = \langle b \sum_n s_n \rangle = b \frac{\partial \ln Z_n}{\partial f} = L \tanh(f), \tag{3.49}$$

where $L = Nb$ is the fully-extended length. Figure 3.4 shows the normalized extension $\langle z \rangle / L$ versus f, revealing a linear regime at small f and saturation for $f \gg 1$. Expanding (3.49) for small f yields

$$\langle z \rangle \simeq \frac{Nb^2}{k_B T} F + \cdots, \tag{3.50}$$

the linear relationship of a Hookean spring with spring constant

$$k = \frac{k_B T}{N b^2}. \tag{3.51}$$

The appearance of $k_B T$ reminds us that this is an *entropic spring*; the resistance to extension arises because of the loss of entropy in the extended state. Indeed, in the fully-extended state there is only one configuration possible (all $s_n = +1$), and hence zero entropy.

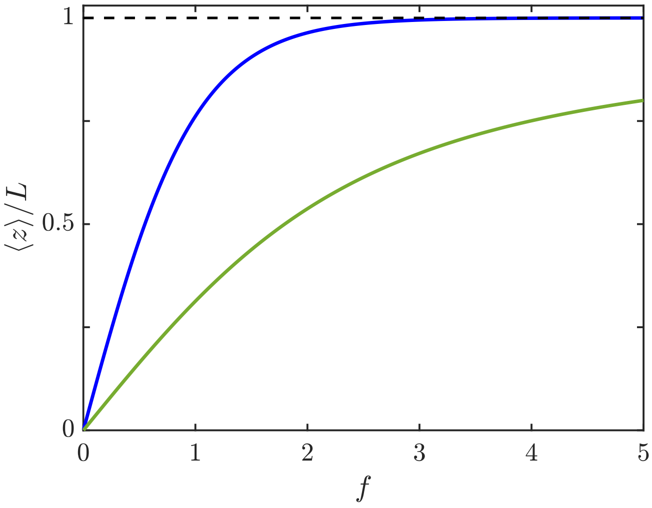

Figure 3.4: Force-extension curves for the freely-hinged chain (green) and the freely-jointed chain (blue). Obtained with `Figure_304_polymers.m`.

3.4.2 *The freely-jointed chain*

It is natural to ask whether the qualitative features of the free-hinged chain are found in more realistic models of polymers. To answer this, we consider the *freely-jointed chain* in which each link may rotate around the previous one on a cone of angle 2θ (Fig. 3.5). Now the extension is

$$z = \sum_{n=1}^{N} b \cos\theta_n, \tag{3.52}$$

with partition function

$$\begin{aligned} Z &= \prod_{n=1}^{N} \left[2\pi \int_0^\pi d\theta_n \sin\theta_n e^{f\cos\theta_n} \right], \\ &= \left[\frac{4\pi \sinh(f)}{f} \right]^N . \end{aligned} \tag{3.53}$$

The average again follows by differentiation, and has the simple form

$$\langle z \rangle = L\mathcal{L}(f) \quad \text{where} \quad \mathcal{L}(f) = \coth(f) - \frac{1}{f}. \tag{3.54}$$

Here, $\mathcal{L}$ is the so-called Langevin function well-known in the theory of magnetism. Figure 3.4 compares this functional relationship with that of the freely-hinged chain, showing qualitative consistency. There is again a linear relation at small forces, with spring constant

$$k = \frac{3k_B T}{Nb^2}. \tag{3.55}$$

The larger entropic spring constant reflects the additional degrees of freedom of the chain.

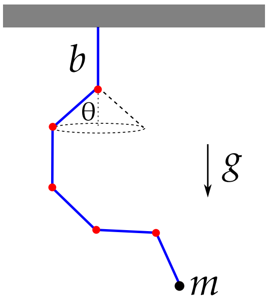

Figure 3.5: The freely-jointed chain.

3.5 *Polymer statistics and random walks*

3.5.1 *General formulation*

Next we study a more general approach to polymer statistics, following the discussion in Doi and Edwards.[8] Consider an arbitrary free

---

[8] M. Doi and S.F. Edwards. *The Theory of Polymer Dynamics*. Clarendon Press, Oxford, UK, 1986

polymer of segment length b, where $\mathbf{r}_n$ ($n = 1, \dots, N$) is the position of the start of each segment and

$$\mathbf{r}_{n+1} = \mathbf{r}_n + \boldsymbol{\zeta}_n, \tag{3.56}$$

with $\boldsymbol{\zeta}_n$ a random displacement of fixed length ($|\boldsymbol{\zeta}_n| = b$). The "end-to-end" displacement $\mathbf{R}$ of the polymer,

$$\mathbf{R} \equiv \mathbf{r}_N - \mathbf{r}_0 = \sum_{n=1}^{N} \boldsymbol{\zeta}_n \tag{3.57}$$

is a quantity of great interest. If, as usual, we denote an average over realisations of random variables (in this case, the $\{\boldsymbol{\zeta}_n\}$), then

$$\langle \mathbf{R} \rangle = \sum_{n=1}^{N} \langle \boldsymbol{\zeta}_n \rangle = 0 \tag{3.58}$$

by symmetry. The average second moment can be calculated in the usual way as

$$\langle \mathbf{R}^2 \rangle = \sum_{m=1}^{N} \sum_{n=1}^{N} \langle \boldsymbol{\zeta}_m \cdot \boldsymbol{\zeta}_n \rangle = Nb^2, \tag{3.59}$$

where we have made us of the relation $\langle \boldsymbol{\zeta}_m \cdot \boldsymbol{\zeta}_n \rangle = \delta_{mn} b^2$ that holds for the independently distributed random variables $\{\boldsymbol{\zeta}_m\}$. The similarity with the Langevin formalism is apparent.

Let us formulate the problem more generally, without the specific requirement that the segments be of a fixed length. We start by defining the probability that a polymer with N segments will have segment positions at $\{\mathbf{r}_k\}$ as

$$P(\{\mathbf{r}_k\}) = \frac{1}{Z} G(\{\mathbf{r}_k\}) \quad \text{with} \quad G = \mathrm{e}^{-\beta U(\{\mathbf{r}_k\})}. \tag{3.60}$$

The energy is typically a sum of near-neighbor interactions and a contribution from an external potential,

$$U(\{\mathbf{r}_k\}) = \sum_{j=1}^{N} U_j(\mathbf{r}_{j-1}, \mathbf{r}_j) + W(\{\mathbf{r}_k\}). \tag{3.61}$$

When $W = 0$, this is just a "random flight" model. Now define the probability distribution $p_j(\mathbf{R}_j)$ of segment lengths

$$p(\mathbf{R}_j) = \exp[-\beta U_j(\mathbf{R}_j)] \quad \text{where} \quad \mathbf{R}_j = \mathbf{r}_j - \mathbf{r}_{j-1}, \tag{3.62}$$

and assume it is normalized ($\int d\mathbf{R} p(\mathbf{R}) = 1$).

The fixed end-to-end-vector partition function $\mathcal{G}$ is defined as the integral over all degrees of freedom of the internal segments such that the end position is $\mathbf{R}$, assuming for convenience that the start of the first segment is at the origin,

$$\begin{aligned} \mathcal{G}(\mathbf{R}; N) &= \int d\mathbf{R}^N G(\{\mathbf{R}_k\}) \delta(\mathbf{r}_N - \mathbf{R}), \\ &= \int d\mathbf{R}^N \prod_{j=1}^{N} p(\mathbf{R}_j) \delta\left(\sum_{k=1}^{N} \mathbf{R}_k - \mathbf{R}\right), \end{aligned} \tag{3.63}$$

where the notation is that of (2.4), namely $d\mathbf{R}^N = d\mathbf{R}_1 d\mathbf{R}_2 \cdots d\mathbf{R}_N$. Now we use an integral representation of a delta function,

$$\delta\left(\mathbf{P}\right) = \int \frac{d^3k}{(2\pi)^3} \mathrm{e}^{i\mathbf{k}\cdot\mathbf{P}}, \tag{3.64}$$

to express $\mathcal{G}$ for a system of identical segments as

$$\mathcal{G} = \int \frac{d^3k}{(2\pi)^3} e^{-i\mathbf{k}\cdot\mathbf{R}} K(\mathbf{k};N), \tag{3.65}$$

where the so-called "characteristic function" is

$$K(\mathbf{k};N) = \left(\int d\mathbf{R}\, p(\mathbf{R}) e^{i\mathbf{k}\cdot\mathbf{R}}\right)^N. \tag{3.66}$$

As an example, consider a fixed-length segment, for which

$$p(\mathbf{R}) = \frac{1}{4\pi b^2}\delta\left(|\mathbf{R}| - b\right), \tag{3.67}$$

and hence

$$K(\mathbf{k};N) = \left(\frac{\sin(kb)}{kb}\right)^N. \tag{3.68}$$

In the limit of large N, it is the small-k behaviour that is important, and if we expand K we find

$$K(\mathbf{k};N) \approx \left(1 - \frac{k^2b^2}{6} + \dots\right)^N \sim \exp(-Nk^2b^2/6). \tag{3.69}$$

For more general distributions, we will obtain the form in 3.69, but with b having the interpretation of an appropriate second moment of $p(\mathbf{R})$. Inverse Fourier transforming in (3.65), we obtain

$$\mathcal{G}(\mathbf{R};N) = \left(\frac{3}{2\pi b^2 N}\right)^{3/2} \exp\left(\frac{-3R^2}{2Nb^2}\right). \tag{3.70}$$

This Gaussian distribution is the central feature of ideal random walks, and is not restricted to a fixed-length distribution p. It is essentially a consequence of the central limit theorem that requires only a finite second moment of the underlying distribution.

3.5.2 *Flory theory and self-avoidance*

We may interpret the argument of the exponential in (3.70) as an effective (entropic) free energy,

$$F_{\text{entropic}}(R) = -k_BT \ln \mathcal{G}(R;N) = k_BT\frac{3R^2}{2Nb^2}. \tag{3.71}$$

This has the form of a (Hookean) entropic spring, with a minimum at $R = 0$ reflecting the fact that stretching the chain lowers its entropy. In a root-mean-square sense, the typical end-to-end distance obeys the scaling form

$$R \sim N^\nu, \tag{3.72}$$

with $\nu = 1/2$ as expected for an ideal random walk. Let us now consider how excluded-volume interactions change this free energy, adopting the scaling point of view first introduced by Flory[9] and extended by many others.[10] The effects of self-avoidance are introduced by means of a short-ranged (indeed, δ function) interaction between segments along the chain of the form

$$\frac{1}{2}vk_BT\int_0^N dn\int_0^N dm\ \delta(\mathbf{R}_n-\mathbf{R}_m), \tag{3.73}$$

where for convenience we have included k_BT in the prefactor.

Using a mean-field argument like that used to calculate the internal energy of a gas in the approach of van der Waals (Eq. 2.10), we estimate the contribution of these interactions to the free energy using the local segment concentration N/R^3,

$$vk_BT\cdot N\cdot\frac{N}{R^3}\sim k_BT\frac{vN^2}{R^3}. \tag{3.74}$$

The total free energy in this *Flory theory* is thus

$$F(R)=k_BT\left[\frac{3R^2}{2N\ell^2}+\frac{vN^2}{R^3}\right]. \tag{3.75}$$

We see a competition between entropy, which favours the smallest R, and excluded-volume effects that tend to swell the chain. Differentiating to find the optimum, R^*, we obtain

$$R^*\sim N^{3/5}. \tag{3.76}$$

As the exponent $\nu=3/5>1/2$, excluded-volume interactions have swollen the chain from its ideal size (3.72).

It is instructive to generalise this to arbitrary spatial dimension d. The only change needed to (3.75) is the form of the local concentration in the excluded volume interaction, which becomes N/R^d. The new balance of terms is

$$\frac{R^2}{N}\sim\frac{N^2}{R^d}, \tag{3.77}$$

which leads immediately to the predicted exponent

$$\nu=\frac{3}{d+2}. \tag{3.78}$$

These are compared to the known values in Table 3.1. The case of $d=1$ is trivial, as such a self-avoiding chain must be fully stretched out, while for $d>4$ the probability of a chain contacting itself is so low as to leave the Gaussian scaling unchanged. Apart from the case $d>4$ we see that Flory theory is remarkably accurate.

d	ν_{Flory}	ν_{exact}	comments
1	1	1	exact result
2	3/4	3/4	exact solution
3	3/5	0.589...	numerical
4	1/2	1/2	upper critical dimension
>4	$3/(d+2)$	1/2	excluded volume irrelevant

Table 3.1: Scaling exponent for self-avoiding walks in d dimensions.

---

[9] P.J. Flory. *Principles of Polymer Chemistry*. Cornell University Press, Ithaca, NY, 1953

[10] P.G. de Gennes. *Scaling Concepts in Polymer Physics*. Cornell University Press, Ithaca, NY, 1979

4

Biological Filaments (Lectures 8-12)

Living systems are replete with filaments, from the polymers such as actin and microtubules that comprise the cytoskeleton to cilia and flagella that power the motility of microorganisms. At larger scales we find slender, undulating organisms such as worms and snakes. In this chapter we discuss the basic differential geometry of filaments in two and three dimensions, their elasticity and principles by which their motion can be understood. We also discuss some key instabilities that are relevant in biological phenomena. Aspects of the analyses presented here find application in the theory of pattern formation, discussed in Chapter 7. There are many excellent reviews on the subject,[1] and concise compendia on differential geometry.[2]

4.1 Essentials of differential geometry of curves

We start the basic differential geometry of curves in the plane. Consider a curve $\mathbf{r}(\alpha)$ in a plane, parameterized by $\alpha \in [0,1]$ (Fig. 4.1). For generality, the range of α is taken to be fixed; it can be any monotonically increasing label along the curve, such as the arclength s normalized by curve length L. Later we will specialise to the arclength representation where appropriate. Let $\mathbf{r}_\alpha \equiv \partial \mathbf{r}/\partial\alpha$ be the *unnormalized* tangent vector, and introduce the metric

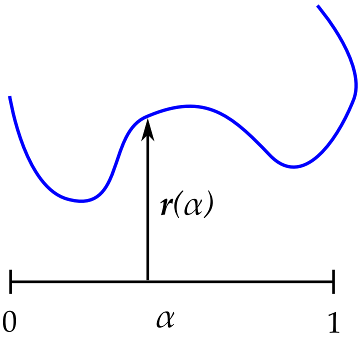

Figure 4.1: A curve in the plane. The vector $\mathbf{r}(\alpha)$ is a map between the unit interval and the blue curve.

$$g = \mathbf{r}_\alpha \cdot \mathbf{r}_\alpha. \tag{4.1}$$

Then the differential of arclength is

$$ds = |d\mathbf{r}| = \sqrt{g}\,d\alpha, \tag{4.2}$$

and the unit tangent to the curve is

$$\hat{\mathbf{t}} = \frac{\mathbf{r}_\alpha}{\sqrt{g}}. \tag{4.3}$$

The normal vector $\hat{\mathbf{n}}$ at each point is orthogonal to the tangent, and its components are given by

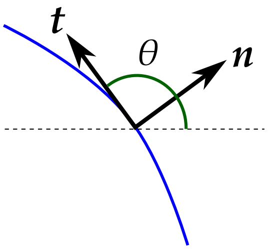

Figure 4.2: The unit tangent and normal vectors to a curve, and the tangent angle θ defined with respect to the x axis.

$$\hat{\mathbf{n}}_i = \epsilon_{ij}\hat{\mathbf{t}}_j, \tag{4.4}$$

where ϵ_{ij} is the Levi-Civita symbol ($\epsilon_{12} = +1$, $\epsilon_{21} = -1$, $\epsilon_{11} = \epsilon_{22} = 0$). The pair $(\hat{\mathbf{t}}, \hat{\mathbf{n}})$ is a local coordinate system (Fig. 4.2) that rotates

---

[1] Powers, T.R. Dynamics of filaments and membranes in a viscous fluid. *Rev. Mod. Phys.*, 82:1607–1631, 2010

[2] S. Lipschutz. *Differential Geometry. Schaum's Outline Series*. McGraw-Hill Education, New York, 1969

as it moves along the curve according to the *Frenet-Serret* equations

$$\frac{\partial}{\partial s}\begin{pmatrix}\hat{\mathbf{t}}\\ \hat{\mathbf{n}}\end{pmatrix}=\begin{pmatrix}0 & -\kappa\\ \kappa & 0\end{pmatrix}\begin{pmatrix}\hat{\mathbf{t}}\\ \hat{\mathbf{n}}\end{pmatrix}, \tag{4.5}$$

where the curvature κ can be positive or negative. Adopting the convention in Fig. 4.2, where the tangent angle θ is with respect to the x axis, we have $\hat{\mathbf{n}}=\cos\theta\mathbf{e}_x+\sin\theta\mathbf{e}_y$ and $\hat{\mathbf{t}}=-\sin\theta\mathbf{e}_x+\cos\theta\mathbf{e}_y$, from which we find

$$\kappa=\frac{\partial\theta}{\partial s}, \tag{4.6}$$

where, in general,

$$\frac{\partial}{\partial s}=\frac{1}{\sqrt{g}}\frac{\partial}{\partial\alpha}. \tag{4.7}$$

In the "Monge representation", where we have a single-valued function $h(x)$ as a function of the external coordinate x, the position vector is $\mathbf{r}(x)=(x,h)$, the tangent is $(1/\sqrt{1+h_x^2}, h_x/\sqrt{1+h_x^2})$, and $\theta=\tan^{-1}h_x$, and we have the familiar result

$$\kappa=\frac{h_{xx}}{(1+h_x^2)^{3/2}}. \tag{4.8}$$

With the formulation above, we can calculate two elementary geometric features of curves, their length L and the area A they enclose, if closed. While we will often deal with open curves (representing, say, elastic filaments), there are times when closed curves are of interest, whether an actual closed loop of DNA or an interface between two states in a reaction-diffusion system, or a simplified model of a cell membrane in two dimensions. The length is trivially

$$L=\int_0^1 d\alpha\sqrt{g}, \tag{4.9}$$

while the area is

$$A=\frac{1}{2}\int_0^1 d\alpha\mathbf{r}\times\mathbf{r}_\alpha, \tag{4.10}$$

where in two dimensions the cross product is the scalar $(\mathbf{a}\times\mathbf{b})=\epsilon_{ij}\mathbf{a}_i\mathbf{b}_j$. The description of space curves is quite similar to the planar case, only now there is an *orthonormal triad* of the tangent $\hat{\mathbf{t}}$, normal $\hat{\mathbf{n}}$ and binormal $\hat{\mathbf{b}}=\hat{\mathbf{t}}\times\hat{\mathbf{n}}$ that evolves with arclength as

$$\frac{\partial}{\partial s}\begin{pmatrix}\hat{\mathbf{t}}\\ \hat{\mathbf{n}}\\ \hat{\mathbf{b}}\end{pmatrix}=\begin{pmatrix}0 & \kappa & 0\\ -\kappa & 0 & \tau\\ 0 & -\tau & 0\end{pmatrix}\begin{pmatrix}\hat{\mathbf{t}}\\ \hat{\mathbf{n}}\\ \hat{\mathbf{b}}\end{pmatrix}, \tag{4.11}$$

where now the curvature κ is strictly ≥ 0 and τ is the torsion.

4.2 *Overdamped filament motion*

Many of the problems of interest in the biological physics of filaments take place at the cellular scale. If we formulate a Reynolds number for these problems,

$$Re=\frac{UL}{\nu}, \tag{4.12}$$

where U is a typical fluid speed, L is a typical length scale for the motion, and the kinematic viscosity of water $\nu \sim 10^6\,\mu\text{m}^2/\text{s}$ (Table 1.1), then with $U \sim 1 - 100\mu\text{m/s}$ and $L \sim 1 - 100\mu\text{m}$, we have $Re \sim 10^{-6} - 10^{-2}$, which is well in the Stokesian regime where inertia can be neglected. It follows that the equations of motion for filaments should be first order in temporal derivatives, reflecting a balance of viscous and elastic forces.

4.2.1 *A variational principle*

It is pedagogically useful to formulate the dynamics through a variational principle, as this provides a way to connect forces to an underlying energy functional, and to assure that the dynamics has an appropriate reparameterisation invariance. With this in mind, we first review the manner in which dissipative contributions can be introduced into the usual Lagrangian formulation of classical dynamics.[3]

Consider a system specified by a single coordinate q and its time derivative $\dot{q}$. In the usual manner, the Lagrangian is

$$\mathcal{L}(q,\dot{q}) = \mathcal{T} - \mathcal{V}, \tag{4.13}$$

where $\mathcal{T}$ and $\mathcal{V}$ are the kinetic and potential energies. From the action $\mathcal{S} = \int dt\mathcal{L}$, the minimum action principle $\delta\mathcal{S} = 0$, yields the Newtonian equation of motion

$$\frac{d}{dt}\frac{\partial\mathcal{L}}{\partial\dot{q}} - \frac{\partial\mathcal{L}}{\partial q} = 0. \tag{4.14}$$

With $\mathcal{T} = m\dot{q}^2/2$ the Euler-Lagrange equation becomes

$$m\ddot{q} = -\frac{\partial V}{\partial q}. \tag{4.15}$$

In the limit of vanishing inertia ($Re = 0$), simply dropping the kinetic energy term leaves us with no dynamics, because dissipative forces are not captured in either $\mathcal{T}$ or $\mathcal{V}$. Instead, we must introduce a *generalised force* associated with dissipation. This quantity is related to the rate at which viscous forces do work. For example, if, as in the case of a sphere moving through a viscous fluid, the viscous force is $\zeta\dot{q}$, where ζ is a drag coefficient, the rate of dissipation (force×velocity) is $\zeta\dot{q}^2$. Thus, we introduce the *Rayleigh dissipation function*

$$\mathcal{R} = \frac{1}{2}\zeta\dot{q}^2\,, \tag{4.16}$$

proportional to the dissipation rate, and obtain the new variational principle in which the derivative of $\mathcal{R}$ with respect to velocity is a generalised force,

$$\frac{d}{dt}\frac{\partial\mathcal{L}}{\partial\dot{q}} - \frac{\partial\mathcal{L}}{\partial q} = -\frac{\partial\mathcal{R}}{\partial\dot{q}}. \tag{4.17}$$

In the overdamped limit, we then have the Aristotelian law

$$\zeta\dot{q} = -\frac{\partial\mathcal{V}}{\partial q}. \tag{4.18}$$

---

[3] H. Goldstein. *Classical Mechanics*. Addison-Wesley, Boston, MA, 2nd edition, 1980

Now we ask how to generalise these ideas to moving curves. We start by formulating the dissipation rate. The simplest generalization of the Stokes drag on a sphere to a moving curve involves a local, *isotropic* drag coefficient ζ, so that

$$\mathcal{R} = \frac{1}{2}\zeta \int d\alpha \sqrt{g}\, \mathbf{r}_t^2, \tag{4.19}$$

and the generalized viscous force is $-\delta\mathcal{R}/\delta\mathbf{r}_t = -\zeta\sqrt{g}\,\mathbf{r}_t$, and thus (renaming $\mathcal{V}$ as $\mathcal{E}$, the energy functional of the curve or filament), the equation of motion for isotropic drag is

$$\zeta\mathbf{r}_t = -\frac{1}{\sqrt{g}}\frac{\delta\mathcal{E}}{\delta\mathbf{r}}, \tag{4.20}$$

where the r.h.s. is a functional derivative. The main result of having formulated the dissipation rate in a reparameterisation invariant manner is the metric factor in 4.20.

For a long, slender object of length L and radius a in three dimensions, the calculation of the drag is a complicated nonlocal problem, but often the dominant behaviour is well-described by *Resistive Force Theory*[4] (RFT) in which there are local drag coefficients $\zeta_\perp$ and $\zeta_\parallel$ for motion perpendicular and parallel to the filament, and ζ_r for rotational motion. These can be understood most simply by appealing to the known drag coefficients for prolate ellipsoids.[5] If the ellipsoid has length L and radius a, then if $L/a \gg 1$ the drag coefficients are

$$\zeta_\parallel = \frac{2\pi\mu}{\ln(L/a) - 1/2}, \quad \zeta_\perp = \frac{4\pi\mu}{\ln(L/a) + 1/2} \tag{4.21}$$

For many applications it is sufficiently accurate to assume $\zeta_\perp = 2\zeta_\parallel$. These can also be derived in a systematic manner through an asymptotic expansion in the aspect ratio of the filament.[6] The rate of energy dissipation is a simple generalisation of 4.19,

$$\mathcal{R} = \frac{1}{2}\int d\alpha\sqrt{g}\left\{\zeta_\parallel\left(\hat{\mathbf{t}}\cdot\mathbf{r}_t\right)^2 + \zeta_\perp\left[\left(\hat{\mathbf{n}}\cdot\mathbf{r}_t\right)^2 + \left(\hat{\mathbf{b}}\cdot\mathbf{r}_t\right)^2\right]\right\}, \tag{4.22}$$

and the general filament equation of motion becomes

$$\left(\zeta_\parallel\hat{\mathbf{t}}\hat{\mathbf{t}} + \zeta_\perp\left[\mathbb{I} - \hat{\mathbf{t}}\hat{\mathbf{t}}\right]\right)\cdot\mathbf{r}_t = -\frac{1}{\sqrt{g}}\frac{\delta\mathcal{E}}{\delta\mathbf{r}}, \tag{4.23}$$

where $\mathbb{I} = \hat{\mathbf{t}}\hat{\mathbf{t}} + \hat{\mathbf{n}}\hat{\mathbf{n}} + \hat{\mathbf{b}}\hat{\mathbf{b}}$ is the unit dyad. If we use the asymptotic result $\zeta_\perp = 2\zeta_\parallel$, then the projection operator on the l.h.s. of 4.23 is proportional to $\mathbb{I} - \hat{\mathbf{t}}\hat{\mathbf{t}}/2$. The inverse of this operator is

$$\left(\mathbb{I} - \frac{1}{2}\hat{\mathbf{t}}\hat{\mathbf{t}}\right)^{-1} = \mathbb{I} + \hat{\mathbf{t}}\hat{\mathbf{t}}, \tag{4.24}$$

and therefore we can write the equation of motion 4.23 as

$$\mathbf{r}_t = -\frac{1}{\zeta_\perp}\left(\mathbb{I} + \hat{\mathbf{t}}\hat{\mathbf{t}}\right)\cdot\frac{1}{\sqrt{g}}\frac{\delta\mathcal{E}}{\delta\mathbf{r}}. \tag{4.25}$$

The above analysis defines the dynamics of the filament centreline, but does not address any twisting deformations that can occur. For

---

[4] J. Gray and G.J. Hancock. The propulsion of sea-urchin spermatozoa. *J. Exp. Biol.*, 32:802, 1955

[5] Oberbeck, A. Ueber stationäre Flüssigkeitsbewegungen mit Berücksichtigung der inneren Reibung. *J. Reine. Angew. Math.*, 81:62–80, 1876

[6] Keller, J.B. and Rubinow, S.I. Slender-body theory for slow viscous flow. *J. Fluid Mech.*, 75:705–714, 1976

long, slender filaments the balance of forces for a filament rotating at angular frequency ω about its long axis has the simple form

$$m = \zeta_r \omega, \tag{4.26}$$

where m is the moment and $\zeta_r = 4\pi\mu a^2$ is the rotational drag coefficient. We shall discuss this at greater length below.

4.2.2 *Elasticity*

In this section we use the general formulation developed above to study filaments governed by the elastic energy[7]

$$\mathcal{E} = \frac{1}{2} A \int_0^L ds\, \kappa^2, \tag{4.27}$$

where A is the bending modulus. This energy penalizes bending in any direction away from a straight filament, which is the ground state. As in our discussion of membrane elasticity, it is useful to express A in terms of thermal energy. Since it has units of energy·length, we can write $A = k_B T L_p$, where L_p is the *persistence length*. The persistence length has a simple physical meaning; if a filament has length L_p and is bent on the scale of its own length, then the energetic cost is thermal energy, since $E \sim A \cdot L_p \cdot 1/L_p^2 \sim A/L_p \sim k_B T$.

filament	L_p	radius	length	L/L_p
DNA	50 nm	1 nm	nm-m	$10^{-2} - 10^{7}$
actin	$10 - 15\,\mu$m	3.5 nm	$1 - 10^{3}\,\mu$m	$0.1 - 10^{2}$
microtubules	5 mm	12 nm	$1 - 100\,\mu$m	$10^{-4} - 10^{-2}$

Table 4.1: The persistence lengths of various biological filaments.

Filaments governed by the elastic energy 4.27 are termed "semi-flexible", and are found throughout the cell. Table 4.1 summarizes the three most important examples. We shall not delve into the detailed derivation of 4.27 here, but note that resistance to bending fundamentally arises from the resistance to stretching. As shown in Fig. 4.3, the outer edge of a bent filament is under extension and the inner edge is compressed. The resistance to stretching or compression is quantified by the Young's modulus Y as the proportionality between the force per unit area applied to an object and its fractional change in length,

$$\frac{\text{force}}{\text{area}} = Y \frac{\Delta L}{L}. \tag{4.28}$$

Y clearly has units of energy/volume, and by comparison to the modulus we deduce that $A \sim Y \cdot \text{length}^4$. As the only length scale of relevance for a filament is its radius a, we deduce that

$$A \sim Y a^4. \tag{4.29}$$

If we take as an example the case of microtubules, we deduce $Y \sim 10^9$ Pa, which is similar to that of plastics.

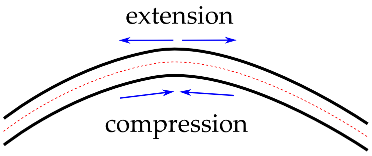

Figure 4.3: A bent filament viewed in longitudinal cross section. Red dashed line indicates neutral plane.

In order to derive the filament dynamics we need the functional derivative of the energy 4.27. This functional is of the general form

$$\mathcal{E} = \int d\alpha f(\mathbf{r}, \mathbf{r}_\alpha, \mathbf{r}_{\alpha\alpha}, \ldots). \tag{4.30}$$

---

[7] L.D. Landau and E.M. Lifshitz. *Theory of Elasticity*. Butterworth-Heinemann, Oxford, UK, 3rd edition, 1986

The quantities $\mathbf{r}_\alpha$ and $\mathbf{r}_{\alpha\alpha}$ show up in the metric factor $\sqrt{g}$ and the elastic term, which can be written in a covariant manner as

$$\kappa^2 = \left[\frac{1}{\sqrt{g}}\partial_\alpha\left(\frac{\mathbf{r}_\alpha}{\sqrt{g}}\right)\right]^2. \tag{4.31}$$

The functional derivative (or "Fréchet" derivative) of 4.30 is

$$\frac{\delta\mathcal{E}}{\delta\mathbf{r}} = \frac{\partial f}{\partial\mathbf{r}} - \frac{\partial}{\partial\alpha}\frac{\partial f}{\partial\mathbf{r}_\alpha} + \frac{\partial^2}{\partial\alpha^2}\frac{\partial f}{\partial\mathbf{r}_{\alpha\alpha}} + \cdots, \tag{4.32}$$

where each successive term arises from one additional integration by parts in the usual manner.

For the remainder of our discussion we will confine ourselves to curves in the plane. A straightforward (if tedious) calculation of this to 4.27 for such filaments yields the result

$$-\frac{1}{\sqrt{g}}\frac{\delta\mathcal{E}}{\delta\mathbf{r}} = A\left(\kappa_{ss} + \frac{1}{2}\kappa^3\right)\hat{\mathbf{n}}. \tag{4.33}$$

Note that this force is purely normal to the filament. As the curvature involves two derivatives of position, κ_{ss} involves four; this is a hallmark of elasticity that is distinct from the effects of tension (as in a violin string), which produces a restoring force proportional to the curvature itself. One might imagine that with an energy that is (curvature)^2 the fourth derivative would be the only term in the force, but this is not the case. The *nonlinear* term κ^3 appears even though this theory is based fundamentally on linear elasticity theory. It is a *geometric nonlinearity* that arises from the fact that the coordinate $\mathbf{r}$ and arclength s are not independent. And it is intuitive physically, if we think of a closed circular loop, where the curvature is constant ($\kappa_{ss} = 0$) and yet there is uniform outward force which would only be relaxed at vanishing curvature (infinite radius).

A small technical aside is needed here. It is tempting (and frequently done in the literature) to adopt a simplified picture in which the energy (4.27) as a functional of the quantity $\mathbf{r}(s)$, ignoring the fact that s and $\mathbf{r}$ are not independent. In this calculation, we simply write

$$\mathcal{E}[\mathbf{r}] = \frac{1}{2}A\int ds\, \mathbf{r}_{ss}^2, \tag{4.34}$$

and deduce the force

$$-\partial_{ss}\left(\frac{\partial}{\partial\mathbf{r}_{ss}}\left(\frac{1}{2}A\mathbf{r}_{ss}^2\right)\right) = -A\mathbf{r}_{ssss}. \tag{4.35}$$

A simple calculation using the Frenet-Serret equations shows that

$$-A\mathbf{r}_{ssss} = A\left(\kappa_{ss} - \kappa^3\right)\hat{\mathbf{n}} + 3A\kappa\kappa_s\hat{\mathbf{t}}, \tag{4.36}$$

which differs from (4.33) in the coefficient of the cubic term in κ and the presence of a tangential component. But those extra terms comprise a total derivative,

$$-\frac{1}{\sqrt{g}}\frac{\delta\mathcal{E}}{\delta\mathbf{r}} = -A\mathbf{r}_{ssss} - \partial_s\left(\frac{3}{2}A\kappa^2\hat{\mathbf{t}}\right). \tag{4.37}$$

We shall now see that the difference between the two calculations represents a tension-like contribution.

If we were to use $\mathcal{E}$ directly as our energy functional, the dynamics will not necessarily preserve the local arclength along the filament. To enforce local inextensibility we introduce a Lagrange multiplier function $\Lambda(\alpha)$ that represents the internal tension,[8] and define

$$\mathcal{F} = \mathcal{E} - \int_0^1 d\alpha \sqrt{g}\Lambda(\alpha). \tag{4.38}$$

The functional derivative of $\mathcal{F}$ is

$$\begin{aligned} -\frac{1}{\sqrt{g}}\frac{\delta \mathcal{F}}{\delta \mathbf{r}} &= -\frac{1}{\sqrt{g}}\frac{\delta \mathcal{E}}{\delta \mathbf{r}} - \left(\Lambda \hat{\mathbf{t}}\right)_s \\ &= A\left(\kappa_{ss} + \frac{1}{2}\kappa^2\right)\hat{\mathbf{n}} + \Lambda\kappa\hat{\mathbf{n}} - \Lambda_s\hat{\mathbf{t}}. \end{aligned} \tag{4.39}$$

The new terms involving Λ can be interpreted as a Young-Laplace force in the normal direction (tension × curvature) and a tangential "Marangoni" force (gradient of tension).

In order to find $\Lambda(s)$, we appeal to some general results for the dynamics of curves in the plane. The equation of motion 4.25 for filaments is of the form

$$\mathbf{r}_t = U\hat{\mathbf{n}} + W\hat{\mathbf{t}}, \tag{4.40}$$

where $U = U(\mathbf{r}, \kappa, \ldots)$ and $W = W(\mathbf{r}, \kappa, \ldots)$ are the normal and tangential velocities. If the filament is *locally inextensible*, then the metric must be time-independent. Computing the time derivative of $\ln\sqrt{g}$ to highlight the reparameterisation invariance, and written out to emphasise that α is time-independent ($\mathbf{r}_{\alpha t} = \mathbf{r}_{t\alpha}$), we have

$$\frac{\partial \ln\sqrt{g}}{\partial t} = \frac{\mathbf{r}_\alpha}{\sqrt{g}} \cdot \frac{\mathbf{r}_{\alpha t}}{\sqrt{g}} = \hat{\mathbf{t}} \cdot \partial_s \mathbf{r}_t = W_s + \kappa U, \tag{4.41}$$

and therefore the incompressibility constraint is $W_s = -\kappa U$. From our filament equation we deduce that

$$U = \frac{1}{\zeta_\perp}\left\{A\left(\kappa_{ss} + \frac{1}{2}\kappa^3\right) + \Lambda\kappa\right\}, \quad W = -\frac{2\Lambda_s}{\zeta_\perp}, \tag{4.42}$$

where the factor of 2 in W arises from the drag coefficient ratio. From 4.41 and 4.42 we find that Λ obeys an inhomogeneous elliptic second-order ODE at each instant of time,

$$\left(\partial_{ss} - \frac{1}{2}\kappa^2\right)\Lambda = \frac{A}{2}\kappa\left(\kappa_{ss} + \frac{1}{2}\kappa^3\right). \tag{4.43}$$

We now see that the difference between the "proper" (4.33) and simplified (4.36) forces is a redefinition of the tension.

The general dynamics 4.40 is an *intrinsic* equation of motion, and it is of interest to the time evolution of geometric quantities such as the tangent angle θ and the curvature κ. As these are scalar quantities they are often easier to study (both analytically and numerically), particularly when a filament is free in space and its absolute position

[8] Goldstein, R.E. and Langer, S.A. Nonlinear dynamics of stiff polymers. *Phys. Rev. Lett.*, 75:1094–1097, 1995

(and possibly its orientation) are unimportant. The tangent vector evolves as $\partial\hat{\mathbf{t}}/\partial t = (U_s - \kappa W)\hat{\mathbf{n}}$ and therefore with $\hat{\mathbf{t}}$ and $\hat{\mathbf{n}}$ defined above 4.6, we have $\partial\hat{\mathbf{t}}/\partial t = -\theta_t\hat{\mathbf{n}}$, and thus

$$\theta_t = -U_s + \theta_s W. \tag{4.44}$$

A bit more work shows that the curvature obeys the PDE

$$\kappa_t = -\left(\partial_{ss} + \kappa^2\right) U + \kappa_s W\ . \tag{4.45}$$

In both (4.44) and (4.45) we see that W enters as an advective term.

4.2.3 *Boundary conditions and biharmonic eigenfunctions*

A final general point to make in discussing filaments is the boundary conditions at their ends. While in some problems there are obvious forces or torques applied at the filament ends, the case of "free" ends with vanishing force and torque are extremely common and deserve attention. It is easiest to think about these problems when the filament is only weakly displaced from straight, where the Monge representation holds and we can approximate the elastic energy as

$$E \simeq \frac{A}{2}\int_0^L dx\, h_{xx}^2. \tag{4.46}$$

To find the boundary conditions we compute the change δE when $h \to h + \delta h$, paying close attention to the surface terms that arise by repeated integration by parts

$$\begin{aligned} \delta E \quad &= A\int_0^L dx h_{xx}\delta h_{xx} = A\left\{ h_{xx}\delta h_x\Big|_0^L - \int_0^L dx h_{3x}\delta h_x \right\} \\ &= A\left\{ h_{xx}\delta h_x\Big|_0^L - h_{xxx}\delta h\Big|_0^L + \int_0^L dx h_{4x}\delta h \right\}. \end{aligned} \tag{4.47}$$

In the usual way, the functional derivative of E is just the coefficient of δh inside the final integral,

$$\frac{\delta E}{\delta h} = A h_{4x}. \tag{4.48}$$

If the surface terms are to vanish for arbitrary δh and δh_x, then

$$h_{xx}(0) = h_{xx}(L) = 0, \quad \text{and} \quad h_{xxx}(0) = h_{xxx}(L) = 0. \tag{4.49}$$

These are the boundary conditions of a free filament. The quantity Ah_{xx} is a torque and Ah_{xxx} is a force; the free ends are torque-free and force-free. When these (or related[9]) conditions hold at both ends, the operator ∂_{4x} is self-adjoint operator and its eigenvalues are real. Its biharmonic eigenfunctions W satisfy an equation of the form

$$AW_{4x} = k^4 W, \tag{4.50}$$

just as $\sin qx$ and $\cos qx$ are eigenfunctions satisfying $f_{xx} = -q^2 f$.

For the "free-free" case (both ends free), a simple superposition of $\sin kx$ and $\cos kx$ will not satisfy boundary conditions that require successive derivatives to vanish. Instead, the functions are

$$W(x) = A\sin kx + B\cos kx + D\sinh kx + E\cosh kx. \tag{4.51}$$

[9] Wiggins, C.H., Riveline, D., Ott, A. and Goldstein, R.E. Trapping and wiggling: elastohydrodynamics of driven microfilaments. *Biophys. J.*, 74:1043–1060, 1998

Computing the derivatives $W_{xx}(0)$ and W_{xxx} we deduce that $E = B$ and $D = A$. Then the problem reduces to the 2×2 system

$$\begin{pmatrix} \sinh kL - \sin kL & \cosh kL - \cos kL \\ \cosh kL - \cos kL & \sinh kL + \sin kL \end{pmatrix} \begin{pmatrix} A \\ B \end{pmatrix} = \begin{pmatrix} 0 \\ 0 \end{pmatrix}. \tag{4.52}$$

Setting the determinant to zero we obtain the condition

$$\cos kL = \frac{1}{\cosh kL}. \tag{4.53}$$

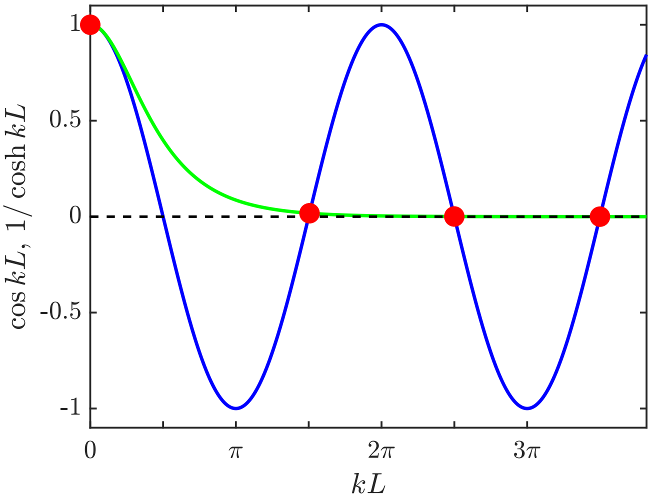

Figure 4.4: Solution of the transcendental relation 4.53. Blue curve is $\cos kL$, green is $1/\cosh kL$, and red dots represent the numerically obtained crossing points. Obtained with `Figure_404_and_405_biharmonic.m`.

The graphical solution to this transcendental relation is shown in Fig. 4.4. There is an infinite discrete set of solutions kL analogous to the trigonometric numbers $n\pi$ in ordinary Fourier series with Dirichlet boundary conditions. Beyond the first solution at $k = 0$, the crossing points are ever closer to the values $(2n + 1)\pi/2$ for $n \geq 1$. Even though these values are like those of a pure Fourier series, the eigenfunctions are qualitatively rather different, as seen in Fig. 4.5.

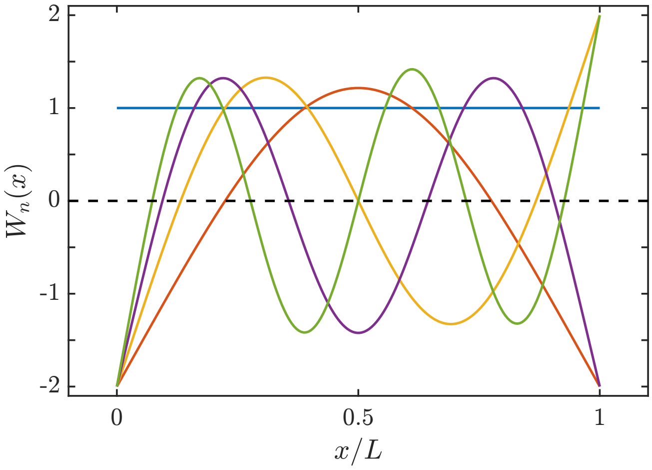

Figure 4.5: The first five biharmonic eigenfunctions $W_n(x)$ for free-free boundary conditions. Obtained with `Figure_404_and_405_biharmonic.m`.

Having established a complete set of orthonormal eigenfunctions of the operator ∂_{4x}, we can now illustrate their utility in the problem of thermal fluctuations of semiflexible polymers. If the filament shape $h(x)$ is expressed as a sum of biharmonic eigenfunctions,

$$h(x) = \sum_n a_n W^{(n)}(x), \tag{4.54}$$

we can, using repeated integration by parts as in (4.47), rewrite the bending energy as a sum over those modes,

$$\begin{aligned}\frac{1}{2}A\int_0^L dx h_{xx}^2 &= \frac{1}{2}A\int_0^L dx h h_{4x} \\ &= \frac{1}{2}A\int_0^L dx \sum_{m=1}^{\infty}\sum_{n=1}^{\infty} a_m a_n \lambda_n W^{(m)} W^{(n)} \\ &= \frac{1}{2}A\sum_{n=1}^{\infty}\lambda_n a_n^2, \end{aligned} \tag{4.55}$$

where in the last relation λ_n is the n^{th} eigenvalue, and we have used the orthonormality the Ws to simplify the result. Once again we have found an energy expressed as a sum of independent quadratic contributions, and thus from equipartition we obtain

$$\langle a_n^2\rangle = \frac{k_BT}{A\lambda_n} \simeq \frac{k_BT}{A}\frac{16L^4}{(2n+1)^4\pi^4}, \tag{4.56}$$

where in the last relation we have used the approximate form of the roots of the transcendental equation (4.53). The variance is

$$\langle h^2(x)\rangle = \frac{k_BT}{A}\sum_n \frac{W^{(n)}(x)^2}{\lambda_n}. \tag{4.57}$$

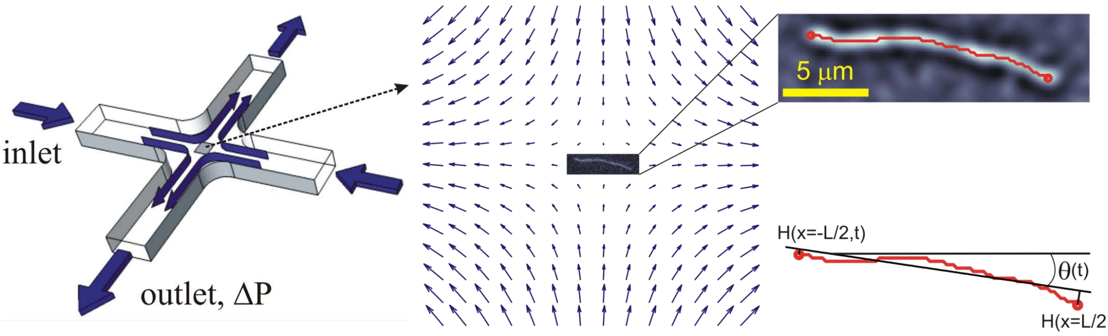

Figure 4.6: Microfluidic setup to study single actin filaments. From Ref. 10.

An experiment to study the dynamics of semiflexible filaments in imposed flow fields was done some time ago, using a microfluidic setup depicted in Fig. 4.6.[10] Single actin filaments can be held at the crossing point of two perpendicular channels meeting at a fourfold junction by means of the pressure difference Δp between the inlets and outlets. This also allows the flow to be changed from compressional to extensional for a filament oriented along either of the orthogonal directions. The vector field show illustrates the hyperbolic flow profile that can be achieved. At right is an image of a fluorescently labelled actin filament and the tracing of its centreline.

The variance of the filament deviation $h(x)$ from its straight configuration, normalised by its value at the endpoint, is shown in Fig. 4.7 for these experiments with actin, compared with the contribution

[10] Kantsler, V. and Goldstein, R.E. Fluctuations, dynamics, and the stretch-coil transition of single actin filaments in extensional flows. *Phys. Rev. Lett.*, 108: 038103, 2012

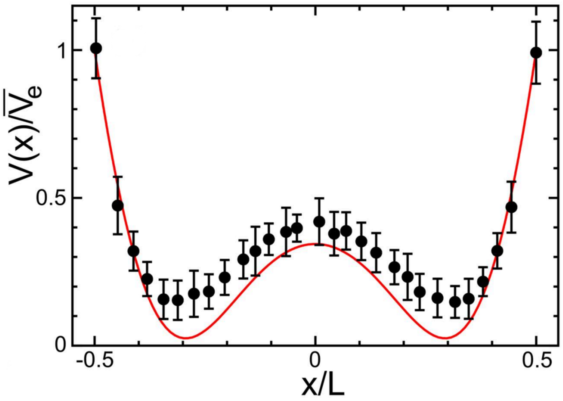

Figure 4.7: Normalised variance of fluctuating actin filaments, from Ref. 10..

from the fundamental mode $n = 1$ in (4.57). The somewhat unusual shape "W" shape arises from the nodes in the first mode, themselves an indirect consequence of the free-filament boundary conditions.

4.3 Instabilities and elastohydrodynamics

Here we work through four pedagogically important problems in elastohydrodynamics that use the formalism described above.

4.3.1 Example 1. Euler Buckling

Our first example is not itself dynamical, but serves to illustrate some useful ways of analyzing bifurcations in elastic systems. It is the classic problem of *Euler buckling*, in which an elastic filament subject to thrusting forces at its ends deforms at a critical force.

Figure 4.8: Buckling of microtubules growing inside a synthetic lipid vesicle. Scale bar is 5 μm . From Ref. 11.

Inside of cells, microtubules often interact with cell membranes and deform them. A series of experiments in the 1990s[11] provided some of the nicest illustrations of the forces at work in these contexts. Figure 4.8 shows an experimental realization of this instability involving microtubules grown by inducing polymerisation of tubulin monomers in solution inside of lipid vesicles. As they grew and the deformed membrane exerts larger and larger thrusting forces on their ends, the microtubules buckle.

Our analysis of Euler buckling will be done using the tangent-angle representation of the curve to illustrate an alternate approach to the Monge representation. Using the geometry of Fig. 4.9, the coordinates $x(s)$ and $y(s)$ of a point at arclength s are related to the tangent angle through $dx/ds = \cos\theta$ and $dy/ds = \sin\theta$. If we

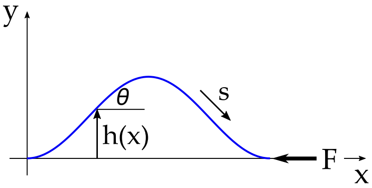

Figure 4.9: Geometry of Euler buckling.

[11] Fygenson, D.K., Marko, J.F. and Libchaber, A. Mechanics of microtubule-based membrane extension. *Phys. Rev. Lett.*, 79:4497–4500, 1997

take the left end of the filament to be at the origin ($x(0) = 0$), then the difference between the fully extended length L and the projected distance between the endpoints is $x(L)$ and $x(0)$ is

$$L - x(L) = \int_0^L ds \left(1 - \frac{dx}{ds}\right) = \int_0^L ds \left(1 - \cos\theta(s)\right). \tag{4.58}$$

The energy functional for the filament includes the bending energy and the work done by the force F in displacing the filament ends,

$$E[\theta] = \int_0^L ds \left[\frac{1}{2}A\theta_s^2 - F\left(1 - \cos\theta\right)\right]. \tag{4.59}$$

The equilibrium condition $\delta E/\delta\theta = 0$ is

$$A\theta_{ss} + F\sin\theta = 0, \tag{4.60}$$

which is the equation of motion of a pendulum in which arclength s stands for time. We rescale the arclength to $\alpha = s/L$ to obtain

$$\theta_{\alpha\alpha} + f\sin\theta = 0, \quad \text{with} \quad f = \frac{FL^2}{A}. \tag{4.61}$$

Let us consider *clamped* boundary conditions, $\theta(0) = \theta(1) = 0$. From everyday experience we expect the buckled shape beyond some threshold force to have a single maximum in the middle of the filament, with $\theta = 0$ there as well. This suggests a trial function

$$\theta(s) \simeq a\sin\left(2\pi\alpha\right). \tag{4.62}$$

Expecting that the amplitude of deflection will be small near the threshold, we linearise (4.61) to obtain

$$\theta_{\alpha\alpha} \simeq -f\theta. \tag{4.63}$$

The function (4.62) will only solve this equation provided $f = f_c$, where the critical force is

$$f_c = 4\pi^2, \quad \text{or} \quad F_c = 4\pi^2\frac{A}{L^2}. \tag{4.64}$$

To put this in perspective, consider microtubules, for which $L_p = 5\,\text{mm} \sim 5\times10^3\,\mu\text{m}$. Using $k_BT = 4\times10^-3\,\text{pN}\cdot\mu\text{m}$, we have $A \sim 20\,\text{pN}\cdot\mu\text{m}^2$. Thus, microtubules whose length is $\sim 20\,\mu\text{m}$ will buckle under a force of $1-2\,\text{pN}$. We return to this estimate later when discussing the effects of molecular motors on cytoskeletal filaments.

The linearised problem (4.63) gives us no information on the amplitude a of the mode that becomes unstable at f_c. Near the bifurcation, we expect that nonlinearities will stabilize the buckled shape at some finite amplitude. We can continue with the the single-mode approximation (4.62) and use a variational approach. First, let us assume we are close to the threshold force and write

$$f = f_c\left(1+\epsilon\right), \tag{4.65}$$

where ϵ is a bifurcation control parameter, and second, expand in the energy functional (4.59) the force contribution, using $\cos\theta = 1 -$

$\theta^2/2 + \theta^4/24 + \cdots$. If we define the dimensionless $\mathcal{E} = LE/A$ and integrate over α we obtain the energy to leading order in ϵ and a,

$$\mathcal{E} \simeq \frac{f_c}{2}\left[-\frac{1}{2}\epsilon a^2 + \frac{1}{32}a^4 + \ldots\right], \qquad (4.66)$$

where we have ignored an unimportant constant additive term.

This is a *Landau theory* for the bifurcation, an expansion in powers of the "order parameter" a, where the coefficient of the quadratic term can change sign as we increase the thrusting force. When $\epsilon < 0$ (below the bifurcation), $\mathcal{E}$ has a single minimum as a function of a, namely $a = 0$, while above there are two mirror-image minima at

$$a_\pm = \pm\sqrt{8\epsilon}, \qquad (4.67)$$

for $\epsilon \geq 0$. The square root dependence on the control parameter is the hallmark of a *pitchfork bifurcation*, as in Fig. 4.10.

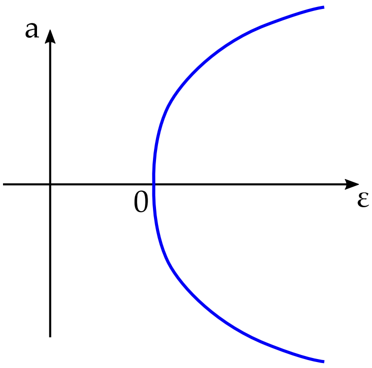

Figure 4.10: Pitchfork bifurcation of Euler buckling amplitude versus dimensionless control parameter ϵ.

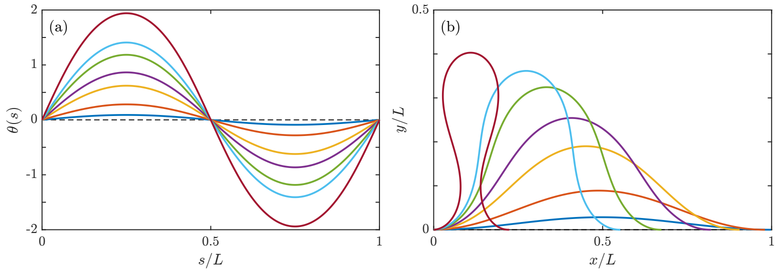

Figure 4.11: Euler buckling. (a) Numerically obtained solutions $\theta(s)$ for $\epsilon = 0.001, 0.01, 0.05, 0.1, 0.2, 0.3, 0.7$, with clamped boundary conditions. (b) The corresponding filament shapes. Obtained with `Figure_411_and_412_Eulerbuckle.m`.

While the general problem (4.61) can be solved analytically, it is a two-point boundary value problem that can be solved numerically in Matlab with a simple code, with results shown in Fig. 4.11.

One important lesson from this type of analysis is the accuracy of the single-mode approximation for the shape (4.62). It is already apparent from Fig. 4.11(a) that θ is qualitatively like the mode $\sin(2\pi s/L)$; Fig. 4.12 compares the numerically obtained maximum amplitude of $\theta(s)$ with the single-mode result (4.62) obtained near the bifurcation. The agreement is excellent even for values of ϵ as large as ~ 0.3.

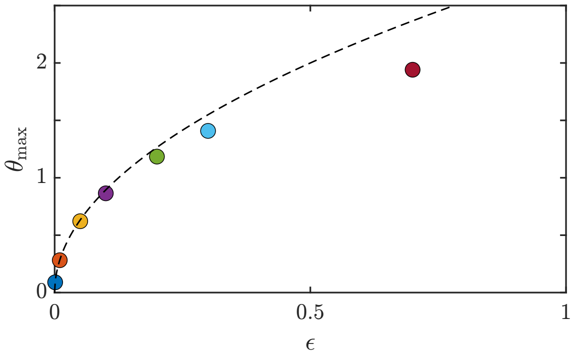

Figure 4.12: Maxima of $\theta(s)$ versus ϵ from numerics (colored symbols, corresponding to curves in Fig. 4.11), compared to analytical approximation near bifurcation (dashed). Obtained with `Figure_411_and_412_biharmonic.m`.

After buckling, the deformed rod behaves like a Hookean spring, whose properties we find by comparing the compressed length to the applied force. The right end of the filament moves a distance

$$\Delta x \simeq \int_0^L ds \frac{1}{2}\theta^2 \simeq \frac{La^2}{4} + \cdots \qquad (4.68)$$

As $a = \sqrt{8\epsilon}$ near the bifurcation, we obtain

$$F - F_c = \frac{F_c}{2L}\Delta x, \tag{4.69}$$

and thus beyond the buckling the effective spring constant is $F_c/2L$.

4.3.2 *Example 2: Wiggling elastica*

Now we move on to the first of three examples of "elastohydrodynamics". This is the problem of the shape of a filament whose end is oscillated periodically. The first example of such a calculation is due to Machin.[12] At the time of his calculation, it was not known whether the observed waveforms of sperm flagella were a consequence of mechanical actuation occurring at one end (the head) or whether there were active forces distributed along the length of the flagella. His result, derived below, showed clearly that the latter was the case, even before the actual discovery of the microscopic mechanism. This calculation served as the basis for much future work, including the self-propulsion[13] that arises from such actuated filaments.

For this problem, it is useful to make a comparison to the classical examples in viscous fluid dynamics known as Stokes Problems I and II. Outlined by Stokes in his famous paper on viscosity,[14] these involve viscous fluids driven by the motion of a boundary parallel to itself, in an impulsive or oscillatory manner, as shown in Fig. 4.13.

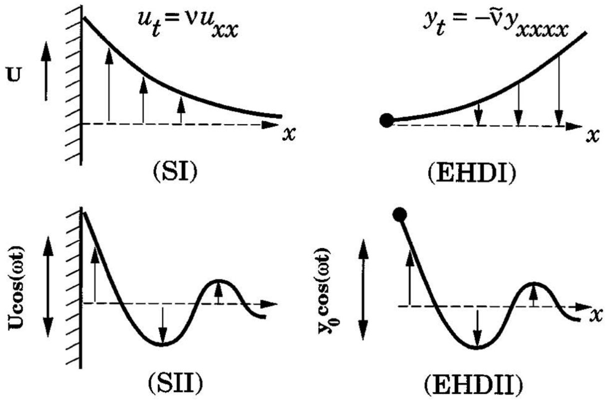

Figure 4.13: Stokes and elastohydrodynamic problems. Stokes problems SI and SII (left) involve impulsively-moved or oscillated walls bounding a viscous fluid. EHD problems I and II a filament is allowed to relax from an initially bent state (or subject to an impulsive transverse flow, or its end is oscillated up and down periodically.

For Stokes Problems I and II (SI & SII), we start from the Navier-Stokes equations for an incompressible fluid with density ρ, viscosity μ, pressure p and velocity field $\mathbf{u}$,

$$\rho\left(\mathbf{u}_t + \mathbf{u}\cdot\nabla\mathbf{u}\right) = -\nabla p + \mu\nabla^2\mathbf{u}, \tag{4.70}$$

and recognize for wall-driven flow that the nonlinear term vanishes by symmetry, and we can ignore the pressure gradient. If the wall moves along $\hat{\mathbf{e}}_y$, then the velocity will be of the form $\mathbf{u} = u(x,t)\hat{\mathbf{e}}_y$. It follows that the function u obeys the diffusion equation

$$u_t = \nu u_{yy}, \tag{4.71}$$

where again $\nu = \mu/\rho$ is the kinematic viscosity.

[12] Machin, K.E. Wave propagation along flagella. *J. Exp. Biol.*, 35:796–806, 1958

[13] Wiggins, C.H. and Goldstein, R.E. Flexive and propulsive dynamics of elastica at low Reynolds number. *Phys. Rev. Lett.*, 80:3879–3882, 1998

[14] Stokes, G.G. On the effect of the internal friction of fluids on the motion of pendulums. *Trans. Camb. Philos. Soc.*, IX, part II:8–106, 1851

In SI, we set the wall in motion at $t = 0$ with speed U. By the linearity of 4.71, it is clear that U is the only velocity scale U. The diffusion equation itself has no intrinsic length other than $\sqrt{\nu t}$, which follows from the scalings we discussed in Chapter 1 (1.14). It follows that the velocity should have the form of a similarity solution

$$u = Uf\left(\chi\right), \quad \chi = \frac{x}{\sqrt{\nu t}}, \tag{4.72}$$

where the function f obeys the ODE

$$f_{\chi\chi} = -\frac{1}{2}\chi f_{\chi}. \tag{4.73}$$

We solve this by setting $g = f_{\chi}$ to obtain $g = A\exp(-\chi^2/4)$, and fix A by the boundary conditions $f(0) = 1$, $f(\infty) = 0$, yielding

$$\frac{u}{U} = 1 - \operatorname{erf}\left(\frac{x}{2\sqrt{\nu t}}\right), \tag{4.74}$$

where erf is the error function. This solution exhibits a diffusively-moving transition region that separates the fluid moving with the wall from that which has yet to be set in motion.

For SII, we consider the situation after any transients have decayed away. If the wall is oscillated at frequency ω then from the diffusion equation 4.71 the only characteristic length is $\sim \sqrt{2\nu/\omega}$ (where we the factor of 2 is for later convenience); this is the *viscous penetration length*. We therefore expect a similarity solution of the form

$$u = U\mathrm{Re}\left\{e^{i\omega t}F\left(\chi\right)\right\}, \quad \chi = \frac{x}{\sqrt{2\nu/\omega}}. \tag{4.75}$$

The function F then obeys the ODE $F_{\chi\chi} = 2iF$, which whose solution is $F \sim e^{\lambda\chi}$, with $\lambda_{\pm} = \pm(1+i)$. Only the root with negative real part is relevant, given the boundary conditions at infinity, yielding

$$u = Ue^{-\chi}\cos\left(\chi - \omega t\right)., \tag{4.76}$$

an spatially-damped traveling wave moving outward from the wall.

Now we turn to elastohydrodynamic problems, where a filament is held at one and and either subject to a transverse flow or oscillated. In either case, we work in the small-amplitude limit for which points on the filament are at $(x, h(x,t))$, where the height function h is assumed to have negligible gradients $|h_x| \ll 1$, so (nearly all) metric factors in the dynamics can be ignored. In either case, the PDE governing small-amplitude deviations of the filament is

$$\zeta_{\perp}h_t = -Ah_{xxxx}. \tag{4.77}$$

We focus on the case of EHDII and, as with SII, consider the situation post-transients in which the left-hand side is forced as $h(0,t) = h_0\cos(\omega t)$, with zero torque ($h_{xx}(0,t) = 0$), and the distant end is free, with $h_{xx}(L) = h_{xxx}(L) = 0$. By analogy with SII, dimensional analysis shows there is an elastohydrodynamic length

$$\ell(\omega) = \left(\frac{A}{\zeta_{\perp}\omega}\right)^{1/4}, \tag{4.78}$$

and we expect a similarity solution of the form

$$h = h_0 \mathrm{Re}\left\{ \mathrm{e}^{i\omega t} F\left(\chi\right) \right\}, \quad \chi = \frac{x}{\ell(\omega)}. \tag{4.79}$$

Then the scaling function obeys an ODE similar to that in SII (4.73),

$$F_{\chi\chi\chi\chi} = -iF. \tag{4.80}$$

Seeking exponential solutions $F \sim \mathrm{e}^{\lambda\chi}$ gives four roots to the equation $\lambda^4 = -i$. These are

$$\begin{aligned} &\lambda_1 = C_8 - iS_8, \quad \lambda_2 = S_8 + iC_8, \\ &\lambda_3 = -C_8 - iS_8, \quad \lambda_4 = -S_8 - iC_8, \end{aligned} \tag{4.81}$$

where $C_8 = \cos(\pi/8) = 0.924\ldots$ and $S_8 = \sin(\pi/8) = 0.383\ldots$. For the semi-infinite filament ($L \to \infty$), only the two roots $\lambda_{3,4}$ with negative real part are relevant, and we find

$$\frac{h_\infty(\chi)}{h_0} = \frac{1}{2}\left\{ \mathrm{e}^{-C_8\chi}\cos\left(\omega t + S_8\chi\right) + \mathrm{e}^{-S_8\chi}\cos\left(\omega t - C_8\chi\right) \right\}. \tag{4.82}$$

Here, in contrast to SII, we see traveling waves in both directions, but the right-ward wave dominates since $S_8 < C_8$. Figure 4.14 shows the infinite-length solution at various points through a cycle.

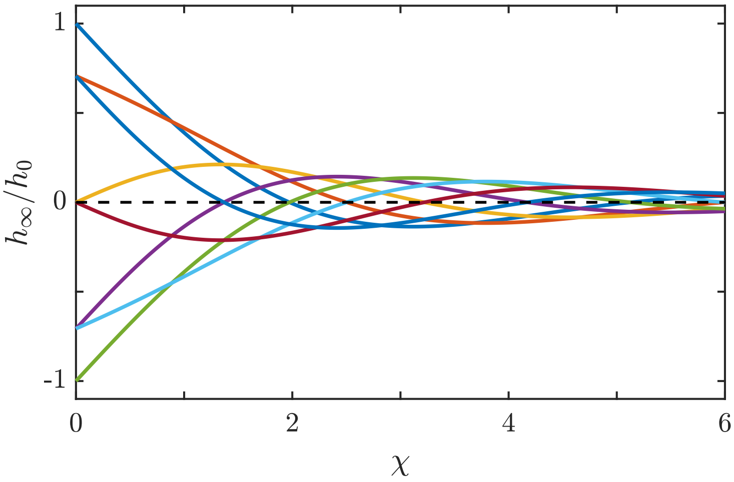

Figure 4.14: The $L \to \infty$ solution 4.82 to EHDII plotted at integer multiples of $\omega t = \pi/4$ through a complete cycle. Obtained with `Figure_414_EHD.m`.

There are three points to emphasise. First, when $L \to \infty$ there are no remaining parameters of the problem when expressed as h/h_0 versus χ; the curves in Fig. 4.14 are "universal" in this limit. This means that the rapid spatial decay of the amplitude is also universal; the amplitude is negligible beyond one wavelength of the pattern. This fact is in sharp contrast to the typical observed waveform of spermatazoa (Fig. 4.15),[15] in which oscillations extend nearly to the distal end of the filament without attenuation. This fact led Machin to conclude that sperm flagella can not be actuated only at the proximal end and must instead be driven by energy input throughout their length. This is indeed correct, as proven by later discoveries of "motor proteins" that cross-connect the microtubule filaments within flagella and by consuming ATP translate filaments relative to one another, inducing bending moments throughout the flagellum.

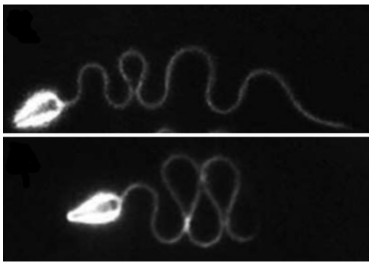

Figure 4.15: Waveforms of spermatozoa in a viscous fluid. From Ref. 15.

[15] Gadêlha, H. and Gaffney, E.A. Flagellar ultrastructure suppresses buckling instabilities and enables mammalian sperm navigation in high-viscosity media. *J. Roy. Soc. Interface*, 16:20180668, 2019

A second point is the value of the EH penetration length itself. Writing $A = k_B T L_p$ and assuming a large aspect ratio so that the logarithmic denominator in the drag coefficient is ~ 5, we find

$$\ell(\omega) \sim 0.7 \left(\frac{\tilde{L}_p}{f}\right)^{1/4} \mu\text{m}, \tag{4.83}$$

where f is measured in Hz and $\tilde{L}_p$ is the persistence length in microns. So, filament oscillations on the experimentally achievable and biophysically relevant frequency scale of $1 - 100$ Hz can bend filaments, with L_p in the range of microns to millimeters, on lengths of microns. This can be done by optical trapping methods.

This calculation can be extended to finite filaments. The problem is still the similarity solution (4.80) with boundary conditions $F(0) = 1$, $F_{\chi\chi}(0) = F_{\chi\chi}(\mathcal{L}) = F_{\chi\chi\chi}(\mathcal{L}) = 0$, where $\mathcal{L} = L/\ell(\omega)$ is the scaled filament length. This linear boundary value problem can be solved by standard schemes (e.g. `bvp4c.m` in Matlab) which are used to compute the filament shapes shown in Fig. 4.16.

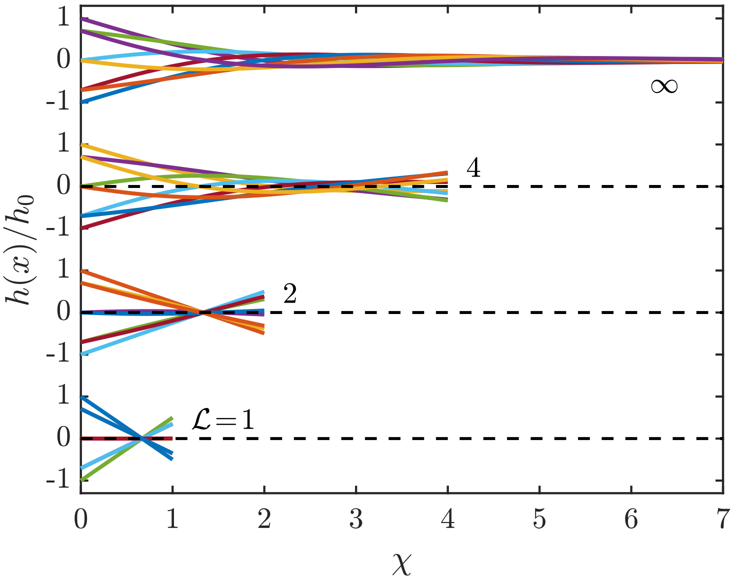

Figure 4.16: Filament shapes for various dimensionless lengths $\mathcal{L}$. As in Fig. 4.14, the waveforms are shown at 8 equally spaced intervals over a cycle. Obtained with `Figure_416_and_417_Machin.m`.

When $\mathcal{L} \leq 1$ the filament is nearly straight throughout the oscillation cycle, pivoting about the point $\chi = 2/3$. By $\mathcal{L} = 2$ a small amount of undulation is observed, and the bending waves are well developed by $\mathcal{L} = 4$, eventually producing the traveling-wave forms of the semi-infinite solution. This leads naturally to a discussion of the propulsive force arising from these motions. We can appeal to an irreversibility argument popularised by Purcell,[16] now known as the "scallop theorem". Since the Stokes equation $0 = -\boldsymbol{\nabla} p + \mu \nabla^2 \mathbf{u}$ has no explicit time derivative, if some particular function $\mathbf{u}$ represents the solution to a problem as time t advances forward, it is an equally valid solution when $t \to -t$ (colloquially, "when the movie is played backwards"). If we took the solution of EHDII for vanishing $\mathcal{L}$, where it reduces to a pivoting rod, and imagine that motion moved the rod, say, to the left, then reversing time must produce

[16] Purcell, E.M. Life at low Reynolds number. *Am. J. Phys.*, 45:1–11, 1977

movement to the right at an equal and opposite speed. But the rod's motion is indistinguishable in the two cases, so the only allowable speed is zero. This is referred to as the "scallop theorem" as a means of highlighting that an object with a single degree of freedom executing cyclic motion will exhibit no net propulsion. As the rod starts to flex during the oscillations, time reversal invariance is broken, so the two movies are not equivalent, and net propulsion can occur.

EHDII provides a particularly simple way to understand this effect, by means of the time-averaged x-component of the force associated with the filament oscillations. Here, we project the left hand side of the general force law (4.23) on to the x axis, yielding for our problem of a curve in the plane[17]

$$F = -\hat{\mathbf{e}}_x \cdot \left(\zeta_\parallel \hat{\mathbf{t}}\hat{\mathbf{t}} + \zeta_\perp \hat{\mathbf{n}}\hat{\mathbf{n}}\right) \cdot \mathbf{r}_t \simeq \left(\zeta_\perp - \zeta_\parallel\right) h_x h_t + \cdots . \tag{4.84}$$

where we have used the leading order tangent and normal vectors

$$\hat{\mathbf{t}} \simeq \hat{\mathbf{e}}_x + h_x \hat{\mathbf{e}}_y, \quad \hat{\mathbf{n}} \simeq -h_x \hat{\mathbf{e}}_x + \hat{\mathbf{e}}_y, \tag{4.85}$$

and written $\mathbf{r}_t \simeq h_t \hat{\mathbf{e}}_y$. Integrating this over the filament yields the total propulsive force generated. Using (4.77), we have

$$\int_0^L dx h_x h_t = -\frac{A}{\zeta_\perp} \int_0^L dx h_x h_{4x}. \tag{4.86}$$

This would seem to be a formidable integral, but a minor miracle occurs in that the quantity $h_x h_{4x}$ is a total derivative,

$$h_x h_{4x} = \frac{d}{dx}\left(h_x h_{3x} - \frac{1}{2} h_{xx}^2\right), \tag{4.87}$$

so the total propulsive force F_p can be expressed in terms of the filament shape at its two ends. If the distant end is free, then $h_{xx}(L) = h_{3x}(L) = 0$, leaving only a contribution from the oscillated end,

$$F_p = \frac{A}{\zeta_\perp}\left(\zeta_\perp - \zeta_\parallel\right) h_x(0,t) h_{xxx}(0,t), \tag{4.88}$$

where we have made explicit the time dependence of the boundary terms. Scaling lengths with $\ell(\omega)$ and assuming the form (4.79), Eq. (4.88) can be written as

$$F_p = h_0^2 \omega \left(\zeta_\perp - \zeta_\parallel\right) \mathrm{Re}\{e^{i\omega t} F_\chi(0)\} \mathrm{Re}\{e^{i\omega t} F_{\chi\chi\chi}(0)\}, \tag{4.89}$$

The prefactor indeed has units of a force (viscosity × length × velocity). Significantly, net propulsion only arises when the parallel and perpendicular drag coefficients differ, as they do for long slender filaments ($\zeta_\perp = 2\zeta_\parallel$). The quadratic dependence on the height function h will give rise to a nonzero mean value of the force averaged over a cycle. Denoting such an average by $\langle F_p \rangle$ we find

$$\langle F_p \rangle = \frac{1}{2}\left(\zeta_\perp - \zeta_\parallel\right) h_0^2 \omega Y(\mathcal{L}), \tag{4.90}$$

where $\mathcal{L} = L/\ell(\omega)$ and

$$Y(\mathcal{L}) = F_\chi^R(0) F_{\chi\chi\chi}^R(0) + F_\chi^I(0) F_{\chi\chi\chi}^I(0), \tag{4.91}$$

[17] Camalet, S. and Jülicher, F. and Prost, J. Self-organized beating and swimming of internally driven filaments. *Phys. Rev. Lett.*, 82:1590–1593, 1999

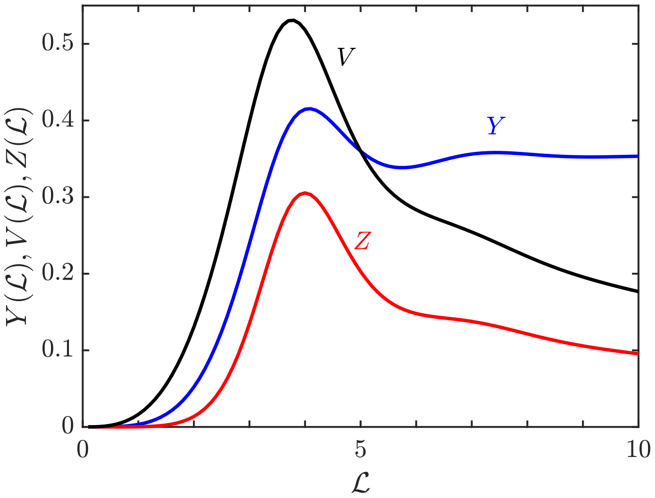

Figure 4.17: Scaling functions $Y(\mathcal{L})$ (blue), $V(\mathcal{L})$ (black, ×5 for clarity), and $Z(\mathcal{L})$ (red) for the propulsive force, swimming speed, and efficiency in EHDII. Obtained with `Figure_416_and_417_Machin.m`.

with $F(\chi) = F^R(\chi) + iF^I(\chi)$. The function $Y(\mathcal{L})$ is shown as the blue curve in Fig. 4.17. The propulsive force indeed tends to zero as the $\mathcal{L}$ decreases and the shapes are time-reversal-invariant, consistent with the scallop theorem. As $\mathcal{L}$ increases, Y displays a maximum followed by attenuated oscillations as it asymptotes to a finite value as $\mathcal{L} \to \infty$. This saturation indicates that beyond $\mathcal{L} \sim 8$ no more of the filament is set in motion and no further propulsive force is gained.

In the regime where the propulsive force has saturated any additional length added to the filament serves only to increase the drag for motion along the x axis, and one therefore expects that the propulsion *speed* of the filament would peak at an intermediate value of $\mathcal{L}$. As we have assumed in EHDII that the filament is nearly straight ($|h_x| \ll 1$, it is consistent to assume that the average lateral propulsive speed $\langle v_x \rangle$ of the undulating filament can be deduced by the simple balance of force $\zeta_\| L \langle v_x \rangle = \langle F_p \rangle$, or

$$\langle v_x \rangle = \frac{\langle F_p \rangle}{\zeta_\| L} = \frac{h_0^2 \omega}{2\ell(\omega)} V(\mathcal{L}), \tag{4.92}$$

where $V(\mathcal{L}) = Y(\mathcal{L})/\mathcal{L}$. As seen in Fig. 4.16, the peak in $\langle F_p \rangle$ implies a peak in speed, and $\langle v_x \rangle$ vanishes as $L \to \infty$ as anticipated.

The average power $P_\|$ associated with the lateral motion is $P_\| = v_x \langle F_p \rangle \sim \langle F_p \rangle^2$. It can be compared to the power

$$P_\perp = \zeta_\perp \langle \int_0^L dx h_t^2 \rangle \tag{4.93}$$

generated by transverse motions. Together, these define the "efficiency" $\varepsilon = P_\| / P_\perp$ of the propulsive mechanism, which has the form

$$\varepsilon \sim \left(\frac{h_0}{\ell(\omega)} \right)^2 Z(\mathcal{L}), \tag{4.94}$$

where the scaling function is

$$Z(\mathcal{L}) = \frac{Y^2(\mathcal{L})}{\mathcal{L} \int_0^{\mathcal{L}} d\chi |F(\chi)|^2}. \tag{4.95}$$

Figure 4.17 shows that the efficiency also displays the peaked behaviour of the other scaling functions, suggesting an optimum length.

4.3.3 *Example 3: Stretch-coil transition under compressional flows*

Our second example of elastohydrodynamics is based on the experimental geometry in Fig. 4.6, in the case in which a filament initially aligned along one channel's long axis is subject to a compressional flow inwards from its two ends. The analysis of this "stretch-coil transition" was first given by Young and Shelley,[18] confirmed at the microscale by later experiments we discuss below. When a filament is subject to a viscous flow of velocity u parallel to its long axis, it will experience a tangential viscous force per unit length of $\zeta_\parallel u$. In the geometry of Fig. 4.6, the in-plane flow is the of a hyperbolic stagnation point, with $\mathbf{u} = (\dot\gamma x, -\dot\gamma y)$, where $\dot\gamma$ is the imposed shear rate, and $\dot\gamma < 0$ for a *compressional* flow and > 0 for *extensional* flow of a filament oriented along x. In equilibrium the force density $-\zeta_\parallel \dot\gamma x$ must balance gradients in the tension $\sigma(x)$ within the filament,

$$\sigma_x = -\zeta_\parallel \dot\gamma x, \tag{4.96}$$

which, subject to the vanishing of σ at the filament ends (here taken at $\pm L/2$), integrates to yield

$$\sigma(x) = \frac{1}{2}\left(\frac{L^2}{4} - x^2\right)\zeta_\parallel \dot\gamma, \tag{4.97}$$

a relation noted much earlier by Batchelor.[19] In the presence of this nonuniform tension, the filament energy functional is

$$E = \frac{1}{2}\int_{-L/2}^{L/2} dx \left(A h_{xx}^2 + \sigma(x) h_x^2\right). \tag{4.98}$$

Just as with Euler buckling, where a concentrated force is applied to one of the filament, here in the presence of a distributed force we expect a buckling transition for sufficiently large (negative) shear rate. The linear stability problem of interest derives from our basic formulation (4.25), but now augmented with an external flow field $\mathbf{u}$ for relative motions of the filament,

$$\mathbf{r}_t - \mathbf{u} = \frac{1}{\zeta_\perp}\left(\hat{\mathbf{n}}\hat{\mathbf{n}} + 2\hat{\mathbf{t}}\hat{\mathbf{t}}\right) \cdot \left\{-A\mathbf{r}_{ssss} + \left(\sigma \hat{\mathbf{t}}\right)_s\right\}, \tag{4.99}$$

where $\mathbf{u}$ is to be evaluated at the filament. In the tensorial term on the r.h.s., we have specialized to a filament deforming in the plane and assumed the asymptotic limit for the drag coefficient ratio. If we now use the standard Monge relations (4.85) for $\hat{\mathbf{t}}$ and $\hat{\mathbf{n}}$ of a weakly-deformed filament, and perform the rescalings

$$\chi = \frac{\pi x}{L}, \quad \tau = \dot\gamma t, \quad H = \frac{h}{L}, \tag{4.100}$$

then a very careful derivation of the linearised dynamics yields

$$4|\Sigma|\left(H_\tau + \mathrm{sgn}(\dot\gamma) H\right) = -H_{4\chi} + \Sigma\left[\left(\frac{\pi^2}{4} - \chi^2\right) H_{\chi\chi} - 4\chi H_\chi\right], \tag{4.101}$$

where the control parameter of the problem is

$$\Sigma = \frac{\mu \dot\gamma L^4}{\pi^3 \ln(L/a\sqrt{e})}, \tag{4.102}$$

---

[18] Young, Y.-N. and Shelley, M.J. Stretch-coil transition and transport of fibers in cellular flows. *Phys. Rev. Lett.*, 99: 058303, 2007

[19] Batchelor, G.K. Slender-body theory for particles of arbitrary cross-section in Stokes flow. *J. Fluid Mech.*, 44:419–440, 1970

and the logarithm in the denominator arises from the RFT drag coefficient. Note that the tension term on the r.h.s. of (4.101) is not a total derivative; the linearised equation of motion is not variational. This arises from the anisotropic drag and the fact that the background flow that enters the drag force is the source of the tension.

The determination of the threshold for the stretch-coil instability is a matter of a numerical solution of the the eigenvalue problem that comes from a separable solution $H(\chi,\tau) = \exp(\omega\tau)F(\chi)$, namely

$$F_{4\chi} - \Sigma\left[\left(\frac{\pi^2}{4} - \chi^2\right)F_{\chi\chi} - 4\chi F_\chi\right] = 4\Sigma\,(\omega - 1)\,F. \qquad (4.103)$$

Our general expectation is that there will be a discrete set of modes analogous to the biharmonic eigenfunctions discussed earlier in this chapter, each of which will be stable at low $\dot{\gamma}$ and attain a positive growth rate ω for sufficiently large shear rate. In the program `Figure_418_stretchcoil.m` we find the different critical values Σ_n^* at which $\omega = 0$ by appropriate choice of the initial guess for the iterative solution.

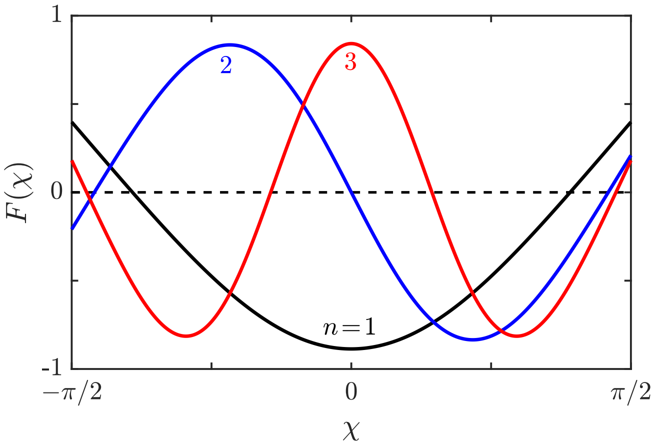

Figure 4.18: The first three critical modes for the stretch-coil instability. Obtained with `Figure_418_stretchcoil.m`.

Such analysis yields the critical value $\Sigma^* = -0.3932$ for the first unstable mode, $\Sigma_2^* = -1.9876$ for the second mode, $\Sigma_3^* = -4.955$ for the third, etc. Those higher order shapes (Fig. 4.18) are visible in the montage of filament shapes shown in Fig. 4.19. The amplitude of the buckled filaments, taken as $1 - \mathcal{L}/L$, where $\mathcal{L}$ is the end-to-end displacement, displays a thermal-fluctuation-rounded pitchfork bifurcation (Fig. 4.19). A theoretical treatment of the combined effects of thermal fluctuations and nonlinearities on the stretch-coil transition has recently been developed.[20]

4.3.4 Example 4: Motor-induced oscillations

Our final example of elastohydrodynamics concerns the effect of molecular motors translating along biological filaments on the shapes of those filaments. Motivation for this comes from observations of the dynamics of microtubules during development of the oocytes (egg cells) of the fruit fly *Drosophila melanogaster*. At intermediate stages of this multi-day process the oocyte is on the order of 100 μm

---

[20] H. Manikantan and D. Saintillan. Buckling transition of a semiflexible filament in extensional flow. *Phys. Rev. E*, 92:041002, 2015

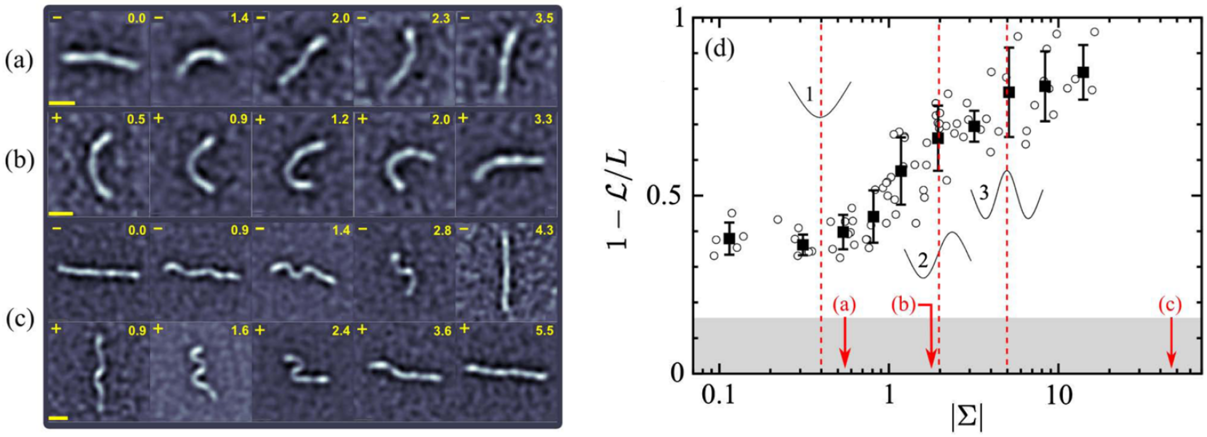

Figure 4.19: (a) Montage of buckling at various values of the shear rate. Scale bars are 3 μm and times are dimensionless values τ since first frame of each row. Control parameter values are (a) $\Sigma = 0.55$, (b) $\Sigma = 1.9$, and (c) $\Sigma = 47$. (b) Order parameter versus dimensionless shear rate. Dashed lines indicate instability thresholds for modes shown. Gray band is noise floor. From Ref. 20.

across, with multitudes of microtubules reaching toward the center, anchored at the periphery. Molecular motors such as kinesin translocate along those filaments, carrying nanometric cargo that plays a role in establishing the future body plan of the organism. As that cargo moves, it entrains fluid, producing complex swirling patterns of fluid motion that can also back-react on the filaments, bending them. Most of the motor-filament pairs in the cytoskeleton are "polar", in the sense that the motors walk in a unique direction along the filament. In the case of these anchored microtubules, it is typically from the anchored end toward the free end. As the motor walks in that direction, there is a corresponding force on the filament directed back toward the anchoring point. This is a *compressive* force akin to that of Euler buckling. And since motors can exert forces on the picoNewton scale and the microtubules can be tens of microns long, our estimates of the Euler buckling force (4.64) show the filaments can indeed be deformed by a single motor. But there is a crucial difference between Euler buckling and the motor-filament situation; in the latter, the force is always tangential to the filament. This is an example of a "follower force", and it is known to have fundamentally distinct properties from Euler buckling.[21] Chief among them is a lack of a variational structure to the dynamics, even in Stokes flow.[22] As we shall see below, this can be traced to the existence of boundary conditions that produce a non-self-adjoint operator.

The simplest setup of the problem is shown in Fig. 4.20. A filament of length L is clamped at the origin along the x axis, and subject to a point force of magnitude Γ tangential to its distal end. We again use the standard form of elastohydrodynamics (4.25) in which the elastic force density is written as

$$-A\mathbf{r}_{ssss} - (\Lambda \mathbf{r}_s)_s\,, \tag{4.104}$$

where Λ is the internal tension. The boundary conditions at the origin are simply $\mathbf{r}(0,t) = 0$ and $\mathbf{r}_s(0,t) = 0$, while at the distal end the torque-free condition requires $\mathbf{r}_{ss}(L,t) = 0$. The condition of force balance at the distal end can be written as

$$-A\mathbf{r}_{sss} - \Lambda(L,t)\mathbf{r}_s(L,t) = -\Gamma \mathbf{r}_s(L,t), \tag{4.105}$$

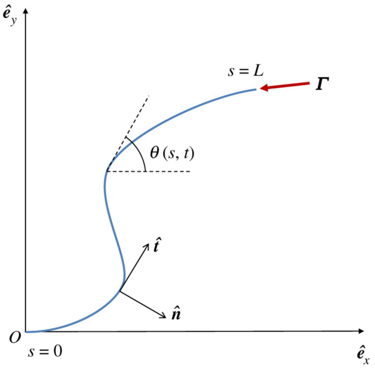

Figure 4.20: Setup for the follower force problem.

[21] Herrmann, G. and Bungay, R.W. On the stability of elastic systems subjected to nonconservative forces. *J. Appl. Mech.*, 31:435–440, 1964

[22] De Canio, G., Lauga, E. and Goldstein, R.E. Spontaneous oscillations of elastic filaments induced by molecular motors. *J. R. Soc. Interface*, 14:20170491, 2017

which is satisfied by $\Lambda(L,t) = \Gamma$ and $\mathbf{r}_{sss}(L,t) = 0$. The tension itself must satisfy the usual differential equation (4.43).

We focus on the stability problem for the straight filament, for which the linearised dynamics takes a simple form. The solution to the tension equation is simply the constant $\Lambda = \Gamma$. We rescale via

$$\chi = \frac{x}{L}, \quad \tau = \frac{At}{\zeta_\perp L^4}, \quad H = \frac{h}{L}, \quad \sigma = \frac{\Gamma L^2}{A}, \tag{4.106}$$

where the temporal rescaling reflects the characteristic bending relaxation time of the filament and $\sigma > 0$ for a compressive force. The governing equation is thus

$$H_\tau = -H_{\chi\chi\chi\chi} - \sigma H_{\chi\chi}, \tag{4.107}$$

with $H(0,\tau) = H_\chi(0,\tau) = H_{\chi\chi}(1,\tau) = H_{\chi\chi\chi}(1,\tau) = 0$. Note that the tension term by itself would correspond to a "backwards" diffusion problem that would be ill-posed without the stabilising fourth derivative from bending elasticity. Were it not for the nontrivial boundary conditions for this problem, we could simply consider separable solutions of the form for plane waves, $H \sim \exp(\omega\tau)\exp(iQ\chi)$, and deduce a growth rate ω for a mode of wavevector Q of the form $\omega = \sigma Q^2 - Q^4$, which displays a band of unstable modes (those with $\omega > 0$ in the range $0 \le Q \le \sqrt{\sigma}$, with a *real* growth rate ω. But in reality we can not ignore the boundary terms, and therein lies the key to the unexpected features of this problem. To see this, we observe that in the linearised approximation, where the tension is a constant, the (rescaled) energy of the system is

$$\mathcal{E} = \frac{1}{2}\int_0^1 d\chi \left(H_{\chi\chi}^2 - \sigma H_\chi^2\right) \tag{4.108}$$

The time derivative of $\mathcal{E}$ itself follows directly from the equation of motion (4.107) and several integrations by parts,

$$\begin{aligned} \mathcal{E}_\tau \;&=\; H_{\chi\chi}H_{\chi\tau}\Big|_0^1 - H_{\chi\chi\chi}H_\tau\Big|_0^1 - \sigma H_\chi H_\tau\Big|_0^1 \\ &\quad + \int_0^1 d\chi\,(H_{\chi\chi\chi\chi} + \sigma H\chi\chi)\,H_\tau. \end{aligned} \tag{4.109}$$

The first two surface terms vanish identically at both ends by virtue of the boundary conditions, as does the third term $H_\chi H_\tau$ at $\chi = 0$, but $H_\chi(1,\tau)H_\tau(1,\tau)$ is not forced to vanish by any boundary conditions. Using (4.107) to simplify the integral in (4.109) we obtain

$$\mathcal{E}_\tau = -\int_0^1 d\chi\,(H_{\chi\chi\chi\chi} + \sigma H\chi\chi)^2 - \sigma H_\chi(1,\tau)H_\tau(1,\tau). \tag{4.110}$$

While the integral is clearly nonpositive, the sign of the surface term is indefinite, so we can not conclude that $\mathcal{E}_\tau < 0$ and indeed the surface term represents the injection of energy into the filament that sustains oscillations. Stated another way, the surface term breaks the self-adjointness of the Sturm-Liouville operator $\partial_{\chi\chi\chi\chi} + \sigma\partial_{\chi\chi}$, and therefore its eigenvalues need not be real.

The eigenvalue problem of interest is obtained by assuming a separable solution to (4.107) $H(\chi,\tau)=\exp(\omega\tau)G(\chi)$, leading to

$$G_{\chi\chi\chi\chi}+\sigma G_{\chi\chi}=-\omega G, \tag{4.111}$$

with boundary conditions $G(0)=G_\chi(0)=G_{\chi\chi}(1)=G_{\chi\chi\chi}(1)=0$. While this can be worked out semi-analytically, its numerical solution provides the student with an opportunity to gain experience with numerical methods for such problems. In the program `Figure_421_and_423_followerforce.m` we implement a finite difference representation of the operator, with careful attention to the one-sided stencils needed to implement the boundary conditions. Figure 4.21 shows the real and imaginary parts of the largest eigenvalue obtained from the matrix representation of the operator.

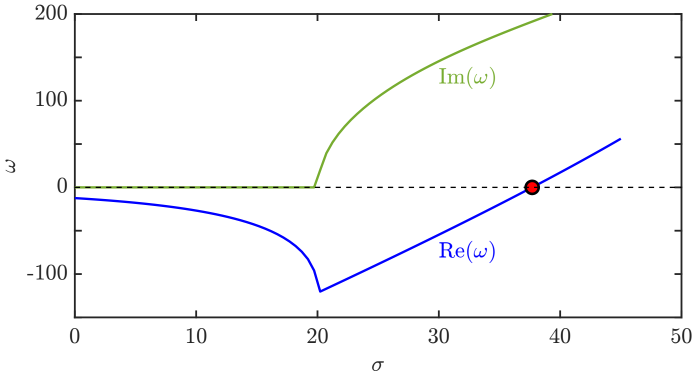

Figure 4.21: Components of complex eigenvalue for follower-force problem as a function of dimensionless motor force σ. Red circle represents onset of supercritical Hopf bifurcation. Obtained with `Figure_421_and_423_followerforce.m`.

The eigenvalue ω is purely real and negative up to $\sigma \simeq 20$, as it is for $\sigma=0$, but beyond that value the imaginary part grows. The real part becomes positive at $\sigma^* \simeq 37.69$ with a finite imaginary part; the classic signature of a Hopf bifurcationHopf bifurcation. It is interesting to see how the character of the leading eigenfunction behaves as the motor strength σ is increased. Figure 4.22 shows the normalized real part of the eigenfunctions $G(\chi)$ for a range of values of σ. For small σ the mode is a simple monotonic function, while at large σ, beyond the bifurcation, it develops a wavelike form.

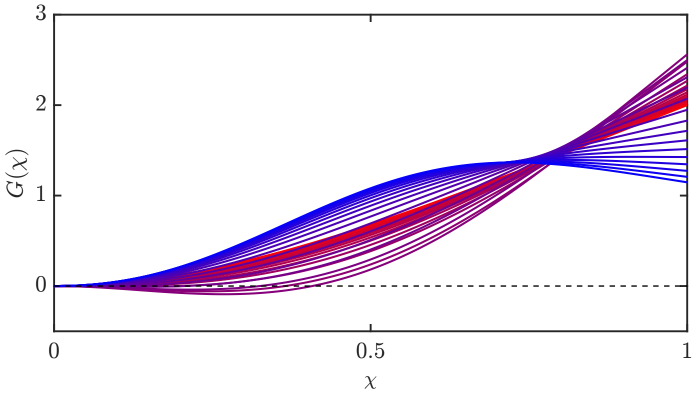

Figure 4.22: Normalised real part of the leading eigenfunction of the follower-force problem. Curves are for a range of σ from 0 to 45, color-coded from red to blue. Obtained with `Figure_421_and_423_followerforce.m`.

As an example, we construct the full waving solution as $Re[\exp(\omega\tau)G(\chi)]$, using the complex leading eigenfunction G found numerically for

$\sigma = 45$, and plot it during one cycle of motion. As shown in Fig. 4.23 the dynamics have the character of flagellar motion.

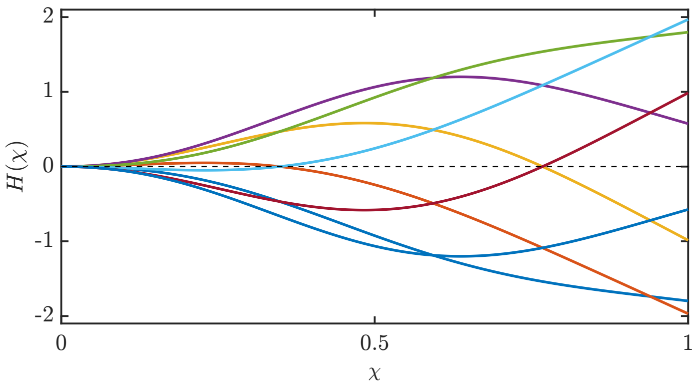

Figure 4.23: Separable solution of follower-force problem at $\sigma = 45$ plotted during one cycle. Obtained with `Figure_421_and_423_followerforce.m`.

5

Surfaces & Membranes (Lectures 13-16)

In these four lectures we consider the properties of biological membranes. We begin with a review of the basic differential geometry of surfaces and some variational aspects in order to understand the pedagogical example of minimal surfaces. Examples of fluctuations of closed objects are studied to understand how global constraints such as fixed enclosed volume affect the spectra. Applications to lipid vesicles are given, along with the physics of intermembrane repulsion due to constrained fluctuations. In the later parts of the chapter we consider the mathematical description of the equilibrium shapes of vesicles and several examples of shape transformations.

5.1 Differential geometry of surfaces

We begin with a brief summary of differential geometry. Consider a surface traced out by the vector $\mathbf{x}(u^\alpha)$ through internal coordinates u^α, $\alpha = 1, 2$. The surface has a metric tensor with components

$$g_{\alpha\beta} = \mathbf{x}_\alpha \cdot \mathbf{x}_\beta, \tag{5.1}$$

where here subscripts denote differentiation, so $\mathbf{x}_\alpha \equiv \partial\mathbf{x}/\partial u^\alpha$. The $\mathbf{x}_\alpha$ are the unnormalized tangent vectors to the surface. They define the unit normal $\hat{\mathbf{n}}$ as, say,

$$\hat{\mathbf{n}} = \frac{\mathbf{x}_1 \times \mathbf{x}_2}{|\mathbf{x}_1 \times \mathbf{x}_2|} = \frac{\mathbf{x}_1 \times \mathbf{x}_2}{\sqrt{g}}, \tag{5.2}$$

or its opposite if we switch $1 \leftrightarrow 2$. Here, $g = \det(g)$ is the determinant of the metric tensor,

$$g = \epsilon_{\alpha\beta} g_{1\alpha} g_{2\beta}\ , \tag{5.3}$$

where ϵ is the Levi-Civita symbol and the summation convention holds. The inverse metric tensor, with coefficients $g^{\alpha\beta}$ is the usual

$$g^{-1} = \frac{1}{g}\begin{pmatrix} g_{22} & -g_{12} \\ -g_{21} & g_{11} \end{pmatrix}. \tag{5.4}$$

The coefficients $h_{\alpha\beta}$ of the second fundamental form are defined by the normal and tangent vectors as

$$h_{\alpha\beta} = -\hat{\mathbf{n}}_\alpha \cdot \mathbf{x}_\beta. \tag{5.5}$$

If we denote by Tr the conventional trace of a matrix, then the mean and Gaussian curvature, H and K, of the surface are

$$H = \frac{1}{2}\mathrm{Tr}\left(h^{\alpha}{}_{\beta}\right) \qquad (5.6a)$$

$$K = \det\left(h^{\alpha}{}_{\beta}\right) , \qquad (5.6b)$$

where $h^{\alpha}{}_{\beta} = g^{\alpha\mu}h_{\mu\beta}$.

5.1.1 Surfaces of Revolution

Let us apply these formal results to a situation that arises in many contexts, an axisymmetric surface. Assuming it is obtained as a surface of revolution by rotating around the z axis, it is described by

$$\mathbf{x} = \zeta(z)\left[\cos\theta\hat{\mathbf{e}}_1 + \sin\theta\hat{\mathbf{e}}_2\right] + z\hat{\mathbf{e}}_3. \qquad (5.7)$$

A simple calculation shows that the normal vector is

$$\hat{\mathbf{n}} = \frac{\cos\theta\hat{\mathbf{e}}_1 + \sin\theta\hat{\mathbf{e}}_2 - r_z\hat{\mathbf{e}}_3}{\sqrt{1+r_z^2}}, \qquad (5.8)$$

while the metric tensor has the simple form

$$g = \begin{pmatrix} \zeta^2 & 0 \\ 0 & 1+\zeta_z^2 \end{pmatrix}. \qquad (5.9)$$

Then, the coefficients of the second fundamental form are

$$h^{\alpha}{}_{\beta} = \begin{pmatrix} -1/\zeta\sqrt{1+\zeta_z^2} & 0 \\ 0 & \zeta_{zz}/(1+\zeta_z^2)^{3/2} \end{pmatrix}, \qquad (5.10)$$

and thus the mean and Gaussian curvatures are

$$H = \frac{1}{2}\left(\frac{\zeta_{zz}}{(1+\zeta_z^2)^{3/2}} - \frac{1}{\zeta\sqrt{1+\zeta_z^2}}\right), \qquad (5.11a)$$

$$K = -\frac{\zeta_{zz}}{\zeta\left(1+\zeta_z^2\right)^2} . \qquad (5.11b)$$

5.1.2 Catenoids

Now we ask how these geometric quantities arise in variational calculations involving surfaces. The simplest context is that of surfaces endowed with an energy per unit area (surface tension), for which the area functional $A[\zeta]$ is of interest,

$$A[\zeta] = \int_{-d}^{d} dz\,\zeta\sqrt{1+\zeta_z^2}. \qquad (5.12)$$

where for convenience we have dropped the 2π from the θ integration. A simple calculation yields the functional derivative of A,

$$\frac{\delta A}{\delta\zeta} = -2\zeta H, \qquad (5.13)$$

where H is the mean curvature (5.11a).

If the surface of interest is endowed with surface tension γ, its surface energy is proportional to γA, and the quantity $-\gamma\delta A/\delta\zeta$ is proportional to the Young-Laplace pressure difference across the surface. In the special case $H = 0$, the pressure difference vanishes and the surface is in equilibrium. This *minimal surface* satisfies

$$\frac{\zeta_{zz}}{1+\zeta_z^2} = \frac{1}{\zeta}. \tag{5.14}$$

A simple calculation shows that the shape

$$\zeta(z) = a\cosh z/a \tag{5.15}$$

is a solution to (5.14) for a range of the parameter a. This the equation of a catenoid, an experimental example of which is shown in Fig. 5.1, where the surface of revolution spans two wire loops.

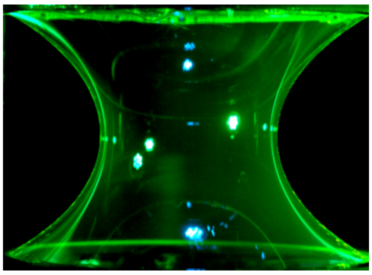

Figure 5.1: A soap film in the form of a catenoid, made visible with dissolved fluorescein illuminated with cyan light.

The solutions (5.15) must solve the boundary condition that they meet the wires, $\zeta(\pm d) = R$, where R is the wire radius. If we define the dimensionless variables

$$\alpha = \frac{a}{R}, \quad D = \frac{d}{R}, \tag{5.16}$$

then the boundary condition can be written as

$$\alpha\cosh(D/\alpha) - 1 = 0. \tag{5.17}$$

Viewing the radius of the hoops as a fixed quantity and the separation $2d$ as adjustable, we see in Fig. 5.2(a) that this transcendental equation has two solutions for small D that merge into one at $D = D_c = 0.6627$, and there are no solutions for larger D. The two branches of solution, labelled $\alpha_\pm$, are shown in Fig. 5.2(b) to merge together in what is known as a saddle-node bifurcation.

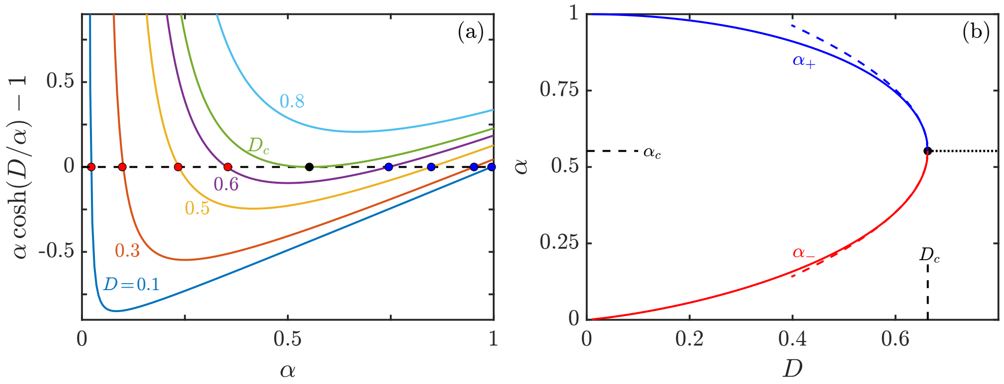

Figure 5.2: Graphical solution of the catenoid equation (a) and solution branches versus nondimensional ring separation (b). Obtained with `Figure_502_and_504_catenoids.m`.

The two branches of solutions correspond to catenoids of very different shapes, as shown in Fig. 5.3. At any given separation, the upper branch (α_+) has a lower area then that of the lower branch (α_-), and is the true least-area surface. The areas of the two branches of solution can be calculated analytically in terms of the solutions $\alpha_\pm$. Expressed in dimensionless form as $\mathcal{A}_\pm = A_\pm/R^2$, they are

$$\mathcal{A}_\pm = \frac{\alpha_\pm}{2}\left[\sinh\left(\frac{2D}{\alpha_\pm}\right) + \frac{2D}{\alpha_\pm}\right], \tag{5.18}$$

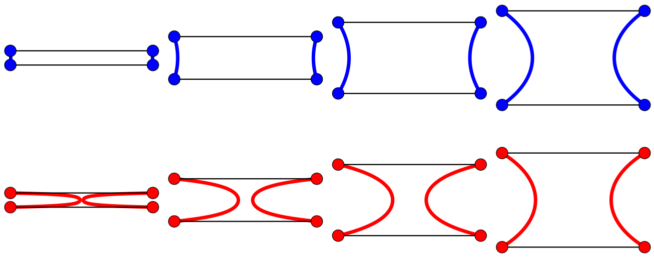

Figure 5.3: Catenoidal solutions at separations $D = 0.1, 0.3, 0.5, 0.662$ for the two branches of solutions in Fig. 5.2(b). The coloured circles represent the imaginary supporting loops, seen in cross section. Obtained with `Figure_503_catenoidsolutions.m`.

and are shown in Fig. 5.4. The upper and lower branches of solution meet at the critical area $\mathcal{A}_c = 1.199\ldots$. A more involved calculation is necessary to show the stability of the two branches, which are indicated in the figure. We shall return to these catenoidal solutions in our study of membrane tethers in Sec. 5.3.2.

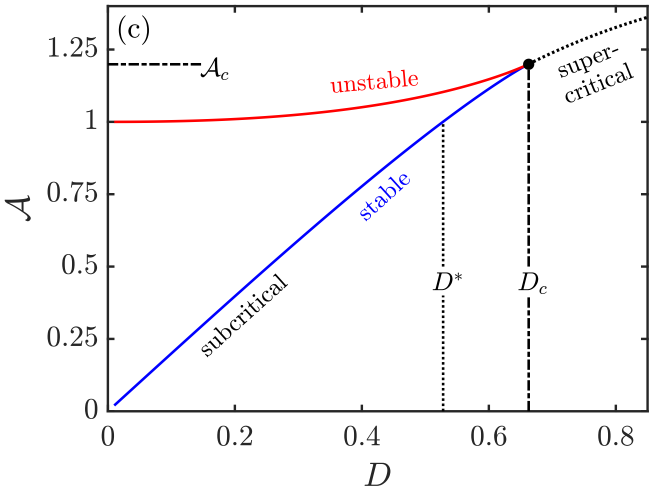

Figure 5.4: Areas of the two branches of solutions of the catenoid equation versus dimensionless ring spacing D. Obtained with `Figure_502_and_504_catenoids.m`.

5.2 Membrane Fluctuations

Next we consider some important problems in the statistical physics of fluctuating membranes: equilibrium thermal fluctuations of bilayer lipid vesicles, fluctuation-induced repulsion between nearby membranes, and the dynamics of red blood cell fluctuations.

5.2.1 Thermal fluctuations of spherical vesicles

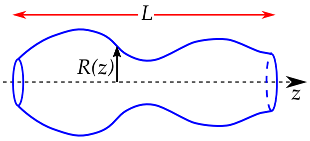

Figure 5.5: A perturbed cylinder.

Before delving into details of this calculation, we note an important feature of fluctuations associated with *closed* objects whose interior volume is a constant. We start with the simple problem of a weakly perturbed cylindrical body of length L, as in Fig. 5.5. The volume V and surface area S of the body are

$$V = \pi \int_0^L dz R^2(z), \qquad S = 2\pi \int_0^L dz R \sqrt{1 + R_z^2}. \tag{5.19}$$

Let R_0 be the cylinder radius prior to any perturbations. As we will be considering the use of equipartition to describe thermal fluctuations, it is necessary to work to second order in deviations from the circle. Under such perturbations, the mean radius ρ_0 will need to differ from R_0 in order to satisfy volume conservation at second order. To see this, assume the body is perturbed by a sum of Fourier modes along its length, but remains axisymmetric,

$$R = \bar{R} + \sum_n a_n \sin q_n z, \tag{5.20}$$

where $\bar{R}$ is to be determined and $q_n = 2\pi n/L$. To quadratic order in the amplitudes a_n, the volume is

$$V \simeq \pi L \left(\bar{R}^2 + \frac{1}{2} \sum_n a_n^2 \right) \tag{5.21}$$

Thus, if V is be unchanged from its unperturbed value $\pi L R_0^2$ to this order in a_n, we must have

$$\bar{R} \simeq R_0 - \frac{1}{4R_0} \sum_n a_n^2. \tag{5.22}$$

If we now compute the surface area to the same order and impose volume conservation, we find that the surface energy γS is

$$\gamma S = 2\pi L R_0 \gamma + \frac{\pi}{2} \frac{\gamma L}{R_0} \sum_n \left[(q_n R_0)^2 - 1 \right] a_n^2 + \cdots . \tag{5.23}$$

The constraint of fixed volume has led to the crucial term -1 inside the square brackets instead of simply a factor of q^2 associated with tension without conservation of volume. Its significance can be seen if we apply equipartition to this energy, from which we conclude that

$$\langle a_n^2 \rangle = \frac{k_B T R_0}{\pi L \gamma \left[(q_n R_0)^2 - 1 \right]}. \tag{5.24}$$

Clearly, there is a divergence when $q_n R_0 = 1$ and the result is not physical for $q_n R_0 < 1$. These indicate an instability at $q_n R_0 = 1$, which is, for $n = 1$, exactly Plateau's criterion that a cylinder longer than its circumference is unstable under the action of surface tension.

The calculation above assumed axisymmetry. Suppose now that we break circular symmetry, using the simpler context of a perturbed circular domain. If its unperturbed radius is R_0, and the perturbed boundary is given as a function of the polar angle θ by

$$\mathbf{r}(\theta) = \left(\bar{R} + \sum_n a_n \sin n\theta \right) \hat{\mathbf{e}}_r \tag{5.25}$$

then the constraint of fixed enclosed area yields the same result as in (5.22), and the line energy γL is

$$\gamma L = 2\pi R_0 \gamma + \frac{\pi\gamma}{2R_0} \sum_n \left(n^2 - 1 \right) a_n^2, \tag{5.26}$$

and hence

$$\langle a_n^2 \rangle = \frac{k_B T R_0}{\pi\gamma \left(n^2 - 1 \right)}. \tag{5.27}$$

Now the reason for the divergence at $n = 1$ is not an instability, but rather that an perturbation of the form $\sin\theta$ is an infinitesimal *translation* of the circle. This is not true for large a_1, where the deformed shape is like a cardioid, as shown in Fig. 5.6. For infinitesimal a_1, such a perturbation costs no energy (in this setup), and would naturally have a divergent amplitude if endowed with energy $k_B T$.

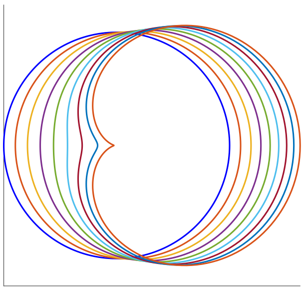

Figure 5.6: A perturbed circle for $a_1 = 0.1, 0.2, \ldots, 0.8$. Obtained with `Figure_506_perturbedcircle.m`.

We can apply these results to understand the spectrum of thermal fluctuations of a lipid bilayer vesicle, a problem studied experimentally some time ago[1] and analyzed in detail by Helfrich,[2], Milner and Safran,[3] and Zhong-can and Helfrich.[4] Consider a spherical vesicle of radius R perturbed by small-amplitude fluctuations, so that points on the surface can be labelled as

$$\mathbf{r}(\theta, \phi) = (R + \eta(\theta, \phi))\, \hat{\mathbf{e}}_r. \tag{5.28}$$

where θ, ϕ are the usual spherical coordinates. The necessary calculation involves expressing the change in the elastic energy

$$E = \frac{1}{2} k_c \int dS (2H)^2, \tag{5.29}$$

up to quadratic order in η. Note that we have, for simplicity, neglected any contribution from spontaneous curvature and from the Gaussian curvature term in (2.66) due to its topological character. The calculation itself is a somewhat tedious exercise in expanding the energy functional for weak perturbations around the sphere, ultimately expressing the relative displacement η / R of the radius as an expansion in spherical harmonics $Y_{lm}(\theta, \phi)$, leading to the result

$$E \simeq 8\pi k_c + \frac{1}{2} k_c \sum_{l,m} l\,(l-1)\,(l+1)\,(l+2)\, |a_{lm}|^2. \tag{5.30}$$

The l-dependent coefficient is vanishes identically for both $l = 0$ and $l = 1$, even without adjustment of the mean radius. This is a special result associated with the scale invariance of the elastic energy (5.29) in the absence of the spontaneous curvature term. When $H_0 \neq 0$, the mean radius of the vesicle must be adjusted to conserve volume at second order, as discussed above. The coefficients scale with mode number as l^4, as expected from elasticity.

5.2.2 *Helfrich repulsion*

An important consequence of thermal fluctuations is the phenomenon of "fluctuation-induced interactions" between elastic objects. These were first proposed by Helfrich[5] in the context of multilayer systems, and rederived later using simplified arguments[6] that we repeat here. More recently, similar considerations have been applied to the structure of DNA in tightly-packed chromosomes.[7]

We consider a two-dimensional elastic membrane initially free in space, but later confined between two impenetrable walls spaced a distance $2d$ apart, as in Fig. 5.7. Starting from the usual elastic energy $E = (k_c/2) \int dS (2H)^2$, adding for generality a tension contribution

[1] Schneider, M.B., Jenkins, J.T. and Webb, W.W. Thermal fluctuations of large quasi-spherical bimolecular phospholipid vesicles. *J. Phys.*, 45:1457–1472, 1984

[2] Helfrich, W. Size distributions of vesicles: the role of the effective rigidity of membranes. *J. Physique*, 47:321–329, 1986

[3] Milner, S.T. and Safran, S.A. Dynamical fluctuations of droplet microemulsions and vesicles. *Phys. Rev. A*, 36: 4371–4379, 1987

[4] Zhong-can, O.-Y. and Helfrich, W. Bending energy of vesicle membranes: General expressions for the first, second, and third variation of the shape energy and applications to spheres and cylinders. *Phys. Rev. A*, 39:5280–5288, 1989

[5] Helfrich, W. Steric interactions of fluid membranes in multilayer systems. *Z. Naturforsch. Teil A*, 33:305–315, 1978

[6] Helfrich, W. and Servuss, R.-M. Undulations, steric interaction and cohesion of fluid membranes. *Nuovo Cim.*, 3D: 137–151, 1984

[7] Marko, J.F. and Siggia, E.D. Fluctuations and supercoiling of DNA. *Science*, 265:506–508, 1994

$\sigma \int dS$, and assuming small gradients, we have

$$E \simeq \frac{1}{2}\int d^2x \left\{ k_c \left(\nabla^2 h\right)^2 + \sigma \left(\boldsymbol{\nabla} h\right)^2 \right\}. \tag{5.31}$$

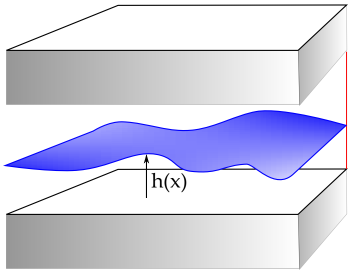

Figure 5.7: A fluctuating elastic membrane confined between two walls.

If we decompose the shape in the usual manner as

$$h(\mathbf{r}) = \sum_{\mathbf{q}} e^{-i\mathbf{q}\cdot\mathbf{r}} \hat{h}(\mathbf{q}), \tag{5.32}$$

then the energy is

$$E = \frac{1}{2} A \sum_{\mathbf{q}} \left(k_c q^4 + \sigma q^2\right) |\hat{h}(\mathbf{q})|^2, \tag{5.33}$$

and by equipartition

$$\langle |\hat{h}(\mathbf{q})|^2 \rangle = \frac{k_B T}{A\left(k_c q^4 + \sigma q^2\right)}. \tag{5.34}$$

It follows that for the unconstrained membrane the variance of displacements is

$$\langle \overline{h^2} \rangle = \frac{k_B T}{2\pi} \int \frac{q dq}{k_c q^4 + \sigma q^2} \tag{5.35}$$

If $\sigma = 0$ (a free membrane), using the cutoff $q_{\text{min}} = \pi/\sqrt{A}$, we find

$$\langle \overline{h^2} \rangle = \frac{k_B T}{4\pi^3 k_c} A. \tag{5.36}$$

The fact that the variance grows with the area A of the membrane led Helfrich and Servuss to argue that there will be a scale A^* at which the variance will be of order d^2, at which point the membrane strongly interacts with the walls. The precise value of the prefactor c in the statement $\langle \overline{h^2} \rangle = cd^2$ varies with the assumptions of the calculation, so we leave it unspecified at the moment. Then,

$$A^* = 4\pi^3 c \left(\frac{k_c}{k_B T}\right) d^2. \tag{5.37}$$

The next step involves the idea that each patch of membrane of area A^* acts as a quasi-independent "particle" confined in the gap of size $2d$, bouncing around in thermal equilibrium like a particle in a confined one-dimensional ideal gas. The pressure exerted on the wall can be deduced from the average force the wall experiences from collisions of the constituent "particles" with some assume mass m. That force is is just the ratio of the momentum transfer $\Delta p = m\Delta v = 2mv$ to the average time interval Δt between collisions with the wall. Since the average velocity vanishes by symmetry, we use $mv \sim m\langle v^2\rangle^{1/2}$, and set $\Delta t = 4d/\langle v^2\rangle^{1/2}$ and thus $F = k_B T/2d$. Dividing by the area A^* we obtain the pressure $P = F/A^*$, or

$$P \sim \frac{(k_B T)^2}{8\pi^3 c k_c} \frac{1}{d^3}. \tag{5.38}$$

The energy per unit area is the integral of P with respect to d,

$$V_{rep}(d) = \frac{1}{16\pi^3 c} \frac{k_B T}{k_c} \frac{k_B T}{d^2}. \tag{5.39}$$

Written in this manner we see naturally that the repulsive interaction can be compared to the van der Waals attraction (2.33) between membranes, whose leading order behaviour for nearby membranes has the same power-law dependence, leading to the sum

$$V_{rep}+V_A \simeq k_BT\left[\frac{1}{16\pi^3 c}\frac{k_BT}{k_c}-\frac{1}{12\pi}\frac{A_H}{k_BT}\right]\frac{1}{d^2}. \tag{5.40}$$

In this expression we have grouped terms to make the relevant dimensionless ratios apparent. Based on this comparison, and excluding any other types of intermembrane interactions, one would conclude that if van der Waals interactions dominate (large A_H then the membranes adhere to each other, while if the fluctuation-induced repulsion dominates (small k_c) they are repelled to infinity. The problem becomes more complicated in the presence of screened electrostatics and if one includes the role of thermal fluctuations.[8]

5.2.3 *Flicker phenomena of red blood cell membranes*

Next we consider a classic problem in the *dynamics* of cell membranes, the "flicker phenomenon" of red blood cells. The name derives from the persistent shimmering observed at the junction of the rim and the centre of erythrocytes, particularly when viewed in phase contrast microscopy. While historical explanations invoked specific biochemical reactions within the cytoplasm of the cells, it is now understood that the phenomenon arises from thermal fluctuations of the red blood cell (RBC) membrane. The first comprehensive treatment of this phenomenon was by Brochard and Lennon,[9] whose analysis we follow here with significant simplifications.

Recall the typical shapes of RBCs, as shown in Chapter 2 (Fig. 5.8). It is apparent that the central region of an RBC consists of roughly parallel sections of the membrane bounding a thin disc of cytoplasm. The cytoplasm itself contains a complex soup of molecular species, and has a different index of refraction from the surrounding water. When light passes through the RBC, the phase shift experienced will depend on the product of the local thickness and the index of refraction difference from the surrounding water, and it is this phase difference that is measured in phase contrast microscopy. It follows that dynamical properties of those fluctuations are of interest, and we must find the equation of motion for membrane deformations.

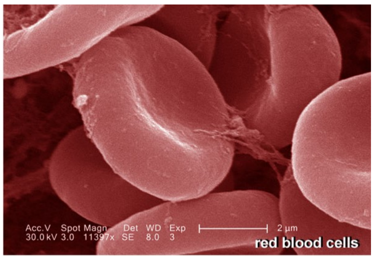

Figure 5.8: Electron micrograph of red blood cells.

Since the experimental method is sensitive to variations in the cytoplasm thickness, the relevant mode of deformation is the *antisymmetric* "peristaltic" mode shown schematically in Fig. 5.9, so if d is the equilibrium thickness, the thickness variation $\delta d = 2h$. The key experimental observations involve measurements of the spatio-temporal correlation function of the thickness fluctuations.

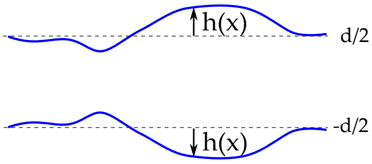

Figure 5.9: Geometry of the calculation for flicker phenomenon.

Before presenting their results, it is useful to make a slight digression to discuss some important features of correlation functions. We frame the discussion in the context of the Langevin equation (5.41) governing the one-dimensional motion of a particle in an optical trap

[8] Lipowsky, R. and Leibler S. Unbinding transitions of interacting membranes. *Phys. Rev. Lett.*, 56:2541–2544, 1986

[9] Brochard, F. and Lennon, J.F. Frequency spectrum of the flicker phenomenon in erythrocytes. *J. Physique*, 36:1035–1047, 1975

(modelled as a harmonic potential),

$$\zeta \dot{x} = -kx + \xi(t), \tag{5.41}$$

where ζ is the drag coefficient, k is the trap stiffness, and $\xi(t)$ is the random noise. We define the Fourier transform pairs

$$\tilde{x}(\omega) = \int dt e^{-i\omega t} x(t), \tag{5.42a}$$

$$x(t) = \int \frac{d\omega}{2\pi} e^{i\omega t} \tilde{x}(\omega). \tag{5.42b}$$

Recall that the choice of where the factor of 2π is located in these relations is a matter of convention, or it can be split symmetrically between the two as a factor of $1/\sqrt{2\pi}$. The only constraint is that the transform of the inverse transform yields the function, or

$$\int_{-\infty}^{\infty} d\omega e^{i\omega t} = 2\pi\delta(t), \tag{5.43}$$

where δ is the Dirac delta. A Fourier transform of (5.41) yields

$$(i\omega\zeta + k)\, \tilde{x}(\omega) = \tilde{\xi}(\omega). \tag{5.44}$$

As before, we can assume that the noise is delta function correlated, and thus the power spectrum $P(\omega) = \langle |\tilde{x}(\omega)|^2 \rangle$ is

$$P(\omega) = \frac{2k_B T\zeta}{\omega^2\zeta^2 + k^2} = \frac{2D}{\omega^2 + \tau^{-2}}. \tag{5.45}$$

where $\tau = \zeta/k$ is the relaxation time, and we used $\langle |\tilde{\xi}(\omega)|^2 \rangle = 2k_B T\zeta$. This result can be used three ways. First, there is the general result connecting the integral of $P(\omega)$ to equilibrium fluctuations,

$$\int_{-\infty}^{\infty} \frac{d\omega}{2\pi} P(\omega) = \langle x^2 \rangle, \tag{5.46}$$

where the r.h.s. is the expectation in equilibrium. We find

$$\int_{-\infty}^{\infty} \frac{d\omega}{2\pi} \frac{2k_B T\zeta}{\omega^2\zeta^2 + k^2} = \frac{k_B T}{k}, \tag{5.47}$$

as we expect from the equipartition result $\langle \frac{1}{2}kx^2 \rangle = \frac{1}{2}k_B T$.

A second connection involves the temporal correlation function of $x(t)$, which follows from the analysis in Sec. 3.3 as

$$\langle x(t)x(0) \rangle = \frac{k_B T}{k} e^{-t/\tau}. \tag{5.48}$$

The celebrated Wiener-Khinchine theorem, derived first by Wiener[10] and extended by Khinchine,[11] states that the power spectrum and the autocorrelation function are Fourier transform pairs. With the optical trap example, this is verified by direct calculation:

$$\int_{-\infty}^{\infty} \frac{d\omega}{2\pi} \frac{2D}{\omega^2 + \tau^{-2}} e^{i\omega t} = \frac{k_B T}{k} e^{-t/\tau}. \tag{5.49}$$

Third, we can define a "susceptibility" Y of the system as the constant of proportionality between the response of the system to an

[10] Wiener, N. Generalized harmonic analysis. *Acta Math.*, 55:117–258, 1930

[11] Khintchine, A. Korrelationstheorie der stationären stochastischen Prozesse. *Math. Ann.*, 109:604–615, 1934

external force and the amplitude of that force. From (5.44) we have $\Upsilon = (1/\zeta)/(i\omega + \tau^{-1})$ which leads to the result that the power spectrum is proportional to the imaginary part of the response function,

$$P(\omega) = -\frac{2k_B T}{\omega}\Im\{\Upsilon\}. \tag{5.50}$$

This is the generalised Fluctuation-Dissipation Theorem.

With these definitions, we may now summarize the findings of Brochard and Lennon. Using a spectrum analyser they determined from the microscopic observations the quantities shown in Fig. 5.10.

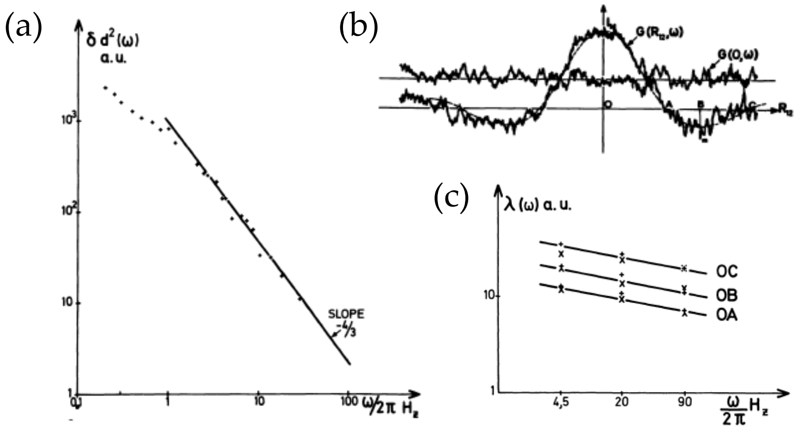

Figure 5.10: Key experimental observations on the flicker phenomenon in erythrocytes. (a) Frequency spectrum of fluctuations at a given point, (b) spatial correlation function (control curve at zero separation verifies that cell is unperturbed), and (c) length scale of correlations. From Ref. 9.

First, they found that the fluctuations in thickness at a given position vary with frequency ω according to

$$\langle \delta d^2(\omega)\rangle \sim \omega^{-4/3}, \tag{5.51}$$

as in Fig 5.10(a). Second, at a given frequency, the spatial correlation is an oscillatory, decaying function of separation [Fig 5.10(b)], and third, the characteristic length scale $\ell(\omega)$ of oscillations in the spatial correlation function decays with frequency approximately as

$$\ell(\omega) \sim \omega^{-1/6}. \tag{5.52}$$

In summary, the autocorrelation function has the scaling form

$$C(R,\omega) \sim \omega^{-4/3} G\left(\frac{R}{\ell(\omega)}\right). \tag{5.53}$$

A complete treatment of the coupled problem of fluid flow in a region bounded by two fluctuating membranes is an algebraically complex problem related to that involved in Taylor's waving sheet model of microorganism motility discussed in Chapter 6, but as the mean intermembrane spacing d is significantly smaller than the lateral extent of the membranes, we can adopt the simplified geometry of a slab with small thickness variations and use lubrication theory to determine the fluid flows. Wile a typical lipid membrane must be thought of as a fluid, the RBC membrane has a complex network of embedded polymers comprising the so-called "spectrin network" that gives it more the characteristics of a soft solid, and thus it is appropriate to consider no-slip boundary conditions on the fluid.

Let us first review the essential results of lubrication theory for the viscous fluid flow between parallel no-slip surfaces at $z = \pm d/2$. We assume that the dominant component of the fluid velocity is that perpendicular to the surface normal, and write

$$\mathbf{u}(x, y, z) \simeq u(\mathbf{x}_\perp, z)\hat{\mathbf{e}}_\perp, \tag{5.54}$$

where $\mathbf{x}_\perp = (x, y)$ is the in-plane coordinate and $\hat{\mathbf{e}}_\perp$ is an in-plane unit vector. In this regime, the viscous term $\nabla^2\mathbf{u}$ in the Stokes equation is dominated by z-derivatives and thus

$$\frac{\partial^2 u(\mathbf{x}_\perp, z)}{\partial z^2} = \frac{\nabla_\perp p}{\mu}, \tag{5.55}$$

where $\nabla_\perp$ is the in-plane component of the gradient. Combining this relationship with the no-slip conditions on u at $z = \pm d/2$ it follows that u can be written in the separable form

$$u(\mathbf{x}_\perp, z) = -\left[\left(\frac{d}{2}\right)^2 - z^2\right]\frac{\nabla_\perp p(\mathbf{x}_\perp)}{2\mu}. \tag{5.56}$$

From this we obtain the in-plane fluid flux $\mathbf{J}(\mathbf{x}_\perp) = \int_{-d/2}^{d/2} dz\mathbf{u}$,

$$\mathbf{J} = -\frac{d^3}{12\mu}\boldsymbol{\nabla}_\perp p, \tag{5.57}$$

and the depth-averaged velocity $\bar{\mathbf{u}} = \mathbf{J}/d$, which obeys Darcy's Law,

$$\bar{\mathbf{u}} = \frac{\mathbf{J}}{d} = -\frac{d^2}{12\mu}\boldsymbol{\nabla}_\perp p. \tag{5.58}$$

Equation 5.56 captures the essence of the dynamics relevant to the flicker phenomenon, which requires an equation of motion for deformations of the membrane shape away from the flat equilibrium. The relevant PDE for the shape evolution can be derived in three steps. First, note that conservation of fluid volume implies

$$\frac{\partial}{\partial t}(d + 2h) = -\boldsymbol{\nabla}_\perp \cdot \mathbf{J}. \tag{5.59}$$

Second, from the lubrication theory above we have (5.57) relating the flux to gradients in the pressure. Finally, the pressure p at the interface is related to the displacement field $h(x)$ via the usual functional derivative. In the long-wavelength approximation, this yields

$$p = k_c\nabla_\perp^4 h. \tag{5.60}$$

Assembling all the pieces, and dropping the subscript $\perp$ for convenience, the equation of motion for h is

$$h_t = \frac{k_c d^3}{24\mu}\nabla^6 h. \tag{5.61}$$

This unusual form, with 6 derivatives, thus arises from a combination of a conservation law, lubrication flow, and elasticity. By dimensional analysis we deduce immediately from (5.65) that for perturbations at frequency ω there is a length scale

$$\ell(\omega) = \left(\frac{k_c d^3}{24\mu\omega}\right)^{1/6}, \tag{5.62}$$

which provides an explanation of the $\omega^{-1/6}$ behaviour shown in Fig. 5.10, provided we can identify this length with the scale of the decay of the correlation function. If we ignore any lateral boundary conditions and Fourier decompose the displacement field via

$$h = h_0 e^{-i\mathbf{q}\cdot\mathbf{x}-i\omega t}, \tag{5.63}$$

where $\mathbf{x}$ is an in-plane coordinate and $\mathbf{q}$ is an in-plane wavevector, we obtain

$$-i\omega = -(k_c d^3/24\mu)q^6, \tag{5.64}$$

indicating exponential *decay* of the modes for all $\mathbf{q}$. They are *stable*.

To find the response function Υ, we introduce an external pressure field p_{ext} that forces the system, and obtain the dynamics

$$h_t - \frac{k_c d^3}{24\mu}\nabla^6 h = \frac{d^3}{24\mu}\nabla^2 p_{ext}. \tag{5.65}$$

By analogy with the optical trapping result, we obtain

$$\Upsilon(q,\omega) = \frac{d^3 q^2}{24\mu}\frac{1}{i\omega + \frac{k_c d^3}{24\mu}q^6}. \tag{5.66}$$

From the generalised Fluctuation-Dissipation theorem (5.50) we obtain the power spectrum

$$\langle|\delta d(q,\omega)|^2\rangle = \frac{k_B T d^3 q^2/12\mu}{\omega^2 + \left(\frac{k_c d^3}{24\mu}\right)^2 q^{12}}. \tag{5.67}$$

By a straightforward calculation, the correlation function of interest is just an inverse transform of the power spectrum,

$$C(R,\omega) = \int \frac{d^2 q}{(2\pi)^2}\langle|\delta d(q,\omega)^2\rangle e^{i\mathbf{q}\cdot\mathbf{R}}. \tag{5.68}$$

Written out explicitly, we obtain

$$C(R,\omega) = \frac{k_B T d^3}{(2\pi)^3 6\mu}\int_0^{2\pi} d\theta \int_0^\infty \frac{e^{iqR\cos\theta} q^3 dq}{\omega^2 + \left(\frac{k_c d^3}{24\mu}\right)^2 q^{12}}. \tag{5.69}$$

By a change of variables to $k = \ell(\omega)q$, this can be written as

$$C(R,\omega) = \frac{k_B T d^3}{(2\pi)^3 6\mu\omega^2\ell^4}\int_0^{2\pi} d\theta \int_0^\infty \frac{e^{ik(R/\ell)\cos\theta} k^3 dk}{1+k^{12}}, \tag{5.70}$$

The θ integral can be done using the relation

$$\int_0^{2\pi} e^{ik\xi\cos\theta} = J_0(k\xi), \tag{5.71}$$

where J_0 is the zeroth order Bessel function. To normalise the correlation function, we examine the remaining integral at $R/\ell = 0$,

$$\int_0^\infty \frac{dk\, k^3}{1+k^{12}} = \frac{1}{4}\int_0^\infty \frac{du}{1+u^3} = \frac{\pi}{6\sqrt{3}}, \tag{5.72}$$

yielding a result that can be written in the compact form

$$C(R,\omega) = \frac{\sqrt{3}}{8\pi^4}\frac{k_BT}{k_c}\frac{\ell^2(\omega)}{\omega}G\left(\frac{R}{\ell(\omega)}\right), \tag{5.73}$$

where the scaling function $G(\chi)$ is

$$G(\chi) = \frac{6\sqrt{3}}{\pi}\int_0^\infty dq\, q^3 \frac{J_0(\chi q)}{1+q^{12}}, \tag{5.74}$$

and the prefactor sets $G(0) = 1$. Figure 5.11 shows the scaling function $G(\xi)$ obtained by numerical integration of (5.74). This result confirms that the correlation function depends only on the ratio $R/\ell(\omega)$, as found experimentally, and that therefore $\ell(\omega)$ is the length scale governing the decay of correlations. The prefactor $\ell^2(\omega)/\omega$ displays the $\omega^{-4/3}$ dependence seen in experiment, and the scaling function $G(\chi)$ shows the exact experimental form shown in Fig. 5.10(b).

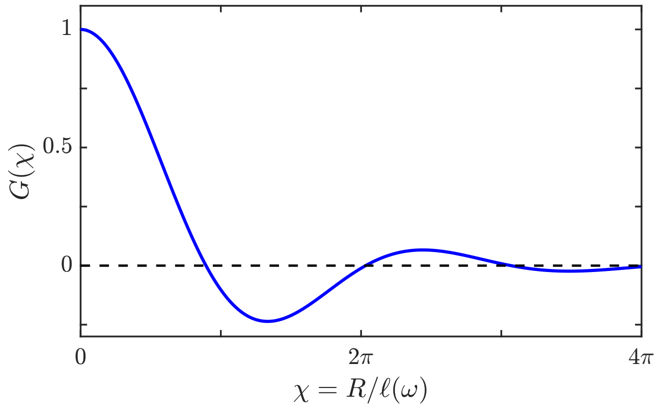

Figure 5.11: Scaling function G of the spatial correlation function of membrane fluctuations as a function of distance scaled by elastohydrodynamic length $\ell(\omega)$. Obtained with `Figure_511_flicker.m`.

5.3 *Shapes and shape transformations*

In this last section of the chapter we study two problems involving the shapes of elastic membranes. These are chosen to illustrate some key points regarding the physics of bending and the competition between elasticity and tension.

5.3.1 *Buckling of two-dimensional vesicles under pressure*

The general problem of finding the equilibrium shapes of fluid membranes governed by the Helfrich elastic energy (2.66) is a challenging one by virtue of the strong nonlinearities in the governing equations and the typical difficulties associated with the differential geometry of surfaces. To gain insight into some of the basic physics involved, we study the problem of "two-dimensional vesicles", which are treated as closed elastic filaments governed by the bending energy (4.27), subject to a pressure difference between the fluid enclosed and that outside, and to a uniform tension. The study of this minimisation problem has a long history, with early work in the 1960s[12] and continuing to the present.[13]

[12] Tadjbakhsh, I. and Odeh, F. Equilibrium States of Elastic Rings. *J. Math. Anal. Appl.*, 18:59–74, 1967

[13] Foster, B., Verschueren, N., Knobloch, E. and Gordillo, L. Pressure-driven wrinkling of soft inner-lined tubes. *New J. Phys.*, 24:013026, 2022

The equilibrium condition for the problem at hand is the normal component of the force on the filament vanish. Expressed in terms of the curvature κ the governing equation is

$$A\left(\kappa_{ss}+\frac{1}{2}\kappa^3\right)-\gamma\kappa-\Pi=0, \tag{5.75}$$

where γ is the tension and Π is the pressure difference. We will study the stability of a circular ground state of some radius R_0, and rescale the various quantities using R_0 and A via

$$K=\kappa R_0, \quad T=\frac{\gamma R_0^2}{A}, \quad P=\frac{\Pi R_0^3}{A}, \quad \eta=\frac{s}{R_0}, \tag{5.76}$$

where $\eta\in[0,2\pi]$, to obtain

$$K_{\eta\eta}+\frac{1}{2}K^3-TK-P=0, \tag{5.77}$$

or, equivalently,

$$\theta_{\eta\eta\eta}+\frac{1}{2}\theta_\eta^3-T\theta_\eta-P=0. \tag{5.78}$$

Given the curvature as a solution to (5.77), we obtain the θ via

$$\theta(\eta)=\int_0^\eta K(\eta'), \tag{5.79}$$

and use θ to obtain the coordinates of the curve as

$$x(\eta)=x_0+\int_0^\eta d\eta'\cos\theta(\eta'), \quad y(\eta)=y_0+\int_0^\eta d\eta'\sin\theta(\eta'), \tag{5.80}$$

where the location (x_0,y_0) of the origin is arbitrary.

To make progress with this problem, we assume that the solution $\theta(\eta)$ as well as the tension T and pressure P can be expanded in powers of a parameter $\epsilon\ll 1$ that serves as a bookkeeping device to keep track of orders. We can assume that system breaks circular symmetry into a shape with m lobes, with $m\geq 2$ (recalling that $m=1$ corresponds to an infinitesimal translation, and $m=0$ is a dilation. The requirement of symmetry under rotations by half a wavelength dictates that both T and P have only even terms in ϵ,

$$\begin{aligned}\theta(\eta)&=\theta^{(0)}(\eta)+\epsilon\theta^{(1)}(\eta)+\epsilon^2\theta^{(2)}(\eta)+\cdots\\ T&=T^{(0)}+\epsilon^2T^{(2)}+\cdots\\ P&=P^{(0)}+\epsilon^2P^{(2)}+\cdots.\end{aligned} \tag{5.81}$$

Direct substitution yields the zeroth order result

$$\theta^{(0)}(\eta)=\eta, \quad T^{(0)}=\frac{1}{2}-P^{(0)}, \tag{5.82}$$

a circle of unit radius ($K^{(0)}=1$), with a base tension determined by the inward pressure $P^{(0)}$. The fact that $T^{(0)}<0$ for $P^{(0)}>1/2$ indicates the possibility of a buckling instability. At order ϵ we find

$$\mathcal{L}\theta^{(1)}(\eta)=0, \tag{5.83}$$

where the operator $\mathcal{L}$ is

$$\mathcal{L} = \partial_{\eta\eta\eta} + \left(P^{(0)} + 1\right)\partial_{\eta},$$
$$\mathcal{L} = \partial_{\eta\eta\eta} + m^2\partial_{\eta}. \tag{5.84}$$

This has the simple solution

$$\theta^{(1)}(\eta) = \sin(m\eta). \tag{5.85}$$

We $\mathcal{L}$ as the derivative with respect to η of the operator that occurs in the Euler buckling problem (4.63), showing further that this membrane problem is related to a buckling instability.

Moving to order ϵ^2 the second order perturbation must solve

$$\mathcal{L}\theta^{(2)} = P^{(2)} + T^{(2)} - \frac{3}{2}m^2\cos^2(ms), \tag{5.86}$$

where the final term arises from a contribution $(3/2)\theta_{\eta}^{(1)^2}$. Here we must be careful to recognise that since $\cos^2(ms) = (1+\cos(2ms))/2$, the r.h.s. of (5.86) has a contribution in the nullspace of the operator $\mathcal{L}$, which involves the functions $\theta(\eta) = 1, \cos(ms), \sin(ms)$. For there to be a bounded solution at this order, the coefficients of all such terms on the r.h.s. must vanish. Here, that condition requires the constant term to vanish, and thus

$$P^{(2)} + T^{(2)} = \frac{3}{4}m^2. \tag{5.87}$$

At this order we do not have separate information on $P^{(2)}$ and $T^{(2)}$. The inhomogeneous solution to (5.86) is then

$$\theta^{(2)}(\eta) = \frac{1}{8m}\sin(2m\eta). \tag{5.88}$$

At cubic order in ϵ we note that the r.h.s has the terms

$$-\left(\frac{1}{2}\theta_{\eta}^{(1)^2} + 3\theta_{\eta}^{(1)}\theta_{\eta}^{(2)}\right) + T^(2)\theta_{\eta}^{(1)}. \tag{5.89}$$

Using the previously obtained results and now requiring the absence of a term proportional to $\cos(ms)$ we find

$$T^{(2)} = \frac{3}{8}\left(m^2 + 1\right), \tag{5.90}$$

so $P^{(2)} = (3/8)\left(m^2 - 1\right)$. This completes the analysis to $\mathcal{O}(\epsilon^2)$.

The shapes that result from the function

$$\theta(\eta) = \epsilon\sin(ms) + \frac{\epsilon^2}{8m}\sin(2ms) \tag{5.91}$$

for $m = 2$ are shown in Fig. 5.12 for increasing values of ϵ. At the largest value, the calculated shape is remarkably similar to the cross-section of the biconcave discoid shape of the red blood cell.

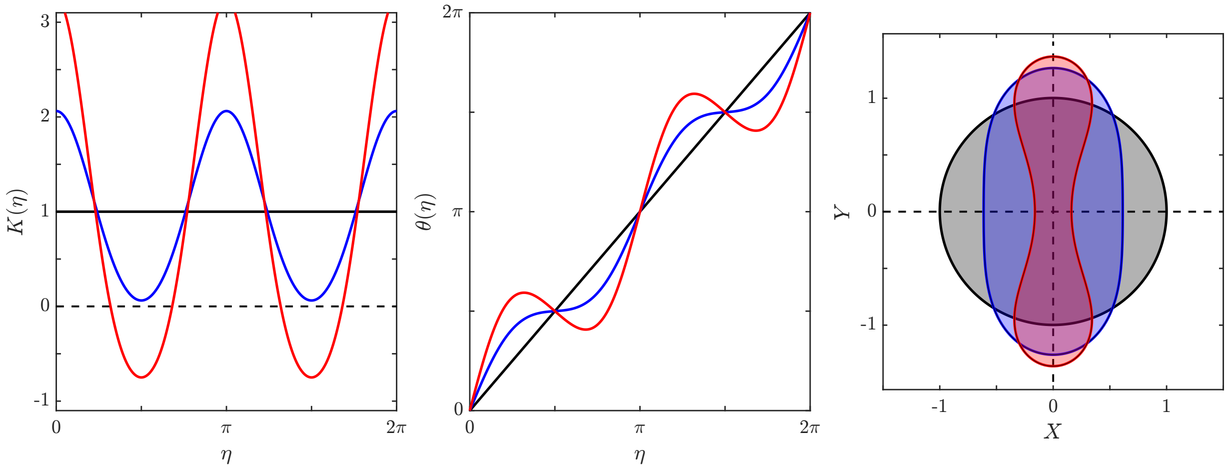

Figure 5.12: Shapes of two-dimensional vesicles under pressure. Panels show (a) scaled curvature $K(\eta)$, (b) tangent angle $\theta(\eta)$, and (c) shape of vesicle for three values of ϵ ($\epsilon = 0$ (black), 0.5 (blue) and 1 (red). Obtained with `Figure_512_2dvesicles.m`.

5.3.2 *Tether formation*

A classic problem in the biological physics of membranes is the formation of "tethers" under the action of a localized force. There are many examples of this phenomenon in living cells, typically associated with cytoskeletal filaments pushing against the cell membrane. A controlled example of this was achieved some time ago[14] using an optical trap to pull a tether from a vesicle (Fig. 5.13). In what follows we outline the basic features of a model for tether formation in elastic membranes subject to large tension, as is the case in these and earlier experiments involving tethers extracted from vesicles.[15]

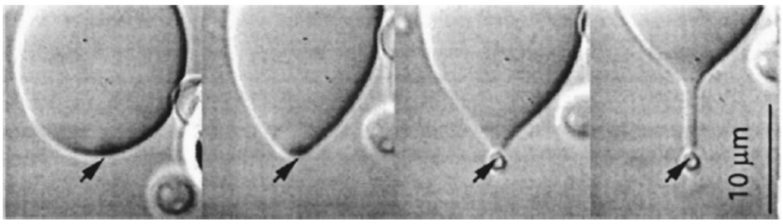

Figure 5.13: Equilibrium shapes of a bilayer lipid vesicle as the force exerted by an optical trap is increased (left to right) and a tether is produced. From Ref. 14.

Here we work through a calculation of perhaps the simplest model for tether formation,[16] in which the object that pokes the membrane is abstracted to a ring of small radius that provides a suitable boundary condition for the surface. Mathematically the problem is defined as the search for energy minimisers of a functional that combines the bending elasticity of fluid membranes and a tension associated with contact of the membrane with a reservoir at some specified chemical potential, given boundary conditions at a large loop of radius R that represents a far-field lipid vesicle, for instance, and a much smaller loop of radius r_0.

Within this picture of a tether, it is necessary first to understand catenoids that span two loops of differing radii. We consider a setup in which a ring of radius R lies in the plane $z = 0$ and a smaller one of radius r_0 is in the plane $z = d$. This calculation requires that we generalise the up-down symmetric catenoid solution (5.15) to include

[14] Fygenson, D.K., Marko, J.F. and Libchaber, A. Mechanics of microtubule-based membrane extension. *Phys. Rev. Lett.*, 79:4497–4500, 1997

[15] Evans, E. and Yeung, A. Hidden dynamics in rapid changes of bilayer shape. *Chem. Phys. Lipids*, 73:39–56, 1994

[16] Powers, T.R., Huber, G. and Goldstein, R.E. Fluid-membrane tethers: minimal surfaces and elastic boundary layers. *Phys. Rev. E*, 65:041901, 2002

a second parameter, which we write in the form

$$\zeta(z) = a \cosh\left(\frac{z-c}{a}\right). \tag{5.92}$$

The boundary condition at $z = 0$ implies that $c/a = \cosh^{-1}(R/a)$, which, when combined with that at $z = d$ yields

$$r_0 = R\cosh\left(\frac{d}{a}\right) - \sqrt{R^2 - a^2}\sinh\left(\frac{d}{a}\right). \tag{5.93}$$

Although formidable in appearance, this is simply a quadratic equation in $x = \exp(d/a)$ whose solution can be put in the form

$$D_\pm = \frac{1}{2}\alpha \ln\left(\frac{\beta \pm \sqrt{\beta^2 - \alpha^2}}{1 - \sqrt{1-\alpha^2}}\right), \tag{5.94}$$

where, as before $D = d/R$ and $\alpha = a/R$, and now $\beta = r_0/R$ is the size ratio of the loops. A graphical representation of these solutions is shown in Fig. 5.14 in which we may interpret the curves as follows: for each chosen loop ratio β the parameter α necessary to match the boundary conditions varies in the range $(0, \beta)$ along the lower branch of each loop as the rings are separated from $D = 0$ up to some maximum spacing indicated by a circle. That maximum spacing is very nearly linear with β, with a slope close to unity; we conclude that catenoids spanning two different sized loops exist only up to a height that is approximately the radius of the smaller loop. A montage of such asymmetric catenoids is shown in Fig. 5.15

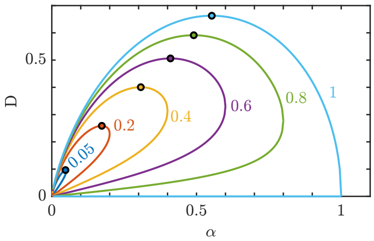

Figure 5.14: Trajectories of (5.94) in the $D - \alpha$ plane for various values of the ring radius ratio β, as indicated. Obtained with `Figure_514_and_515_asymcatenoid.m`.

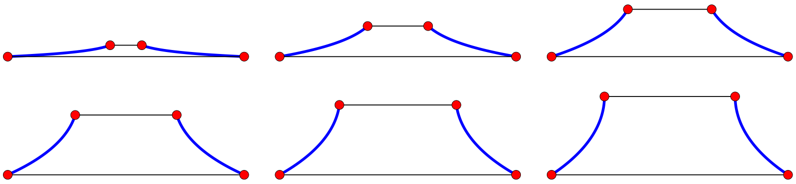

Figure 5.15: Catenoids of maximum height for a range of asymmetry parameters β. Obtained with `Figure_514_and_515_asymcatenoid.m`.

The problem of interest is to find the minimum of the functional

$$E = \frac{1}{2}k_c \int dS(2H)^2 + \sigma \int dS \tag{5.95}$$

for an axisymmetric surface with boundary conditions $\zeta(0) = R$, $\zeta(d) = r_0$, $H(0) = 0$ and the tangent plane at $z = d$ is parallel to the plane. The Euler-Lagrange equation for the Helfrich functional is an amusing exercise in differential geometry which we leave to the student. The result can be expressed in a compact form that has obvious similarities to the equivalent result for planar vesicles (5.75),

$$k_c\left(\nabla^2 H + 2H^3 - 2HK\right) - \sigma H + p = 0, \tag{5.96}$$

where p is the pressure difference between the the inside and outside of the tether. Here ∇^2 is the covariant Laplacian. We shall ignore any pressure difference in this problem, as it can be shown to introduce only minor corrections to the main results.

Rescaling all lengths by the bottom hoop radius R, we obtain

$$\epsilon\left(\nabla^2 H + 2H^3 - 2HK\right) - H = 0, \tag{5.97}$$

where

$$\epsilon = \frac{k_c}{\sigma R^2}. \tag{5.98}$$

We shall be interested in the large-tension limit $\epsilon \ll 1$, as this gives narrow tethers. Written this way, with the small parameter multiplying the highest derivative in the problem, it is clear that a boundary layer is likely to form, as the introduction of bending energy is a singular perturbation. The limit $\epsilon = 0$ is just the minimal surface problem, so the choice $H = 0$ at the bottom loop is consistent with that limit, and no boundary layer will form there. But the tangent condition at the upper loop is inconsistent with $H = 0$ and a boundary layer will form there. Such a layer will be such that the elastic and surface tension contributions balance ($\epsilon\nabla^2 H \sim H$, giving a (dimensionless) length scale $\sim \sqrt{\epsilon}$ (dimensionally, $R\sqrt{\epsilon}$).

To understand the boundary layer problem, we first work in the Monge representation that is suitable for shallow surfaces slightly deformed from the disc at $z = 0$, so $D \ll 1$. A useful pair of coordinates (ξ^1, ξ^2) to describe the surface involves the arclength s along the meridian and the angle φ around the z-axis, so that points on the surface are given by

$$\mathbf{x}(s,\varphi) = r(s)\hat{\mathbf{e}}_r + z(s)\hat{\mathbf{e}}_z, \tag{5.99}$$

with $r_s^2 + z_s^2 = 1$, as s is arclength. The first fundamental form is then

$$g_{ij}d\xi^i d\xi^j = ds^2 + r^2 d\varphi^2, \tag{5.100}$$

while the second fundamental form is

$$K_{ij}d\xi^i d\xi^j = \left(z_s r_{ss} - r_s z_{ss}\right) ds^2 - r z_s d\varphi^2. \tag{5.101}$$

With the previous convention for raising and lowering indices and $g^{ik}g_{kj} = \delta^i_j$ one finds the mean curvature

$$H = \frac{1}{2}g^{ij}K_{ij} = \frac{1}{2}\left[\frac{r_{ss}}{z_s} - \frac{z_s}{r}\right], \tag{5.102}$$

Gaussian curvature

$$K = -\frac{r_{ss}}{r}, \tag{5.103}$$

and Laplacian

$$\nabla^2 = \frac{1}{\sqrt{g}}\partial_i g^{ij}\sqrt{g}\partial_j = \frac{1}{r}\frac{d}{ds}r\frac{d}{ds}. \tag{5.104}$$

Thus, if the surface is described by the height function $z(r)$ above the plane $z = 0$, then to leading order $s \sim r$, $H \sim (1/2)\nabla^2 z$, and the shape equation becomes

$$\epsilon\nabla^4 z - \nabla^2 z = 0, \tag{5.105}$$

where

$$\nabla^2 = \frac{1}{r}\frac{d}{dr}\left(r\frac{d}{dr}\right). \tag{5.106}$$

To complete the specification of this problem we enumerate the boundary conditions. At $r = 1$ we have $z = 0$ and $\nabla^2 z = 0$, while at $r = r_0$ we have $z = d$ and $dz/dr = 0$.

We solve (5.105) order by order in ϵ. At $\mathcal{O}(\epsilon^0)$ we are dealing with the "outer" solution, for which $\nabla^2 z_{out}(r) = 0$, which is solved by

$$z_{\text{out}}(r) = b_1 + b_2 \ln r. \tag{5.107}$$

The condition at $r = 1$ sets $b_1 = 0$, but the zero moment condition does not fix b_2; it is determined at higher order. This outer solution diverges at the inner ring in the limit $r_0 \to 0$, an unphysical feature corrected by the inner solution. To find the inner solution we rescale the radial coordinate to balance the elastic and tension terms,

$$\rho = \frac{r}{\sqrt{\epsilon}}, \tag{5.108}$$

which leads to the amusing equation

$$\frac{1}{\rho}\frac{d}{d\rho}\left(\rho\frac{d}{d\rho}\right)\left\{\frac{1}{\rho}\frac{d}{d\rho}\left(\rho\frac{d}{d\rho}\right) z_{in} + z_{in}\right\} = 0. \tag{5.109}$$

This is solved by

$$\frac{z_{\text{in}}}{d} = c_1 + c_2 \ln\rho + c_3 I_0(\rho) + c_4 K_0(\rho), \tag{5.110}$$

where I_0 and K_0 are modified Bessel functions. The coefficient c_3 vanishes due to the divergence of I_0 as $\rho \to 0$. The boundary conditions at $r = r_0$ yield two constraints, from which we deduce

$$\frac{z_{\text{in}}}{d} = 1 + c_4\left[K_0(\rho) - K_0(\rho_0) + \rho_0 K_1(\rho_0)\ln\left(\frac{\rho}{\rho_0}\right)\right], \tag{5.111}$$

where $\rho_0 = r_0/\sqrt{\epsilon}$. Matching z_{in} and z_{out}, the constant terms of z_{in} must vanish and the coefficient of the log term matches b_2, yielding

$$\frac{z_{\text{out}}}{d} = \frac{\rho_0 K_1(\rho_0)\ln r}{\rho_0 K_1(\rho_0)\ln r_0 + K_0(\rho_0)} \tag{5.112}$$

and

$$\frac{z_{\text{in}}}{d} = \frac{\rho_0 K_1(\rho_0)\ln r + K_0(\rho)}{\rho_0 K_1(\rho_0)\ln r_0 + K_0(\rho_0)}. \tag{5.113}$$

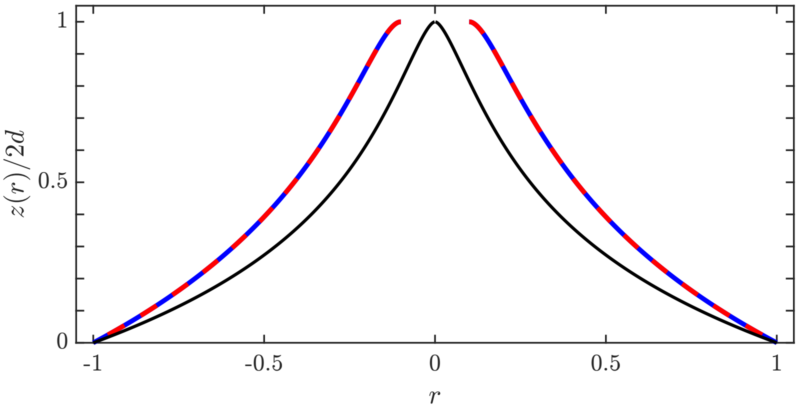

Figure 5.16: Shapes of poked membranes in the Monge representation. Curves are for $\beta = 0.1$ and $\epsilon = 0.005$. Solid blue curve is full numerical solution of (5.105), dashed red is asymptotic solution $z_{composite}(r)$ and black curve is the $\beta \to 0$ limit (5.114). Obtained with `Figure_516_and_517_tethers.m`.

The composite solution is obtained by adding the two and subtracting the common part, which leads to the simple result $z_{\text{comp}} = z_{\text{in}}$. It is then possible to take the limit $r_0 \to 0$ and obtain

$$\lim_{r_0 \to 0} \frac{z_{\text{comp}}}{d} = \frac{\ln r + K_0\left(r/\sqrt{\epsilon}\right)}{-\gamma + \ln\left(2\sqrt{\epsilon}\right)}, \tag{5.114}$$

where $\gamma = 0.5772\ldots$ is Euler's constant. Figure 5.16 compares the full, composite, and limiting composite solutions.

To go beyond this linearised problem and address the formation of a true tether with the observed property of a constant radius along its length, it is generally necessary to invoke numerical methods, particularly to connect such a solution to that obtained above in the small-amplitude limit. Figure 5.17 shows examples of such a calculation, illustrating that indeed a constant-diameter tether emerges from the catenoidal solution at the supporting ring.

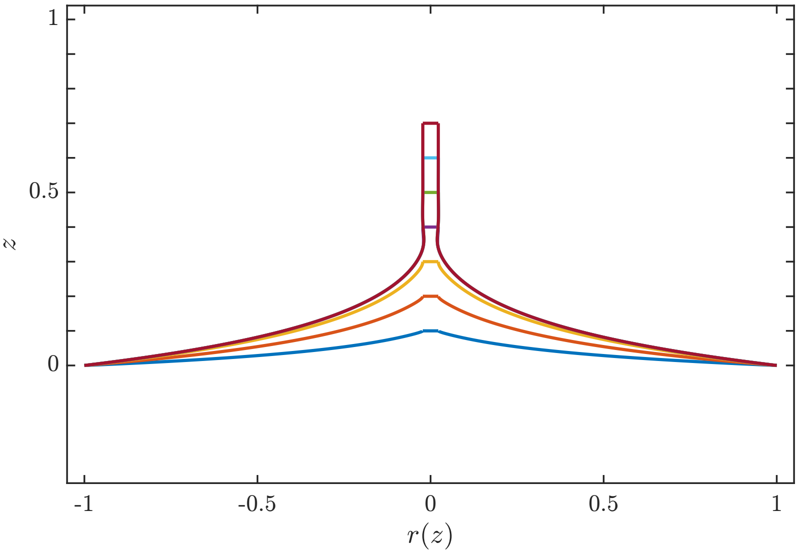

Figure 5.17: Numerical solution of full tether problem for $\epsilon = 0.001$ and $r_0 = 0.1$ for various values of the ring separation d. Obtained with `Figure_516_and_517_tethers.m`.

Analytical results can be obtained if we focus on the fully-developed tether itself. First, in a straight tether, the equilibrium condition (5.97) simplifies to $2\epsilon H^3 - H = 0$, and since in our rescaled units $H = -R/2a$ for a cylinder of radius a, we deduce the tether radius

$$a = \sqrt{\frac{\epsilon}{2}} R = \sqrt{\frac{k_c}{2\sigma}}, \tag{5.115}$$

which is indeed $\ll R$ in the high-tension limit.

Second, it is straightforward to develop a stability analysis around this cylindrical solution, writing $r(z) = a + u(z)$ and expanding

$$\mathcal{E} = \frac{\epsilon}{2} \int dS (2H)^2 + \int dS \tag{5.116}$$

to $\mathcal{O}(u^2)$, using $dz/ds = \sqrt{1 + r'(z)^2}$. One finds

$$\begin{aligned}\mathcal{E} =& 2\pi \int dz \Big[\left(a + \frac{\epsilon}{2a}\right) + \left(1 - \frac{\epsilon}{2a^2}\right)\left(u + \frac{a u_z^2}{2}\right) \\ &+ \frac{\epsilon a}{2}\left(u_{zz}^2 + \frac{u^2}{a^4}\right) + \cdots \Big],\end{aligned} \tag{5.117}$$

where a term that is a total derivative has been omitted. We observe that the first bracketed term in (5.117) is minimised at the equilibrium value of a, at which the second bracketed term vanishes identically, and that the third bracketed term involves two contributions that are each manifestly positive. Thus, at quadratic order the energy is larger than the straight tether and therefore the tether is stable. Thus, while a tether without any bending energy that is longer than its circumference is unstable to the Rayleigh instability, one that is at the equilibrium size determined by the balance of tension and elasticity is stable for arbitrary lengths!

6

Cellular Motion (Lectures 17-20)

In this section we continue to move up the scale of lengths in biological physics to consider the motion of uni- and multicellular organisms.[1] After an overview of the locomotion of flagellated prokaryotic and eukaryotic cells we review historically important models developed to understand the link between flagellar motion and swimming, as well as models that illustrate how hydrodynamic coupling between those appendages can lead to phase synchronisation. This motivates a discussion of the relationship between cell swimming and the elementary force singularities of Stokes flow—the stokeslet and the stresslet—and how those singularities can be used to understand a number of basic experimental observations. We conclude with a discussion of some collective effects involving active matter.

6.1 Cell swimming

Cell motion can take many forms, from crawling on solid substrates by means of membrane extensions ("filopodia" or "lamellipodia"), migration within confluent tissues, to swimming through fluids through the action of moving appendages. Within this course we focus on swimming, as it provides a context that is rich in phenomenology and has proven to be amenable to substantial quantitative analysis.

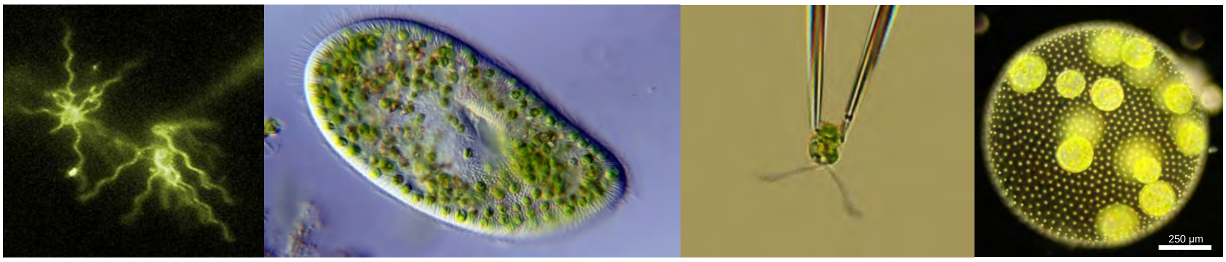

Figure 6.1: Examples of microswimmers. Left to right: *E. coli*, *Paramecium bursara*, *Chlamydomonas reinhardtii*, *Volvox carteri*.

The broad classification of living organisms into prokaryotes (cells without a membrane-bound nucleus) and eukaryotes (possessing a nucleus) serves also to distinguish typical means of swimming seen among unicellular and small multicellular organisms. As shown in Fig. 6.1, prokaryotes consist of a cell body whose dimensions are typically $1-10\,\mu$m, from which emanate one or more helical flagella several times the body length or more. These are rotated at

[1] E. Lauga. *The Fluid Dynamics of Cell Motility*. Cambridge University Press, Cambridge, UK, 2020

frequencies that can reach $10^2 - 10^3\,\mathrm{s}^{-1}$ by the action of rotary motors embedded in the cell wall, powered by a flux of proteins passing through them. Eukaryotes, as exemplified by uni- and multicellular algae, choanoflagellates, etc. achieve motility through the undulations of flagella driven by the action of motor proteins that slide the underlying filaments within the flagellum past each other through conformational changes powered by ATP consumption. These waveforms consist typically of a "power stroke", with a nearly straight flagellum sweeping through a large angle, followed by a "recovery stroke", in which a tightly curled flagellum is brought back to its starting point by moving close to the cell body. Both large unicellular organisms such as *Paramecium* and certain multicellular organisms composed of tens, hundreds, or even thousands of flagellated cells are often termed "ciliates", and the collective beating of their flagella may exhibit perfect frequency and phase locking, or frequency locking and phase modulations termed "metachronal waves".

The regime of Reynolds numbers inhabited by various swimming organisms is summarized in Table 6.1; there is a clear distinction between the Stokesian regime of the flagellated organisms in Fig. 6.1 and that of the larger swimmers familiar to us on a human scale.

organism	length	speed	frequency	Re
bacterium	$10\,\mu$m	$10\,\mu$m/s	100 Hz	10^{-4}
spermatozoon	$100\,\mu$m	$100\,\mu$m/s	10 Hz	10^{-2}
ciliate	$100\,\mu$m	1 mm/s	10 Hz	10^{-1}
tadpole	1 cm	10 cm/s	10 Hz	10^{3}
small fish	10 cm	10 cm/s	10 Hz	10^{4}
penguin	10 m	1 m/s	1 Hz	10^{6}
sperm whale	10 m	1 m/s	0.1 Hz	10^{7}

Table 6.1: Reynolds numbers for various swimming organisms.

6.1.1 The general swimming problem

From a mathematical perspective, our goal is to solve the Stokes equations for incompressible flow,

$$\boldsymbol{\nabla} p = \mu \nabla^2 \mathbf{u}, \quad \boldsymbol{\nabla} \cdot \mathbf{u} = 0, \tag{6.1}$$

where p is the pressure, with a boundary condition that $\mathbf{u}$ on the body equals the specified swimming "gait" $\mathbf{u}^S$, as in Fig. 6.2. With $\mathbf{u}^S$ known, the unknowns are the translational velocity $\mathbf{U}$ and the angular velocity $\boldsymbol{\Omega}$. We assume that the fluid is Newtonian, with viscosity μ and stress tensor

$$\boldsymbol{\sigma} = -p\mathbb{I} + \mu \left(\boldsymbol{\nabla}\mathbf{u} + \boldsymbol{\nabla}\mathbf{u}^T \right), \tag{6.2}$$

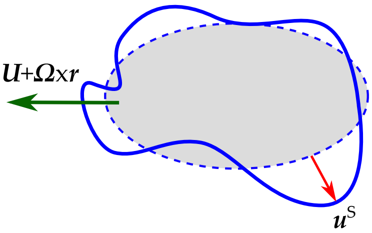

Figure 6.2: A generic swimmer with some reference shape (dashed) deformed by an actuation velocity $\mathbf{u}^S$.

In the absence of any body forces and torques acting on the swimmer, the unknowns are found by demanding that the total force and torque on the swimmer vanish,

$$\mathbf{F}(t) = \iint_S dS\, \boldsymbol{\sigma} \cdot \hat{\mathbf{n}} = 0, \tag{6.3a}$$

$$\mathbf{T}(t) = \iint_S dS\, \mathbf{r} \times (\boldsymbol{\sigma} \cdot \hat{\mathbf{n}}) = 0, \tag{6.3b}$$

where $\hat{\mathbf{n}}$ is the outward normal to the body.

It is often of interest to calculate the power generated by propulsive movements. The rate of working of the swimmer is

$$\dot{W} = -\iint_S dS\, \mathbf{u} \cdot \sigma \cdot \hat{\mathbf{n}}. \tag{6.4}$$

Standard manipulations using the divergence theorem allow us to re-express this result as the volume integral

$$\dot{W} = \iiint_V dV\, \frac{\partial}{\partial x_j} \left(u_i \sigma_{ij}\right). \tag{6.5}$$

Using the incompressibility of the fluid and the symmetry of the strain rate $E_{ij} = (1/2)\left(\partial_j u_i + \partial_i u_j\right)$, we obtain the familiar result

$$\dot{W} = 2\mu \iiint_V dV\, E_{ij} E_{ij}. \tag{6.6}$$

Thus, we can ascertain the dissipation by measuring the fluid velocity field outside of the body,[2,3] or by tracking flagella movements.[4]

6.1.2 Rate independence and scallop theorem

There are two important properties of low Reynolds number propulsion. The first concerns the *dynamics* of surface deformations:

> The distance travelled by a low-Reynolds number swimmer as its surface changes from one configuration to another does not depend on the rate at which the surface deformation occurs, but only on its geometry. For any periodic deformation of a swimmer, the total distance travelled per period is therefore only a function of the sequence of shapes displayed by the swimmer during one period.

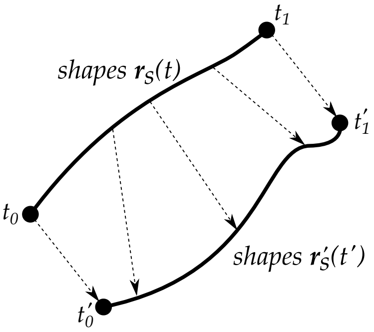

Figure 6.3: Two different paths in shape space.

To establish this, we appeal to Fig. 6.3 where we depict a sequence of shapes $\mathbf{r}_s(t)$ that runs from some time t_0 to t_1, along with a second sequence $\mathbf{r}_s'(t')$ that involves visiting the same shape sequence as $\mathbf{r}_s(t)$ but with a different time parameterization. Thus, as indicated by the dashed arrows, there exists some mapping between any two shape along the sequences. The swimming velocity $\mathbf{U}(t)$ can be expressed as a surface integral of deformation velocity of the shape,

$$\mathbf{U}(t) = \iint_S dS \mathbf{H}(\mathbf{r}_s) \cdot \dot{\mathbf{r}}_s, \tag{6.7}$$

for some tensor $\mathbf{H}(\mathbf{r})$ that does not depend explicitly on time and is found as a solution to the swimming problem.

The total distance travelled is

$$\mathbf{\Delta} = \int_{t_0}^{t_1} dt\, \mathbf{U}(t), \tag{6.8}$$

and the distance along the primed trajectory is

$$\begin{aligned} \mathbf{\Delta}' &= \int_{t_0'}^{t_1'} \mathbf{U}'(t')dt' = \int_{t_0'}^{t_1'} \left[\iint_{S'} dS' \mathbf{H}(\mathbf{r}_s') \cdot \frac{d\mathbf{r}_s'}{dt'}\right] dt' \\ &= \int_{t_0}^{t_1} dt' \left[\iint_{S'} dS \mathbf{H}(\mathbf{r}_s') \cdot \frac{d\mathbf{r}_s'}{dt'}\right] \frac{dt'}{dt} dt \\ &= \int_{t_0}^{t_1} \left[\iint_{S'} dS \mathbf{H}(\mathbf{r}_s) \cdot \frac{d\mathbf{r}_s}{dt}\right] dt = \mathbf{\Delta}, \end{aligned} \tag{6.9}$$

[2] Drescher, K. and Goldstein, R.E. and Michel, N. and Polin, M. and Tuval, I. Direct Measurement of the Flow Field around Swimming Microorganisms. *Phys. Rev. Lett.*, 105:168101, 2010

[3] Guasto, J.S. and Johnson, K.A. and Gollub, J.P. Oscillatory Flows Induced by Microorganisms Swimming in Two Dimensions. *Phys. Rev. Lett.*, 105:168102, 2010

[4] Brumley, D.R., Wan, K.Y., Polin, M. and Goldstein, R.E. Flagellar synchronization through direct hydrodynamic interactions. *eLife*, 3:e02750, 2014

thus proving the rate independence.

The second property of interest is know as the "scallop theorem":

> If a sequence of shapes displayed by a swimmer deforming in a time periodic fashion is identical when viewed under a *time-reversal transformation*, the swimmer cannot move on average.

As first stated by Purcell,[5] this has a key consequence:

> A single degree of freedom *cannot swim* at low Reynolds numbers since one-degree-of-freedom kinematics is necessarily reciprocal.

This is illustrated in Fig. 6.4. Neither (a) a pair of spheres that cyclically move together and apart, nor (b) a hinged object that cyclically opens and closes (i.e. a scallop) can achieve net locomotion. But, (c) a three-link swimmer can swim by following a cycle of shapes.

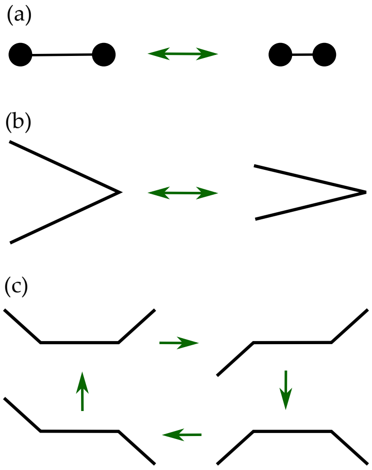

Figure 6.4: Swimming sequences and the scallop theorem.

The need to break time-reversal invariance to achieve locomotion explains the ubiquitous appearance of helical prokaryotic flagella rotated along their long axis or undulating eukaryotic flagella with either sperm-like sinusoidal traveling waveforms (as we saw in our study of wiggling elastica in Sec. 4.3.2), or two distinct phases of beating with very different waveforms. Two classic examples of the latter is shown in Fig. 6.5, taken from the very early study by James Gray of the ciliated gills of the blue mussel *Mytilus edulis*[6] and very recent work on the green alga *Chlamydomonas*.[7] The first phase of a beat cycle is the "power stroke", in which a nearly straight cilium roughly pivots around its attachment point to the underlying tissue or cell, followed by a "recovery stroke" in which the waveform is highly curled and returns to the original position close to the surface.

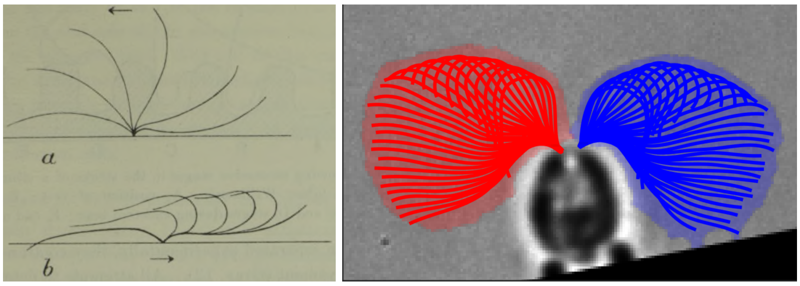

Figure 6.5: Ciliary waveforms. Left panel: sketch of the waveform in the mussel *Mytilus edulis*. (a) Power stroke. (b) Recovery stroke. From Ref. 6. Right panel: flagellar waveforms of the two flagella of *Chlamydomonas reinhardtii*. *Cis* (red) and *trans* (blue) flagella are shown during one complete cycle. From Ref. 7.

6.2 *Flagella and the physics of low-Re propulsion*

First we study the simplest models with which to understand self-propulsion in Stokes flow, including Taylor's "waving-sheet" model, to the approximation known as Resistive Force Theory, Lighthill's analysis of undulating waveforms and the use of RFT to quantify bacterial swimming by rotating helical flagella.

6.2.1 *Taylor's model a single waving sheet*

Inspired by Lord Rothschild's observation[8] that nearby swimming sperm cells synchronised the beating of their flagella, Taylor in 1951[9]

[5] Purcell, E.M. Life at low Reynolds number. *Am. J. Phys.*, 45:1–11, 1977

[6] J. Gray. The mechanism of ciliary movement. *Proc. R. Soc. Lond. B*, 93:104–121, 1922

[7] Leptos, K.C. and Chioccioli, M. and Furlan, S. and Pesci, A.I. and Goldstein, R.E. Phototaxis of *Chlamydomonas* arises from a tuned adaptive photoresponse shared with multicellular Volvocine green algae. *Phys. Rev. E*, 107: 014404, 2023

[8] Rothschild, L. Measurement of Sperm Activity before Artificial Insemination. *Nature*, 163:358–359, 1949

[9] Taylor, G.I. Analysis of the swimming of microscopic organisms. *Proc. R. Soc. A*, 209:447–461, 1951

developed a highly-simplified model for low Reynolds number swimming that consists of a two-dimensionally infinite material sheet in the configuration of a wave of deformation traveling along one direction, as in a carpet with periodic "rucks" (Fig. 6.6). These deformations are a consequence of unspecified internal forces.

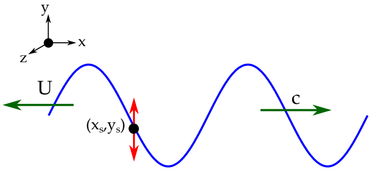

Figure 6.6: Geometry of Taylor's waving sheet model.

Let $\mathbf{x}_s = (x_s, y_s)$ be the coordinates of material points on the sheet, which supports undulations with wavevector k and frequency ω, moving at speed $c = \omega/k$. We expect the sheet is propelled to the left with velocity $\mathbf{U} = -U\hat{\mathbf{e}}_x$, where U is as yet unknown. In the laboratory frame, the fluid is at rest as $y \to \pm\infty$, but in the reference frame moving with the swimming speed the fluid flow far above or below the sheet is $\mathbf{U}_\infty = U\hat{\mathbf{e}}_x$, the x coordinate of a given point will not change, while the y coordinate will simply oscillate up and down as $y_s = B\sin(kx - \omega t)$. We assume the long-wavelength limit $\epsilon \equiv Bk \ll 1$, and use ϵ as the small parameter in a perturbative approach. The frequency and wavevector of the traveling wave serve as natural spatial and temporal scales for nondimensionalising the problem, so the rescaled sheet coordinates are $x_s = x$ and

$$y_s = \epsilon \sin(x - t). \tag{6.10}$$

The problem at hand is to find $\mathbf{u}$ in the half space $y \geq y_s$ (the solution for $y < y_s$ follows from it trivially), subject to two boundary conditions. The first is a connection between the Eulerian description of the flow and the Lagrangian description of the material,

$$\mathbf{u}\big|_{\mathbf{x}_s} = \frac{\partial \mathbf{x}_s}{\partial t} \tag{6.11}$$

Second, the fluid velocity must asymptote to $\mathbf{u} = U\hat{\mathbf{e}}_x$ as $y \to \infty$.

Assuming translational invariance along z, we have a two-dimensional problem (x, y), and introduce a stream function $\psi(x, y)$ such that

$$u_x = \frac{\partial \psi}{\partial y}, \quad u_y = -\frac{\partial \psi}{\partial x}, \tag{6.12}$$

which guarantees the incompressibility condition $\boldsymbol{\nabla} \cdot \mathbf{u} = 0$. (Note this definition of ψ has a minus sign relative to Taylor's choice). The vorticity $\boldsymbol{\omega} = \omega\hat{\mathbf{e}}_z$ is out of the plane and its magnitude satisfies $\omega = -\nabla^2\psi$. Together with the relation $\nabla^2\boldsymbol{\omega} = 0$ from the Stokes equation, we obtain the biharmonic equation for the stream function,

$$\nabla^4\psi = 0. \tag{6.13}$$

We must now solve (6.13) subject to four boundary conditions,

$$u_x(x_s, y_s) = \frac{\partial \psi(x_s, y_s)}{\partial y} = 0, \tag{6.14a}$$

$$u_y(x_s, y_s) = -\frac{\partial \psi(x_s, y_s)}{\partial x} = \frac{\partial y_s}{\partial t} = -\epsilon \cos\phi, \tag{6.14b}$$

$$u_x(x, y \to \infty) = \frac{\partial \psi(x, y \to \infty)}{\partial y} = U, \tag{6.14c}$$

$$u_y(x, y \to \infty) = -\frac{\partial \psi(y \to \infty)}{\partial x} = 0, \tag{6.14d}$$

with the shorthand notation $\phi = x - t$. While the small parameter ϵ appears explicitly in (6.14b), it also appears *implicitly* in both (6.14a) and (6.14b) by virtue of the condition applying at $y_s = \epsilon \sin\phi$.

To solve the above we assume that both ψ and the unknown swimming speed U have regular expansions in ϵ,

$$U = \epsilon U^{(1)} + \epsilon^2 U^{(2)} + \cdots, \qquad \psi = \epsilon\psi^{(1)} + \epsilon^2\psi^{(2)} + \cdots, \tag{6.15}$$

and note that $\nabla^4\psi^{(n)} = 0 \ \forall n$. When expanding the boundary conditions evaluated on the sheet we make use of relationships familiar from the boundary perturbation theory used in Sec. 2.4.2, such as

$$\psi^{(1)}(x_s, y_s) = \psi^{(1)}(x_s, 0) + \epsilon \sin\phi \frac{\partial\psi^{(1)}}{\partial y}(x_s, 0) + \cdots. \tag{6.16}$$

Collecting terms, we find at $\mathcal{O}(\epsilon)$ that

$$\begin{aligned} \frac{\partial\psi^{(1)}}{\partial y}(x,0) &= 0, & \frac{\partial\psi^{(1)}}{\partial x}(x,0) &= \cos\phi, \\ \frac{\partial\psi^{(1)}}{\partial x}(x,\infty) &= 0, & \frac{\partial\psi^{(1)}}{\partial y}(x,0) &= U^{(1)}. \end{aligned} \tag{6.17}$$

The general solution of the biharmonic equation consists of a sum of polynomial terms plus an infinite series of separable solutions,

$$\begin{aligned} \psi =& \psi_0 + ky + Gy^2 + Hy^3 \\ &+ \sum_{n=1}^{\infty} \left[(C_n + D_n y)\, e^{-ny} + (E_n + F_n y)\, e^{ny} \right] e^{in\phi}. \end{aligned} \tag{6.18}$$

The constant ψ_0 is irrelevant, as ψ is only defined up to an arbitrary constant. The term Gy^2 is associated with a shear flow at infinity, which is absent. Absent as well is the Poiseuille-like flow associated with the term Hy^3. The linear term produces a uniform flow at infinity, and we identify $k = U^{(1)}$. In the present case, the forcing from the boundary conditions (6.17) is 2π-periodic, so only the $n = 1$ terms in (6.18) are relevant. Ignoring the growing exponential terms and imposing the boundary conditions (6.17), we find

$$\psi^{(1)} = (1 + y)\, e^{-y} \sin\phi, \quad U^{(1)} = 0. \tag{6.19}$$

There is no swimming speed at this order.

At $\mathcal{O}(\epsilon^2)$ we encounter boundary conditions such as

$$\frac{\partial\psi^{(2)}}{\partial y}(x,0) = -\sin\phi \frac{\partial^2\psi^{(1)}}{\partial y^2}(x,0), \tag{6.20}$$

which are proportional to $\sin^2\phi$. This and the other boundary condition at $(x,0)$ force the system at its first harmonic, leading to

$$\psi^{(2)} = U^{(2)} y + (C_2 + D_2 y)\, e^{-2y} e^{2i\phi}. \tag{6.21}$$

Rather than solve directly for the unknown coefficients, we observe that if we average $\partial\psi^{(2)}/\partial y$ over one wavelength of the traveling wave (and denote the average by angular brackets), the periodic terms give no contribution and thus

$$U^{(2)} = \left\langle \frac{\partial \psi^{(2)}}{\partial y} \right\rangle, \tag{6.22}$$

a relation that holds at *any* value of y. We are free to choose a convenient one, namely $y = 0$ where the boundary condition holds,

$$U^{(2)} = \left\langle \frac{\partial \psi^{(2)}}{\partial y}(x,0) \right\rangle = \left\langle -\sin\phi \frac{\partial^2 \psi^{(1)}}{\partial y^2}(x,0) \right\rangle. \tag{6.23}$$

A simple calculation yields $U^{(2)} = 1/2$, or, in original units,

$$U = \frac{1}{2} c\,(Bk)^2 = \frac{1}{2} B^2 k\omega. \tag{6.24}$$

This is a central result of Taylor's calculation. We conclude: (i) locomotion is possible without inertia, (ii) the swimming speed scales as the square of the wave amplitude, and (iii) to motion is "retrograde", opposite the travelling direction of the wave.

6.2.2 *Taylor's model; two coupled sheets*

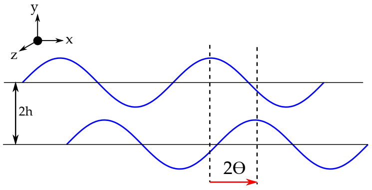

Figure 6.7: Two nearby waving sheets separated on average by $2h$ and with a phase shift Θ.

Taylor was not only interested in the question of propulsion at vanishing Reynolds number, but also in the synchronization of nearby undulating filaments. Following his analysis, we extend the calculation to the case of two nearby sheets separated by a mean distance $2h$ and offset by a phase angle 2Θ, as in Fig. 6.7. Here we quote the essential results, leaving algebraic details to the reader.

Having rescaled x by the wavevector k in (6.10), if the two sheets are separated on average by $2h$, then we define the dimensionless

$$\delta = kh, \tag{6.25}$$

so in these units the sheets are located at

$$\begin{aligned} y &= \delta + y_1 = \delta + \epsilon \sin(\phi + \Theta), \\ y &= -\delta + y_2 = -\delta + \epsilon \sin(\phi - \Theta), \end{aligned} \tag{6.26}$$

where $\phi = x - t$, so the total phase shift is 2Θ. The generalisation of the stream function form (6.18) to the case at hand (for the flow between the sheets) is

$$\begin{aligned} \psi^{(1)} &= (A_1 y \sinh y + B_1 \cosh y) \cos\Theta \sin\phi \\ &\quad + (A_2 y \cosh y + B_2 \sinh y) \sin\Theta \cos\phi. \end{aligned} \tag{6.27}$$

Imposing the boundary condition $\partial\psi^{(1)}/\partial y = 0$ at $y = \pm\delta$ yields

$$\frac{B_1}{A_1} = -(\delta \coth\delta + 1), \quad \frac{B_2}{A_2} = -(\delta \tanh\delta + 1). \tag{6.28}$$

Similarly, imposing the condition $\partial\psi^{(1)}/\partial x = \cos(\phi \pm \Theta)$ at $y = \pm\delta$ yields the pair of conditions

$$A_1 \delta \sinh\delta + B_1 \cosh\delta = 1, \quad A_2 \delta \cosh\delta + B_2 \sinh\delta = 1. \tag{6.29}$$

Solving (6.28) and (6.29) together gives the final results

$$\begin{aligned} A_1 &= -\frac{\sinh\delta}{\sinh\delta\cosh\delta+\delta}, \quad & B_1 &= \frac{\delta\cosh\delta+\sinh\delta}{\sinh\delta\cosh\delta+\delta}, \\ A_2 &= -\frac{\cosh\delta}{\sinh\delta\cosh\delta-\delta}, \quad & B_2 &= \frac{\delta\sinh\delta+\cosh\delta}{\sinh\delta\cosh\delta-\delta}. \end{aligned} \tag{6.30}$$

We focus on the rate of energy dissipation in the system, for which we need the pressure p, which can be obtained by integrating the Stokes equations $\boldsymbol{\nabla} p = \mu\nabla^2\mathbf{u}$. Assuming that the pressure has the same form of expansion as the stream function (6.15), namely $p = \epsilon p^{(1)} + \cdots$, a bit of algebra leads to

$$\frac{p^{(1)}}{2\mu k} = \frac{\sinh y\sinh\delta\cos\Theta\cos\phi}{\sinh\delta\cosh\delta+\delta} - \frac{\cosh y\cosh\delta\sin\Theta\sin\phi}{\sinh\delta\cosh\delta-\delta}, \tag{6.31}$$

which, on the upper surface at $y = \delta$, takes the value

$$\frac{p_1^{(1)}}{2\mu k} = \alpha\cos\Theta\cos\phi - \beta\sin\Theta\sin\phi, \tag{6.32}$$

where

$$\alpha = \frac{\sinh^2\delta}{\sinh\delta\cosh\delta+\delta}, \quad \beta = \frac{\cosh^2\delta}{\sinh\delta\cosh\delta-\delta}. \tag{6.33}$$

The instantaneous rate $\dot{W}$ at which the upper sheet does work on the fluid is $-p(\partial y/\partial t)$, and since both p and y are $\mathcal{O}(\epsilon)$, we expect an expansion of $\dot{W}$ of the form $\dot{W} = \epsilon^2\dot{W}^2 + \cdots$, with

$$\dot{W}^{(2)} = -p_1^{(1)}\frac{\partial y_1}{\partial t}. \tag{6.34}$$

If we user an overbar to denote an average over a temporal cycle of oscillations, and define the (scaled) mean rate of working $\mathcal{W}$ as $\mu k\mathcal{W}^{(2)} = \overline{\dot{W}^{(2)}}$, then we obtain

$$\mathcal{W}(\Theta,\delta) = \alpha + (\beta-\alpha)\sin^2\Theta. \tag{6.35}$$

Since it is evident from (6.33) that $\beta > \alpha$, $\forall\delta$, we deduce that $\mathcal{W}(\Theta,\delta)$ is minimised for $\Theta = 0$; the in-phase synchronised state has the lowest dissipation rate.

Intuitively, since the dissipation rate is a spatial integral of the squares of fluid velocity gradients, it stands to reason that the configuration in which the separation between the sheets is nearly constant throughout the waveform will be less dissipative than states with large thickness variations. This can be made concrete by considering the ratio $\mathcal{R}(\delta) = \mathcal{W}(0,\delta)/\mathcal{W}(\pi/2,\delta))$ of dissipation rates for in-phase and out-of-phase configurations. We find

$$\mathcal{R}(\delta) = \tanh^2\delta\left(\frac{\sinh\delta\cosh\delta-\delta}{\sinh\delta\cosh\delta+\delta}\right), \tag{6.36}$$

which is plotted in Fig. 6.8. This ratio tends to unity at large separation, indicating in that limit that the two sheets do not interact and the dissipation is independent of the phase shift. But for $\delta < 2$ (i.e. $h/\lambda < 1/\pi \sim 0.3$), $\mathcal{R}$ drops to small values, signalling a significant streamlining effect associated with synchronisation.

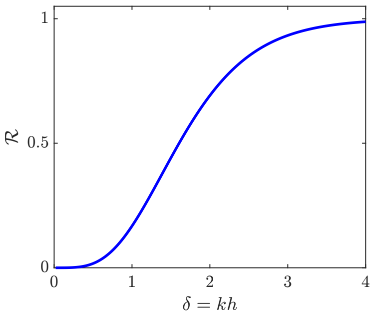

Figure 6.8: Dissipation ratio in Taylor's calculation, as a function of scaled sheet separation. Obtained with `Figure_608_Taylordissipation.m`.

Thus we conclude that *if* nature chooses to minimise the dissipation, then Rothschild's observations are explained. But we should emphasise that while minimisation of dissipation may often hold in dynamical systems, it is not a general principle by which to derive results. Indeed, Taylor's calculation does not actually include any dynamics in the sense of allowing the phase shift itself to evolve under the forces in the system. More recent work[10] shows that introducing elasticity into this problem can lead to an evolution toward synchrony. In Section 6.3 we return to the problem of synchronisation and study in detail a separate class of models that gives insight into synchrony of objects such as cilia and flagella.

6.2.3 *Resistive Force Theory and drag-based thrust*

In our discussion of elastohydrodynamics in Sec. 4.2.1 we introduced the basic ideas of Resistive Force Theory that lead to the general relationships (4.23) and (4.99) between the shape of a filament (given by its tangent vector), its local velocity relative $\mathbf{r}_t$ to any background flow $\mathbf{u}$, and forces acting on it, restated here as a relation for the local force $\mathbf{f}$ acting on the fluid,

$$\mathbf{f} = \left(\zeta_{\parallel}\hat{\mathbf{t}}\hat{\mathbf{t}} + \zeta_{\perp}\left[\mathbb{I} - \hat{\mathbf{t}}\hat{\mathbf{t}}\right]\right)\cdot(\mathbf{r}_t - \mathbf{u}), \tag{6.37}$$

where we will typically assume the large aspect ratio limit $\zeta_{\perp} = 2\zeta_{\parallel}$.

A heuristic argument for drag anisotropy involves recognizing that the action of a slender filament on the fluid velocity can be decomposed into the contributions of a distribution of point forces along the filament.[11] The flow field $\mathbf{u}$ that arises from an elementary point $\mathbf{F}$ is termed a "stokeslet", and the two are linearly related by

$$\mathbf{u}(\mathbf{x}) = \mathbb{G}(\mathbf{x}-\mathbf{x}')\cdot\mathbf{F}, \tag{6.38}$$

where the "Oseen tensor" $\mathbb{G}(\mathbf{r})$ is

$$\mathbb{G}(\mathbf{r}) = \frac{1}{8\pi\mu r}\left(\mathbb{I} + \hat{\mathbf{r}}\hat{\mathbf{r}}\right) \tag{6.39}$$

where $r = |\mathbf{r}|$ and $\hat{\mathbf{r}} = \mathbf{r}/r$ is a unit vector. The intrinsic anisotropy of the stokeslet flow field is seen directly from (6.39) and Fig. 6.9; the flow to the side of a force (where $\mathbf{F}\cdot\hat{\mathbf{r}} = 0$) has magnitude $F/8\pi\mu r$, whereas that in front of the force is $2 \times F/8\pi\mu r$. Furthermore, if we integrate along a filament to obtain the velocity, the relationship will schematically be

$$u \sim \frac{F}{\mu}\int_a^L \frac{1}{r}ds, \tag{6.40}$$

where the filament radius a and length L provide natural cutoffs. One then finds $u \sim (F/\mu)\ln(L/a)$, and hence drag coefficients F/u of the schematic form $\zeta \sim \mu/\ln(L/a)$, consistent with RFT.

We are now in a position to understand the crucial role of drag anisotropy in the generation of net propulsion by both prokaryotic and eukaryotic flagella. In the case of bacteria, propulsion is typically achieved by the rotation of one or more rigid helical flagella by

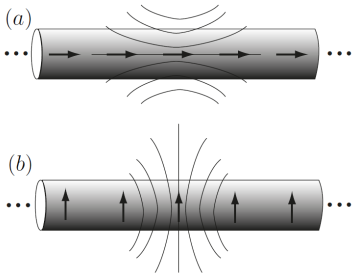

Figure 6.9: Origin of drag anisotropy of slender bodies. (a) Forces along a filament. (b) Forces perpendicular to the long axis of the filament.

---

[10] Elfring, G.J. and Lauga, E. Synchronization of flexible sheets. *J. Fluid Mech.*, 674:163–173, 2011

[11] Keller, J.B. and Rubinow, S.I. Slender-body theory for slow viscous flow. *J. Fluid Mech.*, 75:705–714, 1976

motor proteins embedded in the cell wall. For eukaryotes like spermatozoa and choanoflagellates, the flagellum has a sinusoidal shape deformed by the sliding action of motor proteins along the length of the filament. As shown in Fig. 6.10, in both cases we find segments of the flagellum that are moving down when tilted upward from left to right, and moving up when tilted downward from left to right.

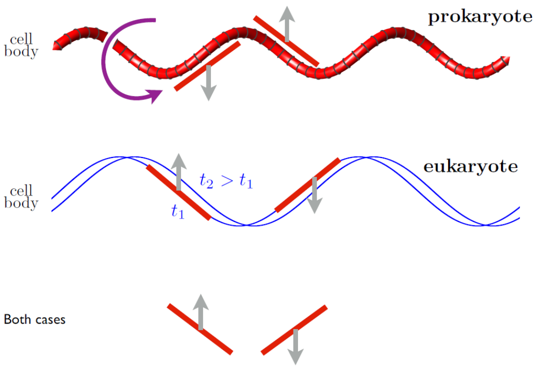

Figure 6.10: Forces due to rotating prokaryotic and undulating eukaryotic flagella.

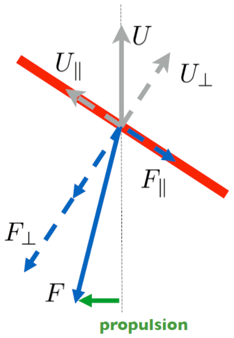

Figure 6.11: Normal and tangential forces on a moving filament segment.

Consider the case shown in Fig. 6.11, and project the upward speed U onto the tangent and normal directions, giving $U_\parallel$ and $U_\perp$. The drag forces $F_\parallel$ and $F_\perp$ are as indicated. The vectorial sum of parallel and perpendicular forces necessarily has a component (shown in green) that is to the left, opposite to the direction of the propagation of the traveling wave of deformation along the filament.

We can verify that this conclusion holds for any inclination angle of the segment by considering a straight segment oriented as in Fig. 6.12. Here, the tangent vector is $\hat{\mathbf{t}} = \left(\cos\theta, \sin\theta\,\hat{\mathbf{e}}_y\right)$ and the segment velocity is $\mathbf{u} = (0, u)$. A simple calculation yields the force

$$\begin{aligned}\mathbf{f} = {} & \left(\zeta_\perp - \zeta_\parallel\right) u \sin\theta\cos\theta\hat{\mathbf{e}}_x \\ & + \left[-\zeta_\perp u + \left(\zeta_\perp - \zeta_\parallel\right) u \sin^2\theta\right]\hat{\mathbf{e}}_y, \qquad (6.41)\end{aligned}$$

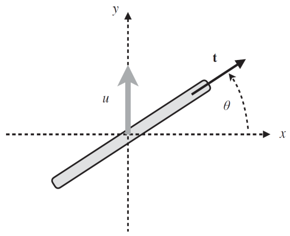

Figure 6.12: A tilted rod segment moving upwards.

and thus $\mathbf{f}\cdot\hat{\mathbf{e}}_x = \left(\zeta_\perp - \zeta_\parallel\right) u \sin\theta\cos\theta$. We deduce that if $u > 0$ and $\sin\theta < 0$ we obtain $\mathbf{r}\cdot\hat{\mathbf{e}}_x < 0$ and if $u < 0$, $\sin\theta > 0$ and again $\mathbf{r}\cdot\hat{\mathbf{e}}_x < 0$; the swimming force component is independent of the sign of u and propulsion is directed forward everywhere. For a helix every point is the same... for a waving flagellum they are different, but all contribute in the same sense.

6.2.4 *Propulsion by a traveling wave of deformation*

Building on the analysis in the previous section, we next seek to understand how drag anisotropy links to the propulsion of flagellar waveforms that exhibit a traveling-wave dynamics, and follow the analysis presented by Lighthill.[12]

In its simplest form the analysis pertains to an infinitely long filament that is characterized by its RFT drag coefficients, the frequency ω and wavelength λ of the traveling waves, as in Fig. 6.13. In the laboratory frame there is an unknown swimming speed $U =$

[12] M.J. Lighthill. *Mathematical Biofluiddynamics*. Society for Industrial and Applied Mathematics, Philadelphia, 1975

$F(\zeta_\perp, \zeta_\parallel, \omega, \lambda, \text{shape})$, where "shape" refers to the detailed waveform. As there is only one natural speed in the problem, $c = \lambda\omega$, we expect

$$\frac{U}{c} = F(\rho, \text{shape}), \tag{6.42}$$

where $\rho = \zeta_\parallel / \zeta_\perp$ and we leave open the possibility (discussed below) that ρ may differ from the usual value $1/2$.

The key to the analysis is a switch to a frame moving at speed $U - c$, in which the undulating filament appears stationary. In this frame points along the curve are moving, and this is possible only if the system is like a conveyor belt in which points move *along* the curve, with the velocity $\mathbf{u}(s$ along the tangent. Because the filament is inextensible, the tangential speed must be the same at all s, and is the wave speed c multiplied by the ratio of arclength to wavelength along one period, $\mathbf{u}(s) = -c(\Lambda/\lambda)\hat{\mathbf{t}}(s)$. Translating back to the laboratory frame, the velocity of points on the filament is

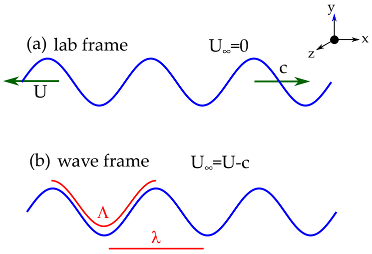

Figure 6.13: Geometry of Lighthill's calculation of propulsion by a slender filament. (a) In the lab frame the filament has traveling waves to the right and swims to the left. (b) In the wave frame the filament is stationary and material points move along the tangent vector.

$$\mathbf{u}(s) = (c - U)\hat{\mathbf{e}}_x - c\frac{\Lambda}{\lambda}\hat{\mathbf{t}}(s). \tag{6.43}$$

Since the force/length on the filament is $\left(\zeta_\perp \mathbb{I} - \left(\zeta_\perp - \zeta_\parallel\right)\hat{\mathbf{t}}\hat{\mathbf{t}}\right) \cdot \mathbf{u}$, the local force component on the filament will be

$$\mathbf{f} \cdot \hat{\mathbf{e}}_x = \zeta_\perp (c - U) - \zeta_\parallel Q\, \hat{\mathbf{t}} \cdot \hat{\mathbf{e}}_x - \left(\zeta_\perp - \zeta_\parallel\right)(c - U)\left(\hat{\mathbf{t}} \cdot \hat{\mathbf{e}}_x\right)^2, \tag{6.44}$$

where $Q = c\Lambda\lambda$. To enforce the condition of zero net force, by integrating (6.44) over one period, we encounter the arclength integrals of $\hat{\mathbf{t}} \cdot \hat{\mathbf{e}}_x$ and $\left(\hat{\mathbf{t}} \cdot \hat{\mathbf{e}}_x\right)^2$. Since $\hat{\mathbf{t}} \cdot \hat{\mathbf{e}}_x = dx(s)/ds$, the first integration trivially yields Λ, but the second integral depends on the precise shape of the filament. Since $\left(\hat{\mathbf{t}} \cdot \hat{\mathbf{e}}_x\right)^2 \leq 1$, we can write the integral as $\beta\Lambda$ for some $\beta \leq 1$. Solving for the speed we obtain

$$\frac{U}{c} = \frac{\left(\zeta_\perp - \zeta_\parallel\right)(1 - \beta)}{\zeta_\perp - \left(\zeta_\perp - \zeta_\parallel\right)\beta} = \frac{(1 - \rho)(1 - \beta)}{1 - (1 - \rho)\beta}. \tag{6.45}$$

The is precisely the form (6.42) anticipated by dimensional analysis, and shows that $U > 0$ for $\rho < 1$ as is the case within RFT; the swimming motion is opposite the wave propagation direction. For typical waveforms one finds $U/c \sim 0.2 - 0.3$, implying a considerable amount of "slip" relative to what one might term the "wood screw" speed c (imagining turning a screw into a piece of wood, where the advancement speed would be precisely the wave speed). If, by some means, $\rho > 1$ then the propulsion speed changes sign. This can happen when a flagellum has fine hairs orthogonal to the main filament, termed "mastigonemes" which at to greatly increase the effective longitudinal drag coefficient.

If we set $y(s) = A \sin ks$ as in Taylor's calculation, and assume $(Ak)^2 \ll 1$, then $1 - \beta \simeq (Ak)^2/2$ and

$$\frac{U}{c} \simeq \frac{1}{2}(Ak)^2, \tag{6.46}$$

in complete agreement with Taylor's result (6.24).

6.2.5 *Bacterial locomotion*

The analysis above provides a relationship between the speed of a traveling wave of deformation moving along a filament and its swimming speed. In this subsection we build on this result to understand the swimming of a bacterium that rotates a helical flagellum. The setup shown in Fig. 6.14 involves a cell swimming at speed U, whose flagellum is rotated by a molecular motor embedded in the cell wall, and whose body rotates in the opposite direction, consistent with a system with no net torque. If we let the body angular speed be Ω and that of the flagellum be $\Omega + \omega$, we seek a relationship between the helical geometry, these frequencies, and the swimming speed U.

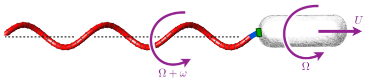

Figure 6.14: Kinematics of bacterial swimming.

We begin by specifying the helix properties as in Fig. 6.15; the filament has diameter $2a$, describes a helix of wavelength λ and radius R, rotating at some angular speed Ω. Because all points on the helix are inclined at the same angle θ with respect to the $x-$axis, we can use the results derived in the context of Fig. 6.12, where the upward speed of the segment shown is $u = -\Omega R$, to deduce that the total drag force acting along x is

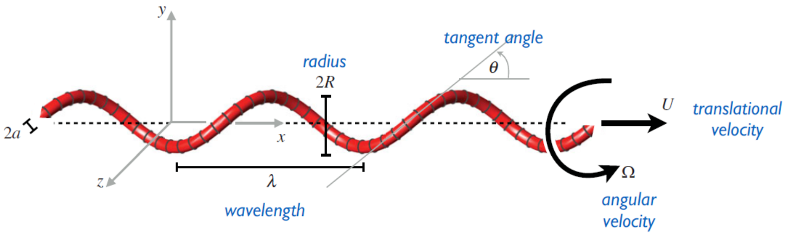

Figure 6.15: Dynamics of a rotating helix.

$$F = f_x L = -\left(\zeta_\perp - \zeta_\|\right) \sin\theta \cos\theta R L \Omega, \tag{6.47}$$

while the total torque along x is

$$T = -f_y R L = -\left(\zeta_\perp \cos^2\theta + \zeta_\| \sin^2\theta\right) R^2 L \Omega. \tag{6.48}$$

For transition along x at speed U the translational drag is

$$F = -\left(\zeta_\perp \sin^2\theta + \zeta_\| \cos^2\theta\right) L U. \tag{6.49}$$

These results can be summarized in a linear relationship between forces and torques on the one hand, and speed and angular speed on the other, of the form

$$\begin{pmatrix} F \\ T \end{pmatrix}_{\text{helix}} = -\begin{pmatrix} A & B \\ B & D \end{pmatrix} \begin{pmatrix} U \\ \Omega \end{pmatrix}_{\text{helix}}, \tag{6.50}$$

where

$$A = \left(\zeta_\perp \sin^2\theta + \zeta_\| \cos^2\theta\right) L, \tag{6.51a}$$

$$B = \left(\zeta_\perp - \zeta_\|\right) \sin\theta \cos\theta R L, \tag{6.51b}$$

$$D = \left(\zeta_\perp \cos^2\theta + \zeta_\| \sin^2\theta\right) R^2 L. \tag{6.51c}$$

Clearly, $A, D > 0$, and if we have a left-handed helix then $\theta > 0$, so $B > 0$. We adopt the common convention that angular speeds are taken to be positive when they appear as clockwise rotations when viewed along the direction of angular velocity. Thus, if $\Omega < 0$ then the propulsive force is in the positive x direction.

The motion of the cell body itself will have a linear relationship of the form (6.51), but with purely diagonal terms in the matrix,

$$\begin{pmatrix} F \\ T \end{pmatrix}_{\text{body}} = -\begin{pmatrix} A_0 & 0 \\ 0 & D_0 \end{pmatrix} \begin{pmatrix} U \\ \Omega \end{pmatrix}_{\text{body}} . \tag{6.52}$$

Next we adopt the simplifying assumption that the dynamical properties of the composite system cell body + flagellum can be obtained by adding the forces and torques that we have separately computed. Apart from the assumptions of RFT, this superposition is also an approximation because it does not take into account the near-field contributions of each part to the flows around the other (this has been done by Higdon.[13] Nevertheless, this simplification has great heuristic value. Within this analysis, we take the angular speed of the helix to be $\Omega + \omega$, and the requirement that the total force and torque vanish can be written as

$$\begin{pmatrix} A_0 & 0 \\ 0 & D_0 \end{pmatrix} \begin{pmatrix} U \\ \Omega \end{pmatrix} + \begin{pmatrix} A & B \\ B & D \end{pmatrix} \begin{pmatrix} U \\ \Omega + \omega \end{pmatrix} = \begin{pmatrix} 0 \\ 0 \end{pmatrix}, \tag{6.53}$$

or, equivalently,

$$\begin{pmatrix} A_0 + A & B \\ B & D_0 + D \end{pmatrix} \begin{pmatrix} U \\ \Omega \end{pmatrix} = -\begin{pmatrix} B\omega \\ D\omega. \end{pmatrix} \tag{6.54}$$

This is readily solved to yield the swimming speed, body rotation frequency and flagellum rotation frequency,

$$U = \frac{BD_0}{B^2 - (A_0 + A)(D_0 + D)}\omega, \tag{6.55a}$$

$$\Omega = \frac{D(A_0 + A) - B^2}{B^2 - (A_0 + A)(D_0 + D)}\omega, \tag{6.55b}$$

$$\Omega + \omega = \frac{D(A_0 + A)}{B^2 - (A_0 + A)(D_0 + D)}\omega. \tag{6.55c}$$

The fact that the energy dissipation in (6.6) is positive leads to the requirement that the matrices in (6.51) and (6.54) be positive definite, and thus $AD - B^2 > 0$ and $(A_0 + A)(D_0 + D) - B^2 > 0$. Experimental observations are that $\omega < 0$ which implies $U > 0$, with $\Omega + \omega < 0$ and $\Omega > 0$, and we therefore conclude that the flagellum and cell body counter-rotate.

The results in (6.55) exhibit an interesting dependence on the flagellar length L. If we consider for simplicity a spherical cell body of radius R_c, with $A_0 = 6\pi\mu R_c$ and $D_0 = 8\pi\mu R_c^3$, and assume $\zeta_\perp = 2\zeta_\parallel = 4\pi\mu/c$, where c is the logarithmic term in (4.21), and rescaling cell radius and flagella length on the helix radius R via

$$\mathcal{U} = \frac{U}{-\omega R}, \quad \tilde{\Omega} = \frac{\Omega}{-\omega}, \quad \rho_c = \frac{R_c}{R}, \quad \ell = \frac{L}{cR}, \tag{6.56}$$

[13] Higdon, J.J.L. The hydrodynamics of flagellar propulsion: helical waves. *J. Fluid Mech.*, 94:331–351, 1979

then the key results in (6.55) can be expressed as

$$\tilde{\mathcal{U}} = \frac{4\ell\rho_c^3 \sin\theta\cos\theta}{[3\rho_c + \ell(1+\sin^2\theta)][4\rho_c^3 + \ell(1+\cos^2\theta)] - \ell^2\sin^2\theta\cos^2\theta}, \tag{6.57a}$$

$$\tilde{\Omega} = \frac{\ell(1+\cos^2\theta)[3\rho_c + \ell(1+\sin^2\theta)] - \ell^2\sin^2\theta\cos^2\theta}{[3\rho_c + \ell(1+\sin^2\theta)][4\rho_c^3 + \ell(1+\cos^2\theta)] - \ell^2\sin^2\theta\cos^2\theta}. \tag{6.57b}$$

Figure 6.16 displays these results for the case $\theta = \pi/6$ and various values of ρ_c. For each cell body size there is an optimum flagellar length for maximum swimming speed, followed by a slow decay in the speed with increasing length. As ℓ increases, the body rotation frequency tends toward the negative of the flagellar rotation frequency, and the net frequency in the laboratory frame vanishes, while at the length of optimum propulsion speed we see $\Omega/(-\omega) \sim 0.3 - 0.6$ for the range of ρ_c considered. As a typical radius R is on the order of a micron, and the factor c in the RFT drag coefficients is ~ 5, the peak length for $\rho_c = 1$ corresponds to a flagellar length of $\sim 15\,\mu$m, which is comparable to that observed in nature.

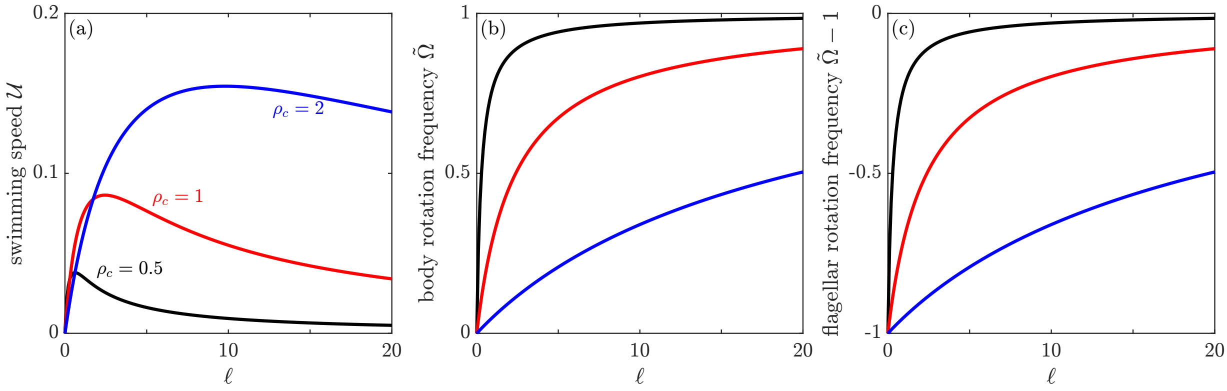

Figure 6.16: Swimming dynamics of a model bacterium, from Eqs. (6.57). Panels display the rescaled (a) swimming speed, (b) cell body rotation frequency, and (c) flagellar rotation frequency in lab frame. Obtained with `Figure_616_bacterialswimming.m`.

In summary, this analysis shows how a combination of the linearity of Stokes flow and the requirements of vanishing force and torque provide the necessary ingredients to determine the swimming and rotation speeds in a model of microorganism locomotion.

6.3 *Models of synchronisation*

In Section 6.2.2 we saw a calculation that suggested that synchronised beating of flagella could arise through a minimum-dissipation principle, but that argument did not provide a dynamical evolution to the state of synchrony. In this section we discuss the pedagogic example of "bead-spring" models that have been developed to study this problem. The analysis leads to a model for the evolution of the phase difference between flagella, and provides interpretable results that can be compared to experiment.

6.3.1 Bead-spring model

When a eukaryotic flagellum moves through its beat cycle it continually exerts a distributed force on the fluid, setting it in motion. That motion in turn creates a distributed force an a second, nearby flagellum, possibly deforming it. A very simple caricature of this dynamics involves representing the flagellum as a single sphere moving on an orbit, exerting a localised force on the fluid and responding to forces from other nearby moving spheres. This idea lies behind a class of "bead-spring" models that has been used to study the problem of synchronisation of flagella. The simplest of these[14] is analytically tractable and *interpretable* in terms of the mechanism of synchronisation, and provides a context within which to study the simplest example of phase dynamics.

The model involves a microsphere of radius a moving along an orbit with instantaneous radius R by the action of a constant tangential force F while connected to the origin by a spring with rest length R_0. Force balance in the tangential and radial directions gives the equations of motion

$$\zeta R\dot{\varphi} = F, \quad \zeta \dot{R} = -\lambda\left(R - R_0\right), \tag{6.58}$$

where λ is the spring constant. The dynamics (6.58) has a trivial fixed point $R = R_0$ and $\omega \equiv \dot{\phi} = F/\zeta R_0$, and we can trade the force F for the product $\zeta R_0 \omega$ in the following.

In the bending of an elastic filament by a localised force at its end, dimensional analysis shows that there is a spring-like response with $\lambda \sim A/L^3$. The drag coefficient would be just that of a sphere in Stokes flow, $\zeta = 6\pi\mu a$. Together, ζ and λ define a relaxation time

$$\tau_\lambda = \frac{\zeta}{\lambda}. \tag{6.59}$$

If we take $a \sim 0.1\,\mu$m, then $\zeta \sim 2 \times 10^{-3}\,pN\cdot$s$/\mu$m, and with $A \sim 4 \times 10^{-22}$N$\cdot$m^2 and $L = 5\,\mu$m (i.e. half the length of a flagellum) we have $\lambda \sim 3\,$pN$/\mu$m, giving $\tau \sim 0.6\,$ms. This can be compared to the beat period of $\sim 20\,$ms for *Chlamydomonas* flagella, showing that we expect elastic relaxation to be fast compared to the orbital motion. This separation of time scales can be used to simplify the analysis.

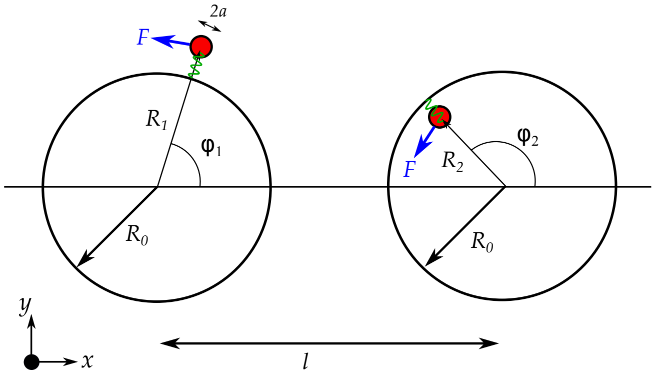

Figure 6.17: Two coupled bead-spring oscillators in the NEL model. Each bead (red circles) is pushed around an orbit by a constant tangential force F and is held by a spring (green) to the equilibrium orbit radius R_0.

Now we generalise the model to two coupled systems whose center-to-center separation is ℓ, as shown in Fig. 6.17. In the coordinate

[14] Niedermayer, T., Eckhardt, B. and Lenz, P. Synchronization, phase locking, and metachronal wave formation in ciliary chains. *Chaos*, 18:037128, 2008

system shown, the position of each of the beads ($i = 1, 2$) and the associated basis vectors are

$$\mathbf{r}_i = R_i(t)\left[\cos\varphi_i(t)\hat{\mathbf{e}}_x + \sin\varphi_i(t)\hat{\mathbf{e}}_y\right] + \delta_{i2}\ell\hat{\mathbf{e}}_x, \tag{6.60}$$
$$\hat{\mathbf{e}}_{r_i} = \cos\varphi_i(t)\hat{\mathbf{e}}_x + \sin\varphi_i(t)\hat{\mathbf{e}}_y, \tag{6.61}$$
$$\hat{\mathbf{e}}_{\varphi_i} = -\sin\varphi_i(t)\hat{\mathbf{e}}_x + \cos\varphi_i(t)\hat{\mathbf{e}}_y. \tag{6.62}$$

The coupled dynamics of the two oscillators generalises (6.58) to account for the fluid flow produced at the sphere 1 due to 2,

$$\zeta\left(R_1\dot{\varphi}_1 - \hat{\mathbf{e}}_{\varphi_1}\cdot\mathbf{v}_{12}\right) = \zeta R_0\omega_1, \tag{6.63}$$
$$\zeta\left(\dot{R}_1 - \hat{\mathbf{e}}_{r_1}\cdot\mathbf{v}_{12}\right) = -\lambda\left(R_1 - R_0\right), \tag{6.64}$$

and likewise for particle 2. Here, we take the flow to be the far-field flow due to a moving sphere,

$$\mathbf{v}_{12} = \frac{\mathbf{s}\cdot\left(\mathbb{I} + \hat{\mathbf{n}}_{12}\hat{\mathbf{n}}_{12}\right)}{|\mathbf{r}_{12}|} + \cdots \tag{6.65}$$

where the vector $\mathbf{r}_{12}$ points from $2 \to 1$ and

$$\mathbf{s} = \frac{3a}{4}\dot{\mathbf{r}}_{12} \simeq \frac{3a}{4}R_2\dot{\varphi}_2\hat{\mathbf{e}}_{\varphi_2}, \tag{6.66}$$

the latter approximation holding under the assumption of small displacements from a circular orbit.

In the "weak-coupling" regime $\ell \gg R$ the terms simplify:

$$\mathbf{r}_{12} \simeq -\ell\hat{\mathbf{e}}_x, \quad |\mathbf{r}_{12}| \simeq \ell, \quad \hat{\mathbf{n}}_{12} \simeq -\hat{\mathbf{e}}_x, \tag{6.67}$$
$$\hat{\mathbf{e}}_{\varphi_1}\cdot\mathbf{s} \simeq \frac{3a}{4}R_2\dot{\varphi}_2\cos(\varphi_1 - \varphi_2), \quad \hat{\mathbf{e}}_{\varphi_1}\cdot\hat{\mathbf{n}}_{12} \simeq \sin\varphi_1, \tag{6.68}$$
$$\mathbf{s}\cdot\hat{\mathbf{n}}_{12} \simeq \frac{3a}{4}R_2\dot{\varphi}_2\sin\varphi_2, \quad \hat{\mathbf{e}}_{\varphi_1}\cdot\mathbf{v}_{12} \simeq -\rho R_2\dot{\varphi}_2 J(\varphi_2, \varphi_2), \tag{6.69}$$
$$\hat{\mathbf{e}}_{r_1}\cdot\mathbf{v}_{12} \simeq \rho R_2\dot{\varphi}_2 K(\varphi_2, \varphi_2), \tag{6.70}$$

where

$$J(\varphi_1, \varphi_2) = -3\cos(\varphi_1 - \varphi_2) + \cos(\varphi_1 + \varphi_2), \tag{6.71}$$
$$K(\varphi_1, \varphi_2) = 3\sin(\varphi_1 - \varphi_2) - \sin(\varphi_1 + \varphi_2), \tag{6.72}$$

and $\rho = 3a/8\ell$ is a scaled measure of the orbital separation. Substituting into the governing equations, we obtain

$$\dot{\varphi}_1 = \frac{R_0}{R_1}\omega_1 - \frac{R_2}{R_1}\rho J(\varphi_1, \varphi_2)\dot{\varphi}_2, \tag{6.73}$$
$$\dot{R}_1 = -\tau_\lambda^{-1}\left(R_1 - R_0\right) + \rho R_2 K(\varphi_1, \varphi_2)\dot{\varphi}_2, \tag{6.74}$$

and likewise for particle 2. If the relaxation time τ_λ is small we can adopt a quasi-steady approximation in which $\dot{R}_1 \simeq 0$, yielding an algebraic relationship for R_1,

$$R_1 \simeq R_0 + \rho\tau_\lambda R_2 K(\varphi_1, \varphi_2)\dot{\varphi}_2. \tag{6.75}$$

This and the equivalent relation for R_2 can now be substituted into the angular dynamics and the result simplified under the assumption that the natural frequencies ω_1 and ω_2 are weakly perturbed by the coupling ρ. The resulting coupled phase dynamics are

$$\dot{\varphi}_1 \simeq \omega_1 - \rho\bar{\omega}J(\varphi_1, \varphi_2) - \rho\tau_\lambda\bar{\omega}^2 K(\varphi_1, \varphi_2), \tag{6.76}$$

$$\dot{\varphi}_2 \simeq \omega_2 - \rho\bar{\omega}J(\varphi_2, \varphi_1) - \rho\tau_\lambda\bar{\omega}^2 K(\varphi_2, \varphi_1), \tag{6.77}$$

where in the coupling terms we have approximated each ω_i by the mean value $\bar{\omega} = (\omega_1 + \omega_2)/2$. The results (6.76) and (6.77) show how the model naturally leads to in-phase synchronisation. Consider the dynamics of the phase difference $\theta = \varphi_1 - \varphi_2$. As $J(\varphi_1, \varphi_2)$ is symmetric under the exchange $1 \to 2$, as is the second term in $K(\varphi_1, \varphi_2)$, the dynamics for θ has a particularly simple form. If we rescale via $T = \bar{\omega}t$ and define

$$\delta = \frac{\Delta\omega}{\bar{\omega}}, \quad \text{and} \quad \gamma = 6\rho\bar{\omega}\tau_\lambda, \tag{6.78}$$

then

$$\theta_T = \delta - \gamma \sin\theta. \tag{6.79}$$

6.3.2 The Adler equation

Equation (6.79) is the fundamental result of the NEL model, and is known as the Adler equation after Robert Adler who first developed it in the context of coupled electronic oscillators.[15] It occupies a prominent place in the general study of phase synchronisation in a broad range of physical and biological systems, from neurons to Josephson junctions. Let us first examine it as a dynamical system.

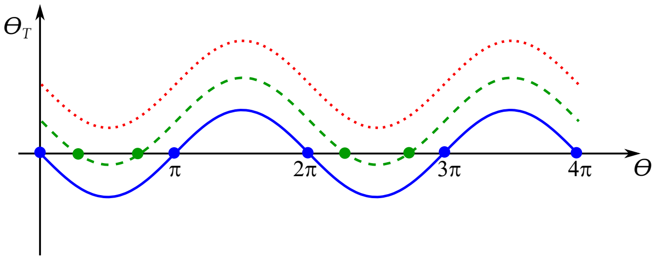

Figure 6.18: Graphical representation of the Adler equation. Curves indicate the r.h.s. of (6.79) for increasing values of $\delta\omega$. Fixed points within the first two periods of $\sin\theta$ are shown by circles.

As shown in Fig. 6.18, the r.h.s of (6.79) supports fixed points at $\theta = n\pi$ for $\delta\omega = 0$, and continues to support two within each interval $[2n\pi, (2n+1)\pi$ for positive $\delta\omega$ up to a critical value $\delta^* = \gamma$, beyond which there are no fixed points. Staying within the first period $[0, 2\pi]$, the fixed points θ^* obey $\theta^* = \sin^{-1}(\delta/\gamma)$. Let us term the smaller of the two θ^*_- and the larger θ^*_+, with $\theta^*_+ = \pi - \theta^*_-$. Small deviations $\psi_\pm$ from each of these obey the linearised dynamics

$$\partial_T \psi_\pm = \pm\sqrt{\gamma^2 - (\delta\omega)^2}\,\psi_\pm + \cdots, \tag{6.80}$$

and thus the smaller root is stable and the latter is unstable; θ^*_- represents stable synchrony. For the special case $\delta = 0$ one can solve exactly the initial value problem to find

$$\theta(T) = 2\tan^{-1}\left(\tan\left(\frac{\theta_0}{2}\right)e^{-\gamma T}\right), \tag{6.81}$$

[15] Adler, R. A Study of Locking Phenomena in Oscillators. *Proc. IEEE*, 61: 1380–1385, 1973

from which we infer that the synchronized state is an attractor for all initial conditions. From the form of γ we see that the time to achieve synchrony can be significantly longer than an orbital period if the oscillators are far apart.

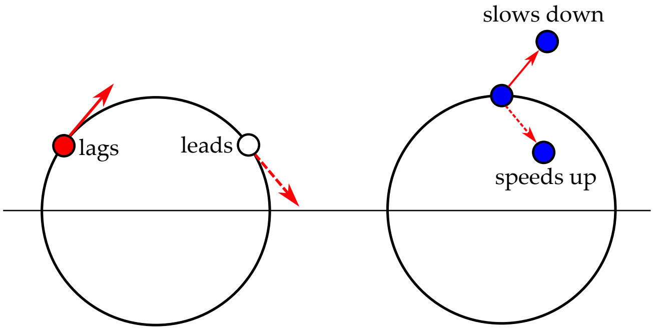

Figure 6.19: Elastohydrodynamic mechanism of synchronisation in the NEL model.

The mechanism of synchronisation can be seen in the diagram in Fig. 6.19, where we consider the effect of the fluid flow produced by particle 1 on particle 2. If 1 lags behind 2, then the flow it produces deflects 2 to a larger orbit. But under the constraint that the internal force F is constant, motion at a larger radius involves a smaller angular velocity $\dot{\varphi}$ to keep the drag force constant, and thus 2 slows down, reducing the lag. Similarly, if 1 leads 2, then the fluid flow pushes 2 to a smaller orbit with a higher angular velocity and 2 speeds up, reducing the lead. Thus, synchronisation in this model involves both hydrodynamical coupling and "waveform compliance".

The Adler equation (6.79) is a gradient flow $\theta_T = -dV(\theta)/d\theta$ in the "tilted washboard" potential

$$V(\theta) = -\delta\theta - \gamma\cos\theta, \tag{6.82}$$

pictured in Fig. 6.20. This connection is significant in light of experimental results shown in Fig. 6.21 on the dynamics of the flagella of *Chlamydomonas reinhardtii*. In these experiments,[16,17] the phase difference is found from the time series of beating flagella by tracking the pixel intensity in small interrogation regions on either side of the cell body (Figs. 6.21(a-l)). In the simplest analysis, the peaks in intensity as flagella move through the regions define the endpoint of each cycle, with the phase angle linearly interpolated in time between.

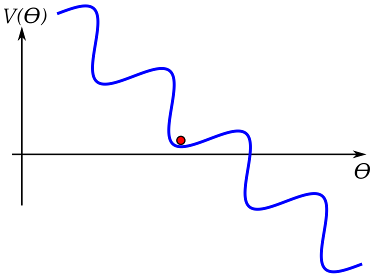

Figure 6.20: Effective potential in the Adler model.

The data in Fig. 6.21(m) on the scaled phase difference $\Delta(t) = (\varphi_1(t) - \varphi_2(t))/2\pi$ shown in blue reveals that within periods of synchrony there are significant fluctuations away from the mean value of Δ (red). A simple calculation shows that the fluctuations observed are too large to arise from timing jitter due to purely equilibrium thermal fluctuations of elastic flagella. The data also show a transition over the course of $\sim 1\,\mathrm{s}$ of the running mean value of Δ by one unit, followed by resynchronisation at that new value. This transition corresponds to the loss of one complete cycle of motion for flagellum 2 relative to flagellum 1. In the language of coupled oscillators this is termed a "phase slip", and corresponds to a transition from one minimum to an adjacent one of the effective potential $V(\theta)$. This kind of

---

[16] Polin, M., Tuval, I., Drescher, K., Gollub, J.P. and Goldstein, R.E. *Chlamydomonas* swims with two 'gears' in a eukaryotic version of run-and-tumble locomotion. *Science*, 325:487–490, 2009

[17] Goldstein, R.E., Polin, M. and Tuval, I. Noise and synchronization in Pairs of Beating Eukaryotic Flagella. *Phys. Rev. Lett.*, 103:168103, 2009

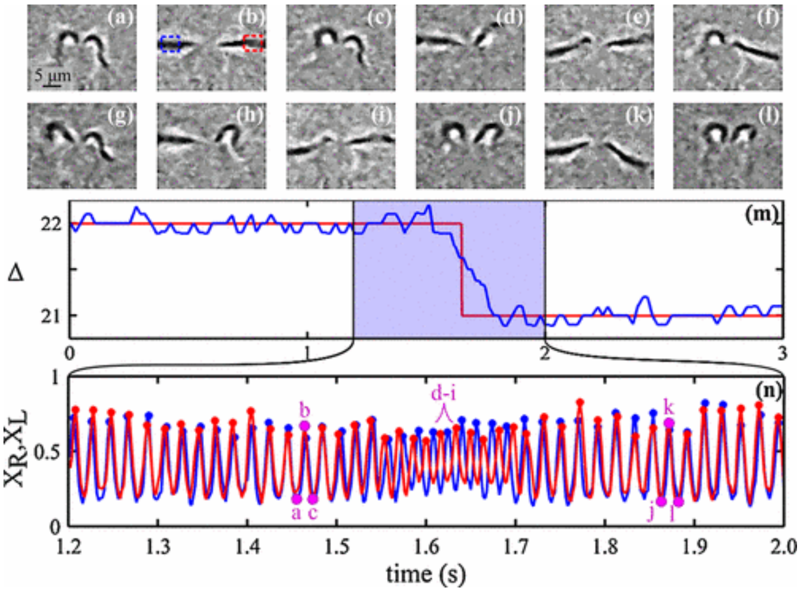

Figure 6.21: Experimental data on flagellar synchronisation in the green alga *Chlamydomonas*, from Ref. 15.

event is not possible within the purely deterministic evolution (6.79) when the potential has truly local minima; it requires some kind of stochastic forcing to provide the energy to hop over the potential energy barrier separating the adjacent minima, as discussed next.

6.3.3 The stochastic Adler equation

In light of these observations, we consider a generalisation of the Adler equation to include random forcing, the Langevin equation

$$\theta_T = -\frac{dV(\theta)}{d\theta} + \xi(t), \tag{6.83}$$

where the noise has the typical properties we discussed in (3.45) of Sec. 3.3, $\langle \xi(t) \rangle = 0$ and $\langle \xi(t)\xi(t') \rangle = 2k_B T_{\text{eff}} \delta(t-t')$, where T_{eff} is some effective temperature. This stochastic Adler equation allows for a heuristic view of synchronisation, in that we can view (6.83) as the overdamped equation of motion of a particle with coordinate θ on the "landscape" defined by $V(\theta)$, subject to noise. Periods of oscillator phase synchrony then correspond to sojourns in one of the minima of V, and the noise induces quasi-thermal fluctuations in a harmonic potential (like the optical trap considered in (5.41) of Sec. 5.2.3 on flicker phenomena of membranes). The linearised dynamics (6.80) around the stable minimum θ_-^* implies that there is an effective harmonic potential there of the form

$$V_{\text{eff}}(\psi) = \frac{1}{2}\sqrt{\gamma^2 - \delta^2}\psi^2. \tag{6.84}$$

It follows from equipartition that the autocorrelation function of ψ is

$$\langle \psi(t)\psi(t') \rangle = \frac{k_B T_{\text{eff}}}{\sqrt{\gamma^2 - (\delta\omega)^2}} e^{-|t-t'|/\tau}, \quad \tau = \frac{1}{\sqrt{\gamma^2 - (\delta\omega)^2}}. \tag{6.85}$$

Phase slips like that shown in the middle panel of Fig. 6.21 are thermally-assisted hops from one minimum of V to an adjacent one, an "activated process" that is well-studied within nonequilibrium statistical physics. Quite generally the rate r of these events is proportional to the Boltzmann factor of the barrier height separating the beginning and final states. Thus, the ratio $R_\pm \equiv p_+/p_-$ of rightward and leftward hops is independent of the proportionality constant and depends only on the energy difference of the two states, which can be read off from (6.82) as $2\pi\delta\omega$, and thus

$$R_\pm = e^{2\pi\delta/T_{\rm eff}}. \tag{6.86}$$

Thus, measurement of (i) the amplitude, (ii) the decay time of the autocorrelation function, and (iii) the relative probability of left-right hopping, provides three relations involving the three parameters of the model $(\gamma, \delta, T_{\rm eff})$, allowing all to be determined from the data.

Finally, we note that the NEL model makes testable predictions regarding the coupling strength due to hydrodynamic interactions. For example, it shows that the coupling constant should vary with flagellar length as $\gamma \sim L^3$; experiments that take advantage of the ability of *Chlamydomonas* to shed and then regrow flagella have been used to confirm this prediction.[18] Second, the dependence of the coupling on the oscillator separation, $\gamma \sim 1/\ell$, a consequence of the hydrodynamical coupling due to stokeslet flows, has been confirmed by examining the interaction between flagella on two separated cells interacting only through the fluid between them.[19]

6.4 *Swimming Cells*

In this section we discuss the representation of swimming cells by force singularities in Stokes flow, setting the stage to discuss the basic features of interactions between swimmers and surfaces.

6.4.1 *Stokeslets*

We begin by recalling the flow field induced by a point force, $\mathbf{u}(\mathbf{x}) = \mathbb{G}(\mathbf{x}-\mathbf{x}')\cdot\mathbf{F}$, with the Oseen tensor

$$\mathbb{G}(\mathbf{r}) = \frac{1}{8\pi\mu r}\left(\mathbb{I} + \hat{\mathbf{r}}\hat{\mathbf{r}}\right), \tag{6.87}$$

where $r = |\mathbf{r}|$ and $\hat{\mathbf{r}} = \mathbf{r}/r$ is a unit vector. We refer to this flow field as a "stokeslet". In terms of components, we have

$$u_i = \frac{F_j}{8\pi\mu}\left(\frac{\delta_{ij}}{r} + \frac{r_i r_j}{r^3}\right), \tag{6.88}$$

so for a force along z, the flow in the $x-z$ plane has components $u_x = (F/8\pi u)xz/r^3$ and $u_z = (F/8\pi\mu)(1/r + z^2/r^3)$, giving rise to the streamlines shown in Fig. 6.22.

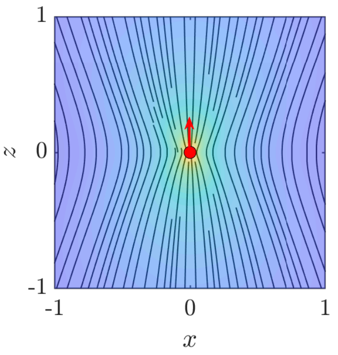

Figure 6.22: Streamlines of a stokeslet at the origin, pointing upwards in the $x-z$ plane. Obtained with `Figure_622_stokeslet.m`.

A biophysical realisation of this flow is seen with an organism like *Volvox* in Figs. 1.2 and 6.1, as its density ρ_V is slightly greater than ρ_w, that of the water it swims through. It is therefore acted on by a downward (negatively) buoyant force

$$\mathbf{F}_b = -\frac{4\pi}{3}\delta\rho_w g R^3 \mathbf{e}_z, \tag{6.89}$$

---

[18] Goldstein, R.E., Polin, M. and Tuval, I. Emergence of Synchronized Beating during the Regrowth of Eukaryotic Flagella. *Phys. Rev. Lett.*, 107:148103, 2011

[19] Brumley, D.R., Wan, K.Y., Polin, M. and Goldstein, R.E. Flagellar synchronization through direct hydrodynamic interactions. *eLife*, 3:e02750, 2014

where the fractional density offset $\delta = (\rho_V - \rho_w)/\rho_w \ll 1$. Inserting typical numbers ($\delta = 0.002$, $R = 200\,\mu$m, and with $\rho_w = 1\,$g/cm^3 and $g = 10\,$m/s^2, we find $|\mathbf{F}_b| \sim 6 \times 10^2\,$pN. This force will balance the viscous drag force $6\pi\mu R u_{\text{settle}}$ to determine the settling speed

$$u_{\text{settle}} = \frac{2}{9}\frac{\delta g R^2}{\nu}, \tag{6.90}$$

where again $\nu = \mu/\rho_w$ is the kinematic viscosity of water, leading to $u_{\text{settle}} \sim 200\,\mu$m/s, consistent with that found experimentally.[20]

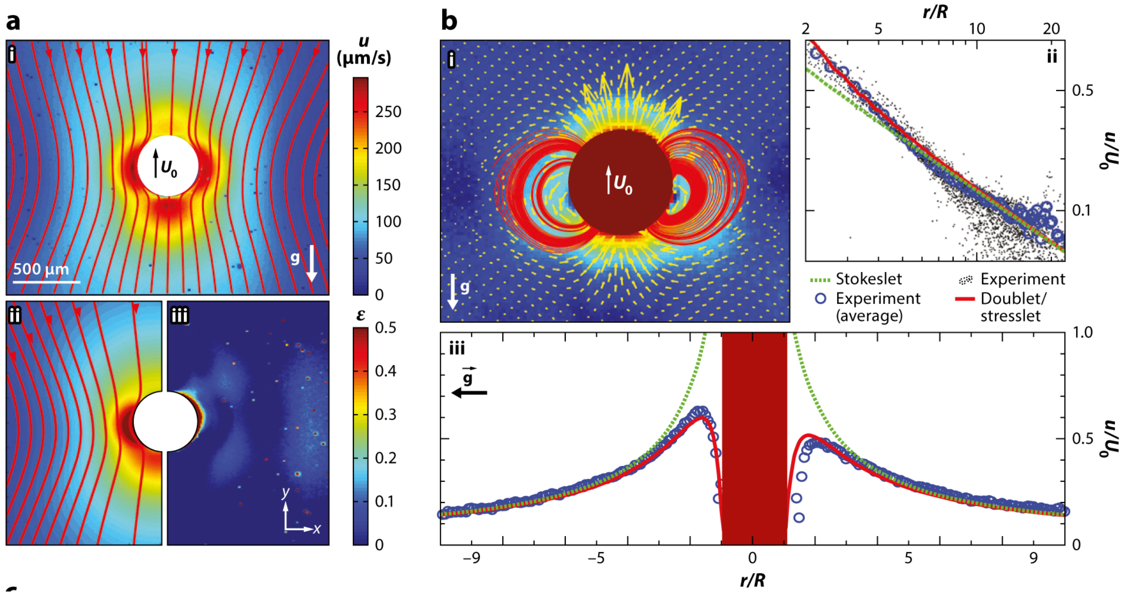

Figure 6.23: Experimentally determined flow field around the alga *V. carteri* algae. From Ref. 2.

Figure 6.23 shows experimental results on the stokeslet flow around *Volvox* colonies from Ref. 2. These include (a) (i) the measured velocity field in the laboratory frame, in terms of streamlines and a heat map of the speed, (ii) a theoretical fit to the stokeslet field and (iii) the very small residuals of the fit. Panels in (b) show the near-field flow, including (i) the magnitude, vector field, and streamlines after subtraction of the stokeslet contribution and (ii) the velocity magnitude along a horizontal cross section through the colony centre. An average stokeslet (green dashed line) follows the observed decay (blue circles) averaged over the sample set (black dots). Deviations from pure stokeslet appear at distances less than $\sim 5R$ and are accounted for by adding higher-order singularities (red solid line). (iii) Vertical section of $\mathbf{u}$ through the centre of a colony, with symbols as in (ii).

6.4.2 *Stresslets and Rotlets*

If there are no body forces such as gravity acting on an organism, the flow around it can not contain any stokeslet contribution and will fall off as $1/r^2$ (or faster), corresponding to force dipoles. From the illustrations in Fig. 6.24, we see that there are two basic types of dipoles. For bacteria and spermatozoa, the head pushed forward on the fluid as the tail pushes backward, while for algae the leading

[20] Drescher, K., Leptos, K.C., Tuval, I., Ishikawa, T., Pedley, T.J. and Goldstein, R.E. Dancing *Volvox*: Hydrodynamic Bound States of Swimming Algae. *Phys. Rev. Lett.*, 102:168101, 2009

flagella push backwards as the trailing body pushes forward. These are, respectively, "pusher" and "puller" dipoles.

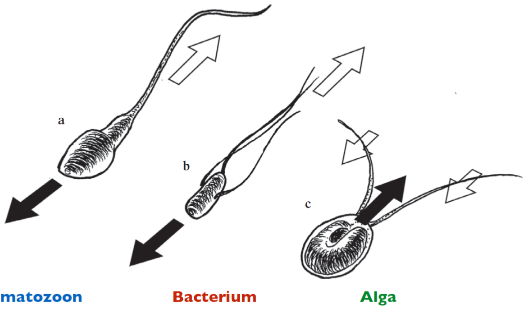

Figure 6.24: Examples of the two types of force-free swimmers described by a force dipole.

To understand the flows produced by pushers and pullers, we consider two forces separated by the vector $\epsilon\ell\mathbf{d}$, where ϵ is a small order-counting parameter. We adopt a temporary notation in which $\mathbf{G}(\mathbf{r};\mathbf{e})$ is the flow at $\mathbf{r}$ due to a force along $\mathbf{e}$. If we choose the origin O as indicated in Fig. 6.25, then the induced fluid flow is

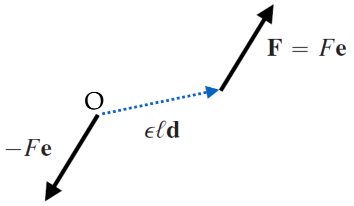

Figure 6.25: A force dipole.

$$\begin{aligned}\mathbf{u}(\mathbf{r}) &= F\mathbf{G}(\mathbf{r}-\epsilon\ell\mathbf{d};\mathbf{e}) - F\mathbf{G}(\mathbf{r};\mathbf{e}) \\ &\simeq -\epsilon\ell F\,(\mathbf{d}\cdot\boldsymbol{\nabla})\,\mathbf{G}(\mathbf{r};\mathbf{e}) + \mathcal{O}(\epsilon^2), \end{aligned} \tag{6.91}$$

where the second relation follows from a Taylor expansion. Setting $\mathcal{P} = \epsilon\ell F$ to be the dipole strength, we may write

$$\mathbf{u}_{\text{dipole}}(\mathbf{r};\mathbf{e},\mathbf{d}) = -\mathcal{P}\mathbf{d}\cdot\boldsymbol{\nabla}\mathbf{G}(\mathbf{r};\mathbf{e}). \tag{6.92}$$

A simple calculation shows that

$$\boldsymbol{\nabla}\mathbf{G}(\mathbf{r};\mathbf{e}) = \frac{1}{8\pi\mu}\left[\underbrace{\frac{(\mathbf{d}\times\mathbf{e})\times\mathbf{r}}{r^3}}_{\substack{\text{antisymmetric:}\\ \mathbf{e}\leftrightarrow\mathbf{d}}} - \underbrace{\frac{(\mathbf{d}\cdot\mathbf{e})\mathbf{r}}{r^3} + \frac{3(\mathbf{e}\cdot\mathbf{r})(\mathbf{d}\cdot\mathbf{r})\mathbf{r}}{r^5}}_{\substack{\text{symmetric:}\\ \mathbf{e}\leftrightarrow\mathbf{d}}}\right], \tag{6.93}$$

where the symmetry of the terms under exchange of $\mathbf{e}$ and $\mathbf{d}$ are indicated. separating terms with differing symmetries, we identify

$$\mathbf{u}^{\text{antisym}}_{\text{dipole}}(\mathbf{r};\mathbf{e},\mathbf{d}) = \frac{\mathcal{P}}{8\pi\mu}\frac{(\mathbf{d}\times\mathbf{e})\times\mathbf{r}}{r^3}, \tag{6.94a}$$

$$\mathbf{u}^{\text{sym}}_{\text{dipole}}(\mathbf{r};\mathbf{e},\mathbf{d}) = \frac{\mathcal{P}}{8\pi\mu}\left(\frac{3(\mathbf{e}\cdot\mathbf{r})(\mathbf{d}\cdot\mathbf{r})\mathbf{r}}{r^5} + \frac{(\mathbf{d}\cdot\mathbf{e})\mathbf{r}}{r^3}\right). \tag{6.94b}$$

We analyze the contributions (6.94) in turn. Recall that the Stokes flow around and viscous torque due to a sphere of radius a rotating with angular velocity $\boldsymbol{\Omega}$ are

$$\mathbf{u} = \frac{a^3}{r^3}\boldsymbol{\Omega}\times\mathbf{r}, \quad \text{and} \quad \mathbf{T} = 8\pi\mu a^3\boldsymbol{\Omega}. \tag{6.95}$$

If we substitute the second relation into the first to eliminate reference to the sphere, we obtain the "rotlet" flow $\mathbf{u}_R(\mathbf{r};\mathbf{T})$, defined as the flow due to a point torque $\mathbf{T}$,

$$\mathbf{u}_R(\mathbf{r};\mathbf{T}) = \frac{1}{8\pi\mu}\frac{\mathbf{T}\times\mathbf{r}}{r^3}, \quad \text{with} \quad \mathbf{T} = \mathcal{P}\mathbf{d}\times\mathbf{e}. \tag{6.96}$$

Rotlet flows arise when external torques act on swimmers, such as when bacteria with internal magnetic particles swim in the earth's magnetic field, but free-swimming cells have no associated rotlet. Instead, as we have seen in Sec. 6.2.5 in the analysis of the composite system of a bacterial cell + flagellum, the requirement of zero torque leads to counter-rotation of the two components. This feature is captured by a *rotlet dipole*, whose flow field falls off as $1/r^3$.

The symmetric contribution in (6.94) is a particular case of the most general far-field flow[21] due to a torque-free and force-free body,

$$\mathbf{u}_S(\mathbf{r};\mathbb{S}) = -\frac{3}{8\pi\mu}\frac{(\mathbf{r}\cdot\mathbb{S}\cdot\mathbf{r})\,\mathbf{r}}{r^5} \sim \frac{1}{r^2}, \tag{6.97}$$

where $\mathbb{S}$ is symmetric and trace-free. Here, the "stresslet" tensor is

$$\mathbb{S} = \mathcal{P}\left[\frac{1}{3}(\mathbf{d}\cdot\mathbf{e})\,\mathbb{I} - \frac{1}{2}(\mathbf{ed}+\mathbf{de})\right]. \tag{6.98}$$

In the symmetric limit $\mathbf{e}=\mathbf{d}$, we have $\mathbb{S} = \mathcal{P}\left(\frac{1}{3}\mathbb{I} - \mathbf{ee}\right)$ and

$$\mathbf{u}_S(\mathbf{r}) = \frac{\mathcal{P}}{8\pi\mu}\left(\frac{3(\mathbf{e}\cdot\mathbf{r})^2}{r^5} - \frac{1}{r^3}\right)\mathbf{r}, \tag{6.99a}$$

$$= \frac{\mathcal{P}}{8\pi\mu}\left(\frac{3\cos^2\theta - 1}{r^2}\right)\hat{\mathbf{e}}_r \tag{6.99b}$$

where the second form is expressed in terms of the polar angle θ from the dipole axis. $\mathcal{P} > 0$ for pushers and $\mathcal{P} < 0$ for pullers, and as expected, the flow falls off as r^{-2} in all directions. Figure 6.26 shows the flows fields for pushers and pullers. The streamline geometry is the same in the two cases, only the direction of motion along them switches. A characteristic feature of the flows is the nodal lines at angles θ_n such that $\cos^2\theta_n = 1/3$ or $\theta_n \simeq \pm 54.7°$.

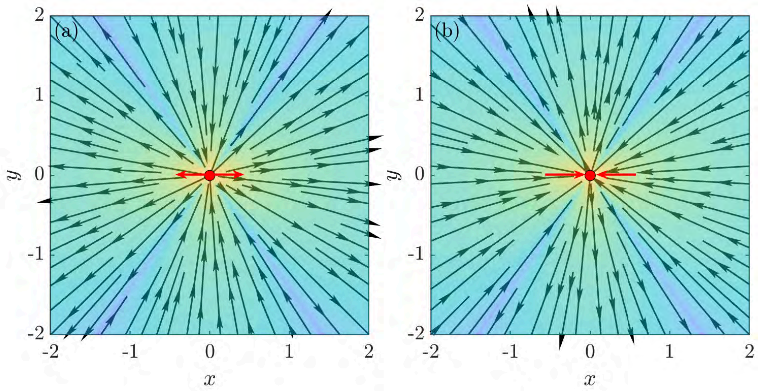

Figure 6.26: Streamlines and vector field of stresslet flows for (a) pushers and (b) pullers. Red arrows indicate directions of forces comprising the dipoles. Obtained with `Figure_626_stresslets.m`.

These results can be compared to experimental measurements of the flow field around individual freely-swimming *E. coli* bacteria shown in Fig. 6.27.[22] These data were obtained by tracking the motion of micron sized tracer spheres around individual cells swimming in the focal plane of the microscope to obtain short traces of the fluid velocity field, and then averaging over a very large number of traces rotated to align the cellular axis in a common direction. The

---

[21] Batchelor, G.K. Slender-body theory for particles of arbitrary cross-section in Stokes flow. *J. Fluid Mech.*, 44:419–440, 1970

[22] Drescher, K., Dunkel, J., Cisneros, L.H., Ganguly, S. and Goldstein, R.E. Fluid dynamics and noise in bacterial cell-cell and cell-surface scattering. *Proc. Natl. Acad. Sci. USA*, 108:10940–10945, 2011

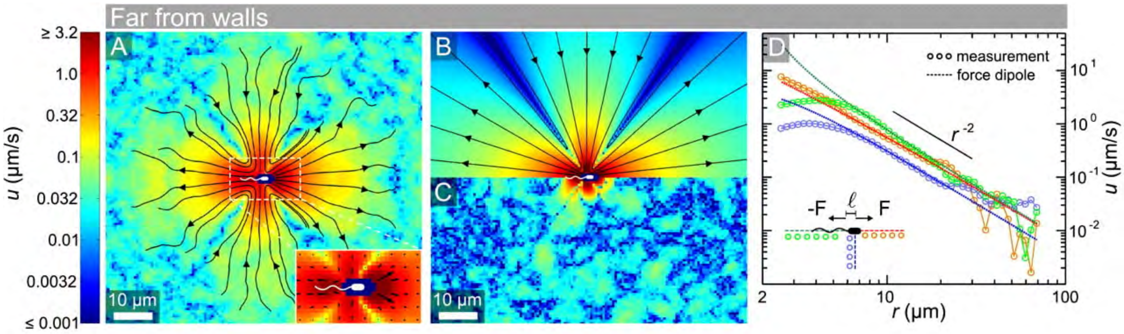

Figure 6.27: Experimentally determined flow field around *E. coli.* (A) Flow field in the frame of reference of the swimming cells. (B) Theoretical stresslet flow field and (C) residuals of the data after subtracting it from the data, showing now systematic trends. (D) Decay of the magnitude of the velocity field in three different directions away from the cell. From Ref. 22.

flow field displays the characteristic topology—forward of the cell body, backward from the flagella, and inward on each side—as well as the $1/r^2$ falloff in magnitude expected from a stresslet. Fitting the data to the theoretical result of two oppositely-directed point forces of magnitude F and separation ℓ yields the values $F = 0.42\,\mathrm{pN}$ and $\ell = 1.9\,\mu\mathrm{m}$, which are consistent with the cell geometry.

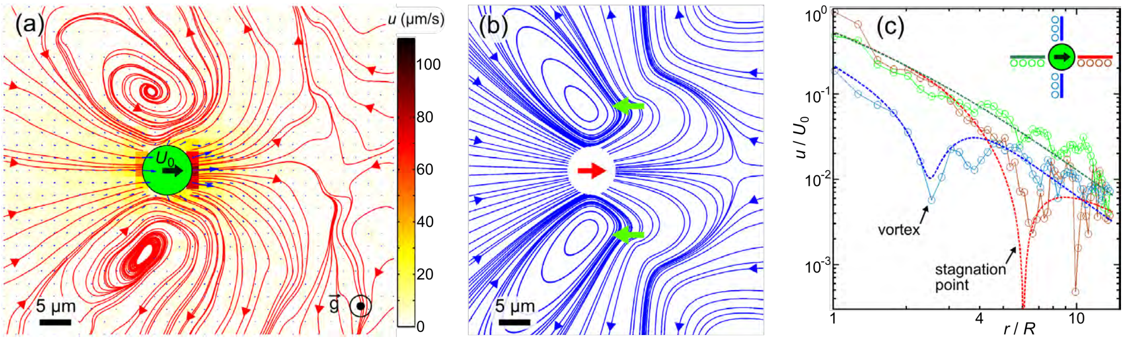

Figure 6.28: Experimentally determined flow field around the alga *C. reinhardtii*. From Ref. 20.

Similar methods can be applied to understand the flow field around a puller organism like *Chlamydomonas*. Figure 6.28 shows the results of such a study, where by the nature of the algorithm the flow that is captured is time-averaged over the flagellar beating. As expected for a puller stresslet, the far-field flow is inward toward both the front and the back of the organism and is outward from the sides, just the opposite of the bacterial flow field. But closer to the cell the near-field is significantly different, with a stagnation point near the front and eddy-like circulation due to the flagella. The overall topology of the flow field is captured by a superposition of three stokeslets, one pointing forward at the cell body, and one each at the middle of the flagella, pointing backwards (with the vectorial sum of the three vanishing). The flow magnitude falls off as $1/r^2$.

6.5 *Microswimmers in External Fields and Flows*

In this section we consider examples of microswimmers in external fields and flows. Moving beyond the simplest effect of gravity, which leads to a net force on a swimmer, we consider the torque associated with unequal mass distribution in an organism, and then combine this with net swimming motions and the effects of fluid vorticity and shear to arrive at a general model for swimmers in flows.

6.5.1 Bottom-Heavy Swimmers

Many of the organisms of interest in biological fluid dynamics have a complex internal distribution of material, such that, as shown in Fig. 6.29, the centre of buoyancy of the organism and its centre of gravity are not coincident, like a ship with a heavy keel. Recognition of the consequences of this feature in algal systems was first made by Kessler[23] and studied in detail by Pedley and Kessler.[24]

As in the figure, we introduce the unit vector $\mathbf{p}$ that points along the major axis of the cell. In the case of an alga like *Chlamydomonas*, $\mathbf{p}$ lies between the two flagella. The displacement of the centre of gravity G from the centre of buoyancy C is taken to be $-h\mathbf{p}$, where h is a small distance. If the colony is tilted from the vertical by an angle θ, then the torque about the centre of mass of the colony is $V\rho_c hg\sin\theta$, where $V = 4\pi R^3/3$ is the colony volume. Balancing this torque against the rotational drag on the sphere, with drag coefficient $\zeta_r = 8\pi\mu R^3$, we obtain the equation of motion

$$\dot{\theta} = -\frac{1}{\tau_{bh}}\sin\theta, \tag{6.100}$$

where the *bottom-heaviness relaxation time* is

$$\tau_{bh} = \frac{6\mu}{\rho_c gh} \sim \frac{6\nu}{g\ell}. \tag{6.101}$$

In the second relation we have used the fact that the colony density is typically very close to water, and thus μ/ρ_c is close to the kinematic viscosity $\nu = 10^6\ \mu\text{m}^2/\text{s}$ of water. As $g = 10^7\ \mu\text{m/s}^2$ in our favourite system of units, we see that a submicron scale of ℓ yields relaxation times of a few seconds, as seen experimentally. The angular dynamics (6.100) can be recast as an equation for $\mathbf{p}$,

$$\dot{\mathbf{p}} = \frac{1}{\tau_{bh}}\mathbf{p}\times(\mathbf{e}_z\times\mathbf{p})\,. \tag{6.102}$$

a formulation that preserves $\mathbf{p}$ as a unit vector.

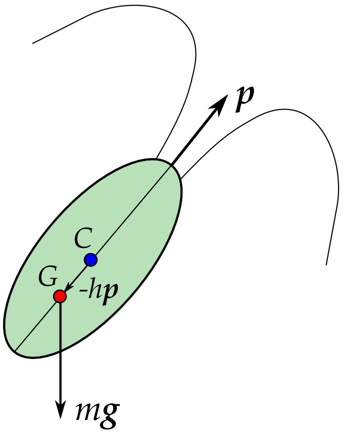

Figure 6.29: Geometry of a biflagellated bottom-heavy swimmer. Centre of gravity (G) differs from centre of buoyancy (C).

6.5.2 Swimmers in flows

Now we ask how a swimming cell responds to ambient fluid flows. Cells can of course respond *passively* through their shape, and *actively* by changing the actuation of their appendages in response to the local flow. Here we consider only the former, and assume that the cell is characterised by its swimming speed U in the direction set by its instantaneous axis vector $\mathbf{p}$ and ignore any intrinsic rotational motion. In the regime of low Reynolds number (and implicitly in the regime of low Stokes number, where particle inertia is sufficiently small that they follow streamlines), we expect that the center of mass of the cell is also advected by the flow $\mathbf{u}(\mathbf{r})$ at the location $\mathbf{r}(t)$, and the equation of motion of the particle would be

$$\dot{\mathbf{r}} = U\mathbf{p} + \mathbf{u}(\mathbf{r}), \tag{6.103}$$

[23] Kessler, J.O. Gyrotactic buoyant convection and spontaneous pattern formation in algal cell cultures. In M.G. Velarde, editor, *Nonequilibrium Cooperative Phenomena in Physics and Related Fields*, pages 241–248. Plenum Press, New York, 1984

[24] Pedley, T.J. and Kessler, J.O. The orientation of spheroidal microorganisms swimming in a flow field. *Proc. R. Soc. Lond. B*, 231:47–70, 1987

where $\mathbf{u}(r)$ is the flow evaluated at the centre of mass of the particle. The subtlety in this approach is that the presence of the particle will disturb the flow, so even in the simple situation where we specify a flow field $\mathbf{u}_\infty(\mathbf{r})$ far away from the cell it is unclear the level of approximation entailed in setting $\mathbf{u}(\mathbf{r}) = \mathbf{u}_\infty(\mathbf{r})$.

A systematic approach to this is given by Faxén's laws,[25] whose derivation we summarise below (see also Ref. 1, Sec. 10.1). We assume that the flow $\mathbf{u}_\infty$ is that specified in the absence of the swimmer, and that in the absence of the flow a rigid spherical swimmer moves with velocity $\mathbf{U}_s$ and angular velocity $\mathbf{\Omega}_s$ For a rigid swimmer, the principle of superposition is valid, so that if $\mathbf{U}_f$ and $\mathbf{\Omega}_f$ are the velocities due to the flow, then the total velocities are

$$\mathbf{U} = \mathbf{U}_s + \mathbf{U}_f, \tag{6.104a}$$

$$\mathbf{\Omega} = \mathbf{\Omega}_s + \mathbf{\Omega}_f. \tag{6.104b}$$

We seek to express $\mathbf{U}_f$ and $\mathbf{\Omega}_f$ in terms of $\mathbf{u}_\infty$.

A useful starting point is the "reciprocal theorem" of Stokes flow, which states that if we have two solutions $\bar{\mathbf{u}}$ and $\hat{\mathbf{u}}$ of the incompressible Stokes equations with no body forces inside the fluid, associated respectively with stress tensors $\bar{\sigma}$ and $\hat{\sigma}$, then the virtual rates of work of one flow on the other are equal, and with $\mathbf{n}$ the outward sphere normal,

$$\int dS\, \bar{\mathbf{u}} \cdot \hat{\sigma} \cdot \mathbf{n} = \int dS\, \hat{\mathbf{u}} \cdot \bar{\sigma} \cdot \mathbf{n}, \tag{6.105}$$

so long as there are no contributions at infinity. This theorem has broad applicability in Stokes flow; the art of using it centres around the choice of the two solutions. Here, we choose the solution $(\hat{\mathbf{u}}, \hat{\sigma})$ to be that of a rigid body moving with instantaneous velocity $\hat{\mathbf{U}}$ and angular velocity $\hat{\mathbf{\Omega}}$, associated with boundary conditions on the swimmer (where $\mathbf{r} = \mathbf{r}_s$),

$$\hat{\mathbf{u}}(\mathbf{r}_s) = \hat{\mathbf{U}} + \hat{\mathbf{\Omega}} \times \mathbf{r}_s. \tag{6.106}$$

Next, choose $\bar{\mathbf{u}} = \mathbf{u} - \mathbf{u}_\infty$, namely the perturbation away from the external flow. This conveniently vanishes at infinity and has the boundary condition

$$\bar{\mathbf{u}}(\mathbf{r}_s) = \hat{\mathbf{U}}_f + \hat{\mathbf{\Omega}}_f \times \mathbf{r}_s - \mathbf{u}_\infty(\mathbf{r}_s). \tag{6.107}$$

As $\hat{\mathbf{u}}$ is the flow associated with the swimmer translating and rotating, the right-hand-side of (6.105) us just $\hat{\mathbf{U}} \cdot \bar{\mathbf{F}} + \hat{\mathbf{\Omega}} \cdot \bar{\mathbf{T}}$, with $\bar{\mathbf{F}}$ and $\bar{\mathbf{T}}$ the net forces and torques on the sphere governed by the $\bar{\mathbf{u}}$ flow. These are identically zero, as is therefore the r.h.s. of (6.105).

Turning to the l.h.s. of (6.105), and noting that for a sphere of radius a in rigid-body motion

$$\hat{\sigma} \cdot \mathbf{n} = -\frac{3\mu}{2a}\hat{\mathbf{U}} - 3\mu\hat{\mathbf{\Omega}} \times \mathbf{n}, \tag{6.108}$$

one finds from the arbitrariness of $\hat{\mathbf{U}}$ and $\hat{\mathbf{\Omega}}$ that $\int dS\, \bar{\mathbf{u}} = \mathbf{0}$ and $\int dS\, \mathbf{n} \times \bar{\mathbf{u}} = \mathbf{0}$. From the boundary conditions and the identities

[25] Faxén, H. Der Widerstand gegen die Bewegung einer starren Kugel in einer zähen Flüssigkeit, die zwischen zwei parallelen ebenen Wänden eingeschlossen ist. *Ann. Phys.*, 373:89–119, 1922

$\int dS\,\mathbf{n} = \mathbf{0}$ and $\int dS\,\mathbf{nn} = (4\pi a^2/3)\mathbb{I}$ we then obtain

$$\mathbf{U}_f = \frac{1}{4\pi a^2}\int dS\mathbf{u}_\infty, \tag{6.109a}$$

$$\boldsymbol{\Omega}_f = \frac{3}{8\pi a^3}\int dS\mathbf{n}\times\mathbf{u}_\infty. \tag{6.109b}$$

These very powerful results express the kinematics of a rigid moving sphere in terms of the imposed flow (not the actual flow), evaluated on its surface. Importantly, that imposed flow is defined everywhere in space, including inside the sphere.

Recalling that we wish to relate the motion of the sphere to the value of the fluid velocity at its centre, while (6.109a) requires it on the sphere surface, we Taylor expand the velocity around the centre. By symmetry the relevant terms involve higher and higher order contributions of the form $\nabla^{2n}\mathbf{u}_\infty$, which all vanish for $n \geq 2$ by the Stokes equation, leaving a simple relation between the translational velocity and the external flow evaluated at the particle position. This leads leads to the positional dynamics

$$\dot{\mathbf{r}} = \mathbf{U}_s + \mathbf{u}_\infty(\mathbf{r}) + \frac{a^2}{6}\nabla^2\mathbf{u}_\infty(\mathbf{r}). \tag{6.110}$$

The final term is generally of order $(a/L)^2$, where L is the length scale for gradients of the fluid velocity, and can be neglected in most applications where the confining geometry is large compared to the particle size. We shall henceforth ignore it.

The final result for the motion of a spherical particle concerns its angular velocity as given by (6.109b). Applying the divergence theorem to the surface integral and noting that the vorticity $\boldsymbol{\omega} = \boldsymbol{\nabla}\times\mathbf{u}$ is harmonic in Stokes flow, the mean value theorem for the Laplacian (the mean value of a harmonic function over a sphere is its value at the centre) leads to the result

$$\boldsymbol{\Omega}_f = \frac{1}{2}\boldsymbol{\nabla}\times\mathbf{u}_\infty(\mathbf{r}). \tag{6.111}$$

We conclude that the evolution equation for the orientation vector of a spherical particle, the partner relation to (6.110), is

$$\dot{\mathbf{p}} = \frac{1}{2}\left(\boldsymbol{\nabla}\times\mathbf{u}_\infty(\mathbf{r})\right)\times\mathbf{p}. \tag{6.112}$$

Already in our discussion of the instability of semiflexible filaments under compressional flows (Fig. 4.19) we saw that elongated objects can rotate in flows that lack vorticity but instead have a finite rate-of-strain. This implies that there must be an additional contribution to the evolution equation for $\mathbf{p}$ beyond that in (6.112). It also raises the question of whether for elongated self-propelled swimmers there is an additional contribution beyond (6.110). A careful analysis[26] of these questions is summarized below.

To begin, we define $\mathbf{x}_c(t)$ to be the position of the centre of a rod of length L, parameterized by arclength $s \in (-L/2, L/2)$ relative to that centre. Choosing the orientation vector $\mathbf{p}$ to lie along the rod's

[26] Hohenegger, C. and Shelley, M. J. Dynamics of complex biofluids. In *New Trends in the Physics and Mechanics of Biological Systems: Lecture Notes of the Les Houches Summer School: Volume 92, July 2009*. Oxford University Press, 2011

tangent, a point on the rod is at $\mathbf{x}_c(t) + s\mathbf{p}$ and its velocity is

$$\mathbf{u}_{\text{rod}}(s,t) = \dot{\mathbf{x}}_c + s\dot{\mathbf{p}}. \tag{6.113}$$

It must also be the case that this velocity is expressible in terms of the values of the flow-induced velocities $\mathbf{U}_f$ and $\mathbf{\Omega}_f$ via

$$\mathbf{u}_{\text{rod}}(s,t) = \mathbf{U}_f + \mathbf{\Omega}_f \times (s\mathbf{p}). \tag{6.114}$$

Our goal is to find $\dot{\mathbf{x}}_c (= \mathbf{U}_f)$ and $\dot{\mathbf{p}} (= \mathbf{\Omega}_f \times \mathbf{p})$.

We assume that the imposed velocity varies linearly in space,

$$\mathbf{u}_\infty(\mathbf{r}) = \mathbb{A} \cdot \mathbf{r}, \tag{6.115}$$

where the constant tensor $\mathbb{A}$ is trace-free. The motion of a self-propelled rod is described within resistive force theory as discussed in (4.23) and (4.99) in the context of filament motion, so that the hydrodynamic force density along the filament is

$$\mathbf{f}(s,t) = -\left[\zeta_\parallel \mathbf{pp} + \zeta_\perp (\mathbb{I} - \mathbf{pp})\right] \cdot \left[\mathbf{u}_{\text{rod}}(s,t) - \mathbf{u}_\infty(\mathbf{x}_c + s\mathbf{p})\right]. \tag{6.116}$$

Given our assumptions, the final bracketed term in (6.116) is

$$\dot{\mathbf{x}}_c - \mathbb{A} \cdot \mathbf{x}_c + s(\dot{\mathbf{p}} - \mathbb{A} \cdot \mathbf{p}). \tag{6.117}$$

The requirement that the rod is overall force-free is $\int_{-L/2}^{L/2} \mathbf{f} = \mathbf{0}$, and since the drag tensor is constant, we can see that the term linear in s in (6.117) integrates to zero, and thus

$$\mathbf{U}_f = \dot{\mathbf{x}}_c = \mathbb{A} \cdot \mathbf{x}_c, \tag{6.118}$$

or equivalently $\mathbf{U}_f = \mathbf{u}_\infty(\mathbf{x}_c)$, exactly the same result as a sphere. This result, along with (6.117), therefore implies that the relative velocity between the rod and fluid varies with arclength as $\mathbf{u}_{\text{rod}} - \mathbf{u}_\infty = s(\dot{\mathbf{p}} - \mathbb{A} \cdot \mathbf{p})$, but since all the arclength dependence is known, we can express the force density as $\mathbf{f}(s,t) = s\tilde{\mathbf{f}}(t)$, where $\tilde{\mathbf{f}}$ only depends on time. The condition that the filament be torque free then becomes

$$\int_{-L/2}^{L/2} ds\, s\mathbf{p}(t) \times s\tilde{\mathbf{f}}(t) = \frac{L^3}{12}\mathbf{p}(t) \times \tilde{\mathbf{f}}(t) = \mathbf{0}, \tag{6.119}$$

which shows that $\tilde{\mathbf{f}} \parallel \mathbf{p}$, and we may therefore write $\tilde{\mathbf{f}}(t) = \Gamma(t)\mathbf{p}(t)$ for some function Γ.

The calculation is completed by noting that the relation (6.116) can be inverted (as we did in deriving (4.99)) to obtain

$$\mathbf{u}_{\text{rod}} - \mathbf{u}_\infty = -\frac{1}{\zeta_\perp}(\mathbb{I} + \mathbf{pp}) \cdot \mathbf{f}, \tag{6.120}$$

and thus, with $\mathbf{f}$ simplified as above, we must have

$$s(\dot{\mathbf{p}} - \mathbb{A} \cdot \mathbf{p}) = -\frac{s\Gamma}{\zeta_\perp}(\mathbb{I} + \mathbf{pp}) \cdot \mathbf{p} = -\frac{2s\Gamma}{\zeta_\perp}\mathbf{p}. \tag{6.121}$$

Hence, $\dot{\mathbf{p}} - \mathbb{A} \cdot \mathbf{p} = -(2\Gamma/\zeta_\perp)\mathbf{p}$. Taking the dot product with $\mathbf{p}$ and noting that $\mathbf{p} \cdot \dot{\mathbf{p}} = 0$ since $\mathbf{p}$ is a unit vector, we obtain

$$\Gamma = \frac{\zeta_\perp}{2}\mathbf{p} \cdot \mathbb{A} \cdot \mathbf{p}, \tag{6.122}$$

and finally

$$\dot{\mathbf{p}} = (\mathbb{I} - \mathbf{pp}) \cdot (\mathbb{A} \cdot \mathbf{p}) \,. \tag{6.123}$$

With some further vector calculus manipulations one can show that $\mathbb{A}$ can be expressed in terms of the rate-of-strain tensor $\mathbb{E}$ and vorticity $\boldsymbol{\omega}$ such that the final evolution equation for $\mathbf{p}$ takes the form

$$\dot{\mathbf{p}} = \boldsymbol{\Omega}_f \times \mathbf{p}, \quad \boldsymbol{\Omega}_f = \frac{1}{2}\boldsymbol{\omega} + \mathbf{p} \times (\mathbb{E} \cdot \mathbf{p}) \,. \tag{6.124}$$

The result (6.124) has the very same vorticity contribution as the rigid sphere and an additional contribution from the rate-of-strain tensor. This second contribution describes the alignment effect we saw in experiments on actin filaments discussed in Chapter 4.

Thus far, we have obtained the contribution to the angular velocity from the rate-of-strain tensor for spheres, where there is no contribution, and for extremely elongated rods, where we found (6.124). These results are special cases of a more general result due to Jeffery,[27] who computed the contribution for spheroids Combining his result with bottom-heaviness and the vorticity contribution, we obtain "Jeffery's equation",

$$\dot{\mathbf{p}} = \frac{1}{\tau_{bh}}\mathbf{p} \times (\mathbf{e}_z \times \mathbf{p}) + \frac{1}{2}\omega \times \mathbf{p} + \alpha \mathbf{p} \cdot \mathbb{E} \cdot (\mathbb{I} - \mathbf{pp}) \,, \tag{6.125}$$

where, α is a parameter of the ellipsoid given in terms of the ratio r of the major to minor axes,

$$\alpha = \frac{r^2 - 1}{r^2 + 1}, \tag{6.126}$$

with $\alpha = 0$ for a sphere and $\alpha \to 1$ for a highly elongated object.

There are many interesting and biologically relevant results that follow from Jeffery's equation (6.125) applied to a range of flow geometries and particle shapes. In the following two subsections we illustrate a few key results for swimmers far from surfaces.

6.5.3 Gyrotaxis in Poiseuille flow

As a first example, we consider spherical ($\alpha = 0$), bottom-heavy swimmers in pressure-driven channel flow. Assuming a channel width of $2L$, the standard parabolic flow profile is

$$\mathbf{u} = U_0 \left(1 - \frac{x^2}{L^2}\right) \mathbf{e}_z, \tag{6.127}$$

where U_0 is the maximum flow speed, achieved along the centreline $x = 0$. The vorticity of this flow is

$$\omega = \frac{2U_0 x}{L^2}\mathbf{e}_y, \tag{6.128}$$

and with $\mathbf{p} = (\cos\phi(t), 0, \sin\phi(t))$, we obtain the coupled dynamics

$$\dot{x} = U\cos\phi, \tag{6.129a}$$

$$\dot{z} = U\sin\phi + U_0\left(1 - \frac{x^2}{L^2}\right), \tag{6.129b}$$

$$\dot{\phi} = -\frac{xU_0}{L^2} + \frac{1}{\tau_{bh}}\cos\phi. \tag{6.129c}$$

---

[27] Jeffery, G.B. The motion of ellipsoidal particles immersed in a viscous fluid. *Proc. R. Soc. Lond. A*, 102:161–179, 1922

A natural set of rescalings uses the channel half-width L to scale space and the relaxation time τ_{bh} to scale time, and we introduce

$$X = \frac{x}{L}, \quad Z = \frac{z}{L}, \quad T = \frac{t}{\tau_{bh}}, \tag{6.130}$$

leading to

$$X_T = \beta \cos\phi, \tag{6.131a}$$

$$Z_T = \beta \sin\phi + \beta_0 \left(1 - X^2\right), \tag{6.131b}$$

$$\phi_T = -\beta_0 X + \cos\phi, \tag{6.131c}$$

where

$$\beta_0 = \frac{U_0 \tau_{bh}}{L}, \quad \text{and} \quad \beta = \frac{U \tau_{bh}}{L} \tag{6.132}$$

are the ratios of the bottom-heaviness relaxation time to the time necessary for the maximum flow or the swimming organism to move the channel half-width. Note that $\beta > 0$, while β_0 can be of either sign; $\beta_0 > 0$ is an upward channel flow, $\beta_0 < 0$ is downward.

The dynamical system (6.131) allows us to understand the phenomenon of *gyrotaxis*, the tendency of bottom-heavy organisms to swim into regions of vorticity. If $\beta_0 < 0$ (downward flow), then we can see from (6.131c) that ϕ will tend to increase when $X > 0$, meaning that the cell rotates to point toward the flow centreline. Likewise, ϕ decreases when $X < 0$ leading again to motion toward the center of the parabolic flow. For a flow with constant vorticity it is possible for there to be a fixed inclination angle ϕ, but in the case of Poiseuille flow the trajectories eventually reach the centreline with the cell pointing upwards, but being advected downward at the same time (if $\beta_0 + \beta < 0$), as depicted in Fig. 6.30. This leads to the phenomenon of gyrotactic focusing of algae, first described by Kessler, in which a thin concentrated plume of algae forms at the centreline.

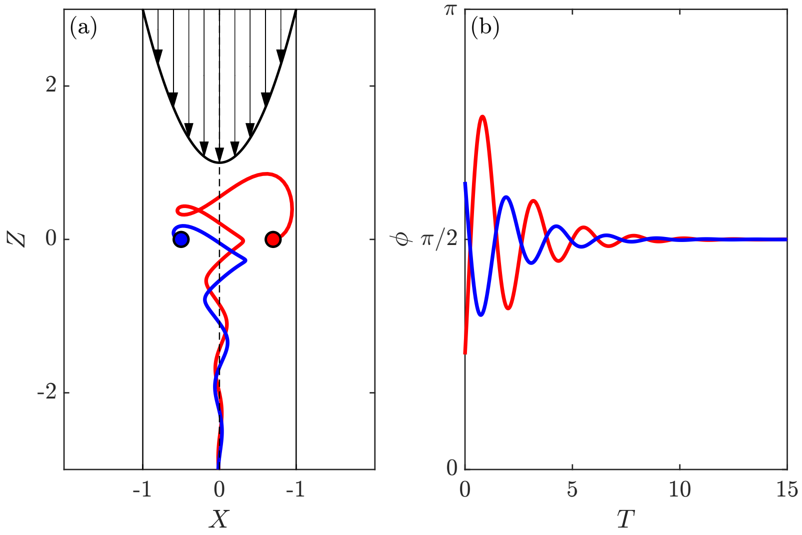

Figure 6.30: Gyrotaxis of a bottom-heavy organism in channel flow. (a) Trajectory for downward parabolic flow, showing motion to centreline, with $\beta = 2.5$, $\beta_0 = -3$, starting at $X = 0.7$, $Z = 0$, and $\phi = \pi/4$ (red) and $X = -0.5$, $Z = 0$, and $\phi = 5\pi/8$ (blue). (b) Corresponding tilt angles. Obtained with `Figure_630_gyrotaxis.m`.

6.5.4 *Jeffery Orbits in a flow with constant shear rate*

An important application of the general formula for the motion of swimming cells in flows concerns the behaviour of elongated cells in the simplest shear flow, that with constant shear rate. Let us therefore consider a velocity field

$$\mathbf{u} = \dot{\gamma} y \mathbf{e}_x, \tag{6.133}$$

where $\dot{\gamma}$ is the shear rate. If we restrict ourselves to motion in the $x - y$ plane and write the orientation vector as $\mathbf{p} = (\cos\phi(t), \sin\phi(t)$, then we obtain from our general equation of motion (6.103)

$$\dot{x} = \dot{\gamma} y + U\cos\phi(t), \tag{6.134a}$$

$$\dot{y} = U\sin\phi(t). \tag{6.134b}$$

The associated vorticity and rate of strain tensor are

$$\boldsymbol{\omega} = -\dot{\gamma}\mathbf{e}_z, \quad \mathbf{E} = \frac{\dot{\gamma}}{2}\begin{pmatrix} 0 & 1 \\ 1 & 0 \end{pmatrix}. \tag{6.135}$$

Writing $\dot{\mathbf{p}} = \boldsymbol{\Omega} \times \mathbf{p}$ and $\boldsymbol{\Omega} = \Omega\mathbf{e}_z$, and noting that $\dot{\phi} = \Omega$, some algebraic manipulations lead to the evolution

$$\dot{\phi} = -\frac{\dot{\gamma}}{r^2+1}\left(\cos^2\phi + r^2\sin^2\phi\right). \tag{6.136}$$

The substitution $f = r\tan\phi$ reduces the equation to

$$\frac{\dot{f}}{1+f^2} = -\frac{\dot{\gamma}}{r+r^{-1}}, \tag{6.137}$$

leading to the recognition of an arctan relation, and finally to

$$\tan\phi(t) = -\frac{1}{r}\tan\left(\frac{t\dot{\gamma}}{r+r^{-1}}\right), \tag{6.138}$$

where $t = 0$ is the time when $\phi = 0$. This result indicates that $\phi(t)$ is periodic in time with orbital period

$$T_{\text{orbit}} = \frac{2\pi}{\dot{\gamma}}\left(r + r^{-1}\right). \tag{6.139}$$

Figure 6.31(a) shows the time evolution of ϕ for three values of r. For $r = 1$ we have uniform rotation with $\phi = \dot{\gamma}t/2$, but for larger r the function develops plateaus of nearly constant value, connected by

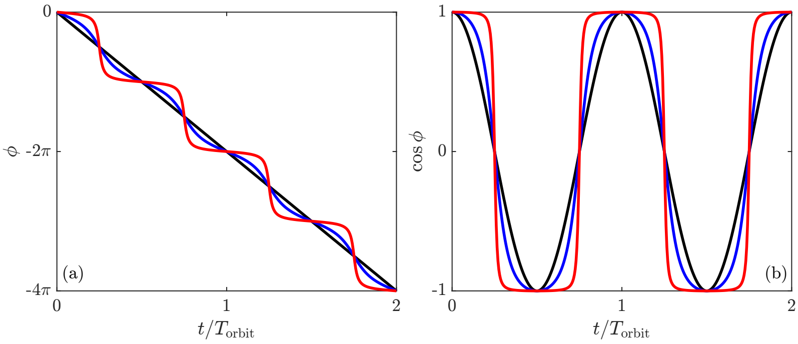

Figure 6.31: Dynamics of the orientation angle in Jeffery orbits for various aspect ratios of the cell. Curves are angle ϕ in (6.138) for $r = 1$ (black), $r = 2$ (blue) and $r = 10$ (red). Obtained with `Figure_631_and_632_Jefferyorbits.m`.

rapid transitions to the next plateau. This is seen even more clearly in Fig. 6.31(b) where we plot the projection $\cos\phi$. Note the important feature that $\phi(t)$ does not depend on the vertical position $y(t)$, sd the vorticity and rate-of-strain are constant for this linear shear profile.

The swimming trajectories in this shear flow follow from the general equation of motion (6.103) with the given $\phi(t)$. If we introduce the scaled time $T = t/T_{\text{orbit}}$ and scale lengths with the quantity $\ell = UT_{\text{orbit}}$, giving $X = x/\ell$ and $Y = y/\ell$, then

$$X_T = 2\pi(r + r^{-1})Y + \cos\Phi(T), \tag{6.140a}$$

$$Y_T = \sin\Phi(T), \tag{6.140b}$$

where, in these rescaled units, we have

$$\Phi(T) = \tan^{-1}\left\{-\frac{1}{r}\tan(2\pi T)\right\}. \tag{6.141}$$

In this form, we see that for a given value of r the dynamics is otherwise parameter-free, so the trajectories are in a sense "universal", but they do depend on the initial conditions. As the equation of motion has no explicit dependence on X, the dynamics are independent of the value of $X(0)$, but the explicit appearance of Y in (6.140) leads to a one-parameter family of solution parameterized by $Y(0)$. Numerically integrating the equations of motion (6.140) reveals that there is a spatially-dependent competition. dependent on $Y(0)$, between the tendency for approximately closed orbits and large-scale advection with the shear flow. Fig. 6.32 shows this for the case $r = 5$.

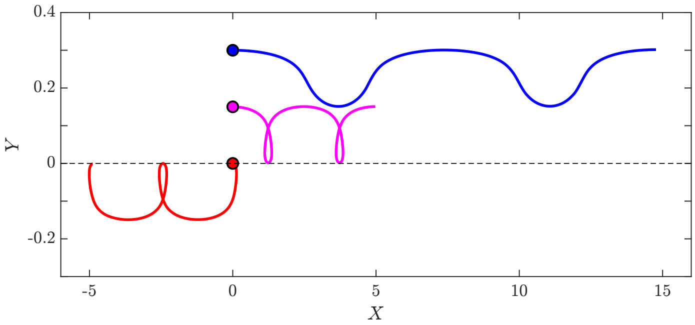

Figure 6.32: Jeffery orbits in the laboratory frame for $r = 5$. Curves correspond to different initial positions as denoted by the solid circles. Vertical scale is exaggerated for clarity. Obtained with `Figure_631_and_632_Jefferyorbits.m`.

6.6 *Surface-Mediated Interactions*

We close this chapter on cellular motion with a discussion of the basic aspects of the interactions between microswimmers and surfaces, in which we adopt the singularity description of the swimmers. The two most important flows of interest are those due to stokeslets or stresslets near no-slip and free surfaces.

6.6.1 *Singularities Near Surfaces*

Consider first a stokeslet near a stress-free surface, such as an air-water interface. In the geometry of Fig. 6.33, suppose an upward-pointing force is at $z = h$. Placing a mirror-image stokeslet at $z = -h$

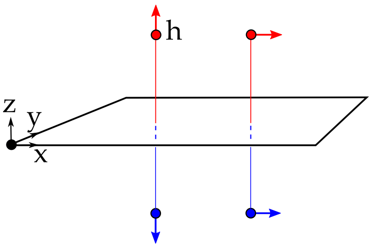

Figure 6.33: Geometry of stokes singularities near a free surface. Singularity is located at red circle, image is located at blue circle on opposite side of the surface $z = 0$. For the vertical stokeslet the image is of the opposite sign, while for the horizontal stokeslet it points in the same direction.

leads, by symmetry, to a vanishing of the vertical fluid velocity at $z = 0$ and the vanishing of tangential derivatives of the horizontal velocity. If a stokeslet due to a point force with components F_j (for $j = 1, 2, 3$) has the flow (6.88), then the image system yields

$$u_i(\mathbf{x}) = \frac{F_j}{8\pi\mu}\left[\left(\frac{\delta_{ij}}{r} + \frac{r_i r_j}{r^3}\right) - \left(\frac{\delta_{ij}}{R} + \frac{R_i R_j}{R^3}\right)\right], \tag{6.142}$$

where, if the singularity is located at (x_s, y_s, h) and the location of the flow is (x, y, z), then the quantities r and R in (6.142) are

$$r = \left[(x - x_s)^2 + (y - y_s)^2 + (z - h)^2\right]^{1/2}, \tag{6.143a}$$

$$R = \left[(x - x_s)^2 + (y - y_s)^2 + (z + h)^2\right]^{1/2}. \tag{6.143b}$$

Suppose first that the force points upward, away from the surface, so $F_j = F\delta_{j3}$. If the lateral position of the singularity is $(x_s = y_s = 0)$, and it is at $z_s = h$, the $(i = 1, 3)$ components of the flow are

$$u_x^{\perp} = \frac{F}{8\pi\mu}\left\{\frac{x(z-h)}{r^3} - \frac{x(z+h)}{R^3}\right\}, \tag{6.144a}$$

$$u_z^{\perp} = \frac{F}{8\pi\mu}\left\{\frac{1}{r} - \frac{1}{R} + \frac{(z-h)^2}{r^3} - \frac{(z+h)^2}{R^3}\right\}. \tag{6.144b}$$

It is easily seen that u_z vanishes identically at $z = 0$, where $r = R$, as does $\partial u_x/\partial z$. Figure 6.34(a) shows the fluid velocity vector field and heat map of velocity magnitude. While the fluid velocity falls off with distance as $1/r$ around a stokeslet in free space, the decay is altered by the presence of the surface. For example, in the case of a vertically-oriented force we find from (6.144) that directly above the singularity ($x = 0$) the vertical flow decays as $u_z(0, z) \sim h/z^2$. This can be compared to the situation with a point force along x, whose image points in the same direction, giving velocity components

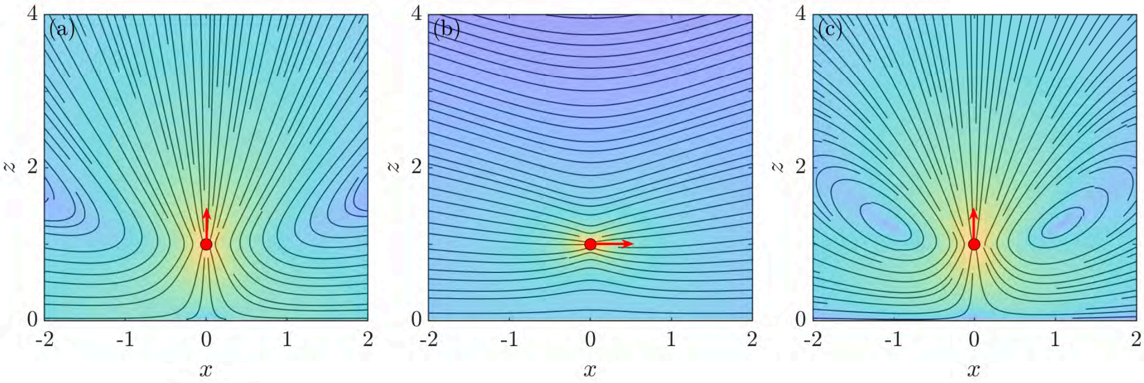

Figure 6.34: Stokeslet flow fields near for (a) vertical and (b) horizontal stokeslets near a stress-free surface, and (c) vertical stokeslet near a no-slip surfaces. Red circles indicate location of singularities at $z = 1$, where surface is at $z = 0$. Colors indicate magnitude of fluid velocity on a logarithmic scale. Obtained with `Figure_633_and_634_stokesletsurf.m`.

$$u_x^{\parallel} = \frac{F}{8\pi\mu}\left\{\frac{1}{r} + \frac{1}{R} + \frac{(z-h)^2}{r^3} + \frac{(z+h)^2}{R^3}\right\}, \tag{6.145a}$$

$$u_z^{\parallel} = \frac{F}{8\pi\mu}\left\{\frac{x(z-h)}{r^3} + \frac{x(z+h)}{R^3}\right\}. \tag{6.145b}$$

the streamlines of which are shown in Fig. 6.34(c). In this case, the parallel flow $u_x^{\parallel}$ far above the singularity retains its $1/z$ falloff.

The problem of a stokeslet near a *no-slip* surface is much more involved, as all three components of the velocity $\mathbf{u}$ must vanish on the surface. Blake was the first to solve this analytically in his 1971 PhD thesis.[28,29] The method of solution involves a two-dimensional Fourier transform of the governing equations along the directions of the surface, followed by solution of the resulting ODEs along the perpendicular direction, and then inversion of the transforms. Written in a form consistent with the notation in (6.142), the solution is

$$\begin{aligned} u_i = \frac{F_j}{8\pi\mu}\Bigg[&\left(\frac{\delta_{ij}}{r}+\frac{r_ir_j}{r^3}\right)-\left(\frac{\delta_{ij}}{R}+\frac{R_iR_j}{R^3}\right)\\ &+2h\left(\delta_{j\alpha}\delta_{\alpha k}-\delta_{j3}\delta_{3k}\right)\frac{\partial}{\partial R_k}\left\{\frac{hR_i}{R^3}-\left(\frac{\delta_{i3}}{R}+\frac{R_iR_3}{R^3}\right)\right\}\Bigg] \end{aligned} \tag{6.146}$$

where $\alpha = 1,2$. The quantity $\delta_{j\alpha}\delta_{\alpha k}-\delta_{j3}\delta_{3k}$ is nonzero only when $j = k$ and is $+1$ for $j = 1$ or 2 and -1 for $j = 3$. The solution involves terms with prefactors proportional to various powers of h. That with no prefactor is just the image stokeslet as in (6.142). The term proportional to $2hF$ has the interpretation of a force dipole (as it is the derivative of terms associated with a force), while that scaling as $2h^2F$ is a source dipole (the derivative of a source).

For the same vertically-oriented force ($F_j = F\delta_{j3}$), the flow is

$$u_x^{\perp} = \frac{F}{8\pi\mu}\left\{\frac{x(z-h)}{r^3}-\frac{x(z-h)}{R^3}-\frac{6hxz(z+h)}{R^5}\right\}, \tag{6.147a}$$

$$u_z^{\perp} = \frac{F}{8\pi\mu}\left\{\frac{1}{r}-\frac{1}{R}+\frac{(z-h)^2}{r^3}-\frac{z^2+h^2}{R^3}-\frac{6hz(z+h)^2}{R^5}\right\}. \tag{6.147b}$$

This flow field is shown in Fig. 6.34(c), where we observe the new feature of *closed streamlines*. These do not appear when the force is parallel to the surface. For the perpendicular case, the existence of recirculating flows is thought to have implications for filter-feeding of organism that attach themselves to surfaces with a slender stalk.[30] The no-slip surface has a strong effect on the far-field behaviour of the flow. For example, for a vertical stokeslet, the flow falls off as $1/r^3$, while $u \sim 1/r^2$ for a force parallel to the surface. The slower fall-off for forces oriented parallel to the surface suggests, for example, that in the action of cilia at the surface of organisms the movements parallel to the surface are more important for propulsion and fluid transport than those perpendicular to the surface.

The general result that gradients of elementary flow fields yield higher-order singularities can be used to understand the flow field generated by a bacterium swimming parallel to a no-slip surface. Using the general formulation (6.146), we first obtain the flow field in the $x-y$ plane associated with a point force along x,

$$u_x^{\parallel} = \frac{F}{8\pi\mu}\left\{\left(\frac{1}{r}+\frac{x^2}{r^3}\right)-\left(\frac{1}{R}+\frac{x^2}{R^3}\right)-2h\left(\frac{z}{R^3}+\frac{3x^2z}{R^5}\right)\right\}, \tag{6.148a}$$

$$u_y^{\parallel} = \frac{F}{8\pi\mu}\left\{\frac{xy}{r^3}-\frac{xy}{R^3}+\frac{6hxyz}{R^5}\right\}. \tag{6.148b}$$

[28] J.R. Blake. Note on the image system for a stokeslet in a no-slip boundary. *Math. Proc. Camb. Phil. Soc.*, 70:303–310, 1971

[29] Blake, J.R. and Chwang, A.T. Fundamental singularities of viscous flow. Part I: The image systems in the vicinity of a stationary no-slip boundary. *J. Eng. Math.*, 8:23–29, 1974

[30] Higdon, J.J.L. The generation of feeding currents by flagellar motions. *J. Fluid Mech.*, 94:305–330, 1979

The streamlines of this flow field are shown in Fig. 6.35(a), and we observe from (6.148) that $u \sim 1/r^2$ in the far field. The gradient of (6.148) is shown in Fig. 6.35(b), which is proportional to the flow field of a stresslet near a no-slip surface. Again we see the generation of strong recirculation regions.

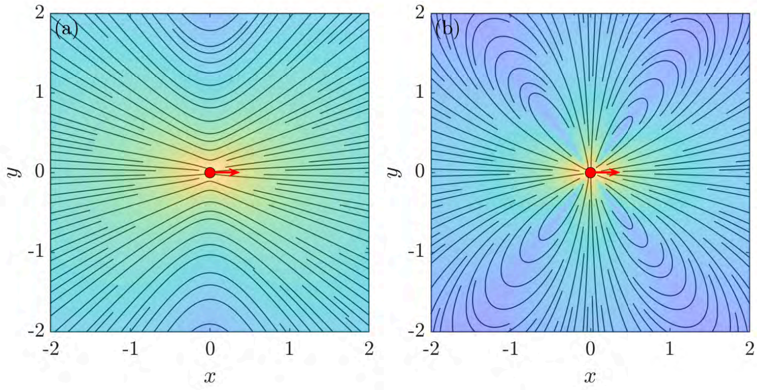

Figure 6.35: Stokeslet and stresslet flows near a no-slip surface. (a) In-plane flow due to a point force along x. (b) Gradient of the flow in (a), giving a stresslet flow field. Colors indicate magnitude of fluid velocity on a logarithmic scale. Obtained with `Figure_629_and_630_stokesletsurf.m`.

The techniques used to determine the bacterial flow field in Fig. 6.27 have been applied to the situation when a bacterium swims parallel to a nearby no-slip surface. Figure 6.36 shows the measured flow field, its comparison with the ideal stresslet field, and the falloff of the velocity magnitude with distance, decaying as $1/r^3$.

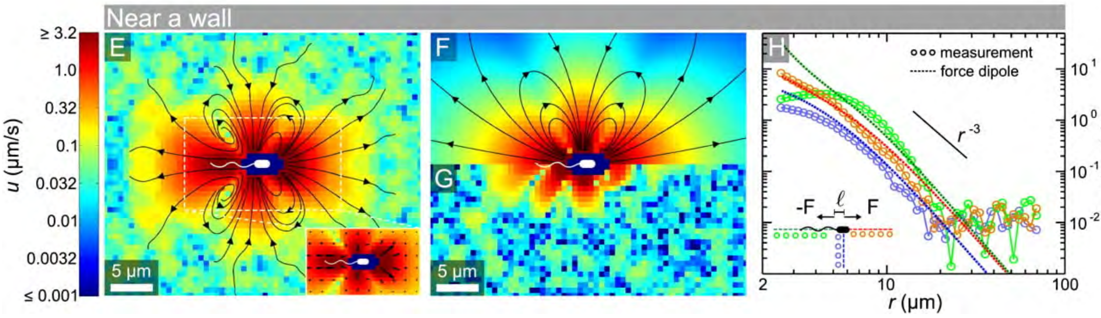

Figure 6.36: Experimentally determined flow field around the bacterium *E. coli*. From Ref. 22.

6.6.2 *Attraction and reorientation of stresslets by surfaces*

When a microswimmer approaches a surface there are certain key hydrodynamic interactions between them and the surface that are important in various phenomena within biological physics. The general protocol for calculating the effects of a surface on a swimmer involves (i) finding the image system appropriate to the swimmer, (ii) calculating the vorticity and rate-of-strain tensor of the singularity+images, and (iii) determining the translation and rotation of the swimmer via Jeffery's equation. Since this can become algebraically involved, we focus here on two examples involving stress-free surfaces, here where the image system is the simplest and defer more complex calculations to the Example Sheet.

The first example concerns the interaction of a stresslet oriented parallel to a stress-free surface. Here we can appeal to the flow field of a stresslet in free space (6.99) to write the solution for the entire flow field for a stresslet oriented along $\mathbf{e}_x$ at position $(0,0,h)$ with image at $(0,0,-h)$ near a free surface in the $x-y$ plane as

$$u_x^{\parallel}(x,z) = \frac{\mathcal{P}}{8\pi\mu}\left\{\left(\frac{3x^2}{r^5}-\frac{1}{r^3}\right)x + \left(\frac{3x^2}{R^5}-\frac{1}{R^3}\right)x\right\}, \tag{6.149a}$$

$$u_z^{\parallel}(x,z) = \frac{\mathcal{P}}{8\pi\mu}\left\{\left(\frac{3x^2}{r^5}-\frac{1}{r^3}\right)(z-h) + \left(\frac{3x^2}{R^5}-\frac{1}{R^3}\right)(z+h)\right\}, \tag{6.149b}$$

where $r=\sqrt{x^2+(z-h)^2}$ and $R=\sqrt{x^2+(z+h)^2}$. It is straightforward to verify that $u_z^{\parallel}$ vanishes at $z=0$ as does $\partial u_x^{\parallel}/\partial x$ there, as required. If we now evaluate this flow at the stresslet location $(0,h)$ we find the wall-induced velocity is

$$u_z^{\parallel}(0,h) = -\frac{\mathcal{P}}{32\pi\mu h^2}. \tag{6.150}$$

This is an attractive interaction for a pusher stresslet $\mathcal{P}>0$, and a repulsion for a puller. A nearly identical result holds for a no-slip surface, with only a change in the numerical factor in the denominator. Experiments[31] indicate that this is likely the dominant effect leading to surface accumulation of bacteria and spermatozoa.

Next we consider a stresslet oriented at some angle ϕ with respect to the stress-free surface, for which the velocity components are

$$\begin{aligned} u_x^{\phi}(x,z) = \frac{\mathcal{P}}{8\pi\mu}\Bigg\{&\left(\frac{(3x\cos\phi+(z-h)\sin\phi)^2}{r^5}-\frac{1}{r^3}\right)x \\ &+\left(\frac{(3x\cos\phi+(z+h)\sin\phi)^2}{R^5}-\frac{1}{R^3}\right)x\Bigg\}, \end{aligned} \tag{6.151a}$$

$$\begin{aligned} u_z^{\phi}(x,z) = \frac{\mathcal{P}}{8\pi\mu}\Bigg\{&\left(\frac{(3x\cos\phi+(z-h)\sin\phi)^2}{r^5}-\frac{1}{r^3}\right)(z-h) \\ &+\left(\frac{(3x\cos\phi+(z+h)\sin\phi)^2}{R^5}-\frac{1}{R^3}\right)(z+h)\Bigg\}, \end{aligned} \tag{6.151b}$$

A direct calculation shows that the vorticity contribution $(1/2)\boldsymbol{\omega}$ gives rise to the angular dynamics

$$\dot{\phi} = -\frac{3\mathcal{P}}{64\pi\mu h^3}\sin\phi\cos\phi, \tag{6.152}$$

with additional contributions when the particle in non-spherical. This leading contribution has the feature that for pullers there are stable fixed points at $\phi=0,\pi$, while for pushers the stable fixed points are at $\phi=\pm\pi/2$. We conclude that pushers will be oriented parallel to the wall but pushers will either swim into or away from the wall.

6.6.3 *Surface-mediated attraction of stokeslets*

In a final illustration of the key features of flows near surfaces, we study the interaction of two organisms near a no-slip surface, following an analysis first given by Squires.[32] As shown in Fig. 6.37, we

[31] Berke, A.P. and Turner, L. and Berg, H.C. and Lauga, E. Hydrodynamic Attraction of Swimming Microorganisms by Surfaces. *Phys. Rev. Lett.*, 101:038102, 2008

[32] Squires, T.M. Effective pseudo-potentials of hydrodynamic origin. *J. Fluid Mech.*, 443:403–412, 2001

consider two spherical colonies of radius R that by some means are maintained at an upper, no-slip wall, with gravity acting downwards. Assuming that each can be represented by a stokeslet of strength F, from (6.147) we read off the lateral flow at some distance x from one colony in isolation, evaluated at an offset distance R from the surface,

$$u_x(x) = -\frac{3R^3F}{2\pi\mu}\frac{x}{(x^2+4R^2)^{5/2}}. \tag{6.153}$$

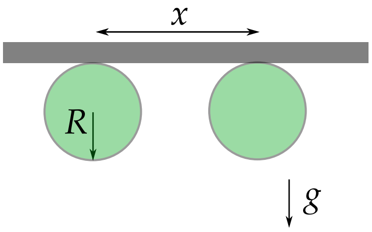

Figure 6.37: Two spherical microswimmers near an upper no-slip surface, with gravity pointing downward.

This has the important feature that when the force is pointing *away* from the wall (either pointing upwards at a bottom wall or pointing downwards at an upper wall) the lateral flow is *inwards* towards the singularity. If a second such particle is also similarly near the wall, they will mutually advect each other so that their separation r evolves with twice the speed u_x. If we rescale the separation as $X = x/R$ and time as $T = Ft/\mu R^2$, then we obtain the equation of motion

$$\frac{dX}{dT} = -\frac{3}{\pi}\frac{X}{(X^2+4)^{5/2}}. \tag{6.154}$$

There are several interesting points about this dynamical law. First, it is a gradient flow in the sense that $dX/dT = -dV(X)/dx$, with

$$V(X) = -\frac{1}{\pi}\frac{1}{(x^2+4)^{3/2}}, \tag{6.155}$$

a potential illustrated in Fig. 6.38. We can therefore interpret the fluid-mediated interaction as a direct mechanical interaction between the spheres, characterised by a potential energy function.

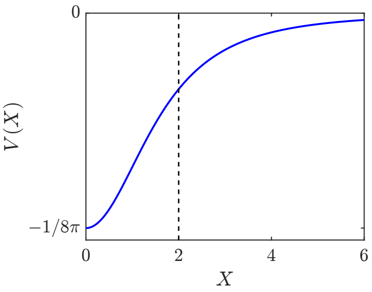

Figure 6.38: Effective potential for hydrodynamic interaction between two stokeslets near a no-slip surface. Contact occurs at $X = 2$ (dashed line).

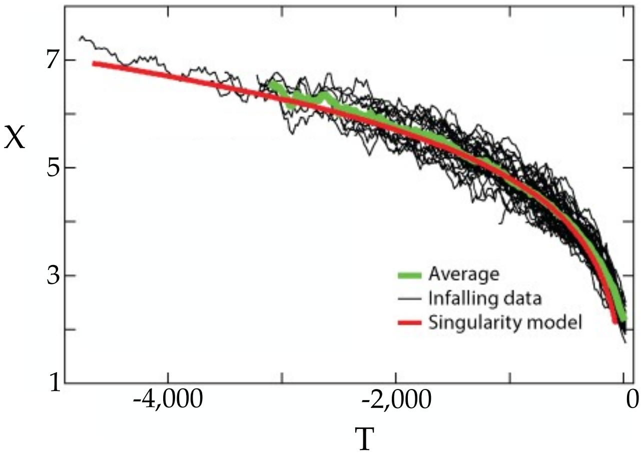

Figure 6.39: Infalling dynamics of two *Volvox* colonies. From Ref. 19.

A second result of the rescaled dynamics (6.154) is that it is totally parameter-free, and therefore the infalling trajectories of spheres toward contact ($X = 2$) should be universal. Figure 6.39 shows the solution to this compares remarkably well to data on the "infalling" of *Volvox* colonies as they approach each other toward contact, forming what is termed a "bound state".

7

Kinetics & Pattern Formation (Lectures 21-24)

The problem of understanding biological patterns —whether at the scale of a bacterium or a forest—has occupied a central role in most discussions of mathematical biology for decades. The seminal work of Alan Turing in 1952[1] led to a profound change in our understanding of the potential for systems of reacting and diffusing chemicals to produce spatio-temporal patterns, and is a natural focus in this chapter. In building up to that study, we first cover some of the most basic aspects of chemical kinetics in order to understand the origins of particular kinds of generic nonlinearities found in these systems, and to introduce the important role of separations of time scales in problems of this type.

7.1 *Michaelis-Menten kinetics*

Many of the key concepts in chemical kinetics can be understood using the Michaelis-Menten model[2] of enzyme kinetics. In general, an enzyme is a molecule that accelerates a chemical reaction without itself being consumed. In the MM scheme, an enzyme E interacts with a substrate S to form an "enzyme-substrate complex" C, which dissociates into the enzyme and the reaction product P. In standard notation, the reaction scheme is written as

$$\mathrm{E}+\mathrm{S} \underset{\mathrm{k}_{-1}}{\overset{\mathrm{k}_1}{\rightleftharpoons}} \mathrm{C} \xrightarrow{\mathrm{k}_2} \mathrm{E}+\mathrm{P} \qquad (7.1)$$

where k_1, k_{-1}, k_2 are the rate constants for the formation of C, the breakup of C and dissociation of C, respectively. In this scheme we have neglected the back reaction that would convert the product to the complex. In translating this scheme into dynamical equations, we imagine a fluid volume within which are the various species $E, S, \ldots$, whose average concentrations serve to determine the rates of reaction. In using these concentrations to define the kinetics, there is an implicit assumption that the system is "well mixed", as in a so-called "continuously stirred tank reactor". If we use our previous notation for chemical concentrations and let $s = [S]$, $e = [E]$, $c = [C]$, and $p = [P]$, then the law of mass action gives the differential equations

[1] Turing, A. The chemical basis of morphogenesis. *Phil. Trans. R. Soc. London B*, 237:37–72, 1952

[2] Michaelis, L. and Menten, M.L. Die Kinetik der Invertinwirkung (English translation). *Biochem. Z.*, 49:333–369, 1913

for the concentrations

$$\frac{de}{dt} = -k_1 es + k_{-1}c + k_2 c \tag{7.2a}$$
$$\frac{ds}{dt} = -k_1 es + k_{-1}c \tag{7.2b}$$
$$\frac{dc}{dt} = k_1 es - k_2 c - k_{-1}c \tag{7.2c}$$
$$\frac{dp}{dt} = k_2 c\ . \tag{7.2d}$$

Note that there are no nonlinearities higher than second order in this scheme. The dynamics of p are completely decoupled from the other reactions, so it is completely known once $c(t)$ is known,

$$p(t) = k_2 \int_0^t c(t')dt',$$

and we need not consider it any further.

In the typical situation, the initial state of the system has a specified amount of substrate and enzyme, but the reaction has not yet begun, and thus we set

$$s(0) = s_0, \quad c(0) = 0, \quad e(0) = e_0, \quad p(0) = 0. \tag{7.3}$$

By the structure of the reaction scheme the total amount of enzyme is fixed, and one readily verifies that $e + c$ must be conserved, since

$$\frac{de}{dt} + \frac{dc}{dt} = 0, \tag{7.4}$$

and hence $e + c = e_0$ at all times. The system of three remaining reactions after eliminating that for p can thus be reduced to two by setting $e = e_0 - c$, yielding

$$\frac{ds}{dt} = -k_1 e_0 s + (k_1 s + k_{-1})c \tag{7.5}$$
$$\frac{dc}{dt} = k_1 e_0 s - (k_1 s + k_{-1} + k_2)c \tag{7.6}$$

As in all problems of this type, we now nondimensionalise the equations. The enzyme is typically present at much lower concentrations than the substrate, so we identify the small parameter $\epsilon = e_0/s_0$. Let the rescaled time be $\tau = k_1 e_0 t$, and set

$$u(\tau) = \frac{s(t)}{s_0}, \quad \lambda = \frac{k_2}{k_1 s_0}, \tag{7.7}$$
$$v(\tau) = \frac{c(t)}{e_0}, \quad k = \frac{k_1 + k_2}{k_1 s_0}, \tag{7.8}$$

Then we have the final equations for the substrate and complex,

$$\frac{du}{d\tau} = -u + (u + k - \lambda)v, \quad u(0) = 1, \tag{7.9a}$$
$$\epsilon\frac{dv}{d\tau} = u - (u + k)v, \qquad v(0) = 0. \tag{7.9b}$$

In this form, with ϵ multiplying the highest (time) derivative in the problem, it is clear that a finite ϵ is a singular perturbation to the

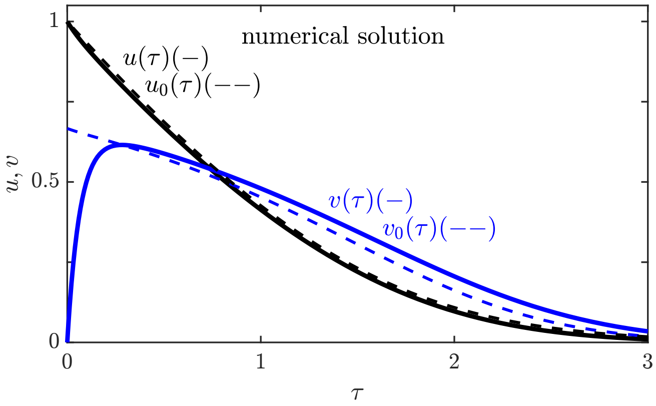

Figure 7.1: Solutions to the Michaelis-Menten dynamics. Full numerical solution of (7.9a) and (7.9b) (solid lines) for $\epsilon = 0.1$, $k = 0.5$ and $\lambda = 1$, compared to steady-state approximation (dashed). Obtained with `Figure_701_and_704_MichaelisMenten.m`.

$\epsilon = 0$ problem and the solutions should exhibit a kind of boundary layer in time. This can be seen in Fig. 7.1(a), where we plot with solid lines the numerical solution of (7.9a) and (7.9b); the variable $v(\tau)$ climbs very rapidly from its initial value to a peak at a time of order ϵ, and then decays much more slowly. The behaviour of both u and v at times much larger than ϵ matches quite closely a steady-state approximation (dashed) discussed next.

7.1.1 *Steady-state approximation*

If we simply ignore the possibly singular nature of ignoring the time derivative in the v equation and set $dv/d\tau = 0$, we obtain an *algebraic* relationship between u and v that is trivially solved as

$$v_0 = \frac{u_0}{u_0 + k}, \tag{7.10}$$

where the subscript indicates the order of ϵ. If we return to the u equation (7.9a) and substitute the steady-state result (7.10) we obtain the single dynamics

$$\frac{du_0}{dt} = -\frac{\lambda u_0}{u_0 + k}. \tag{7.11}$$

Note that having reduced the full MM dynamics, consisting of two first order ODEs, to a single first order ODE, we have lost the ability to impose the two initial conditions in the problem ($u(0) = 1, v(0) = 0$). This is a typical feature of problems with singular perturbations. It is simple enough to solve this equation to obtain the implicit form

$$\tau = (1 - u_0 - k \ln u_0)/\lambda. \tag{7.12}$$

This satisfies the initial condition $u_0(0) = 1$, but the partner relation (7.10) does not satisfy $v_0(0) = 0$. Nevertheless, the comparison in Fig. 7.1 between u_0 and v_0 and the full numerical solutions shows that they agree well beyond times of order ϵ.

Returning to the fundamental result (7.10), we see in dimensional units that the rate of reaction $R = dp/dt$ would be

$$R = V_{\max}\frac{s}{s + K_m}, \tag{7.13}$$

where $K_m = (k_{-1} + k_2)/k_1$ is known as the Michaelis constant and $V_{\max} = k_2 e_0$. As shown in Fig. 7.2, this rate law exhibits a linear

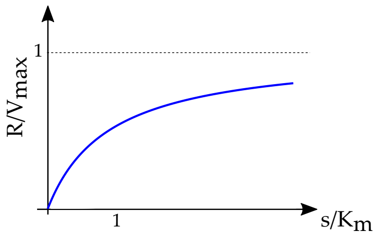

Figure 7.2: Michaelis-Menten reaction rate versus substrate concentration.

dependence at small substrate concentrations that rolls over to saturate at the maximum rate $V_{\max}$ at large s, reaching $V_{\max}/$ at $s = K_m$. The Michaelis constant has the interpretation of the substrate concentration at which the reaction reaches half its maximum rate. The constants K_m and $V_{\max}$ can be determined from a plot of $1/R$ versus $1/s$, as $1/R = (1 + K_m/s)/V_{max}$. This is the so-called Lineweaver-Burk plot,[3] as shown in Fig. 7.3.

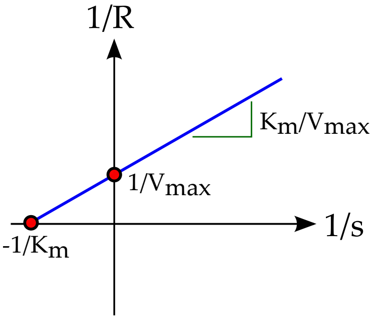

Figure 7.3: The Lineweaver-Burk plot used to determine parameters of Michaelis-Menten dynamics.

The result (7.10) occupies a central place in the quantitative description of biochemical reactions, and is used widely in the modeling of systems for which there is only partial information on the complete kinetics, for it incorporates the nearly universal feature of saturation of rates due to the presence of fast variables that are implicitly present. A particularly important feature of this result is its strong nonlinearity despite the original reaction scheme having only quadratic nonlinearities.

7.1.2 *Matched asymptotic approximation*

To find an approximate analytical solution to the Michaelis-Menten dynamics for small ϵ we will use standard methods well-described elsewhere.[4] The solution we have found by setting $\epsilon = 0$ is to be viewed as the "outer" solution, but importantly that of u_0 derives from (7.11) but without yet imposing boundary conditions:

$$u_0 + k \ln u_0 = -\lambda\tau + C, \tag{7.14}$$

where C will be determined by matching to the inner solution.

To find the inner solution, we must identify the relevant inner time scale, which we can do by defining a scaled variable T as

$$T = \frac{\tau}{\delta(\epsilon)}, \tag{7.15}$$

where $\delta(\epsilon)$ is the as yet unknown inner time that we will find on the basis of balancing terms in the rescaled dynamics. By direct substitution into (7.9a) and (7.9b) we obtain

$$\begin{aligned} \frac{1}{\delta}\frac{dU}{dT} &= -U + (U + k - \lambda)v, \quad U(0) = 1, &\text{(7.16a)}\\ \frac{\epsilon}{\delta}\frac{dV}{dT} &= U - (U + k)V, \quad V(0) = 0. &\text{(7.16b)} \end{aligned}$$

where the inner solution is (U, V). It is now clear that in order that the time derivative balances the terms on the r.h.s. of (7.16b) we must have $\delta(\epsilon) \propto \epsilon$ and we are free to set the proportionality constant to unity and thus find $T = \tau/\epsilon$. In other kinds of problems the balancing of terms can be more subtle, but as ϵ only appears in the time derivative, here it is simple. We therefore find that the equations to be solved to find the inner solution are

$$\begin{aligned} \frac{dU}{dT} &= \epsilon\left[-U + (U + k - \lambda)v\right], \quad U(0) = 1, &\text{(7.17a)}\\ \frac{dV}{dT} &= U - (U + k)V, \quad V(0) = 0. &\text{(7.17b)} \end{aligned}$$

[3] Lineweaver, H. and Burk, D. The Determination of Enzyme Dissociation Constants. *J. Am. Chem. Soc.*, 56:658–666, 1934

[4]

Now, ϵ appears on the r.h.s. of (7.17a) and we can expect there to be a regular perturbation expansion of the solutions in the form $U(T,\epsilon) = U_0(T) + \epsilon U_1(T) + \ldots$ and $V(T,\epsilon) = V_0(T) + \epsilon V_1(T) + \ldots$. Direct substitution shows that the zeroth order problem is

$$\frac{dU_0}{dT} = 0, \quad U_0(0) = 1, \tag{7.18a}$$

$$\frac{dV_0}{dT} = U_0 - (U_0 + k)V_0, \quad V(0) = 0. \tag{7.18b}$$

This is easily solved to yield

$$U_0(T) = 1, \qquad V_0(T) = \frac{1}{1+k}\left[1 - e^{-(1+k)T}\right]. \tag{7.19}$$

Here we note that the argument of the exponential is $(1+k)\tau/\epsilon$, which reveals the singular nature of the perturbation as $\epsilon \to 0$.

Next we match the inner and outer solutions to find C in (7.14), and introduce an intermediate time scale $T_i = \tau/\psi(\epsilon)$ with

$$\lim_{\epsilon\to 0} \psi(\epsilon) = 0, \quad \lim_{\epsilon\to 0} \frac{\psi(\epsilon)}{\delta(\epsilon)} = \infty. \tag{7.20}$$

The matching condition is then simply that the limit of the outer solution at some fixed T_i as $\epsilon \to 0$ equals that of the inner solution,

$$\lim_{\epsilon\to 0}\left[u_0(\tau)|_{\tau=\psi T_i}\right] = \lim_{\epsilon\to 0}\left[U_0(T)|_{T=T_i\psi/\delta}\right], \tag{7.21}$$

which implies $u_0(0) = 1$ since $U_0 = 1$. Thus, $C = 1$ in (7.14) and therefore $u_0 + k\ln u_0 = -\lambda\tau + 1$. One readily verifies that the matching condition on the complex concentration is

$$v_0(0) = \lim_{\epsilon\to 0}\left\{\frac{1}{1+k}\left[1 - e^{-(1+k)T_i\psi/\delta}\right]\right\} = \frac{u_0(0)}{u_0(0)+k}, \tag{7.22}$$

and that this is automatically satisfied.

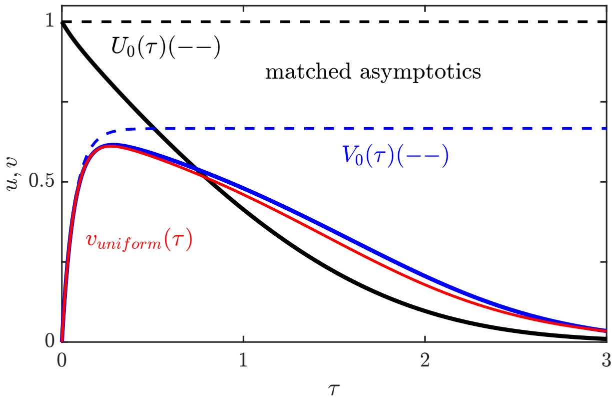

Figure 7.4: Matched asymptotic solutions to the Michaelis-Menten dynamics. Inner and uniform solutions to the matched asymptotic problem (dashed) compared to the numerical solutions. Obtained with `Figure_701_and_704_MichaelisMenten.m`.

A *uniform approximation* $\tilde{u}_0(\tau)$is obtained by a standard recipe: add the inner and outer approximations and subtract their common part. In this case, we have

$$\tilde{u}_0(\tau) = u_0(\tau) + U_0\left(\frac{\tau}{\epsilon}\right) - 1 \Rightarrow \tilde{u}_0(\tau) = u_0(\tau), \tag{7.23}$$

since $U_0 \equiv 1$. The uniform approximation for the complex is

$$\tilde{v}_0(\tau) = v_0(\tau) + V_0\left(\frac{\tau}{\epsilon}\right) - \frac{1}{1+k} \tag{7.24a}$$

$$= \frac{u_0(\tau)}{u_0(\tau)+k} - \frac{e^{-(1+k)\tau/\epsilon}}{1+k}, \tag{7.24b}$$

These results are shown in Fig. 7.4b, where we see excellent agreement with the full numerics over the entire time range.

7.1.3 Cooperativity in Reaction Rates

The Michaelis-Menten scheme is the simplest example of a biochemical kinetics displaying a saturating reaction rate, and has the noteworthy feature that at small substrate concentrations s, the rate is linear in s. Such is not always the case in biochemical systems. One well known example is provided by the binding of oxygen to hemoglobin, the protein carrier of oxygen in the blood. Each of the fours subunits of hemoglobin can bind a molecule of oxygen. The analogue of the enzyme-substrate complex concentration (7.10) is then the fractional occupancy of binding sites on hemoglobin. As a function of the partial pressure of oxygen in the blood, the occupancy exhibits a characteristic "sigmoidal" shape shown in Fig. 7.5. This arises from the feature of "cooperativity", in which the binding of one oxygen molecule triggers a conformational change in the hemoglobin that facilitates the binding of subsequent molecules. Such behaviour is also known as *allosterism* and hemoglogin is said to be "allosteric".

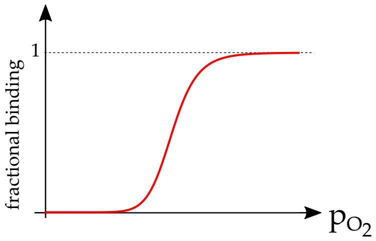

Figure 7.5: Schematic sigmoidal binding curve of oxygen to hemoglobin, as a function of the partial pressure of oxygen.

This produces a very large change in absorbed oxygen over a relatively small shift in oxygen concentration. Thus, the high partial pressure of oxygen in the lungs loads the hemoglobin nearly completely, while in the tissues of the body the lower oxygen concentration leads to off-loading from hemoglobin. Thus, cooperativity produces a response akin to a switch. The first treatment of this problem was given by Monod, Wyman and Changeux.[5]

Sigmoidal reaction kinetics can arise also from an enlarged kinetic scheme with multiple complexes. For example, consider an allosteric enzyme E that reacts with a substrate S to produce a product P,

$$\mathrm{E} + \mathrm{S} \underset{\mathrm{k}_{-1}}{\overset{\mathrm{k}_1}{\rightleftharpoons}} \mathrm{C}_1 \tag{7.25a}$$

$$\mathrm{C}_1 + \mathrm{S} \xrightarrow{\mathrm{k}_2} \mathrm{C}_2 \xrightarrow{\mathrm{k}_3} \mathrm{C}_1 + \mathrm{P}, \tag{7.25b}$$

where C_1 and C_2 are enzyme-substrate complexes and the ks are the corresponding rate constants. It is a straightforward exercise to write down the evolution equations for e, s, c_1, c_2 and p that follow from the law of mass action, and to verify that conservation of enzyme implies the constancy of $c_1 + c_2 + e$. If we then assume initial conditions $s(0) = s_0$, $e(0) = e_0$, $c_1(0) = c_2(0) = p(0) = 0$, and rescale with $\epsilon = e_0/s_0$, $\tau = k_1 e_0 t$, $u = s/s_0$, and $v_i = c_i/e_0$, the nondimensional

---

[5] Monod, J., Wyman, J. and Changeux, J.-P. On the Nature of Allosteric Transitions - a Plausible Model. *J. Mol. Biol.*, 12:88–118, 1965

reaction mechanism can be reduced to the form

$$\frac{du}{d\tau} = f(u, v_1, v_2), \tag{7.26a}$$

$$\epsilon \frac{dv_1}{d\tau} = g_1(u, v_1, v2), \tag{7.26b}$$

$$\epsilon \frac{dv_2}{d\tau} = g_2(u, v_1, v2). \tag{7.26c}$$

where the functions f, g_1 and g_2 depend on the three dimensionless quantities $\alpha = k_{-1}/k_1 s_0$, $\beta = k_2/k_1$ and $\gamma = k_3/k_1 s_0$. Invoking the steady-state approximation, one then finds the rate of production

$$\frac{dp}{dt} = A \frac{u^2}{\alpha + u + (\beta/\gamma)u^2} , \tag{7.27}$$

where A is a constant. This functional form is a simple example of a sigmoidal relationship. It is one example of a more general form

$$\frac{s^n}{K_m + s^n} \tag{7.28}$$

which is known as the *Hill equation*, with n being the *Hill coefficient*. The larger is n, the more sigmoidal and cooperative the reaction. Systems with n as large as 10 or more are known, producing "ultrasensitive" responses.[6]

7.1.4 *Slaving*

The appearance of strong nonlinearities in the effective dynamics of slow variables in systems with a strong separation of time scales can be seen within a very simple model with only quadratic underlying nonlinearities. Suppose that there are two degrees of freedom p, q, where q is a slow variable (as in the Michaelis-Menten substrate concentration) and p is fast (as in the MM complex concentration),

$$\frac{dq}{dt} = \alpha q - \beta p q \tag{7.29a}$$

$$\epsilon \frac{dp}{dt} = \gamma p - \delta q^2. \tag{7.29b}$$

We interpret the terms αq and γp as representing autocatalysis. In the steady state approximation, $p = \delta q^2/\gamma$ and the slow dynamics is

$$\frac{dq}{dt} \simeq \alpha q - \frac{\beta\delta}{\gamma} q^3. \tag{7.30}$$

Importantly, the r.h.s. of (7.30) has the form $-dV(q)/dq$, where

$$V(q) = -\frac{1}{2}\alpha q^2 + \frac{\beta\delta}{4\gamma} q^4. \tag{7.31}$$

Thus, just as in our study of Euler buckling, we have a potential capable of producing a pitchfork bifurcation as a function of α. This corresponds to the physical scenario of overdamped dynamic, and in fact produces a bifurcation as a function of α, from a function with a single minimum for $\alpha < 0$ to a double well. The key point to take away from this simple example is that by slaving fast variables to slow ones we can obtain very strong nonlinearities in the effective equations of motion for the slow degrees of freedom, and these can exhibit bifurcations and even bistability.

---

[6] P. Cluzel, M. Surette and S. Leibler. An ultrasensitive bacterial motor revealed by monitoring signaling proteins in single cells. *Science*, 287:1652–1655, 2000

7.2 *Excitable media: Neurons and the FHN model*

One of the most important developments in biological physics in the 20th century was the quantitative understanding of electrical impulse propagation along neurons. This was achieved through a long sequence of experimental and theoretical work, culminating in the celebrated work of Hodgkin and Huxley (HH),[7] which gave a complete description of pulses of electrical activity known as action potentials that travel down axons at speeds that can reach m/s. Here we present a very brief summary of the key features of neurons that are captured by mathematical models of their dynamics.

Axons are long, slender cylindrical structures that extend from neurons. Their diameter is typically in the range of $1 - 20\,\mu$m, although there are a few notably large exceptions such as the "giant squid axon" that can exceed 1 mm in diameter. As shown schematically in Fig. 7.6, the axon itself is defined by a biological membrane a few nanometers thick that separates the fluid inside from that surrounding the axon. Within the membrane are specialized protein structures that produce and regulate a large difference in concentrations of certain ions in those fluid regions. These include "pumps" that actively and selectively transfer ions across the membrane as they consume chemical energy, and "channels" that can open and close to regulate the passive flow of ions across the membrane. Na^+ ions may have a concentration of 150 mM outside and 15 mM inside, while K^+ is 5 mM inside and 150 mM outside. As mentioned in the introduction, the Nernst equation relates the electric potential difference across a membrane to the concentrations on the two sides

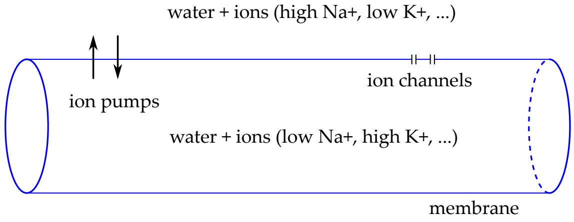

Figure 7.6: Schematic of an axon.

$$V = \frac{k_B T}{e} \ln\left(\frac{C_{\mathrm{out}}}{C_{\mathrm{in}}}\right) \tag{7.32}$$

where the prefactor has the value 25 mV. The typical concentration ratios yield voltages on the scale of $60 - 70$ mV.

One of the key developments of HH, and Cole & Cole before them,[8] was to take advantage of the large size of the squid axon to insert an electrode inside it, oriented parallel to the long axis. This allowed measurements of the electrical properties without any spatial effects (a "space clamp"), so that the unusual properties of the ion channels could be studied in isolation. The basic phenomenology of electrical impulse generation in an axon that was found is depicted in Fig. 7.7. In the absence of any stimulus, there is a "resting potential" difference of ~ 70 mV across the membrane. If a perturbation is made, say by injecting current into the system, that voltage can

[7] Hodgkin, A.L. and Huxley, A.F. A quantitative description of membrane current and its application to conductance and excitation in nerve. *J. Physiol.*, 117:500–544, 1952

[8] K.S. Cole. *Membranes, Ions and Impulses. A Chapter in Classical Biophysics*. University of California Press, Berkeley, 1968

be made more positive to see the reaction of the axon. Provided that perturbation is sufficiently small, it will relax back to the resting potential on the scale of $\sim 1\,\mathrm{s}$. However, a perturbation beyond a threshold leads to a very large positive spike that corresponds to rapid "depolarization" (associated with an influx of Na$^+$, followed by a "repolarisation" process that slightly undershoots the resting potential ("hyperpolarisation"), associated with an outflow of K^+ ions, and finally a slower return to the resting potential. During that return the axon is resistant to further perturbations and is said to be in a "refractory period". An important feature of the action potential is the strong separation of time scales between the fast dynamics of sodium influx and the slow dynamics of potassium outflow.

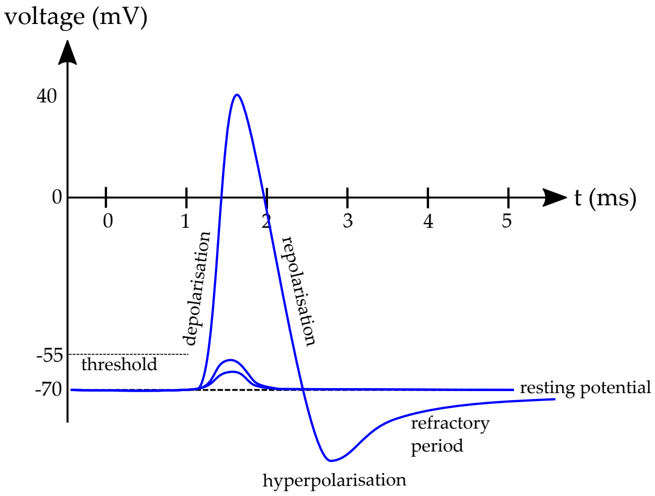

Figure 7.7: Schematic of an action potential.

A key component of the mathematical model of HH is its treatment of the nonlinear features of ion channels. In modern terminology, they are said to be "voltage-gated", meaning that their conductance is dependent on the voltage across the membrane. Thus, beyond the threshold, as the membrane depolarizes the conductance increases, allowing further depolarisation, and further increased conductance. The HH model combines this feature with the physics of current transport along the fluid-filled interior of axons to arrive at a complete model of action potential generation and propagation.

While able to capture the experimental data on voltages and currents during action potentials, the HH model is extremely cumbersome and not easily amenable to analytical study. A decade after their work came the papers by FitzHugh[9] and Nagumo, et al.[10] reporting vast simplifications of the dynamics to two coupled dynamical variables. Now known as the FitzHugh-Nagumo (FHN) model, this formulation is in fact remarkably rich and capable of exhibiting many properties beyond those associated with neurons, particularly in spatially-extended systems. We focus on aspects of this model with particular pedagogical value.

As a model of the nonlinear dynamics of voltages across a neuronal membrane, the FHN model consists of two variables, u and v

[9] FitzHugh, R. Impulses and physiological states in theoretical models of nerve membrane. *Biophys. J.*, 1:445–466, 1961

[10] Nagumo, J. and Arimoto, S. and Yoshizawa, S. An active pulse transmission line simulating nerve axon. *Proc. IRE*, 50:2061–2070, 1962

that obey the coupled ODEs

$$\dot{u} = c\left(v + u - \frac{1}{3}u^3 - V_0\right), \tag{7.33a}$$

$$\dot{v} = -\frac{1}{c}\left(u - a + bv\right), \tag{7.33b}$$

where V_0 is some external voltage, $0 < b < 1$, $1 - 2b/3 < a < 1$, and $c \gg 1$. The large value of c creates a separation of time scales such that the variable u is fast and v is slow.

The FHN model has an interesting variational structure that gives insight into its dynamical regimes. If we rewrite (7.34) and (7.35) as

$$\dot{u} = c\left(u - \frac{1}{3}u^3 - V_0\right) + cv, \tag{7.34}$$

$$\dot{v} = -\frac{1}{c}\left(-a + bv\right) - \frac{1}{c}u, \tag{7.35}$$

then we observe that a dynamic that incorporates only the first, bracketed terms on each of the right hand sides of (7.34) and (7.35) has the variational form

$$\dot{u} = -\frac{\partial E}{\partial u}, \quad \dot{v} = -\frac{\partial E}{\partial v}, \tag{7.36}$$

where

$$E = -\frac{1}{2}u^2 + \frac{1}{12}u^4 + V_0 u + \frac{1}{2}bv^2 - av, \tag{7.37}$$

and this truncated dynamics would drive E downward in time. On the other hand, including only the final terms in each equation yields

$$\dot{u} = cv, \quad \dot{v} = -\frac{1}{c}u, \tag{7.38}$$

which is just the Hamiltonian dynamics $\dot{u} = dH/dv, \dot{v} = -dH/du$ of a harmonic oscillator with

$$H = \frac{1}{2c}u^2 + \frac{1}{2}cv^2. \tag{7.39}$$

Equivalently, $\ddot{u} = -u$, so this structure naturally leads to oscillations at unit frequency. It is the competition between the dissipative and oscillatory tendencies of the dynamics that leads to interesting behaviour.

Finally, note that if we rescale time in (7.34) and (7.35) as $t = c\tau$, then they take the form

$$\epsilon u' = v + u - \frac{1}{3}u^3 - V_0, \tag{7.40a}$$

$$v' = -\left(u - a + bv\right), \tag{7.40b}$$

where $' = d/d\tau$ and $\epsilon = 1/c^2$. Thus, $\epsilon \ll 1$ for $c \gg 1$ and u is the fast variable while v is slow, a separation of time scales analogous to that in the Michaelis-Menten dynamics (7.9a) and (7.9b).

Next we examine the FHN dynamics in detail, considering first the case $V_0 = 0$. As is typical for dynamical systems analysis, we first establish fixed points, which must simultaneously satisfy $\dot{u} = 0$

and $\dot{v} = 0$, where the curves so defined in the $u - v$ plane are termed *nullclines*. In this case, they are

$$v = \frac{1}{3}u^3 - u, \tag{7.41a}$$

$$v = \frac{a-u}{b}. \tag{7.41b}$$

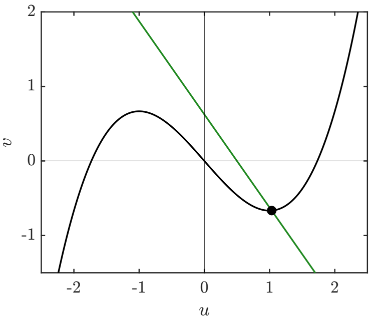

Figure 7.8: Nullclines of the FHN model for $V_0 = 0$. Obtained with `Figure_708_to_711_FitzHughNagumo.m`.

These are plotted in Fig. 7.8. The slope of the cubic nullcline at $u = 0$ is -1, whereas the second nullcline slope is $-1/b$, and thus the restriction $0 < b < 1$ guarantees the latter is larger and there is only a single intersection of the two nullclines, and therefore only one fixed point (FP) (u^*, v^*) and it can easily be shown that $u^* > 1$.

If we write the generic two-component dynamics as

$$\dot{u} = f(u, v), \tag{7.42a}$$

$$\dot{v} = g(u, v), \tag{7.42b}$$

then it is the Jacobian

$$J = \begin{pmatrix} f_u & f_v \\ g_u & g_v \end{pmatrix}, \tag{7.43}$$

where $f_u = \partial f / \partial u|_{u^*, v^*}$ that determines the stability of the FP. Perturbations of the form $u = u^* + \delta u$, $v = v^* + \delta v$ will grow as $e^{\sigma t}$ with the growth rate σ found as the solution to the condition

$$\begin{vmatrix} f_u - \sigma & f_v \\ g_u & g_v - \sigma \end{vmatrix} = 0, \tag{7.44}$$

or $\sigma^2 - \mathrm{Tr}\sigma + \mathrm{Det}$, where $\mathrm{Tr} = f_u + g_v$ and $\mathrm{Det} = f_u g_v - f_v g_u$, giving

$$\sigma_\pm = \frac{1}{2}\left\{\mathrm{Tr} \pm \sqrt{\mathrm{Tr}^2 - 4\mathrm{Det}}\right\}. \tag{7.45}$$

For stability, the real part of both roots must be negative, which requires $\mathrm{Tr} < 0$. If $0 < \mathrm{Det} < \mathrm{Tr}^2/4$ the square root is real but less then $|\mathrm{Tr}|$ and the roots are negative, while for larger Det the square root yields an imaginary contribution, and still the real part of σ is negative. Thus, stability requires $\mathrm{Tr} < 0$ and $\mathrm{Det} > 0$. In our case,

$$J\Big|_{z=0} = \begin{pmatrix} c(1 - u^{*2}) & c \\ -1/c & -b/c \end{pmatrix} \propto \begin{pmatrix} - & + \\ - & - \end{pmatrix} \tag{7.46}$$

and indeed $\mathrm{Tr} < 0$ and $\mathrm{Det} > 0$, so the FP is linearly stable.

Let us now examine the dynamics of the FHN model, starting from an initial condition that is only slightly displaced from the FP (u^*, v^*) for $V_0 = 0$. Obviously, if we keep $V_0 = 0$ then both u and v flow back to u^* and v^*. Next we turn on a small V_0 (0.2). The $\dot{v} = 0$ nullcline does not change but the $\dot{u}$ nullcline moves *upward* and the system adjusts to the new fixed point with only small excursions in both u and v from their initial values, as shown in Fig. 7.9. For these parameter values, $\mathrm{Tr}^2 - 4\mathrm{Det} < 0$ and the growth rates $\sigma_\pm$ are complex, leading to the observed spiraling approach to the FP.

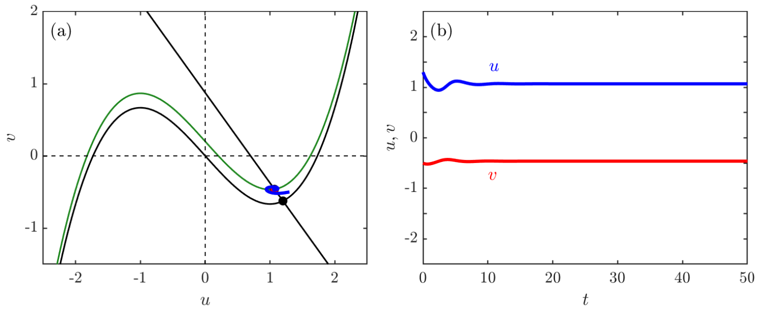

Figure 7.9: Dynamics of the FHN model I. (a) Phase plane analysis of trajectory (blue) starting from an initial condition near the $V_0 = 0$ fixed point, with $a = 0.7$, $b = 0.8$, $c = 3$ and $V_0 = 0.2$. Nullclines for $V_0 = 0$ are shown in black, that for $V_0 = 0.2$ in green. (b) Time courses of u (blue) and v (red). Obtained with `Figure_708_to_711_FitzHughNagumo.m`.

This behaviour is analogous to the cases in Fig. 7.7 in which the perturbation is sub-threshold.

Now we increase V_0 to 0.3. As shown in Fig. 7.10, this leads to a single large excursion in the phase plane that eventually converges to the new fixed point, and corresponds to a single "firing" event. Note that the variable u makes a large negative excursion, which can be interpreted as the depolarisation spike in Fig. 7.7, followed by a smaller positive peak that represents the hyperpolarisation epoch of the action potential. The separation of time scales can be seen in the slow decay of u to the FP relative to its initial very rapid change.

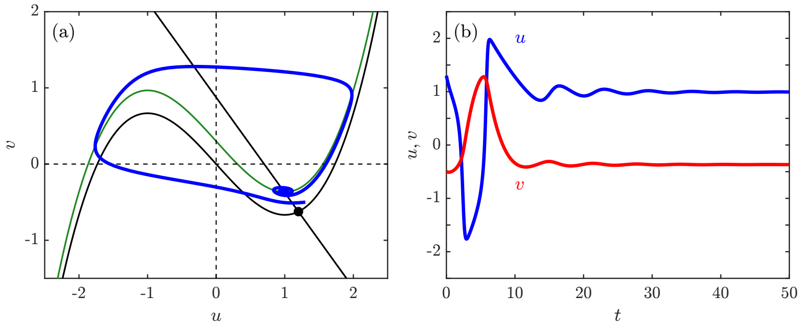

Figure 7.10: Dynamics of the FHN model II. As in Fig. 7.9 except for $V_0 = 0.3$, producing a single firing event. Obtained with `Figure_708_to_711_FitzHughNagumo.m`.

Finally, we increase V_0 to 0.4 and find that the system enters a regime of repeated large excursions in the phase plane, and thus a "train" of pulses (Fig. 7.11).

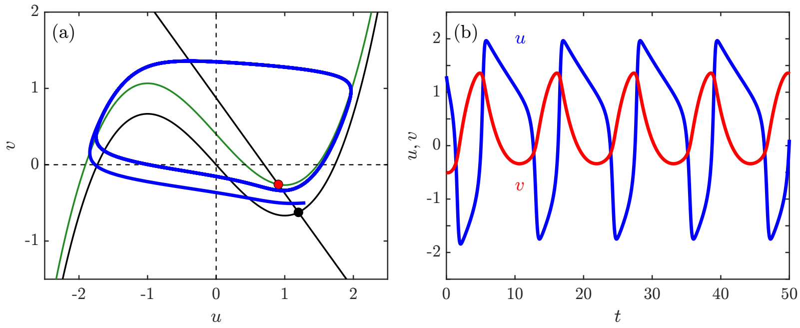

Figure 7.11: Dynamics of the FHN model III. As in Fig. 7.9 except for $V_0 = 0.4$, leading to periodic firing. Obtained with `Figure_708_to_711_FitzHughNagumo.m`.

We thus see that the FHN model in the slow inhibitor limit displays all the features of an "excitable medium" as exemplified by neurons; small-amplitude response for stimuli below a threshold, a single large-amplitude response beyond that threshold, and periodic large-amplitude responses for even higher stimuli. An important lesson from the study of this model is that the precise algebraic form of the nullclines is less important than the overall geometry. The excitable dynamics fundamentally requires nullcline intersection with a single stable fixed point. In the next section we consider the situation with multiple fixed points and a fast inhibitor.

7.3 *Front Propagation*

The possibility that a system of chemical reactions can lead to competing states, as discussed above, leads naturally to a scenario in which those states occupy different regions of space, separated by an identifiable boundary. To the extent that dynamics like the law of mass action pertain not only to well-mixed chemicals but also to populations of organisms, it is then not surprising that such "fronts" may exist in contexts such as the spread of infectious diseases or in population genetics. A classic example of the former is provided by the spread of the plague in the middle ages,[11] as shown by the advancing contour lines in Fig. 7.12. We see the boundary of infected regions steadily marching northward from the southern tips of Italy and France in late 1347 to Hungary and southern England by late 1348, Poland by late 1349 and beyond. The natural question that arises from this steady motion is to understand first why there is a sharp boundary and second, the factors that determine its speed.

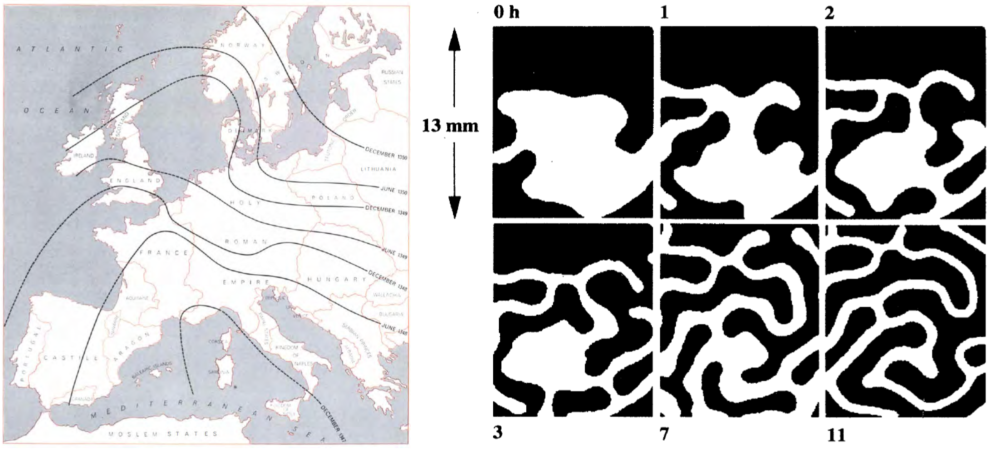

Figure 7.12: Examples of front propagation. Left: spread of the black plague in Europe during the Middle Ages, from Langer. Right: Interacting chemical fronts.

An example of sharp boundaries in chemical systems was discovered in 1993 in the ingenious experiments of Lee, McCormick, Ouyang and Swinney.[12] Using the ferrocyanide-iodate-sulfite system that was know to exhibit bistability in a well-mixed context, they engineered a two-compartment reaction vessel in which subset of the reactants were in each one, with a boundary between the two composed of a porous medium. This allowed chemical reactions within the medium, free of any contributions from fluid motion. Using a pH indicator to visualise the different chemical states, they discovered the patterns show in Fig. 7.12, in which the black-white boundaries repel each other, leading to a space-filling, labyrinthine pattern.

There are many ways, both formal and informal, to begin to un-

[11] Langer, W.L. The Black Death. *Sci. Am.*, 210:114–121, 1964

[12] Lee, K.J., McCormick, W.D., Ouyang, Q. and Swinney, H.L. Pattern Formation by Interacting Chemical Fronts. *Science*, 261:192–194, 1993

derstand the mathematical principles that underlie front propagation. Here we adopt a particular class of models that allows for a variety of behaviours and reveals the key techniques to determine the front speed. Building on the class of dynamics seen in the previous section, of the variational type $q_t = -\partial V/\partial q$, we include a diffusive contribution and work in one spatial dimension to obtain

$$u_t = m u_{xx} + f(u)\,, \qquad \text{where} \qquad f(u) = -\frac{\partial F}{\partial u}, \tag{7.47}$$

where we call the diffusion constant m for later convenience. By construction, the dynamics of u is variational, with the form

$$u_t = -\frac{\delta \mathcal{E}}{\delta u}, \quad \mathcal{E}[u] = \int_{-\infty}^{\infty} dx \left\{ \frac{1}{2} m \left(\boldsymbol{\nabla} u\right)^2 + F(u) \right\}. \tag{7.48}$$

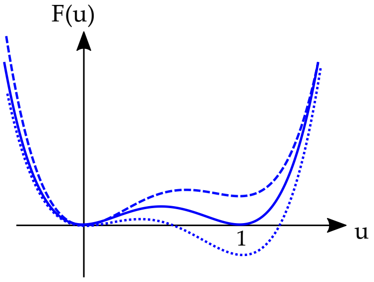

Figure 7.13: A potential $F(u)$ with two competing, locally stable states. As a parameter is varied, the more stable state switches from $u = 0$ (dashed) to $u = 1$ (dotted).

As we are considering the possibility of bistability, a useful general form of the function $F(u)$, shown in Fig. 7.13, has two local minima, potentially of distinct depths, separated by a local maximum at $u = 0$. There can be a kink or front either between the two locally stable states, or between the unstable state and one of the stable ones. Our goal is to find the speed of front propagation in these two cases.

A simple pedagogical model for $f(u)$ involves a cubic nonlinearity and a single control parameter r,

$$f(u) = -F'(u;r) = -u(u-r)(u-1), \quad \text{for } 0 < r < 1, \tag{7.49}$$

as shown in Fig. 7.14. There are three fixed points; $u = 0, 1$ and $u = r$. Integrating this function we obtain the effective potential

$$F(u;r) = \frac{1}{4}u^2(1-u)^2 + \left(r - \frac{1}{2}\right)\left(\frac{1}{2}u^2 - \frac{1}{3}u^3 - \frac{1}{12}\right). \tag{7.50}$$

In writing F this way, we have split out the first term, which represents the product of parabolas centred at $u = 0$ and $u = 1$, giving two minimum with $F(0;r) = F(1;r) = 0$, and the second term that represents the contribution of the control parameter to changing those depths. The result is a function such that $F(0;r) = -(r - 1/2)/12$ and $F(1;r) = (r - 1/2)/12$ and the difference between the two is

$$\Delta F = F(1;r) - F(0;r) = \frac{1}{6}\left(r - \frac{1}{2}\right). \tag{7.51}$$

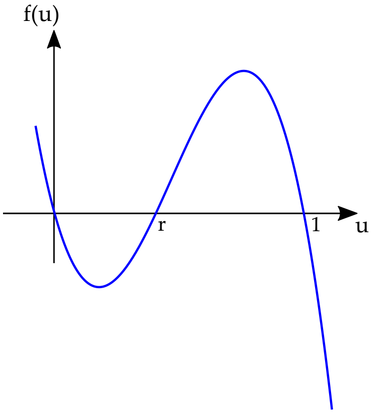

Figure 7.14: The function $f(u)$.

For $r < 1/2$ the state $u = 1$ is the more stable, and for $r > 1/2$ the state $u = 0$ is more stable.

We first need to establish some terminology and methods that will be useful for many subsequent discussions. The chief technique is a *linear stability analysis* of a stationary state. Let us examine in turn the three states $\bar{u}$ that are zeros of $f(u)$, and hence satisfy $u_t = 0$. In each case we write $u = \bar{u} + \hat{u}$, linearize the dynamics in $\hat{u}$, set $\hat{u} = e^{ikx}e^{\sigma t}$ and find the growth rate $\sigma(k)$ as a function of the wavevector k. If $\sigma < 0$, $\bar{u}$ is stable, while if $\sigma > 0$ $\bar{u}$ is unstable. In adopting this plane wave perturbation we are ignoring any lateral boundaries and the boundary conditions (Dirichlet or Neumann) that might pertain there. Such simplifications are not always justified (see Sec. 7.4.3), but here they are helpfully simplifying.

Near $\bar{u} = 0$, we find

$$\hat{u}_t = m\hat{u}_{xx} - r\hat{u}, \tag{7.52a}$$
$$\sigma = -r - mk^2. \tag{7.52b}$$

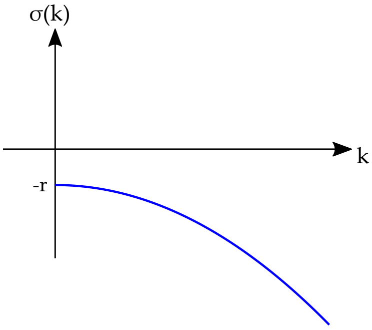

Figure 7.15: Growth rate for the stable state $\bar{u} = 0$.

As we see in Fig. 7.15, $\sigma < 0$ for all k, recalling that $0 \le r \le 1$. Hence, $\hat{u} = 0$ is stable.

Near $u = 1$, we have

$$\hat{u}_t = m\hat{u}_{xx} - (1-r)\hat{u}, \tag{7.53a}$$
$$\sigma = -(1-r) - mk^2, \tag{7.53b}$$

which is identical in form to the $\hat{u} = 0$ case, except for the exchange of $r \to 1 - r$, a symmetry of the full problem. This state is also therefore stable for all k. These results are intuitive, as from the form of F the states $u = 0$ and $u = 1$ are clearly stable minima in the absence of diffusion, and become even more so in its presence.

Near $u = r$, we find

$$\hat{u}_t = m\hat{u}_{xx} + r(1-r)\hat{u}, \tag{7.54a}$$
$$\sigma = r(1-r) - mk^2. \tag{7.54b}$$

Now the situation is qualitatively different (Fig. 7.16), as there is a band of modes extending from $k = 0$ to $k = \sqrt{r(1-r)/m}$ in which $\sigma > 0$, with stable modes at larger k. Intuitively, the maximum in F at $u = 0$ is unstable to homogeneous perturbations, and diffusion only restabilises perturbations at sufficiently small wavelengths.

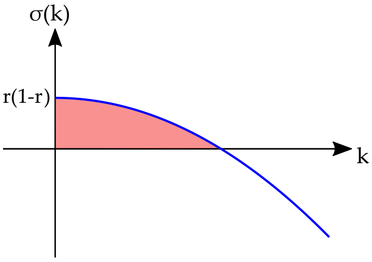

Figure 7.16: Growth rate for the state $\bar{u} = r$, showing band of unstable modes extending to $k = 0$.

Given the above, we now consider a front between the locally stable states at $u = 0$ and $u = 1$, with $u \to 1$ as $x \to -\infty$, $u \to 0$ as $x \to \infty$. By symmetry this front will not move if $r = 1/2$ because there is no energy difference between the states $u = 0$ and $u = 1$. For r near $1/2$ we expect the the front profile and speed can be obtained perturbatively relative to that at $r = 1/2$. We start with the governing PDE,

$$mu_{xx} - u\left(u - \frac{1}{2}\right)(u-1) = 0. \tag{7.55}$$

Multiplying through by u_x and integrating we find

$$\frac{1}{2}mu_x^2 - F(u;1/2) + C = 0, \tag{7.56}$$

where the integration constant C can be seen to vanish from the boundary conditions. As $F(u;1/2)$ has the simple form given in (7.50), a straightforward integration yields

$$u = \frac{1}{2}\left[1 - \tanh\left(\frac{x}{2\sqrt{2m}}\right)\right], \tag{7.57}$$

a profile (Fig. 7.17) whose width is controlled by m. Looking back at the energy functional $\mathcal{E}$ (7.48), we see that this front shape is a compromise between energetic penalties for gradients, which would be minimized by spreading out the transition region to infinite width, making U constant, and for deviations from the minima of F, which would be minimized by shrinking the transition region to zero width.

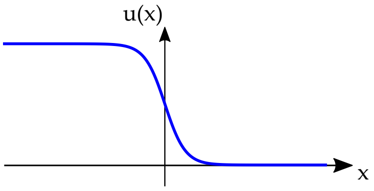

Figure 7.17: Stationary front shape for $r = 1/2$.

To determine the behavior of the case $r \neq 1/2$, we first derive a heuristic result and then proceed to a more systematic method. For the general equation of motion

$$u_t = m u_{xx} - F'(u), \tag{7.58}$$

subject to boundary conditions as above at $x = \pm\infty$. The only aspect of F of relevance is that it exhibits two locally stable minima of differing depth, as in Fig. 7.18.

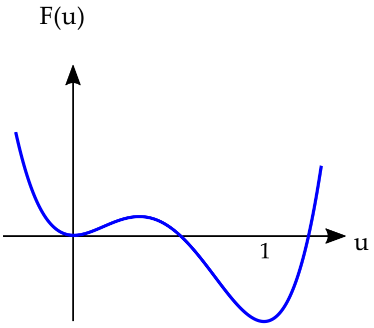

Figure 7.18: Generic form of $F(u)$.

After some initial transient we expect there to be a steady, uniformly moving solution, and thus seek a solution of the form

$$u(x,t) = U(x - vt), \tag{7.59}$$

for some unknown speed v. Substituting, we find

$$mU_{zz} + vU_z = -\{-F(U)\}', \tag{7.60}$$

which we have written in a form that suggests a parallel with the Newtonian dynamics. Eq. (7.60) is just the equation of motion of a particle of "mass" m, "position" U as a function of "time" z, with a drag coefficient v and an effective potential $-F(U)$ that is an upside-down version of the potential in Fig. 7.18.

In light of this mapping to a mechanical problem, we can view the problem of the front shape to be equivalent to the mechanical problem shown in Fig. 7.19: find the trajectory of a particle that starts at time $-\infty$ at position $U = 1$ and ends up as time goes to $+\infty$ at the local maximum of the effective potential at $U = 0$, as shown in Fig. 7.19. Since the particle must lose a precise amount of energy to arrive at the lower potential and neither over- nor undershoot, there is clearly a unique value of the friction coefficient v (front speed) to achieve $U \to 0$ as $t \to \infty$.

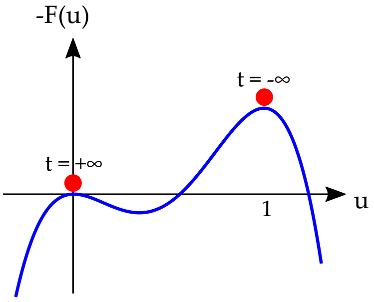

Figure 7.19: Effective potential in the stable-to-stable traveling-wave solution.

The stable-to-stable front propagation problem can be contrasted with the stable-to-unstable one using the above mechanical analogy. Now, the fictitious particle that starts at $U = 1$ must end up at the intermediate minimum of $-F$ at infinite time (Fig. 7.20). Clearly, any damping coefficient greater than the critical value v_c that allows the particle to asymptote to the lower maximum will suffice. Those just above v_c will lead to decaying oscillations of the particle around the minimum, while those above a second critical value will exhibit monotonic decay. It is quite often the case that the underlying nonlinear dynamics does exhibit a unique front speed. Often, the selected front speed is the critically-damped one, but the analysis of this problem is beyond the scope of this course.

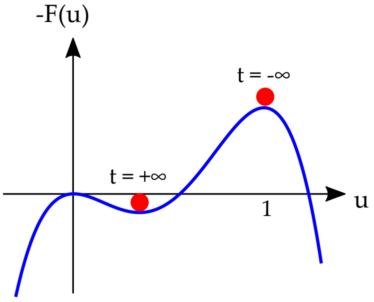

Figure 7.20: Mechanical analogy in the unstable-to-stable case.

For the stable-to-stable front we can obtain a quantitative understanding of the front speed by taking the traveling wave result (7.60), multiplying by U_z and integrating over the whole domain of z,

$$\frac{1}{2} m U_z^2 |_{-\infty}^{\infty} + v \int_{\infty}^{\infty} dz U_z^2 = \int_{-\infty}^{\infty} \frac{dF}{dU} \frac{dU}{dz} dz = -\Delta F, \tag{7.61}$$

where the energy difference ΔF is given in (7.51) and the first term vanishes by the boundary conditions at infinity. We can then formally solve for the front speed as

$$v = \frac{-\Delta F}{\int_{-\infty}^{\infty} dz U_z^2}. \tag{7.62}$$

It is intuitive that the front speed should be proportional to the energy difference ΔF. The denominator in this expression can be thought of as a kind of drag coefficient. In the spirit of a perturbative analysis near $r = 1/2$, the leading order front speed can be obtained by using the stationary front profile to evaluate the denominator. Rather than do complicated integrals with hyperbolic functions, we use the first integral (7.56) to obtain $U_z^2 = (1/2m)U^2(1-U)^2$ so, with appropriate choice of sign for the square root, $U_z = -(1/\sqrt{2m})U(1-U)$ and thus $\int U_z^2 dz = \int U_z dU = 1/6\sqrt{2m}$ and thus for the front transitioning from $u = 1$ at the left to $u = 0$ at the right the speed is

$$v = -\sqrt{2m}\left(r - \frac{1}{2}\right). \tag{7.63}$$

A consistency check is that when $r < 1/2$ the lower energy state is indeed $u = 1$ and the front moves to the right. We will return to this result in the context of a more systematic perturbation theory for a two-component reaction-diffusion system.

7.4 Reaction-Diffusion Systems

7.4.1 Phenomenology

Systems of reacting and diffusing chemicals are ubiquitous in biological systems, essentially responsible for life's processes inside cells. While many biological pathways involve numerous coupled reaction-diffusion systems, much of our intuition is built on models with just a few coupled species. In this section we review on a phenomenological level some considerations that indicate the importance of examining at least two coupled species in order to obtain pattern-forming dynamics consistent with observations. This leads naturally into Turing's analysis, covered in the next section.

Let us start from a generic structure of a nonlinear PDE that embodies diffusion and nonlinear chemical kinetics. From our previous discussions we expect the form

$$u_t = \mathcal{L}u + \mathcal{N}(u)\,, \quad \mathcal{L}u = \alpha u + D u_{xx}. \tag{7.64}$$

Here, we group both autocatalysis (coefficient α) and diffusion into the linear operator $\mathcal{L}$. Linearising around $u = 0$ we find the growth rate $\sigma(k) = \alpha - Dk^2$, seen before in Fig. 7.16, but now with α a free parameter. As we move from $\alpha < 0$ to $\alpha > 0$ the system goes from stable at all wavelengths to unstable in a band of modes that extends to $k = 0$, as in Fig. 7.21. This dynamical structure would not produce patterns with an identifiable (finite) length scale.

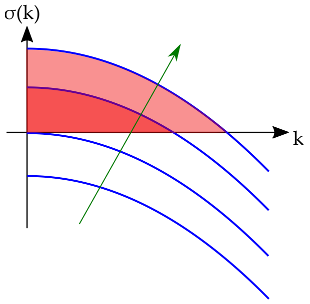

Figure 7.21: Generic growth rate curves for a single species reaction-diffusion system. Green arrow indicates progression of growth curves as a control parameter is increased.

A more interesting possibility is when both long and short wavelength are damped and $\sigma(k)$ is positive only in an interval of finite k, as in Fig. 7.22. This band of unstable modes typically increases in width as a control parameter is varied, starting from a critical k^* when σ has a maximum just crossing the axis. The maximum of σ defines the fastest growing mode, which often determines the wavelength $\lambda^* = 2\pi/k^*$ of the finite-amplitude patterns beyond onset.

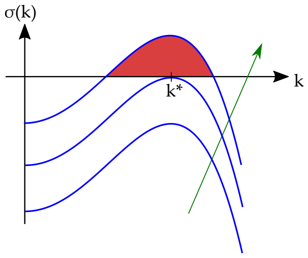

Figure 7.22: Growth curves for a pattern-forming system as a parameter is increased (green arrow).

In order to obtain growth curves like those in Fig. 7.22 with a single species we would require the linear operator $\mathcal{L}$ to have higher-order derivatives than those from diffusion. Respecting parity symmetry ($x \to -x$) of the underlying physics, σ should be a function only of even powers of k, and the simplest form would be

$$\sigma(k) \sim \alpha + \beta k^2 - \gamma k^4 + \dots, \tag{7.65}$$

corresponding to the linearised PDE

$$u_t = \alpha u - \beta u_{xx} - \gamma u_{4x} + \dots. \tag{7.66}$$

While mathematically acceptable, such higher-order derivative theories for a single degree of freedom are generally hard to justify *a priori* in a system of chemical reactions (although such terms do arise in the theory of elasticity), except in the presence of nonlocality (as discussed in Sec. 7.2). Instead, the simplest local mechanism to produce this is to couple two diffusive systems together, for then the linear stability problem involves a $2x2$ matrix with entries at most of order k^2, leading to a determinental equation of order k^4.

The FHN model considered in previous sections in the context of electrophysiology and front propagation provides the basis for a suitable two-variable reaction-diffusion system. In the language of chemical reactions, this generalised FHN model has two species: u, the *activator*, and v, the *inhibitor*. They evolve according to the PDEs

$$u_t = D\nabla^2 u + f(u) - \rho v \tag{7.67a}$$

$$\epsilon v_t = \nabla^2 v + \alpha u - \beta v, \tag{7.67b}$$

in which we have scaled space and time in order that the diffusion constant of the inhibitor is unity. The presence of the relative diffusion constant D can lead to the key phenomenon of *lateral inhibition* for $D \ll 1$ as we discuss below. We may be interested in a whole range of values for ϵ, not necessarily small. The various terms on the right hand sides of these equations have the following interpretation: The function $f(u)$ embodies autocatalysis and bistability in the manner we have discussed earlier in this chapter. The term $-\rho v$ represents inhibition of the activator due to the presence of the inhibitor. In the inhibitor equation, αu represents stimulation of the inhibitor due to the activator, while $-\beta v$ describes self-limitation of the inhibitor. Depending on the structure of f and the values of the various coefficients, the FHN model can produce homogeneous states, stripes and other periodic patterns, and even rotating spiral waves. It is a "standard model" of pattern formation.

As in our discussion of the FHN model of electrophysiology, this PDE version has a mixed variational structure.[13] To align this discussion with the literature, we adopt a slightly modified version that results in a more symmetric form by including an additional term linear in u in the activator dynamics and setting $\alpha = \beta = 1$,

$$u_t = D\nabla^2 u - u(u-r)(u-1) - \rho(v-u), \tag{7.68a}$$

$$\epsilon v_t = \nabla^2 v + u - v. \tag{7.68b}$$

The model is then invariant under the simultaneous transformations $u \to 1-u$, $v \to 1-v$ and $r \to 1-r$. It is now straightforward to verify that the model (7.68b) has the variational form

$$u_t = -\frac{\delta \mathcal{E}}{\delta u} - \rho v, \quad \epsilon v_t = -\frac{\delta \mathcal{E}}{\delta v} + u, \tag{7.69}$$

with

$$\mathcal{E} = \int d^2x \left\{ \frac{1}{2} D \left(\boldsymbol{\nabla} u\right)^2 + F(u) - \frac{1}{2}\rho u^2 + \frac{1}{2}\left(\boldsymbol{\nabla} v\right)^2 + \frac{1}{2} v^2 \right\}. \tag{7.70}$$

As before, terms involving the functional derivative of $\mathcal{E}$ are gradient flows, and the remaining terms have a Hamiltonian form($u_t = -\rho v$; $\epsilon v_t = u$). The FHN dynamics thus embodies a competition between terms which are dissipative and would tend to reach a stationary state and those which would produce oscillations. We focus on the regime in which gradient flow contributions dominate.

The presence of the parameter ϵ in the FHN inhibitor dynamics indicates that the *fast inhibitor limit* corresponds to $\epsilon \ll 1$, much like in the Michaelis-Menten dynamics where the enzyme-substrate complex dynamics are fast compared to those of the substrate itself. Let us adopt the steady-state approximation in which we set $\epsilon = 0$ without delving into the details of the short-time behaviour. As in the MM case, this assumption leads to an instantaneous-in-time relationship between u and v, except that here it is nonlocal in space,

$$(\nabla^2 - 1)v = -u. \tag{7.71}$$

This is mathematically equivalent to the Debye-Hückel problem we considered in Chapter 2 (Eq. 2.43), except with a source term on the r.h.s. The solution to (7.71) is given in terms of the Green's function G for the modified Helmholtz operator $(\nabla^2 - 1)$,

$$v(\mathbf{x}) = \int d\mathbf{x}' G(\mathbf{x}-\mathbf{x}')u(\mathbf{x}'). \tag{7.72}$$

In the two spatial dimensions we are considering here,

$$G(\mathbf{x}-\mathbf{x}') = \frac{1}{2\pi} K_0(|\mathbf{x}-\mathbf{x}'|), \tag{7.73}$$

where K_0 is the modified Bessel function. Thus, in the fast inhibitor limit we can rewrite the dynamics as a single *nonlocal* PDE for the activator,

$$u_t = D\nabla^2 u + f(u) + \rho u - \rho \int d\mathbf{x}' G(\mathbf{x}-\mathbf{x}')u(\mathbf{x}'). \tag{7.74}$$

[13] Goldstein, R.E., Muraki, D.J. and Petrich, D.M. Interface proliferation and the growth of labyrinths in a reaction-diffusion system. *Phys. Rev. E*, 53:3933–3957, 1996

The u dynamics is variational in this limit, $u_t = -\delta\mathcal{E}/\delta u$, where

$$\mathcal{E} = \int d\mathbf{x} \left\{ \frac{1}{2} D |\boldsymbol{\nabla} u|^2 + F(u) - \frac{1}{2}\rho u^2 \right\} \\ + \frac{1}{2}\rho \int d\mathbf{x} \int d\mathbf{x}' u(\mathbf{x}) G(\mathbf{x}-\mathbf{x}') u(\mathbf{x}'). \tag{7.75}$$

Not surprisingly, the new contribution is like the electrostatic energy of a system with a charge distribution $u(\mathbf{x})$ within screened electrostatics. This feature underlies the repulsion of fronts in the bistable regime of the FHN model, as we shall see below.

The fast-inhibitor limit provides us with a particularly simple context in which to understand a pattern-forming system instability, since the dynamics is contained within a single PDE. While those dynamics are nonlocal in real space they are local in Fourier space. Thus, if we linearise the equation of motion (7.74) around the state $u = 0$ and assume the usual plane wave perturbation, then the growth rate of modes is simply

$$\sigma(k) = -Dk^2 - r + \rho\frac{k^2}{1+k^2}. \tag{7.76}$$

Figure 7.23a shows a plot of $\sigma(k)$ for several values of ρ and r at fixed D, illustrating how this system conforms to the anticipated curve in our phenomenological discussion in Fig. 7.22. This is a particularly easy problem in which to see that a system of reaction-diffusion equations can lead to a finite-wavelength instability.

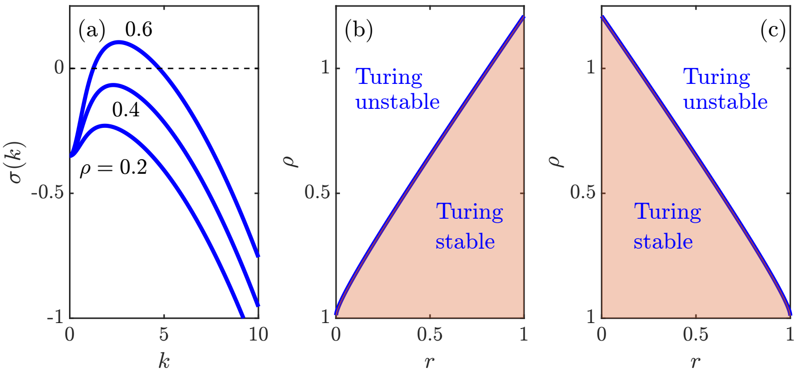

Figure 7.23: Stability analysis of FHN model in the fast-inhibitor limit. (a) Growth rate versus k for$D = 0.01$, $r = 0.35$ and various values of ρ as indicated. (b) Stability diagram around $u = 0$, using (7.77). (c) Stability diagram around $u = 1$. Obtained with `Figure_722_FHNgrowth.m`.

Given the shape of $\sigma(k)$ it is clear that the threshold for the onset of a finite-wavelength instability occurs with $\sigma(k) = 0$ and $d\sigma(k)/dk = 0$ for some k_c. The second relation may also be chosen as $d\sigma/dk^2 = 0$ for convenience. One finds the threshold lies along a curve in the $r - \rho$ plane given by

$$\rho_c(r) = \left(\sqrt{r} + \sqrt{D}\right)^2, \tag{7.77}$$

along which the critical wavevector is

$$k_c = \left(\frac{r}{D}\right)^{1/4}. \tag{7.78}$$

By the symmetry of the model, the stability condition for the $u = v = 1$ base state is $\rho(r) = \rho_c(1-r)$. These two boundaries are shown in Figs. 7.23b&c.

7.4.2 *Front Propagation II*

The FHN model provides a useful context to understand the problem of front propagation beyond the heuristic argument presented earlier. We begin by recalling from (7.57) that in the absence of inhibitor coupling the stationary front at $r = 1/2$ is

$$u(x) = \frac{1}{2}\left[1 - \tanh\left(\frac{x}{2\sqrt{2D}}\right)\right], \tag{7.79}$$

and thus the width of the transition region scales as $\sim \sqrt{D}$. This defines the length scale of the "inner" region of the problem, in the sense of matched asymptotics, while the "outer" region is on an $\mathcal{O}(1)$ scale. In addition to assuming $D \ll 1$, we shall also take ρ and $r - 1/2$ to be small to develop a systematic perturbation theory. We use the experimental image in Fig. 7.12 as motivation, and assign $u = 0$ to white and $u = 1$ to black.

In the outer region we rewrite the equations to put all small terms on the r.h.s. Assuming a one-dimensional system, we have

$$u(u-r)(u-1) = Du_{xx} - \rho\,(v-u) - u_t, \tag{7.80a}$$

$$v_{xx} - v + u = \epsilon v_t, \tag{7.80b}$$

where in addition to the terms in D, ρ, and $r - 1/2$, we have also anticipated that the explicit time dependence will be small. As there may be multiple interfaces between black and white, we write the outer solution as

$$u(x) \sim u^0(x) = \begin{cases} 1 & \text{(black)} \\ 0 & \text{(white),} \end{cases} \tag{7.81}$$

and

$$v^0_{xx} - v^0 \sim -u^0 = -\begin{cases} 1 & \text{(black)} \\ 0 & \text{(white).} \end{cases} \tag{7.82}$$

Thus, v^0 solves a screened electrostatic Poisson problem with a source given by the piecewise constant function $u^0(x)$.

If $r \neq 1/2$, the front positions $Q^j(t)$ will evolve in time, and it is thus natural to examine the inner region of the front using the shifted and rescaled variable

$$\eta = \frac{x - Q^j(t)}{\sqrt{D}}, \tag{7.83}$$

and to consider u as a function of η; $u = U(\eta, t)$. Now define the scaled operator from the r.h.s. of the governing PDE at $r = 1/2$ as

$$S[U] = U_{\eta\eta} - U\,(U - 1/2)\,(U-1)\,. \tag{7.84}$$

Then a simple calculation shows that the inner equations are

$$S[U] = -\frac{Q^j_t}{\sqrt{D}}U_\eta - 6\Delta F U\,(U-1) + \rho\,(V-U) + U_t, \tag{7.85a}$$

$$V_{\eta\eta} = D\,(V-U) + \epsilon D V_t. \tag{7.85b}$$

The homogeneous solutions to the left-hand sides of (7.85a) and (7.85b) are simply the stationary front solution

$$U^0(\eta) = \frac{1}{2}\left[1 \mp \tanh\left(\frac{\eta}{2\sqrt{2}}\right)\right], \tag{7.86a}$$

$$V^0 = v^0\left(x = Q^j\right). \tag{7.86b}$$

Here, as $\eta \to \pm\infty$ these match the outer solutions u^0 and v^0 at the interface where $x \to (Q^j)^{\pm}$. The $\mp$ sign is fixed by the orientation of the front; a negative sign corresponds to a left-to-right transition from $u = 0$ to $u = 1$. Note that to leading order the inhibitor field is constant within this inner region, much as the substrate concentration in Michaelis-Menten kinetics is constant in the inner region.

The leading-order front solutions are stationary, but they will be set in motion by the effects of the r.h.s. terms in (7.85a) and (7.85b). We assume the asymptotic balance

$$\frac{Q^j_t}{\sqrt{D}} \sim \Delta F \sim \rho \ll 1. \tag{7.87}$$

We thus assume that the solutions can be expanded in a regular series in the small parameter ρ of the form

$$U(\eta) \sim U^0(\eta) + \rho U^1(\eta) + \cdots. \tag{7.88}$$

Substituting into (7.85a) and (7.85b), and identifying the derivative of the operator S as

$$S'[U^1] = U^1_{\eta\eta} - F''(U^0; 1/2)U^1, \tag{7.89}$$

we find the zeroth order solution to be simply the homogeneous solutions already identified, and the first-order correction to satisfy

$$\begin{aligned}\rho S'[U^1] = &\left[\pm\frac{Q^j_t}{\sqrt{2D}} + 6\Delta F\right] U^0(U^0 - 1)\\ &+ \rho\left[v^0(x = Q^j) - U^0\right],\end{aligned} \tag{7.90}$$

where we used the identity $\sqrt{2}U^0_\eta = \mp U^0(U^0 - 1)$ to combine terms. We have arrived at a key result in the theory of pattern formation, for Eq. 7.90 is an inhomogeneous PDE in which the forcing on the r.h.s. involves an unknown quantity (here, Q^j_t). As the full solution to (7.90) is the sum of its homogeneous solution and a particular solution of the inhomogeneous equation, the requirement that the solution be bounded (a condition which itself can be deduced from the original PDE formulation of the problem) requires that the r.h.s. be orthogonal to the nullspace of the operator on the l.h.s. This is the so-called Fredholm alternative. The nullspace of interest can be deduced easily since the operator

$$\partial_{\eta\eta} - F''(U^0; 1/2) \tag{7.91}$$

is exactly that which appears if we differentiate the equation $S[\mathcal{U}] = 0$ with respect to η, implying that the nullspace is the function $\mathcal{U}^0_\eta$.

This result can also be understood as a consequence of the translational invariance of the stationary front $\mathcal{U}^0$, and the fact that the derivative ∂_η is the infinitesimal generator of displacements.

With this result for the nullspace, and defining the inner product for the orthogonality condition as

$$\langle U^0_\eta, \bullet \rangle \equiv \int_{-\infty}^{\infty} d\eta U^0_\eta \bullet . \tag{7.92}$$

the orthogonality of the r.h.s. of (7.90) yields immediately

$$Q^j_t \sim \mp 6\sqrt{2D} \left\{ \Delta F + \rho \left[v^0(x = Q^j) - \frac{1}{2} \right] \right\} . \tag{7.93}$$

This general result can now be applied to several important cases. For the case of a single front, we consider the case of a pattern that is white ($u = 0$) to the right of an interface at $x = Q(t)$ and black ($u = 1$) to the left,

$$u^0(x) \sim \begin{cases} 1, & x \leq Q(t) \\ 0, & x \geq Q(t). \end{cases} \tag{7.94}$$

The outer inhibitor field can be solved in a piecewise manner with continuity at the black/white boundary, yielding

$$v^0(x) \sim \begin{cases} 1 - \frac{1}{2}e^{+(x-Q)}, & x \leq Q(t) \\ \frac{1}{2}e^{-(x-Q)}, & x \geq Q(t). \end{cases} \tag{7.95}$$

Here, we have imposed the condition that $v^0 \to 0$ at infinity. Since $v^0(x = Q) = 1/2$, there is no $\mathcal{O}(\rho)$ correction to the front speed,

$$Q_t = -6\sqrt{2D}\Delta F = -\sqrt{2D} \left(r - \frac{1}{2} \right) , \tag{7.96}$$

in complete agreement with the heuristic argument (7.63).

A second application of the one-dimensional front propagation result (7.93) is the case of two fronts of opposite sense facing each other, with

$$u^0(x) = \begin{cases} 1 & -\infty < x \leq -Q(t) \\ 0 & -Q(t) \leq x \leq +Q(t) \\ 1 & +Q(t) \leq x < +\infty. \end{cases} \tag{7.97}$$

The solution of the outer inhibitor field is

$$v^0(x) = \begin{cases} 1 - \sinh Q \, e^{+x} & -\infty < x \leq -Q(t) \\ e^{-Q} \cosh x & -Q(t) \leq x \leq +Q(t) \\ 1 - \sinh Q \, e^{-x} & +Q(t) \leq x < +\infty. \end{cases} \tag{7.98}$$

and thus the inhibitor contribution to the front speed is

$$v^0(x = Q) = \frac{1}{2} \left(1 - e^{-2Q} \right) , \tag{7.99}$$

and the speed itself is

$$Q_t = \sqrt{2D} \left[\left(r - \frac{1}{2} \right) + 3\rho e^{-2Q} \right] . \tag{7.100}$$

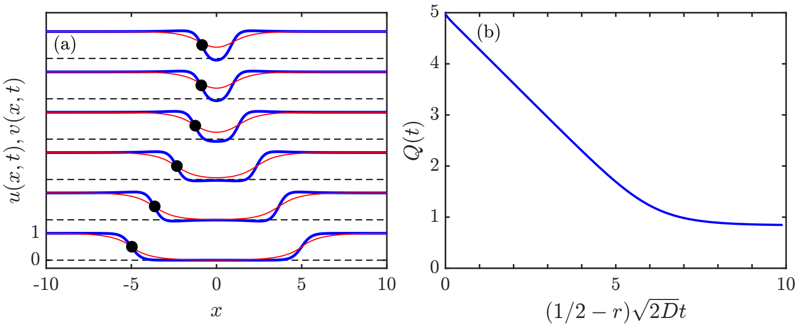

Figure 7.24: Dynamics of two nearby fronts in the FHN model. Parameters are $D = 0.04$, $r = 0.4$ and $\rho = 0.15$. (a) Activator (blue) and inhibitor (red) fields for two approaching fronts, with time increasing upwards. Black circles indicate location of $u = 1/2$, the midpoint of the fronts. (b) Distance between fronts as a function of scaled time. Obtained with `Figure_724_FHNfronts.m`.

Figure 7.24 shows the time evolution of a pair of fronts that start at a large separation Q, with $r < 1/2$, so the $u = 1$ state is more stable and the two fronts approach one another. As they do, the leftward (negative) speed from the term $r - 1/2$ will be reduced as Q decreases by the repulsive effect of the overlapping inhibitor fields, eventually vanishing at a distance

$$Q^* = -\frac{1}{2}\ln\left(\frac{1/2-r}{3\rho}\right). \tag{7.101}$$

This front repulsion is one of the best indications of the effects of lateral inhibition and the separation of length scales between the activator and the inhibitor. Although the predictions of this leading-order asymptotic analysis typically require the parameter ρ to be as small as ~ 0.01 for a quantitative match, the phenomenology is well-captured by this coarsest level of approximation.

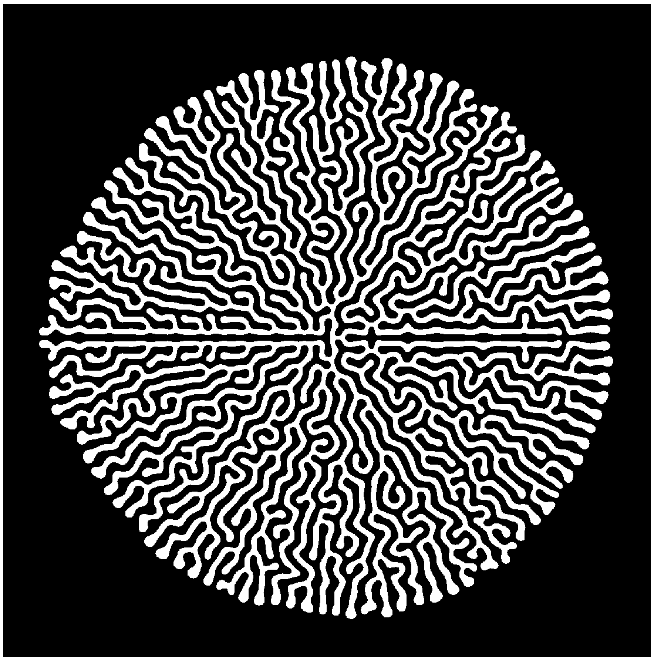

Figure 7.25: Labyrinthine pattern formation in the FHN model. Parameters are $D = 0.01$, $r = 0.52$, and $\rho = 0.15$. Obtained with `Figure_725_labyrinth.m`.

The results above show that there is a regime in parameter space in which nearby approaching fronts repel each other sufficiently strongly as to be prevented from crossing. This is the basic observation of Lee, et al. seen in Fig. 7.12. The FHN model in the fast-inhibitor limit also reproduces the labyrinthine patterns seen in experiment. Figure 7.25 shows the result of a particularly large-scale numerical study that illustrates this scenario.

7.4.3 The Turing Instability

Now we move to a more general discussion of the possible pattern-forming instabilities of a two-species model. We consider a model with concentrations $u(\mathbf{x},t)$ and $v(\mathbf{x},t)$ in a domain $\mathcal{D}$ on whose boundary $\partial\mathcal{D}$ there are the no-flux conditions $\hat{\mathbf{n}}\cdot\boldsymbol{\nabla}u\Big|_{\partial\mathcal{D}} = \hat{\mathbf{n}}\cdot\boldsymbol{\nabla}v\Big|_{\partial\mathcal{D}} = 0$. The pair of reaction-diffusion equations is written in the general form familiar from our discussion of the FHN model, Eqs. 7.42a and 7.42b, only now including two possibly different diffusion constants,

$$u_t = D_u\nabla^2 u + f(u,v), \tag{7.102a}$$

$$v_t = D_v\nabla^2 v + g(u,v), \tag{7.102b}$$

where f and g are some smooth functions of their arguments, representing, for example, autocatalysis, feedback inhibition, etc.

The central result of Turing involves the possible instability of a reaction-diffusion system under conditions in which the homogeneous (i.e. reaction-only) dynamics is stable. Thus, we assume that f and g are such that there exists a uniform steady state (u^*,v^*) such that $f(u^*,v^*) = g(u^*,v^*) = 0$ whose Jacobian entries f_u, f_v, g_u, g_v at (u^*,v^*) are such that

$$\mathrm{Tr} = f_u + g_v < 0 \quad \text{and} \quad \mathrm{Det} = f_u g_v - f_v g_u > 0. \tag{7.103}$$

If we perturb this homogeneous steady state with spatial-temporal variations $u = u^* + p(\mathbf{x},t)$, $v = v^* + q(\mathbf{x},t)$, we obtain the dynamics

$$p_t = f_u p + f_v q + D_u\nabla^2 p, \tag{7.104a}$$

$$q_t = g_u p + g_v q + D_v\nabla^2 q, \tag{7.104b}$$

Next we observe that it will always be possible to expand a function in the domain $\mathcal{D}$ as an infinite series of eigenfunctions of the Helmholtz equation

$$\nabla^2 w_k + k^2 w_k = 0 \quad (\text{in } \mathcal{D}), \tag{7.105a}$$

$$\hat{\mathbf{n}}\cdot\boldsymbol{\nabla}w_k = 0 \qquad (\text{on } \partial\mathcal{D}). \tag{7.105b}$$

For example, in $d = 1$ with $\mathcal{D} = [0,L]$, we have $w_k = \cos(kx)$ and $k = n\pi/L$ for integers n. If we then write

$$p = \sum_k \hat{p}_k \mathrm{e}^{\sigma(k)t} w_k(\mathbf{x}), \tag{7.106a}$$

$$q = \sum_k \hat{q}_k \mathrm{e}^{\sigma(k)t} w_k(\mathbf{x}), \tag{7.106b}$$

then the 2×2 stability matrix takes the modified form

$$J_{\mathrm{mod}} = \begin{pmatrix} f_u & f_v \\ g_u & g_v \end{pmatrix} + \begin{pmatrix} -D_u k^2 & 0 \\ 0 & -D_v k^2 \end{pmatrix}. \tag{7.107}$$

While the trace of J_{mod} is just the sum of the traces of the two matrices in (7.107),

$$\text{Tr}_{\text{mod}} = \underbrace{f_u + g_v}_{\text{Tr<o}} - (D_u + D_v)k^2, \tag{7.108}$$

and is < 0 since $f_u + g_v < 0$ by hypothesis and the diffusive contributions are manifestly negative. In contrast, it is generally the case for two matrices M and N that

$$\text{Det}(M + N) \neq \text{Det}(M) + \text{Det}(N). \tag{7.109}$$

Were this to be true, then Det_{mod} would be positive definite since Det > 0 and the determinant of the second matrix in (7.107) is $D_u D_v k^4 > 0$ as well. In fact, the modified determinant is

$$\text{Det}_{\text{mod}} = \underbrace{f_u g_v - f_v g_u}_{\text{Det>0}} - \underbrace{(D_u g_v + D_v f_u)\,k^2}_{?} + \underbrace{D_u D_v k^4}_{>0}, \tag{7.110}$$

where we have indicated that it is the middle term whose sign is unclear. For convenience, write (7.110) as $\text{Det}_{\text{mod}} = Ak^4 - Bk^2 + C$, with $A, C > 0$. Recalling that the general condition for stability is a negative trace and positive determinant, the criterion for *instability* can be summarized as follows: The reaction-diffusion system is unstable if, for some k among the allowed wavevectors, $\text{Det}_{\text{mod}} < 0$. Given the known signs in (7.110), this can only happen if $B > 0$, or

$$D_u g_v + D_v f_u > 0, \tag{7.111}$$

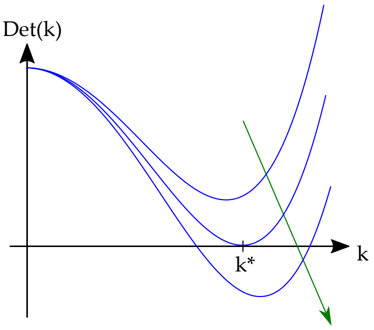

Figure 7.26: Behaviour of the determinant of the stability matrix.

for then, as shown in Fig. 7.26, the function Det_{mod}(k) can dip below the axis. If we let $x = k^2$, then any crossings of the axis must be roots of the quadratic equation $Ax^2 - Bx + C = 0$, namely $x_\pm = (1/2)(B \pm \sqrt{B^2 - 4AC})$, with $B^2 - 4AC > 0$. The smallest value of B is that which yields the tangent condition shown as the middle curve in Fig. 7.26, namely $B = \sqrt{4AC}$.

We thus conclude that the onset of the instability occurs at

$$D_v f_u + D_u g_v = \sqrt{4 D_u D_v \text{Det}}. \tag{7.112}$$

If we define the diffusivity ratio

$$d = \frac{D_u}{D_v}, \tag{7.113}$$

then the condition (7.112) is

$$f_u + d g_v = 2\sqrt{d\text{Det}}. \tag{7.114}$$

Since the r.h.s. of this equation is clearly > 0, we conclude that the conditions that the homogeneous fixed point be stable and that the diffusive system be unstable require the simultaneous equations

$$f_u + g_v < 0, \tag{7.115a}$$
$$f_u + d g_v > 0, \tag{7.115b}$$

which clearly is not possible when $d = 1$. That is, a Turing instability at equal diffusivities is not possible. Without loss of generality, we can take $D_u > D_v$, so $d > 1$. If both conditions (7.115b) hold then f_u and g_v must have opposite signs, with $f_u < 0$ and $g_v > 0$. Then we can view the onset condition (7.114) as a quadratic equation for $\sqrt{d}$, whose solution is

$$\sqrt{d} = \frac{\sqrt{\text{Det}} + \sqrt{\text{Det} - f_u g_v}}{g_v}. \tag{7.116}$$

This is the minimum possible value for the diffusivity ratio for there to be a Turing instability. Finally, we can examine the typical length scale of the instability. Since $\text{Det}_{\text{mod}} = Ax^2 - Bx + C$, where $x = k^2$, the condition of a double root of $\text{Det}_{\text{mod}}(k) = 0$ implies a turning point which yields the condition

$$k_c = \sqrt{\frac{C}{A}} = \left(\frac{\text{Det}}{D_u D_v}\right)^{1/2}. \tag{7.117}$$

We may now summarize the fundamental features of the Turing instability. A two-component reaction-diffusion system that has a stable homogeneous FP can, given suitable conditions on the ratio of diffusion constants of the two species, become unstable to a finite-wavelength instability. As we have focused only on the results obtainable from linear stability analysis we can say nothing definite about the fate of a system beyond the instability, but generically one expects the nonlinearities in the system to stabilize finite-amplitude patterns with a characteristic wavelength close to that at onset. As in many other pattern-forming systems,[14] the precise form of those nonlinearities will determine the symmetries of the patterns, distinguishing for example between stripes and spots.

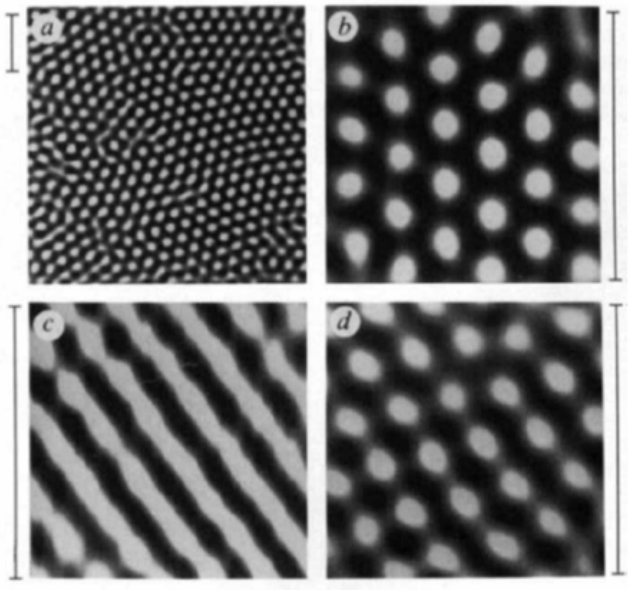

Figure 7.27: Experimental observation of the Turing instability in a reaction-diffusion system, from Ref. 18.

Although Turing's work appeared in 1952, it was many years before the biological community took notice of it[15] in any significant way, but many of the terms he introduced in describing his model, such as "morphogen", have been adopted universally in biology (and

[14] Cross, M.C. and Hohenberg, P.C. Pattern formation outside of equilibrium. *Rev. Mod. Phys.*, 65:851–1112, 1993

[15] E.F. Keller. *Making sense of life. Explaining biological development with models, metaphors, and machines*. Harvard University Press, Cambridge, MA, 2003

biological physics). It was not until the early 1990s that experimental demonstrations of his predictions were reported. These were reported by the Bordeaux group of Castets et al.,[16,17] followed by the Austin group of Ouyang and Swinney.[18] Each of these groups utilized experimental setups with two reservoirs, each containing a non-reacting subset of chemicals, linked by a porous medium in which reactions occur without the disturbing effects of fluid motion. The Austin experiments in particular allowed for spatially extended patterns in two dimensions without any imposed chemical gradients. Figure 7.27 shows that patterns in the form of stripes and hexagonal arrays of spots were observed.

We close this section by noting that reaction-diffusion patterns are not restricted to the stationary ones we have focused on. Turing himself in his 1952 paper established that there could be oscillatory patterns as well, and we know this is the case from studies of the Belousov-Zhabotinski reaction,[19] which is famous for the rotating spiral waves and target patterns that it produces (Fig. 7.28). Similar patterns occur in a range of living systems, from slime molds to the heart, as we mention below. The remarkable history of the discovery of oscillatory dynamics in the BZ reaction also provides a case study in the resistance of science to new ideas.[20]

Figure 7.28: Patterns in the Belousov-Zhabotinski reaction in a Petri dish.

7.5 *Chemotaxis and Instabilities*

7.5.1 *Background*

In previous sections we focused on systems of chemical reactions described by reaction-diffusion equations consisting of nonlinear kinetic terms and spatial diffusion, of the general form (7.102a) and (7.102b). Of significance is the feature that the diffusive contributions are "diagonal" in the sense that the stability matrix (7.107) has diffusive terms only on the diagonal and there is no spatial cross-talk between the various components. Here we turn to the continuum description of populations of organisms that includes their directed motion in response to chemical cues, the phenomenon of "chemotaxis". We shall see that this leads to fundamentally distinct contributions to the governing PDEs, with new kinds of instabilities.

7.5.2 *Phenomenology of Dictyostelium discoideum*

Chemotaxis is found in a broad range of organisms, from bacteria to much larger and more complex eukaryotes. Among these many organisms, one can distinguish between those that swim through a fluid environment (like bacteria) and those that move along solid surfaces (like amoebae). In this section we focus on the historically important case of crawling cells of the species *Dictyostelium discoideum*, whose striking behaviour motivated many important developments in the theory of biological pattern formation.

The genus *Dictyostelium* consists of eukaryotic cells that are abundant in the soil, typically feeding on bacteria. They are often referred

[16] Castets, V. and Dulos, E. and Boissonade, J. and De Kepper, P. Experimental evidence of a sustained standing Turing-type nonequilibrium chemical pattern. *Phys. Rev. Lett.*, 64:2953–2956, 1990

[17] De Kepper, P. and Castets, V. and Dulos, E. and Boissonade, J. Turing-type chemical patterns in the chlorite-iodide-malonic acid reaction. *Physica D*, 49:161–169, 1991

[18] Ouyang, Q. and Swinney, H.L. Transition from a uniform state to hexagonal and striped Turing patterns. *Nature*, 352:610–612, 1991

[19] K.S. Kiprijanov. Chaos and beauty in a beaker: The early historyof the Belousov-Zhabotinsky reaction. *Ann. Phys. (Berlin)*, 3-4:233–237, 2016

[20] A.T. Winfree. The prehistory of the Belousov-Zhabotinsky oscillator. *J. Chem. Educ.*, 8:661–663, 1984

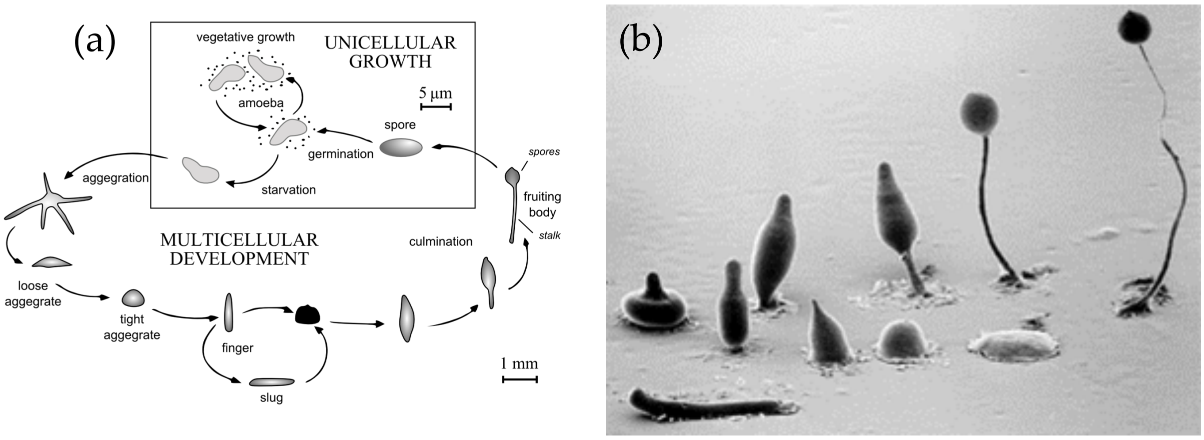

Figure 7.29: Life cycle of *Dictyostelium discoideum*.

to as cellular "slime moulds", and can exhibit both uni- and multicellular lifestyles. as shown in Fig. 7.29. In the former the cells feed on bacteria in the environment and have little if any communication with each other. In the typical laboratory setting of a population of cells on the surface agar in a petri dish, one observes that if the cells are starved for some hours, they transition to a multicellular form by a complex, multistage process that begins with the emission of the chemical cyclic AMP (cAMP) by a small subset of cells dispersed throughout the population. This diffuses to neighbouring cells, stimulating them to release cAMP as well, eventually leading to process in which the population produces a mixture of target patterns or rotating spiral waves of cAMP (Fig. 7.30). Although it is difficult to visualise the cAMP directly, as the waves pass over cells they trigger cellular elongation that can be visualised.

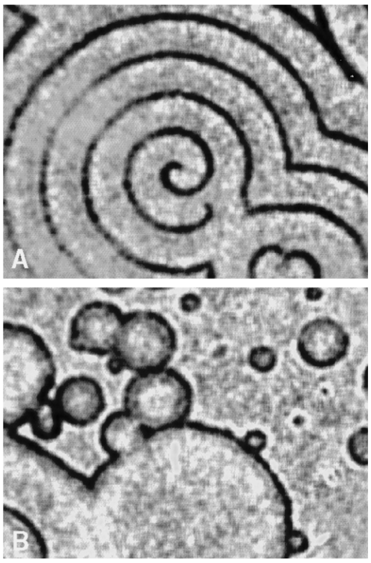

Figure 7.30: Spiral and target patterns in *Dictyostelium discoideum*.

As the wave pattern continues for some hours, cells begin to chemotactically move toward the centers of the targets or spirals and to form there a dense multicellular body. As shown in Fig. 7.31, that body then can migrate as a whole and eventually differentiates into an upright form with a base, stalk, and spores at the top. These spores can persist in a dormant state for long periods of time, eventually carried away by wind or passing animals to regions with more available food, where they germinate and produce again the unicellular organisms, completing the life cycle.

Figure 7.31: The streaming instability in *Dictyostelium discoideum*.

7.5.3 *The Keller-Segel Model*

During the phase of the *Dictyostelium* life cycle in which chemotaxis begins in response to the waves of cAMP, it is observed that while the gradients of cAMP are in the radial direction with respect to the centres of targets or spirals, the initially uniform distribution of cells develops *transverse* modulations leading eventually to the formation of radial "streams" along which cells move toward the centres. This transverse instability (Fig. 7.31) was the subject of the important work by Keller and Segel in the early 1970s,[21,22] which established the key continuum formulation of chemotactic dynamics.

As Keller and Segel point out, a full description of chemical waves

[21] Keller, E.F. and Segel, L.A. Initiation of slime mold aggregation viewed as an instability. *J. Theor. Biol.*, 26:399–415, 1970

[22] Keller, E.F. and Segel, L.A. Model for chemotaxis. *J. Theor. Biol.*, 30:225–234, 1971

and chemotaxis requires at least four variables; the cell concentration $n(\mathbf{x},t)$, the concentration $c(\mathbf{x},t)$ of cyclic AMP, the concentration $p(\mathbf{x},t)$ of phosphodiesterase, an enzyme that breaks down cAMP, and the concentration $i(\mathbf{x},t)$ of the cAMP-phosphodiesterase complex that is the intermediate in the chemical reaction. The starting point for their model is the assumption that cell division can be neglected on the time scales of interest in the experiment, and thus there is a conservation law

$$n_t = -\boldsymbol{\nabla} \cdot \mathbf{J}_n, \tag{7.118}$$

where the flux $\mathbf{J}_n$ of cells has both diffusive and chemotactic contributions, written as

$$\mathbf{J}_n = -D_n \boldsymbol{\nabla} n + nr\boldsymbol{\nabla} c. \tag{7.119}$$

The first term is the standard Fickian form, where D_n is the cellular diffusion constant that arises from their random motions, and is assumed constant. The chemotactic part embodies the fact that cells climb up gradients in cAMP, and we can interpret the product $r\boldsymbol{\nabla} c$ as the typical chemotactic velocity $\mathbf{u}_c$, with the coefficient $r(c)$ potentially varying with the cAMP concentration. Keller and Segel suggest a form $r(c) \sim 1/c$ that represents logarithmic sensing ($\mathbf{u}_c \sim \boldsymbol{\nabla} \ln c$). Thus, the variable n evolves according to the nonlinear equation

$$n_t = D_n \nabla^2 n - \boldsymbol{\nabla} \cdot (nr\boldsymbol{\nabla} c)\,. \tag{7.120}$$

Even if the response function $r(c)$ is a constant, the system is quadratically nonlinear.

The time evolution of cAMP reflects not only production by the amoebae at a rate $nf(c)$, where f is the production rate per cell, but also diffusion with diffusivity D_c and enzyme kinetics via the reaction scheme

$$\mathrm{cAMP} + \mathrm{PDE} \underset{\mathrm{k}_{-1}}{\overset{\mathrm{k}_1}{\rightleftharpoons}} \mathrm{C} \xrightarrow{\mathrm{k}_2} \mathrm{PDE} + \mathrm{P}, \tag{7.121}$$

where the product is non-chemotactically active. Combining all the contributions, and including diffusion of each species, we obtain the cAMP, PDE, and complex dynamics

$$c_t = D_c \nabla^2 c + nf(c) - k_1 cp + k_{-1} i, \tag{7.122a}$$
$$i_t = D_i \nabla^2 p + k_1 cp - (k_{-1} + k_2)\, i, \tag{7.122b}$$
$$p_t = D_p \nabla^2 p + ng(c,p) - k_1 cp + (k_{-1} + k_2)\, i. \tag{7.122c}$$

To make progress with the full dynamics (7.120), (7.122a), (7.122b), and (7.122c), KS invoke the steady-state assumption for the complex,

$$k_1 cp - (k_{-1} + k_2)\, i = 0, \tag{7.123}$$

ignore diffusion of i, and utilise conservation of PDE via $p + i = p_0$, where p_0 is the initial concentration of PDE. As in MM kinetics, this removes two equations from the problem, leaving only the coupled dynamics of the cell and cAMP concentrations, in the form

$$n_t = D_n \nabla^2 n - \boldsymbol{\nabla} \cdot (rn\boldsymbol{\nabla} c), \tag{7.124a}$$

$$c_t = D_c \nabla^2 c + nf(c) - k(c)c, \tag{7.124b}$$

where

$$k(c) = \frac{p_0 k_2}{K_m + c}, \tag{7.125}$$

and $K_m = (k_{-1} + k_2)/k_1$ as in Michaelis-Menten theory.

There are obvious similarities between this two-variable system and that of the Turing instability in the sense that the reaction terms on the r.h.s. of (7.124b) embody production and degradation in familiar forms. But the key difference is the presence of an *off-diagonal* spatial term from chemotaxis. To explore the consequences of this term, we simplify the model further by taking the functions $k(c)$ and $f(c)$ to be constant, and also assuming the chemotactic response coefficient r to be independent of c, yielding

$$n_t = D_n \nabla^2 n - r\boldsymbol{\nabla} \cdot (n\boldsymbol{\nabla} c), \tag{7.126a}$$

$$c_t = D_c \nabla^2 c + \alpha n - \beta c, \tag{7.126b}$$

Noting that the n dynamics is of a flux form that conserved the total number of cells, we choose the mean cell concentration n_0 as a reference value for rescaling. The homogeneous system has an obvious fixed point at

$$c_0 = \frac{\alpha}{\beta} n_0. \tag{7.127}$$

Setting

$$\rho = \frac{n}{n_0}, \quad \chi = \frac{c}{c_0}, \quad T = \alpha t, \quad \mathbf{X} = \sqrt{\frac{\alpha}{D_c}}\mathbf{x}, \tag{7.128}$$

we obtain

$$\rho_T = d\nabla^2 \rho - \gamma \boldsymbol{\nabla} \cdot (\rho \boldsymbol{\nabla} \chi), \tag{7.129a}$$

$$\chi_T = \nabla^2 \chi + \lambda (\rho - \chi), \tag{7.129b}$$

where

$$d = \frac{D_n}{D_c}, \quad \gamma = \frac{r c_0}{D_c}. \tag{7.130}$$

With this simplified system we linearise around the fixed point $\rho = \chi = 1$ via

$$\rho = 1 + \delta\rho, \qquad \chi = 1 + \delta\chi, \tag{7.131}$$

to obtain the linearised system

$$\delta\rho_T = d\nabla^2 \delta\rho - \gamma \nabla^2 \delta\chi, \tag{7.132a}$$

$$\delta\chi_T = \nabla^2 \delta\chi + \lambda (\delta\rho - \delta\chi), \tag{7.132b}$$

The linear stability problem for perturbations of the form $\mathrm{e}^{i\mathbf{k}\cdot\mathbf{X} + \sigma T}$ is

$$\begin{vmatrix} -dk^2 - \sigma & \gamma k^2 \\ \lambda & -k^2 - \lambda - \sigma \end{vmatrix} = 0. \tag{7.133}$$

If we write this as $\sigma^2 + b\sigma + c = 0$, with $b = \lambda + (d+1)k^2$ and $c = k^2[d(\lambda + k^2) - \lambda\gamma]$, then $\sigma_\pm = (-b \pm \sqrt{b^2 - 4c})/2$. It is straightforward to show that

$$b^2 - 4c = (1-d)^2 k^4 + 2\lambda(1 - d + 2\gamma)k^2 + \lambda^2, \tag{7.134}$$

and for $d < 1$ is positive. With b manifestly positive, we deduce that if $c > 0$ we have stability (both roots negative). In other words, the condition for stability is

$$\lambda\,(\gamma - d) < dk^2. \tag{7.135}$$

To understand the relevant values of k for this criterion to hold we Taylor expand the root σ_+ for small k, obtaining

$$\sigma_+(k) = (\gamma - d)\,k^2 - \frac{1}{\lambda}\left(1 - d + 2\gamma^2\right)k^4 + \cdots . \tag{7.136}$$

The same calculation shows that σ_- is strictly negative as $k \to 0$. Thus, we see that as γ increases beyond d the first instability is at $k = 0$, but there is a peak in the growth rate for $\gamma > d$, at $k^* \sim \sqrt{\gamma - d}$. Figure 7.32 shows $\sigma_+(k)$ as γ increases.

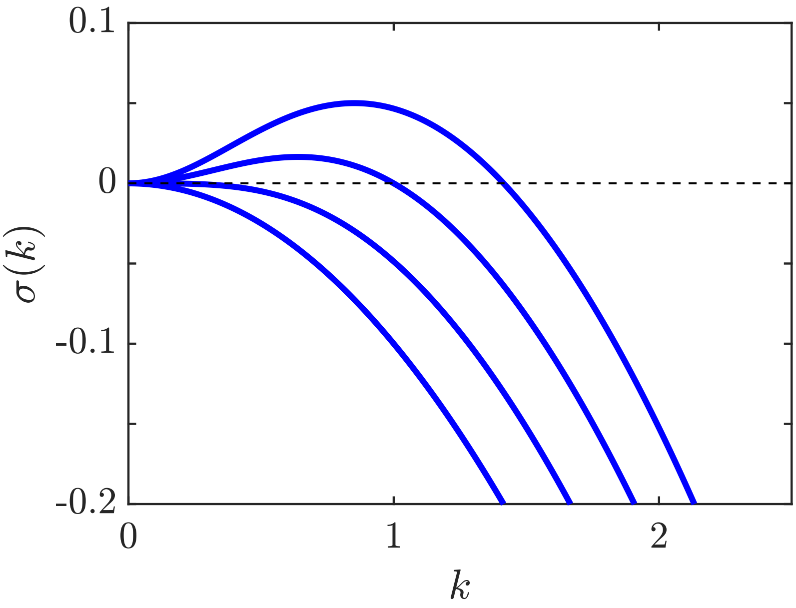

Figure 7.32: Growth rate $\sigma_+(k)$ versus k in the Keller-Segel model. Parameters are $d = 0.1$, $\lambda = 1$, and $\gamma = 0.1, 0.2, 0.3, 0.4$. Obtained with `Figure_732_KSgrowth.m`.

This instability represents the transverse instability seen in the *Dictyostelium* system (Fig. 7.31). The mechanism behind the instability is the essential feedback between cAMP production and chemotaxis; a local fluctuation in cell density n leads to a local increase in cAMP production, producing a gradient in cAMP the points toward the peak in n, followed by chemotaxis toward the peak, further increasing n. The potential runaway effect is tamed by both cell and cAMP diffusion, along with cAMP degredation. Under certain circumstances, in certain spatial dimensions, a true singularity does arise from the KS equations.[23]

[23] Childress, S. and Percus, J.K. Nonlinear Aspects of Chemotaxis. *Math. Biosci.*, 56:217–237, 1981

8
Bibliography

M. Abramowitz and I.A. Stegun. *Handbook of Mathematical Functions with Formulas, Graphs, and Mathematical Tables*. Dover Publications Inc, Mineola, N.Y., 1965.

B. Audoly and Y. Pomeau. *Elasticity and Geometry: From hair curls to the non-linear response of shells*. Oxford University Press, Oxford, UK, 2010.

K.S. Cole. *Membranes, Ions and Impulses. A Chapter in Classical Biophysics*. University of California Press, Berkeley, 1968.

B. Corti. *Osservazioni Microscopische sulla Tremella e sulla Circolazione del Fluido in Una Pianta Acquajuola*. Appresso Giuseppe Rocchi, Lucca, Italy, 1774.

P.G. de Gennes. *Scaling Concepts in Polymer Physics*. Cornell University Press, Ithaca, NY, 1979.

M. Doi and S.F. Edwards. *The Theory of Polymer Dynamics*. Clarendon Press, Oxford, UK, 1986.

P.J. Flory. *Principles of Polymer Chemistry*. Cornell University Press, Ithaca, NY, 1953.

H. Goldstein. *Classical Mechanics*. Addison-Wesley, Boston, MA, 2nd edition, 1980.

van Leeuwenhoek, A. IV. Part of a letter from Mr. Antony van Leeuwenhoek, concerning the worms in sheeps livers, gnats, and animalcula in the excrements of frogs. *Philos. Trans. R. Soc.*, 22: 509–18, 1700.

Brown, R. XXVII. A brief account of microscopical observations made in the months of June, July, and August, 1827, on the particles contained in the pollen of plants; and on the general existence of active molecules in organic and inorganic bodies. *Philos. Mag.*, 4:161–73, 1828.

Engelmann, T.W. Ueber Sauerstoffausscheidung van Pfalnzenzellen im Mikrospektrum. *Pflüger, Arch.*, 27:485–89, 1882.

Goldstein, R.E. Coffee stains, cell receptors, and time crystals: Lessons from the old literature. *Phys. Today*, 71:32–38, 2018.

Berg, H.C. and Purcell, E.M. Physics of chemoreception. *Biophys. J.*, 20:193–219, 1977.

Goldstein, R.E. Are theoretical 'results' results? *eLife*, 7:e40018, 2018.

Maxwell, J.C. Remarks on the mathematical classification of physical quantities. *Proc. London Math. Soc.*, s1-3:224, 1869.

Purcell, E.M. Life at low Reynolds number. *Am. J. Phys.*, 45:1–11, 1977.

Goldstein, R.E. Green algae as model organisms for biological fluid dynamics. *Annu. Rev. Fluid Mech.*, 47:343–375, 2015.

Einstein, A. Investigations on the theory of the Brownian movement. *Ann. d. Phys.*, 17:549–560, 1905.

Sutherland, W. LXXV. A dynamical theory of diffusion for non-electrolytes and the molecular mass of albumin. *Phil. Mag.*, 9: 781–785, 1905.

Haldane, J.B.S. On Being the Right Size, 1927.

Hodgkin, A.L. and Huxley, A.F. A quantitative description of membrane current and its application to conductance and excitation in nerve. *J. Physiol.*, 117:500–544, 1952.

Hyman, A.A., Weber, C.A. and Jülicher, F. Liquid-liquid phase separation in biology. *Annu. Rev. Cell Dev. Biol.*, 30:39–58, 2014.

Mayer, J.E. Statistical Mechanics of Condensing Systems. I. *J. Chem. Phys.*, 5:67, 1937.

van der Waals, J.D. *Over de Continuiteit van den Gas- en Vloeistoftoestand (On the continuity of the gas and liquid state)*. PhD thesis, Leiden University, 1873.

Holstein, B.R. The van der Waals interaction. *Am. J. Phys.*, 69:441, 2001.

Herzfeld, K.F. On atomic properties which make an element a metal. *Phys. Rev.*, 29:701–705, 1927.

Bussi, Y., Shimoni, E., Weiner, A., Kapon, R., Charuvi, D., Nevo, R., Efrati, E., Reich, Z. Fundamental helical geometry consolidates the plant photosynthetic membrane. *Proc. Natl. Acad. Sci. USA*, 116:22366–22375, 2019.

Sculley, M.J., Duniec, J.T., Thorne, S.W., Chow, W.S. and Boardman, N.K. The stacking of chloroplast thylakoids. Quantitative analysis of the balance of forces between thylakoid membranes of chloroplasts, and the role of divalent ions. *Arch. Bioch. Biophys.*, 201: 339–346, 1980.

Hamaker, H.C. The London-van der Waals attraction between spherical particles. *Physica*, 4:1058–1072, 1937.

Verwey, E.J.W. and Overbeek, J.Th.G. *Theory of the Stability of Lyophobic Colloids*. Elsevier Publishing Company, Inc., New York, 1948.

Debye, P. and Hückel, E. The theory of electrolytes. I. Lowering of freezing point and related phenomena (English translation). *Phys. Zeit.*, 24:185–206, 1923.

Marcelja, S. and Radić, N. Repulsion of interfaces due to boundary water. *Chem. Phys. Lett.*, 42:129–130, 1976.

Lis, L.J., McAlister, M., Fuller, N., Rand, R.P. and Parsegian, V.A. Interactions between neutral phospholipid bilayer membranes. *Biophys. J.*, 37:657, 1982.

Canham, P.B. The minimum energy of bending as a possible explanation of the biconcave shape of the human red blood cell. *J. Theor. Biol.*, 26:61–76, 1970.

Helfrich, W. Elastic properties of lipid bilayers: theory and possible experiments. *Z. Naturforsch. Teil C*, 28:693–703, 1973.

Winterhalter, M. and Helfrich, W. Effect of surface charge on the curvature elasticity of membranes. *J. Phys. Chem.*, 92:6865–6867, 1988.

Goldstein, R.E., Pesci, A.I. and Romero-Rochín, V. Electric double layers near modulated surfaces. *Phys. Rev. A*, 41:5504–5515, 1990.

Duplantier, B., Goldstein, R.E., Romero-Rochín, V. and Pesci, A.I. Geometrical and topological aspects of electric double layers near curved surfaces. *Phys. Rev. Lett.*, 65:508–511, 1990.

Balian, R. and Bloch, C. Distribution of eigenfrequencies for the wave equation in a finite domain: I. Three-dimensional problem with smooth boundary surface. *Ann. Phys. (N.Y.)*, 60:401–447, 1970.

Planck, M. Ueber das Gesetz der Energieverteilung im Normalspektrum. *Ann. Phys.*, 309:553–563, 1901.

Brown, R. XXIV. Additional remarks on active molecules. *Philos. Mag.*, 6:161–66, 1829.

Ashkin, A. Acceleration and trapping of particles by radiation pressure. *Phys. Rev. Lett.*, 24:156–159, 1970.

Ashkin, A. Optical trapping and manipulation of neutral particles using lasers. *Proc. Natl. Acad. Sci. USA*, 94:4853–4860, 1997.

Neuman, K.C. and Block, S.M. Optical trapping. *Rev. Sci. Instrum.*, 75:2787–2809, 2004.

Powers, T.R. Dynamics of filaments and membranes in a viscous fluid. *Rev. Mod. Phys.*, 82:1607–1631, 2010.

J. Gray and G.J. Hancock. The propulsion of sea-urchin spermatozoa. *J. Exp. Biol.*, 32:802, 1955.

Oberbeck, A. Ueber stationäre Flüssigkeitsbewegungen mit Berücksichtigung der inneren Reibung. *J. Reine. Angew. Math.*, 81:62–80, 1876.

Keller, J.B. and Rubinow, S.I. Slender-body theory for slow viscous flow. *J. Fluid Mech.*, 75:705–714, 1976.

Goldstein, R.E. and Langer, S.A. Nonlinear dynamics of stiff polymers. *Phys. Rev. Lett.*, 75:1094–1097, 1995.

Wiggins, C.H., Riveline, D., Ott, A. and Goldstein, R.E. Trapping and wiggling: elastohydrodynamics of driven microfilaments. *Biophys. J.*, 74:1043–1060, 1998.

Kantsler, V. and Goldstein, R.E. Fluctuations, dynamics, and the stretch-coil transition of single actin filaments in extensional flows. *Phys. Rev. Lett.*, 108:038103, 2012.

Fygenson, D.K., Marko, J.F. and Libchaber, A. Mechanics of microtubule-based membrane extension. *Phys. Rev. Lett.*, 79:4497–4500, 1997.

Machin, K.E. Wave propagation along flagella. *J. Exp. Biol.*, 35:796–806, 1958.

Wiggins, C.H. and Goldstein, R.E. Flexive and propulsive dynamics of elastica at low Reynolds number. *Phys. Rev. Lett.*, 80:3879–3882, 1998.

Stokes, G.G. On the effect of the internal friction of fluids on the motion of pendulums. *Trans. Camb. Philos. Soc.*, IX, part II:8–106, 1851.

Gadêlha, H. and Gaffney, E.A. Flagellar ultrastructure suppresses buckling instabilities and enables mammalian sperm navigation in high-viscosity media. *J. Roy. Soc. Interface*, 16:20180668, 2019.

Camalet, S. and Jülicher, F. and Prost, J. Self-organized beating and swimming of internally driven filaments. *Phys. Rev. Lett.*, 82:1590–1593, 1999.

Young, Y.-N. and Shelley, M.J. Stretch-coil transition and transport of fibers in cellular flows. *Phys. Rev. Lett.*, 99:058303, 2007.

Batchelor, G.K. Slender-body theory for particles of arbitrary cross-section in Stokes flow. *J. Fluid Mech.*, 44:419–440, 1970.

H. Manikantan and D. Saintillan. Buckling transition of a semiflexible filament in extensional flow. *Phys. Rev. E*, 92:041002, 2015.

Herrmann, G. and Bungay, R.W. On the stability of elastic systems subjected to nonconservative forces. *J. Appl. Mech.*, 31:435–440, 1964.

De Canio, G., Lauga, E. and Goldstein, R.E. Spontaneous oscillations of elastic filaments induced by molecular motors. *J. R. Soc. Interface*, 14:20170491, 2017.

Schneider, M.B., Jenkins, J.T. and Webb, W.W. Thermal fluctuations of large quasi-spherical bimolecular phospholipid vesicles. *J. Phys.*, 45:1457–1472, 1984.

Helfrich, W. Size distributions of vesicles: the role of the effective rigidity of membranes. *J. Physique*, 47:321–329, 1986.

Milner, S.T. and Safran, S.A. Dynamical fluctuations of droplet microemulsions and vesicles. *Phys. Rev. A*, 36:4371–4379, 1987.

Zhong-can, O.-Y. and Helfrich, W. Bending energy of vesicle membranes: General expressions for the first, second, and third variation of the shape energy and applications to spheres and cylinders. *Phys. Rev. A*, 39:5280–5288, 1989.

Helfrich, W. Steric interactions of fluid membranes in multilayer systems. *Z. Naturforsch. Teil A*, 33:305–315, 1978.

Helfrich, W. and Servuss, R.-M. Undulations, steric interaction and cohesion of fluid membranes. *Nuovo Cim.*, 3D:137–151, 1984.

Marko, J.F. and Siggia, E.D. Fluctuations and supercoiling of DNA. *Science*, 265:506–508, 1994.

Lipowsky, R. and Leibler S. Unbinding transitions of interacting membranes. *Phys. Rev. Lett.*, 56:2541–2544, 1986.

Brochard, F. and Lennon, J.F. Frequency spectrum of the flicker phenomenon in erythrocytes. *J. Physique*, 36:1035–1047, 1975.

Wiener, N. Generalized harmonic analysis. *Acta Math.*, 55:117–258, 1930.

Khintchine, A. Korrelationstheorie der stationären stochastischen Prozesse. *Math. Ann.*, 109:604–615, 1934.

Tadjbakhsh, I. and Odeh, F. Equilibrium States of Elastic Rings. *J. Math. Anal. Appl.*, 18:59–74, 1967.

Foster, B., Verschueren, N., Knobloch, E. and Gordillo, L. Pressure-driven wrinkling of soft inner-lined tubes. *New J. Phys.*, 24:013026, 2022.

Evans, E. and Yeung, A. Hidden dynamics in rapid changes of bilayer shape. *Chem. Phys. Lipids*, 73:39–56, 1994.

Powers, T.R., Huber, G. and Goldstein, R.E. Fluid-membrane tethers: minimal surfaces and elastic boundary layers. *Phys. Rev. E*, 65: 041901, 2002.

Drescher, K. and Goldstein, R.E. and Michel, N. and Polin, M. and Tuval, I. Direct Measurement of the Flow Field around Swimming Microorganisms. *Phys. Rev. Lett.*, 105:168101, 2010.

Guasto, J.S. and Johnson, K.A. and Gollub, J.P. Oscillatory Flows Induced by Microorganisms Swimming in Two Dimensions. *Phys. Rev. Lett.*, 105:168102, 2010.

Brumley, D.R., Wan, K.Y., Polin, M. and Goldstein, R.E. Flagellar synchronization through direct hydrodynamic interactions. *eLife*, 3:e02750, 2014.

J. Gray. The mechanism of ciliary movement. *Proc. R. Soc. Lond. B*, 93:104–121, 1922.

Leptos, K.C. and Chioccioli, M. and Furlan, S. and Pesci, A.I. and Goldstein, R.E. Phototaxis of *Chlamydomonas* arises from a tuned adaptive photoresponse shared with multicellular Volvocine green algae. *Phys. Rev. E*, 107:014404, 2023.

Rothschild, L. Measurement of Sperm Activity before Artificial Insemination. *Nature*, 163:358–359, 1949.

Taylor, G.I. Analysis of the swimming of microscopic organisms. *Proc. R. Soc. A*, 209:447–461, 1951.

Elfring, G.J. and Lauga, E. Synchronization of flexible sheets. *J. Fluid Mech.*, 674:163–173, 2011.

Higdon, J.J.L. The hydrodynamics of flagellar propulsion: helical waves. *J. Fluid Mech.*, 94:331–351, 1979.

Niedermayer, T., Eckhardt, B. and Lenz, P. Synchronization, phase locking, and metachronal wave formation in ciliary chains. *Chaos*, 18:037128, 2008.

Adler, R. A Study of Locking Phenomena in Oscillators. *Proc. IEEE*, 61:1380–1385, 1973.

Polin, M., Tuval, I., Drescher, K., Gollub, J.P. and Goldstein, R.E. *Chlamydomonas* swims with two 'gears' in a eukaryotic version of run-and-tumble locomotion. *Science*, 325:487–490, 2009.

Goldstein, R.E., Polin, M. and Tuval, I. Noise and synchronization in Pairs of Beating Eukaryotic Flagella. *Phys. Rev. Lett.*, 103:168103, 2009.

Goldstein, R.E., Polin, M. and Tuval, I. Emergence of Synchronized Beating during the Regrowth of Eukaryotic Flagella. *Phys. Rev. Lett.*, 107:148103, 2011.

Drescher, K., Leptos, K.C., Tuval, I., Ishikawa, T., Pedley, T.J. and Goldstein, R.E. Dancing *Volvox*: Hydrodynamic Bound States of Swimming Algae. *Phys. Rev. Lett.*, 102:168101, 2009.

Drescher, K., Dunkel, J., Cisneros, L.H., Ganguly, S. and Goldstein, R.E. Fluid dynamics and noise in bacterial cell-cell and cell-surface scattering. *Proc. Natl. Acad. Sci. USA*, 108:10940–10945, 2011.

Kessler, J.O. Gyrotactic buoyant convection and spontaneous pattern formation in algal cell cultures. In M.G. Velarde, editor, *Nonequilibrium Cooperative Phenomena in Physics and Related Fields*, pages 241–248. Plenum Press, New York, 1984.

Pedley, T.J. and Kessler, J.O. The orientation of spheroidal microorganisms swimming in a flow field. *Proc. R. Soc. Lond. B*, 231:47–70, 1987.

Faxén, H. Der Widerstand gegen die Bewegung einer starren Kugel in einer zähen Flüssigkeit, die zwischen zwei parallelen ebenen Wänden eingeschlossen ist. *Ann. Phys.*, 373:89–119, 1922.

Hohenegger, C. and Shelley, M. J. Dynamics of complex biofluids. In *New Trends in the Physics and Mechanics of Biological Systems: Lecture Notes of the Les Houches Summer School: Volume 92, July 2009*. Oxford University Press, 2011.

Jeffery, G.B. The motion of ellipsoidal particles immersed in a viscous fluid. *Proc. R. Soc. Lond. A*, 102:161–179, 1922.

J.R. Blake. Note on the image system for a stokeslet in a no-slip boundary. *Math. Proc. Camb. Phil. Soc.*, 70:303–310, 1971.

Blake, J.R. and Chwang, A.T. Fundamental singularities of viscous flow. Part I: The image systems in the vicinity of a stationary no-slip boundary. *J. Eng. Math.*, 8:23–29, 1974.

Higdon, J.J.L. The generation of feeding currents by flagellar motions. *J. Fluid Mech.*, 94:305–330, 1979.

Berke, A.P. and Turner, L. and Berg, H.C. and Lauga, E. Hydrodynamic Attraction of Swimming Microorganisms by Surfaces. *Phys. Rev. Lett.*, 101:038102, 2008.

Squires, T.M. Effective pseudo-potentials of hydrodynamic origin. *J. Fluid Mech.*, 443:403–412, 2001.

Turing, A. The chemical basis of morphogenesis. *Phil. Trans. R. Soc. London B*, 237:37–72, 1952.

Michaelis, L. and Menten, M.L. Die Kinetik der Invertinwirkung (English translation). *Biochem. Z.*, 49:333–369, 1913.

Lineweaver, H. and Burk, D. The Determination of Enzyme Dissociation Constants. *J. Am. Chem. Soc.*, 56:658–666, 1934.

Monod, J., Wyman, J. and Changeux, J.-P. On the Nature of Allosteric Transitions - a Plausible Model. *J. Mol. Biol.*, 12:88–118, 1965.

P. Cluzel, M. Surette and S. Leibler. An ultrasensitive bacterial motor revealed by monitoring signaling proteins in single cells. *Science*, 287:1652–1655, 2000.

FitzHugh, R. Impulses and physiological states in theoretical models of nerve membrane. *Biophys. J.*, 1:445–466, 1961.

Nagumo, J. and Arimoto, S. and Yoshizawa, S. An active pulse transmission line simulating nerve axon. *Proc. IRE*, 50:2061–2070, 1962.

Langer, W.L. The Black Death. *Sci. Am.*, 210:114–121, 1964.

Lee, K.J., McCormick, W.D., Ouyang, Q. and Swinney, H.L. Pattern Formation by Interacting Chemical Fronts. *Science*, 261:192–194, 1993.

Goldstein, R.E., Muraki, D.J. and Petrich, D.M. Interface proliferation and the growth of labyrinths in a reaction-diffusion system. *Phys. Rev. E*, 53:3933–3957, 1996.

Cross, M.C. and Hohenberg, P.C. Pattern formation outside of equilibrium. *Rev. Mod. Phys.*, 65:851–1112, 1993.

Castets, V. and Dulos, E. and Boissonade, J. and De Kepper, P. Experimental evidence of a sustained standing Turing-type nonequilibrium chemical pattern. *Phys. Rev. Lett.*, 64:2953–2956, 1990.

De Kepper, P. and Castets, V. and Dulos, E. and Boissonade, J. Turing-type chemical patterns in the chlorite-iodide-malonic acid reaction. *Physica D*, 49:161–169, 1991.

Ouyang, Q. and Swinney, H.L. Transition from a uniform state to hexagonal and striped Turing patterns. *Nature*, 352:610–612, 1991.

K.S. Kiprijanov. Chaos and beauty in a beaker: The early historyof the Belousov-Zhabotinsky reaction. *Ann. Phys. (Berlin)*, 3-4:233–237, 2016.

A.T. Winfree. The prehistory of the Belousov-Zhabotinsky oscillator. *J. Chem. Educ.*, 8:661–663, 1984.

Keller, E.F. and Segel, L.A. Initiation of slime mold aggregation viewed as an instability. *J. Theor. Biol.*, 26:399–415, 1970.

Keller, E.F. and Segel, L.A. Model for chemotaxis. *J. Theor. Biol.*, 30:225–234, 1971.

Childress, S. and Percus, J.K. Nonlinear Aspects of Chemotaxis. *Math. Biosci.*, 56:217–237, 1981.

E.F. Keller. *Making sense of life. Explaining biological development with models, metaphors, and machines*. Harvard University Press, Cambridge, MA, 2003.

L.D. Landau and E.M. Lifshitz. *Quantum Mechanics. Non-relativistic theory*. Pergamon Press, Oxford, UK, 2nd edition, 1965.

L.D. Landau and E.M. Lifshitz. *Theory of Elasticity*. Butterworth-Heinemann, Oxford, UK, 3rd edition, 1986.

E. Lauga. *The Fluid Dynamics of Cell Motility*. Cambridge University Press, Cambridge, UK, 2020.

M.J. Lighthill. *Mathematical Biofluiddynamics*. Society for Industrial and Applied Mathematics, Philadelphia, 1975.

C.C. Lin and L.A. Segel. *Mathematics Applied to Deterministic Problems in the Natural Sciences*. Macmillan Publishing Co., Inc., New York, 1974.

S. Lipschutz. *Differential Geometry. Schaum's Outline Series*. McGraw-Hill Education, New York, 1969.

D.A. McQuarrie. *Statistical Mechanics*. Harper & Row, New York, 1976.

P. Nelson. *Biological Physics: Energy, Information, Life*. Chiliagon Science, Philadelphia, PA, student edition, 2020.

R. Phillips, J. Kondev, J. Theriot, H.G. Garcia, and N. Orme. *Physical Biology of the Cell*. Garland Science, Boca Raton, FL, 2nd edition, 1998.

J.S. Rowlinson and B. Widom. *Molecular Theory of Capillarity*. Oxford University Press, Oxford, 1982.

C. Tanford. *The hydrophobic effect: formation of micelles and biological membranes*. Wiley, New York, 1973.

D.W. Thompson. *On Growth and Form*. Dover Publications, Mineola, N.Y., the complete revised edition, 1992.

9
Index